

Spectroscopic Investigations of Hydrogen Bond Dynamics in Liquid Water

by

Christopher J. Fecko

B.A. Swarthmore College, 1998

Submitted to the Department of Chemistry
in partial fulfillment of the requirements for the degree of

Doctor of Philosophy

at the

Massachusetts Institute of Technology

June 2004

© Massachusetts Institute of Technology. All rights reserved.

Signature of Author: _____
Christopher J. Fecko
May 10, 2004

Certified by: _____
Andrei Tokmakoff
Associate Professor of Chemistry
Thesis Supervisor

Accepted by: _____
Robert W. Field
Professor of Chemistry
Chairman, Departmental Committee on Graduate Studies

This doctoral thesis has been examined by a committee of the Department of Chemistry that included:

Professor Keith A. Nelson _____
Chair

Professor Jianshu Cao _____

Professor Andrei Tokmakoff _____
Thesis Supervisor

Spectroscopic Investigations of Hydrogen Bond Dynamics in Liquid Water

by

Christopher J. Fecko

Submitted to the Department of Chemistry on May 20, 2004
in partial fulfillment of the requirements for the degree of
Doctor of Philosophy

Abstract

Many of the remarkable physical and chemical properties of liquid water are due to the strong influence hydrogen bonds have on its microscopic dynamics. However, because of the fast timescales involved, there are relatively few experimental techniques capable of directly probing rearrangements of water's hydrogen bonded network. In this thesis, I investigate ultrafast intermolecular dynamics of water with time-resolved Raman and time-resolved infrared spectroscopies. These two sets of measurements provide a complimentary view of the collective and local behavior of molecular motions. Using a novel Raman technique, spatially masked optical Kerr effect spectroscopy, I first measured interaction-induced fluctuations in the isotropic many-body polarizability of water and several other liquids. In contrast to the behavior of simple liquids, the isotropic response of water is exceedingly fast and distinct from the well-known anisotropic response. I then designed and built an optical parametric amplifier that produces sub-50 fs pulses of mid-IR light to investigate the intermolecular dynamics of water through their effect on the OH oscillator of HOD in D₂O. By analyzing the results of three-pulse vibrational echo and polarization-selective pump-probe measurements with a comprehensive theory to describe vibrational dynamics, I extracted the timescales for vibrational relaxation, dephasing and molecular reorientations. At short times, vibrational dephasing reflects an underdamped 180 fs hydrogen bond oscillation, but the long time behavior indicates collective structural reorganization of the hydrogen bond network a 1.4 ps timescale. The anisotropy decays on timescales of 50 fs and 3 ps, which are attributed to librations and rotational diffusion, respectively. Lastly, I used two-dimensional infrared spectroscopy to investigate the frequency dependence of the dynamics. Preliminary results reflect a distribution of timescales for both local motion and collective reorganization.

Thesis Supervisor: Andrei Tokmakoff
Title: Associate Professor of Chemistry

Acknowledgements

I am grateful to a large number of people who have influenced my path in life and supported me along the way, allowing me the privilege of completing a Ph.D. at such a distinguished institution. I have been lucky to have positive role models who have taught me the value of hard work, a good education, and critical thinking from my early years through my time in graduate school.

My scientific interest was established in high school chemistry classes taught by Ron Pallack, who took great pride in challenging students to reach beyond the elementary science presented in textbooks. However, it was through impeccable teaching and personal interactions with the chemistry and physics professors at Swarthmore College that I gained a true love of science. The mentoring of Tom Stephenson fostered my interest in physical chemistry, and provided me the first opportunity to experience the excitement and satisfaction of scientific research. Tom educated me on the finer points of spectroscopy and taught me many broader skills that have been invaluable in my graduate career.

During my time at MIT, I have had the opportunity to interact with many gifted scientists, who have not only aided with specific problems in my research, but have furthered my intellectual development through challenging discussions and collaborations. I am indebted to the brilliant members of "Team Water", most notably Joel Eaves and Joe Loparo. I have benefited many times from Joel's ability to attack problems with analytical fervor, and

can only hope that I take some of this with me, along with some of his scientific cynicism that has naturally rubbed off on me along the way. Joe's invaluable technical abilities and dedication to completing the "hardest optical experiment", allow me to describe him as the perfect lab partner. He has brought hilarity to our lab and has become a true friend. I have enjoyed working with Joe through the trials and tribulations of our project and am proud to leave it in his hands. My work on the water project has also benefited greatly from discussions with Phil Geissler, an exceptional theorist, and Sean Roberts, our newest contributor.

I owe much gratitude to all of the other current and past members of the Tokmakoff group for enhancing my time in graduate school. In particular, I was lucky to work with Nuri Demirdöven and Munira Khalil for over five years, who accomplished amazing research in the Tokmakoff group and continue to make a large impact in their new endeavors. Their dedication and persistent work ethic have inspired me throughout our time here. I have also greatly benefited from interactions with Oleg Golonzka, Chris Cheatum, Hoi Sung Chung, Justine McCracken, Adam Smith, Matt DeCamp, Lauren DeFlores and Ziad Ganim.

Of course, the research presented here has been driven by my advisor, Andrei Tokmakoff, who has provided me with the knowledge, motivation and enthusiasm to complete my doctoral education. I consider myself lucky to have the opportunity to participate in the early stages of a group that is sure to revolutionize the field of time-resolved spectroscopy under his leadership. Andrei has taught me the importance of risk-taking and self-assurance in science and I will long remember much of his insightful advice. More recently, Andrei has permitted me to work primarily on evenings and weekends so that I can watch my daughter during the weekdays, and I am grateful for his flexibility and

willingness to accommodate my growing family. I would also like to thank the other members of my thesis committee, Jianshu Cao and Keith Nelson, for comments and advice.

My family has consistently offered me the guidance, unfailing support and love that allow me to continue my education and pursue my scientific interests. My parents, Bill and Ethel Fecko, were the earliest and most important teachers in my life. They instructed me on matters much more important than how to be a good scientist. The monetary and personal sacrifice that they continue to make for the benefit of my education astonishes me. I can only hope that I can be as good of a parent to my own children. I also owe so much to my in-laws, Denny and Sandy Koehler, who are the kindest people in the world and have adopted me as a true son. I am lucky to have found such a loving second family. The rest of my family, my brothers, sisters, grandparents, aunts, uncles, nieces and nephews, have all provided love and support in so many ways throughout my life. I would particularly like to thank those that have gone above and beyond the call of duty to visit us from out-of-town to baby-sit, since I could not have completed this degree without their help.

Above all, I dedicate this work to my beautiful wife Jill and our little bundle of joy Madalyn. Jill has provided me with an unbelievable amount of support and encouragement over the last 10+ years, but most notably through my time in graduate school. She has shared my frustrations and hardships, and lifted me out of the “depths of despair” more times than I’d like to admit. She is an amazing scientist herself, but is always looking to praise my achievements above her own remarkable record. I thank God every day for her love. More recently, I have witnessed her devotion and passion as the mother of our daughter, and have fallen even more deeply in love with her as a result. Madalyn and her future brothers and sisters are the newfound motivation for my work.

Contents

List of Figures.....	11
-----------------------------	-----------

List of Tables	14
-----------------------------	-----------

1. Introduction.....	15
-----------------------------	-----------

1.1 Why study water?	15
----------------------------	----

1.2 Context of this work.....	17
-------------------------------	----

1.3 Thesis outline	22
--------------------------	----

References.....	25
-----------------	----

2. Isotropic and anisotropic Raman scattering from molecular liquids	29
---	-----------

2.1 Introduction.....	29
-----------------------	----

2.2 Theory	32
------------------	----

2.2.1 Many-body polarizability tensor.....	32
--	----

2.2.2 Interaction representation of the polarizability	33
--	----

2.2.3 Translational and rotational contributions to the polarizability	36
--	----

2.2.4 Response function.....	37
------------------------------	----

2.3 Experiment.....	41
---------------------	----

2.3.1	Heterodyne detected polarization	41
2.3.2	SM-OKE spectroscopy	45
2.3.3	Methods.....	49
2.3.4.	Data analysis	51
2.4	Results and Discussion	54
2.4.1	Acetonitrile, carbon disulfide and methanol.....	54
2.4.2	Water.....	64
2.4.3	Isotropic spectra of hydrogen bonding liquids.....	72
2.5	Conclusion	76
	References.....	77
3.	Theory and modeling of time-resolved IR experiments	84
3.1	Introduction.....	84
3.2	Theoretical framework.....	86
3.2.1	Third order polarization for a multilevel system	86
3.2.2	Nonlinear spectroscopy of an anharmonic oscillator.....	95
3.2.3	Calculation of experimental signals.....	104
3.3	Numerical calculations.....	107
	References.....	111
4.	Mid-IR BBO/KnbO₃ OPA.....	115
4.1	Introduction.....	115
4.2	Design and fabrication of the 3 μ m OPA	118

4.3	Characteristics of the mid-IR pulses	127
4.4	Conclusion	132
	References.....	133
5.	Ultrafast hydrogen bond dynamics in the IR spectroscopy of water	135
5.1	Introduction.....	135
5.2	Theory.....	139
	5.2.1 Response function formalism	139
	5.2.2 FWM experiments	149
	5.2.3 Numerical calculations.....	151
5.3	Experiments	152
5.4	Results.....	157
5.5	Self-consistent data modeling.....	162
5.6	Discussion.....	173
5.7	Conclusions.....	184
	References.....	187
6.	Heterogeneous dynamics in water revealed by 2DIR spectroscopy	194
6.1	Introduction.....	194
6.2	IR signatures of heterogeneous dynamics.....	196
6.3	2DIR spectroscopy.....	199
6.4	Experimental methods	203
6.5	Treatment of the data	208

6.6	Results and Discussion	210
	References.....	218
Appendix – C++ code for numerical calculation of FWM signals for water		222
A.1	Introduction.....	222
A.2	Header	224
A.3	Main	225
A.4	Functions.....	238
A.5	Amoeba and Amotry.....	294
A.6	Complex class	299
Curriculum Vitae		302

List of Figures

1-1	Depolarized Raman and infrared absorption spectra of water.....	21
2-1	Schematic representation of SM-OKE spectroscopy.....	46
2-2	Measured and reconstructed anisotropic and isotropic acetonitrile OKE signals.....	53
2-3	Self-consistent, polarization-selective acetonitrile OKE signals.....	55
2-4	Polarization-selective Fourier transform Raman spectra of acetonitrile.....	56
2-5	Anisotropic and isotropic Raman spectra of acetonitrile, CS ₂ and methanol.....	58
2-6	Low-frequency behavior of anisotropic and isotropic lineshapes.....	59
2-7	Self-consistent anisotropic and isotropic OKE signals for water.....	65
2-8	Polarization-selective Fourier transform Raman spectra of water.....	68
2-9	Comparison of experimental nuclear response functions to simulation.....	70
3-1	General Feynman diagrams for FWM experiments of a multilevel system.....	91
3-2	Pulse sequence and time variables in a homodyne FWM experiment.....	94
3-3	Feynman and ladder diagrams for FWM experiments of an anharmonic oscillator....	97
3-4	Pulse sequence and time variables in a heterodyne FWM experiment.....	106
4-1	Fundamental and overtone absorption spectra for the OH stretch of HOD/D ₂ O.....	116
4-2	Type-I KNB tuning curve for 800 nm pump pulses.....	120
4-3	Schematic diagram of the laser system used to pump the OPA.....	120
4-4	Pulse spectra of the signal beams resulting from angle tuning KNB and BBO.....	122

4-5	Pulse energy stability histograms for components in the laser system.....	124
4-6	Experimental configuration of the OPA	125
4-7	Dispersion of common mid-IR materials.....	127
4-8	Time and frequency characteristics of the mid-IR pulses generated by the OPA	131
5-1	Absorption spectrum of HOD/D ₂ O in the OH stretching region.....	136
5-2	Feynman and ladder diagrams used to model the hot ground state contribution.....	148
5-3	Experimental layout of the IR interferometer for the 3PEPS experiment	154
5-4	Experimental vibrational echoes, 3PEPS decay, and their fits for HOD/D ₂ O.....	159
5-5	Experimental polarization-dependent pump-probe signals for HOD/D ₂ O.....	161
5-6	Anisotropy decay for HOD/D ₂ O.....	162
5-7	Experimental parallel pump-probe signal and fits with different HGS parameters...	163
5-8	Temperature-dependent FTIR, HGS lineshape, and dispersed pump-probes.....	165
5-9	Rotational correlation functions from experiment and simulation	167
5-10	Extracted OH frequency correlation function and comparison to results from computer simulations	168
5-11	Coherent transients observed in the PP signal	170
5-12	Dispersed 3PEPS decays and comparison to calculations.....	172
5-13	Comparison of pump-probe signals for a sample in a cell verses flowed as a jet	174
5-14	Unified dephasing, orientational and lifetime dynamics of HOD/D ₂ O	176
5-15	Joint probability distributions from computer simulations.....	180
6-1	Hydrogen bonded and non-hydrogen bonded contributions to the OH lineshape.....	197
6-2	Time-dependent Stokes shifts predicted by computer simulations.....	199
6-3	Pulse sequence of a 2DIR experiment	200

6-4	Cartoon of 1D and 2D lineshapes in the slow and fast modulation limits.....	202
6-5	Experimental layout for the 2DIR experiment.....	204
6-6	Pulse delay interferogram	206
6-7	Typical time-time 2DIR surface of HOD/D ₂ O	210
6-8	Comparison of the homogeneous dynamics observed with 2DIR and 3PEPS.....	211
6-9	Fourier transform 2DIR spectrum for $\tau_2 = 160$ fs.....	212
6-10	Comparison of experimentally measured FT-2DIR spectra with calculations in the response function limit and from computer simulations.....	214

List of Tables

3-1	Nonvanishing tensor components for the orientational response function.....	93
3-2	Density matrix pathways that contribute to the phase matched signal in the RWA....	98
4-1	Comparison of the single-pass pulse energies from KNB and BBO	123
5-1	Summary of experimental results for vibrational dynamics of HOD/D ₂ O.....	186
5-2	Best-fit parameters for the OH frequency correlation function	186

Chapter 1

Introduction

1.1 Why study water?

Water is often perceived to be a simple liquid because it is transparent to visible light, odorless and encountered in everyday life. Even its molecular structure is simple, consisting of only three light atoms. However, from the standpoint of physical chemistry, the properties of water are far from simple.^{1,2} For example, it has anomalously high melting, boiling and critical temperatures, as well as an unusually large dielectric constant, surface tension, and viscosity. Many of the anomalies of water originate in the tendency of individual molecules to participate in four hydrogen bonds simultaneously, leading to an arrangement of molecules that is relatively sparse on short length scales and linked together on much longer length scales through a continuous network of hydrogen bonds. Thermal motions drive the dynamical rearrangement of this network by breaking and reforming individual hydrogen bonds.^{3,4} However, because each partner in a hydrogen bond interacts strongly with its other neighbors, these local processes are influenced by the organization of the rest of the network, resulting in a complicated relationship between local and collective molecular motions.⁵⁻⁷ This dynamical behavior leads to further anomalous properties, such as the ultrafast solvation

of transient charge distributions and unusually high mobility of protons in water.⁸⁻¹¹ In fact, it has a large impact on all physical, chemical and biological processes that occur in aqueous solutions.

Much of the current understanding of the intermolecular dynamics of water is derived from computer simulations,^{3-6,12,13} because only a small number of experiments have been performed that provide molecular-level detail on timescales relevant to the rearrangements of the hydrogen bond network.^{8,9,14-16} However, simulations rely on water models that have been parameterized to reproduce thermodynamic or static parameters,¹⁷ so it is not clear that the dynamics they predict (especially on extremely short timescales) follow the true behavior of water. Thus, additional experiments capable of measuring fast intermolecular dynamics of water are needed to resolve uncertainties that remain about interactions between water molecules, such as identifying the most important degrees of freedom for breaking and reforming hydrogen bonds and defining the relative importance of local versus collective forces in this process.

In this thesis, I present several spectroscopic investigations of the ultrafast dynamics of water molecules, to uncover principals that govern rearrangements of the hydrogen bond network. All of the experiments observe intermolecular dynamics through their effects on a series of short light pulses, but several techniques have been used to selectively probe different aspects of these dynamics. I describe a series of novel polarization-dependent time-resolved Raman experiments that measure the intermolecular dynamics of liquids through the many-body polarizability, separating signal contributions according to the symmetry properties of the molecular motions.¹⁸ The isotropic Raman spectra of hydrogen bonding liquids measured by this method exhibit a high frequency feature that is probably indicative

of a strong coupling between the intra- and intermolecular degrees of freedom. I also present a series of time-resolved infrared (IR) experiments on the OH stretch of HOD in D₂O, which measure frequency shifts of the OH oscillator due to the influence of the solvent. These experiments required the design and fabrication of a new mid-IR light source, as well as the development of a significant theoretical framework to interpret the results. After discussing these, I present vibrational echo peak shift and pump probe measurements that observe both local and collective behavior in the intermolecular dynamics.^{19,20} The local, deterministic motion of individual hydrogen bonds dominates the fastest vibrational dephasing, while larger-scale structural rearrangements of the network are apparent at longer times. More advanced two-dimensional IR spectroscopies reveal dynamics that depend on the local molecular environment, which is significant for the development of theories to describe rearrangements of the hydrogen bond network in terms of the breaking and reforming of individual bonds.

1.2 Context of this work

The results presented in this thesis build upon decades of prior experimental and theoretical investigations of the properties of water.^{1,3,6,8,9,12-14,21-30} While a full review of the prior work is beyond the scope of this document, some knowledge of the conclusions, particularly with regards to the intermolecular dynamics and vibrational spectroscopy of water, is helpful to understand the present experiments.

In a landmark paper over 30 years ago, Rahman and Stillinger investigated the properties of liquid water with a computer simulation, which was one of the first simulations of a molecular liquid.¹² Many of their results, which are surprisingly accurate for the

computational power available at that time (according the standards of more recent simulations using refined water models and simulation techniques), highlight the influence of hydrogen bonding on the static and dynamical properties of the liquid. For example, the velocity autocorrelation function of water contained fast oscillations that were not present in the velocity autocorrelation function of liquid argon, and were attributed to the structural rigidity imposed by hydrogen bonds. The rotational autocorrelation function also exhibited unique behavior, with a fast (< 100 fs) decay component due to hindered rotations, referred to as librations.

Since the work of Rahman and Stillinger, numerous computer simulations have addressed the intermolecular ordering and dynamics of liquid water,^{3,6,13,22-25} many of which focus on the development of methods and interaction potentials to describe hydrogen bond dynamics. Some have questioned whether it is important to consider more sophisticated approaches, such as the inclusion of polarizability and quantum mechanical effects to capture the true behavior,^{10,31-33} but further experimental results are needed to resolve these issues. However, one important idea that has emerged from a number of simulations frames the dynamics of water in terms of an energy landscape picture, reminiscent of that used to describe glasses and supercooled liquids.⁶ In this picture, the total potential energy of a water sample is represented as a highly multidimensional surface containing many local minima. Fast molecular motions, such as those observed in the simulations of Rahman and Stillinger, correspond to dynamics within individual wells, while larger scale rearrangements of the hydrogen bond network involve transitions between different wells. Collective processes have been implicated in both types of dynamics.

One of the most useful experimental tools to investigate these fast motions is vibrational spectroscopy, because both intra- and intermolecular vibrations are sensitive to interactions between molecules. The vibrational spectrum of water (Fig. 1-1) has provided a great deal of information about local environments within the liquid as well as some dynamical timescales for molecular processes.^{1,34} Isolated water (H₂O) molecules have three normal modes: a symmetric stretch (3657 cm⁻¹), bend (1595 cm⁻¹) and asymmetric stretch (3756 cm⁻¹). Although these bands are sharp in spectra of water vapor, they broaden and shift considerably in the liquid due to intermolecular interactions. The two stretching bands broaden into a single OH stretch feature (ν_s) that is centered at a much lower frequency than either of the original bands (this feature may also include a contribution from the bend overtone), while the bend (ν_b) also broadens but is shifted to a higher frequency. Hydrogen bonding explains these observations, since the extra intermolecular force lengthens the OH bond distance, decreasing the stretch frequency, but adds an extra restoring force for angular deviations to increase the bend frequency. The lines broaden because the liquid contains a distribution of intermolecular distances and angles, indicating that structural information is encoded in the vibrational frequency shifts. Systematic investigations of solids containing hydrogen bonds confirm the relationship between frequency and intermolecular structure,^{35,36} although it was not explored for liquids until recently.^{19,37,38}

Time-resolved mid-IR experiments exploit the relationship between vibrational frequency and structure by measuring time dependent frequency changes, referred to as spectral diffusion, and relating these to intermolecular structural changes.^{19,39,40} Ideally, the experiments would record the time dependence of the vibrational frequency for single molecules, and then infer changes in the solvent configuration around those molecules.

However, bulk samples are used because of experimental constraints, complicating interpretation of the results but not eliminating the usefulness of these techniques. In this case, spectral diffusion is quantitatively measured by the frequency correlation function:

$$C(t) = \langle \delta\omega(t) \delta\omega(0) \rangle \quad (1-1)$$

where $\omega(t)$ is the vibrational frequency at time t , $\delta\omega(t)$ is the difference between $\omega(t)$ and its time-averaged value, and the brackets denote an ensemble average at equilibrium. By exciting the OH stretching vibration of a dilute solution of HOD in D₂O, time-resolved IR studies observe localized OH oscillators isolated in a bath of D₂O molecules whose dynamics closely resemble that of H₂O. Hole burning experiments with mid-IR pulses have measured 0.5 – 1 ps spectral diffusion timescales, which have been interpreted as the characteristic timescales for hydrogen bond making and breaking.⁴¹⁻⁴³ However, this technique suffers from limited time resolution, and there is also a lack of concrete evidence to support the interpretation. Chapter 5 covers these experiments in more detail.

Bands in the low frequency region of the vibrational spectra correspond to intermolecular motions. The depolarized Raman spectrum, which probes the dynamical many-body polarizability of the system, exhibits particularly well-defined features: a broad band that extends from 400-1000 cm⁻¹, and two narrow features at 175 cm⁻¹ and 60 cm⁻¹.^{1,14,34} The same bands have been measured with optical-heterodyne detected optical Kerr effect (OHD-OKE) spectroscopy,^{15,16} which is a time-domain technique that also probes the many-body polarizability, and inelastic neutron scattering.^{44,45} Walrafen assigned them to the normal modes of a five-molecule hydrogen-bonded structure with C_{2v} symmetry, since they resemble bands in the low frequency spectrum of ice I.¹⁴ The broad peak is due to librations (ν_L) of water molecules on sub-100 fs timescales. Walrafen suggested that some of the

breadth might arise from librations about the three molecular moments of inertia. The peaks at 175 cm^{-1} and 60 cm^{-1} are due to longitudinal (ν_T) and transverse (ν_B) intermolecular motions, which roughly correspond to hydrogen bond stretching and bending motions, respectively. Experiments and simulations have indicated that all of the features involve the motions of many molecules and are therefore inherently collective.^{6,46}

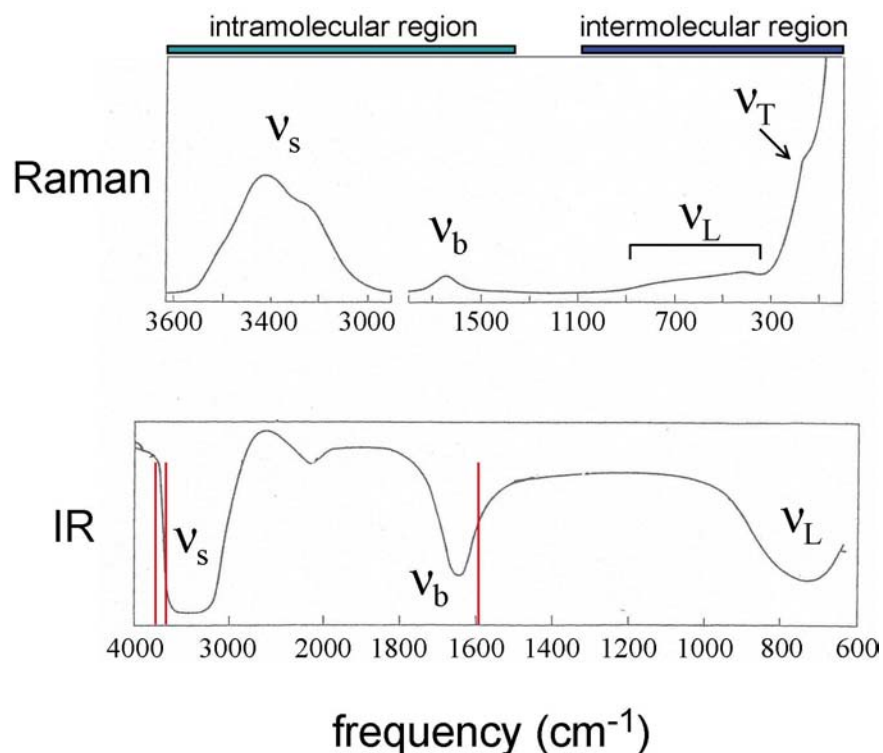


Figure 1-1. (Color) Depolarized Raman (top) and infrared (bottom) vibrational spectra of liquid water (H_2O). The most prominent features at frequencies above 1200 cm^{-1} correspond to intramolecular vibrations, while those at lower frequencies are due to intramolecular motions. Specific assignments are described in the text. Vertical lines in the IR spectrum indicate normal mode vibrational frequencies in the vapor phase. (taken from Ref. 1)

It is worth stressing that experiments which probe the intramolecular bands and those which probe the intermolecular bands provide complimentary information about the intermolecular dynamics of water. The former case observes the effect that these dynamics have on a local variable, namely the OH stretching frequency, while the latter directly

measures the collective dynamics. However, prior to the work presented in this thesis, there was a disconnect between the results interpretations from the two types of experiments. For example, time-resolved IR experiments had not been able to access the fast dynamics present in the low frequency Raman spectrum to compare the spectral densities and thus make a better experimental assessment of the local versus collective nature of these intermolecular dynamics. The present investigation utilizes both techniques as well as computer simulations to create a more unified description of the intermolecular dynamics of water. The results fit well into the energy landscape picture, in which fast motions of local coordinates are observed at early times, while larger scale rearrangements are reflected at longer times.

1.3 Thesis outline

Although a great deal has been learned about water from its low frequency depolarized Raman spectrum, which measures anisotropic contributions to the many-body polarizability, relatively little attention has been paid to the isotropic component of water's polarizability. We have developed an experimental technique, spatially masked optical Kerr effect (SM-OKE) spectroscopy, which directly measures the isotropic contribution to the transient birefringence of molecular liquids.¹⁸ **Chapter 2** describes SM-OKE and OHD-OKE measurements of the isotropic and anisotropic Raman spectra for CS₂, acetonitrile, methanol and water. The isotropic and anisotropic spectra, which form a complete and independent basis for describing nonresonant third-order experiments, separate the intermolecular dynamics by symmetry. The isotropic spectrum is especially interesting because it only measures polarizability fluctuations due to interactions between molecules. We found that the isotropic and anisotropic lineshapes are similar for non-hydrogen-bonding

liquids, while the high-frequency wing of the isotropic spectrum exhibits new features for methanol and water. The isotropic response of water is especially notable, since it is also quite different from the depolarized spectrum at lower frequencies. Several possible origins for this behavior are discussed.

The remainder of the thesis is devoted to investigations of the intermolecular dynamics of water using time-resolved IR techniques. As with previous studies, our experiments probe the OH stretch vibrational dynamics of a dilute solution of HOD in D₂O. In **Chapter 3**, I develop a theoretical formalism for resonant nonlinear experiments of an anharmonic oscillator, which is used in later chapters to extract meaningful quantities from the experimental data. The theory is based on a treatment of four wave mixing spectroscopies of multilevel systems linearly coupled to a bath of harmonic oscillators with arbitrary time scales.^{47,48} It quantifies bath-induced fluctuations in the transition energy with a frequency correlation function, molecular rotations with a reorientational correlation function and vibrational population relaxation with a phenomenological decay rate. By assuming harmonic scaling relationships, the third-order material response function is completely specified with these three dynamical quantities and the average fundamental and overtone transition frequencies. Our treatment is geared toward numerical evaluation of the experimental signals, and details of this calculation are provided in **Chapter 3** as well as in the **Appendix**.

Measurement of the fastest dynamics in water with time-resolved IR spectroscopy required the generation of ultrashort pulses centered near the OH absorption line at 3 μm . **Chapter 4** outlines the design and fabrication of a new white-light seeded, two-stage optical parametric amplifier (OPA) to meet these specifications. It presents calculations and

experiments to justify the crystal choices and some information about other optical components that optimize the OPA to produce short pulses. The output pulse spectrum is typically 400 cm^{-1} broad, which spans the entire fundamental and most of the overtone OH transitions, and thus ensures that all relevant dynamics are measured. The time amplitude profiles extracted from a second harmonic frequency resolved optically gated autocorrelation are usually sub-50 fs in duration, but pulses as short as 42 fs have been observed. The phase profiles are also usually quite flat.

I present our main investigations into the intermolecular dynamics of water using time-resolved IR techniques in **Chapters 5** and **6**. The experiments and theory in the former chapter assumes that the intermolecular dynamics of individual molecules are independent of their environment, while the latter chapter investigates heterogeneous dynamics. Both rely on computer simulations performed by collaborators to relate the experimentally observed vibrational dynamics to molecular quantities.

Chapter 5 presents a set of three pulse vibrational echo peak shift and polarization-dependent pump-probe measurements to separate contributions from dephasing, reorientations and population relaxation to the vibrational dynamics.^{19,20} The vibrational correlation function extracted from these measurements exhibits a sub-60 fs initial decay, a recurrence that peaks at 180 fs, and a long-time decay of 1.4 ps. Computer simulations reveal that the OH frequency shifts arise from changes in the molecular electric field that acts on the oscillator. The fast initial decay and recurrence are dominated by local forces, and specifically reflect an underdamped hydrogen bond oscillation. The longer time scale is due to collective structural reorganizations. The reorientational correlation function also decays with < 60 fs component, as well as a 3 ps slow component. These are due to librations and

rotational diffusion. Our value for the population lifetime, 700 fs, agrees with previous experimental results.

Finally, heterogeneous dynamics are measured in **Chapter 6** with two-dimensional IR spectroscopy. The preliminary results are compared to calculations of the two-dimensional lineshapes using a correlation function approach, which neglects heterogeneous dynamics, and the results of computer simulations,⁴⁹ which predict dynamics that are very sensitive to the hydrogen-bonded state of the OH oscillator. The experimental results suggest that the true behavior lies in between these two limits.

References

- (1) Eisenberg, D.; Kauzmann, W. *The Structure and Properties of Water*; Clarendon Press: Oxford, 1969.
- (2) *Water - A Comprehensive Treatise*; Franks, F., Ed.; Plenum: New York, 1972-1982; Vol. 1-7.
- (3) Luzar, A.; Chandler, D. *Nature* **1996**, *379*, 55.
- (4) Luzar, A.; Chandler, D. *Phys. Rev. Lett.* **1996**, *76*, 928.
- (5) Ohmine, I.; Tanaka, H.; Wolynes, P. G. *J. Chem. Phys.* **1988**, *89*, 5852.
- (6) Ohmine, I.; Tanaka, H. *Chem. Rev.* **1993**, *93*, 2545.
- (7) Bopp, P. A.; Kornyshev, A. A.; Sutmann, G. *J. Chem. Phys.* **1998**, *109*, 1939.
- (8) Jarzeba, W.; Walker, G. C.; Johnson, A. E.; Kahlow, M. A.; Barbara, P. F. *J. Phys. Chem.* **1988**, *92*, 7039.
- (9) Jimenez, R.; Fleming, G. R.; Kumar, P. V.; Maroncelli, M. *Nature* **1994**, *369*, 471.
- (10) Schmitt, U. W.; Voth, G. A. *J. Chem. Phys.* **1999**, *111*, 9361.

- (11) Geissler, P. L.; Dellago, C.; Chandler, D.; Hutter, J.; Parrinello, M. *Science* **2001**, *291*, 2121.
- (12) Rahman, A.; Stillinger, F. H. *J. Chem. Phys.* **1971**, *55*, 3336.
- (13) Stillinger, F. H. *Adv. Chem. Phys.* **1975**, *31*, 1.
- (14) Walrafen, G. E. *J. Chem. Phys.* **1964**, *40*, 3249.
- (15) Palese, S.; Schilling, L.; Miller, R. J. D.; Staver, P. R.; Lotshaw, W. T. *J. Phys. Chem.* **1994**, *98*, 6308.
- (16) Castner, E. W., Jr.; Chang, Y. J.; Chu, Y. C.; Walrafen, G. E. *J. Chem. Phys.* **1995**, *102*, 653.
- (17) Robinson, G. W.; Zhu, S.-B.; Singh, S.; Evans, M. W. *Water in Biology, Chemistry and Physics*; World Scientific: New Jersey, 1996; Vol. 9.
- (18) Fecko, C. J.; Eaves, J. D.; Tokmakoff, A. *J. Chem. Phys.* **2002**, *117*, 1139.
- (19) Fecko, C. J.; Eaves, J. D.; Loparo, J. J.; Tokmakoff, A.; Geissler, P. L. *Science* **2003**, *301*, 1698.
- (20) Loparo, J. J.; Fecko, C. J.; Eaves, J. D.; Roberts, S. T.; Tokmakoff, A. *Phys. Rev. Lett.* **2004**, submitted.
- (21) Pauling, L. The Structure of Water. In *Hydrogen Bonding: Papers Presented at the Symposium on Hydrogen Bonding (1957; Slovenia)*; Hadzi, D., Ed.; Pergamon Press: New York, 1959; pp 1.
- (22) Sceats, M. G.; Stavola, M.; Rice, S. A. *J. Chem. Phys.* **1979**, *70*, 3927.
- (23) Stanley, H. E. *J. Phys. A* **1979**, *12*, L329.
- (24) Stillinger, F. H.; Weber, T. A. *J. Phys. Chem.* **1983**, *87*, 2833.
- (25) Errington, J. R.; Debenedetti, P. G. *Nature* **2001**, *409*, 318.

- (26) *The Physics and Physical Chemistry of Water*; Franks, F., Ed.; Plenum Press: New York, 1975; Vol. 1.
- (27) Rice, S. A. Conjectures on the Structure of Amorphous Solid and Liquid Water. In *Structure of Liquids*; Schuster, P., Ed.; Springer-Verlag: New York, 1975; Vol. 60.
- (28) Lang, E. W.; Ludemann, H.-D. *Angew. Chem. Int. Ed.* **1982**, *21*, 315.
- (29) Cunsolo, A.; Ruocco, G.; Sette, F.; Masciovecchio, C.; Mermet, A.; Monaco, G.; Sampoli, M.; Verbeni, R. *Phys. Rev. Lett.* **1999**, *82*, 775.
- (30) Keutsch, F. N.; Saykally, R. J. *PNAS* **2001**, *98*, 10533.
- (31) Rick, S. W.; Stuart, S. J.; Berne, B. J. *J. Chem. Phys.* **1994**, *101*, 6141.
- (32) Xu, H.; Stern, H. A.; Berne, B. J. *J. Phys. Chem. B* **2002**, *106*, 2054.
- (33) Silvestrelli, P. L.; Parrinello, M. *J. Chem. Phys.* **1999**, *111*, 3572.
- (34) Walrafen, G. E. Raman and Infrared spectral investigations of water structure. In *Water: A Comprehensive Treatise*; Franks, F., Ed.; Plenum: New York, 1972; Vol. 1; pp 151.
- (35) Novak, A. Hydrogen bonding in solids. Correlation of spectroscopic and crystallographic data. In *Structure and Bonding*; Dunitz, J. D., Hemmerich, P., Holm, R. H., Ibers, J. A., Jorgenson, C. K., Neilands, J. B., Reinen, D., Williams, R. J. P., Eds.; Springer-Verlag: New York, 1974; Vol. 18; pp 177.
- (36) Mikenda, W. *J. Mol. Struct.* **1986**, *147*, 1.
- (37) Rey, R.; Moller, K. B.; Hynes, J. T. *J. Phys. Chem. A* **2002**, *106*, 11993.
- (38) Lawrence, C. P.; Skinner, J. L. *J. Chem. Phys.* **2003**, *118*, 264.
- (39) Bratos, S.; Leicknam, J.-C. *J. Chem. Phys.* **1994**, *101*, 4536.
- (40) Bratos, S.; Leicknam, J.-C. *J. Mol. Liquids* **1995**, *64*, 151.

- (41) Bratos, S.; Gale, G. M.; Gallot, G.; Hache, F.; Lascoux, N.; Leicknam, J.-C. *Phys. Rev. E* **2000**, *61*, 5211.
- (42) Bakker, H. J.; Nienhuys, H.-K.; Gallot, G.; Lascoux, N.; Gale, G. M.; Leicknam, J.-C.; Bratos, S. *J. Chem. Phys.* **2002**, *116*, 2592.
- (43) Laenen, R.; Simeonidis, K.; Laubereau, A. *Bull. Chem. Soc. Jpn.* **2002**, *75*, 925.
- (44) Teixeira, J.; Bellissent-Funel, M.-C.; Chen, S. H.; Dorner, B. *Phys. Rev. Lett.* **1985**, *54*, 2681.
- (45) Teixeira, J.; Bellissent-Funel, M.-C.; Chen, S. H. *J. Phys. Condens. Matter* **1990**, *2*, 105.
- (46) Walrafen, G. E. *J. Phys. Chem.* **1990**, *94*, 2237.
- (47) Sung, J.; Silbey, R. J. *J. Chem. Phys.* **2001**, *115*, 9266.
- (48) Sung, J.; Silbey, R. J. *J. Chem. Phys.* **2003**, *118*, 2443.
- (49) Eaves, J. D. *Vibrational dynamics from the molecule's perspective*, Massachusetts Institute of Technology, 2004.

Chapter 2

Isotropic and anisotropic Raman scattering from molecular liquids

2.1 Introduction

Understanding the dynamics associated with local and long-range structures within molecular liquids continues to be an experimental challenge, because only limited methods exist which are simultaneously sensitive to collective molecular structure and the time-dependent evolution of these structures. For room-temperature molecular liquids, dynamics that occur on the 10^{-15} to 10^{-11} second time scale have a wide variety of molecular motions and interactions associated with them, including molecular translation and reorientation, Coulombic interactions, collision-induced effects, and hydrogen bonding. Numerous femtosecond optical and infrared spectroscopies have been used to study these dynamics in equilibrium neat liquids or as the response of a solvent to charge redistribution. The persistent complication is that experiments are not in themselves effective at resolving the nature and time-scale of one process from another, or describing the correlation of one motion with another.

Among the most widely used time-domain spectroscopies employed to study collective liquid motions are methods based on impulsive Raman excitation with nonresonant femtosecond pulses. These experiments have been used to probe the polarizability relaxation dynamics of a variety of polar and non-polar liquids and solutions, supercooled liquids, polymers, and liquid crystals.¹⁻⁸ Nonresonant third-order nonlinear experiments are straightforward to perform, but they observe collective motions through the many-body polarizability, thus requiring copious amounts of modeling and simulation to relate observables to molecular quantities.⁹ The most common model is the interaction representation of the polarizability, in which the polarizability is calculated using Coulombic interactions between individual molecules. However, the observed low-frequency Raman spectral density for most systems is nearly featureless, making it difficult to extract conclusive information about the motions that contribute. More selective methods of probing would help to constrain the modeling of these systems.

One advantage of using Raman experiments to study intermolecular dynamics is that the response function is a tensor quantity. Since the many-body polarizability tensor can be separated into isotropic and anisotropic components, Raman spectroscopy with polarized light can distinguish between contributions to the molecular dynamics based on symmetry arguments.¹⁰⁻¹² Whereas the anisotropic component is dominated by molecular reorientation or collective motions with reorientational character, the isotropic response is selective to motions that are totally symmetric in the ensemble average. The isotropic response is entirely due to intermolecular interactions, and may give the best indication of the frequency dependence of translational density fluctuations. It should be important for testing the predictions of mode coupling theory, which describes density fluctuations.¹³ In the past, the

isotropic response has received little attention, since most experimental configurations (such as OHD-RIKES transient birefringence¹) probe only the anisotropic response. However, new methods with polarization control of all of the optical fields are being developed for measuring different tensor elements of the third-order response.¹⁴⁻²¹

In this chapter, I present a simple method for directly observing the isotropic nonresonant response from molecular liquids. The spatially masked optical Kerr effect (SM-OKE) is a two pulse experiment that measures the isotropic response and other tensor elements that include isotropic dynamics. By treating the probe pulse as a Gaussian beam with spatially varying phase, I demonstrate that a partially closed iris introduces an in-phase local oscillator for heterodyne detection. This allows experiments with parallel polarizations to measure a nonresonant (birefringent) response in the form of a nonlinear SM-OKE signal.

We applied this method to the study of four model molecular liquids: carbon disulfide, acetonitrile, methanol, and water. These liquids have been well studied by experiment and simulation. Furthermore, we can compare the isotropic and anisotropic response from weakly and strongly interacting liquids, from polar and nonpolar liquids, and from protic and aprotic polar solvents.

To begin our description of the experiment, and the selective nature of the isotropic and anisotropic responses, Section II presents the different representations of the many-body polarizability through which we observe the system. The emphasis is on the interaction representation of the polarizability. Section III describes the theory and implementation of the SM-OKE experiment. The experimental results for all liquids are then presented and discussed in Section IV. The isotropic response effectively suppresses molecular reorientation in all liquids, and is quite distinct from the anisotropic response in the

hydrogen-bonding liquids. For water, the isotropic response is particularly curious, since it is exceeding fast and completely different from the well-characterized anisotropic response.

2.2 Theory

2.2.1 Many-body polarizability tensor

The experimental observable of nonresonant optical spectroscopies that encodes information about the structure and dynamics of liquids is the many-body polarizability, $\Pi(t)$. To obtain a molecular picture of liquids, this laboratory frame quantity must be decomposed into contributions from microscopic quantities. Because the polarizability is a function of all $3N$ nuclear coordinates, and intermolecular interactions within the liquid state are extremely complex, the best choice for a physically meaningful microscopic representation is not readily apparent. One approach is to expand the polarizability in a Taylor-series about a set of equilibrium nuclear coordinates.^{22,23} This implies that the liquid behaves as a collection of damped oscillators over short time intervals and therefore lends itself to a normal mode treatment of the liquid.²⁴⁻²⁹ A second approach involves a quasi-perturbative site-basis construction of the many-body polarizability by the addition of intermolecular interactions to a collection of gas phase molecular polarizabilities.³⁰⁻³⁶ To provide additional physical insight, the polarizability can be further decomposed into contributions from rotational and translational degrees of freedom.^{27,30,35} The relationship between the normal mode basis and the site basis representation of the polarizability is non-trivial.²² The interaction representation of the polarizability provides a more intuitive framework for a qualitative interpretation of our low-frequency spectra, and it will therefore be discussed in this section.

2.2.2 Interaction representation of the polarizability

The polarizability of an isolated molecule is described by the molecular (M) polarizability tensor

$$\boldsymbol{\alpha}^M(t) = \alpha \mathbf{I} + \boldsymbol{\beta}(t) \quad (2-1)$$

where $\alpha = \text{Tr}(\boldsymbol{\alpha}^M(t))/3$ is the isotropic component, \mathbf{I} is the unit matrix, and the anisotropic part is the product of the gas phase anisotropy with the traceless molecular orientation tensor, $\boldsymbol{\beta}(t) = \gamma \mathbf{Q}(t)$. In the case of molecules with axially symmetric charge distributions, the orientation tensor is the second Legendre polynomial of the unit vector along the molecular axis, $\mathbf{Q}(t) = \frac{1}{2}(\hat{\mathbf{u}}(t)\hat{\mathbf{u}}(t) - \mathbf{I})$. For isolated molecules, the polarizability varies with the displacement of intramolecular degrees of freedom, which are often neglected for intermolecular polarizabilities.

In condensed phase systems, the total polarizability can be decomposed into a contribution from the individual molecules (M) and interaction-induced (II) contributions that are due to interactions between molecules:³⁰

$$\boldsymbol{\Pi}(t) = \boldsymbol{\Pi}^M(t) + \boldsymbol{\Pi}^{\text{II}}(t) \quad (2-2)$$

$$\boldsymbol{\Pi}^M(t) = \sum_{n=1}^N \boldsymbol{\alpha}_n^M(t). \quad (2-3)$$

The molecular term is merely the sum of the isolated molecular polarizabilities.

In order to treat the II polarizability, a model is needed for intermolecular interactions within the fluid. For weakly interacting molecular liquids, a standard assumption is that electronic overlap and frame distortions may be neglected, and that intermolecular

interactions take place via long-range multipolar forces.^{9,37,38} Molecular dynamics (MD) simulations have established that truncation of the interactions after the dipole-induced-dipole (DID) term adequately describes depolarized Raman scattering in many simple fluids.^{30,31,39} In the DID approximation, the Π term takes the form:

$$\mathbf{\Pi}^{\text{II}}(t) \cong \sum_{n=1}^N \sum_{m \neq n} \boldsymbol{\alpha}_n^M(t) \mathbf{T}^{(2)}(r_{nm}(t)) \tilde{\boldsymbol{\alpha}}_m^M(t) \quad (2-4)$$

where $\mathbf{T}^{(2)}(r_{mn}(t)) = \nabla_i \nabla_j (r_{mn}(t))^{-1}$ is the time-dependent dipole interaction tensor and $\tilde{\boldsymbol{\alpha}}_m^M(t)$ is the effective polarizability of molecule m that accounts for the local field from all other molecules.

$$\tilde{\boldsymbol{\alpha}}_m^M(t) = \boldsymbol{\alpha}_m^M(t) + \sum_{p=1}^N \sum_{p \neq m} \boldsymbol{\alpha}_p^M(t) \mathbf{T}(r_{mp}(t)) \boldsymbol{\alpha}_p^M(t) + \dots \quad (2-5)$$

Intermolecular interactions act as a time-dependent modification to the isolated molecular polarizability, since the total molecular polarizability is a function of intermolecular distances and orientations. From a computational point of view, the polarizability of a single molecule can be calculated to all orders of the DID approximation by using an iterative algorithm,³⁵ by matrix inversion,³¹ or through the use of a renormalized interaction tensor.^{40,41} The first order DID approximation, in which $\tilde{\boldsymbol{\alpha}}_m^M(t)$ is replaced by the isolated molecule polarizability in Eq. (2-4), is used below. The range of validity of this approximation is questionable; recent calculations point to the importance of cancellation effects between 2, 3 and 4 body interactions, especially at long times.^{31,32} Other studies have suggested that the inclusion of higher order multipole terms or electronic overlap terms is crucial for a calculation of the many-body polarizability.^{38,42-44}

Partitioning the polarizability according to Eq. (2-2) provides a physical basis for its interpretation. For rigid molecules, the only contribution a single molecule can make to the time-dependent correlation function is through rotation. Because a closely packed environment hinders molecular rotation in liquids, molecular reorientation contributes on picosecond time-scales and is often treated diffusively.³⁹ The II term can be modulated by the change in orientation of one molecule with respect to another, or by a change in the intermolecular distance between the two. Thus, it is a measure of local orientational and density fluctuations within the liquid. The II polarizability is also sensitive to changes in electronic distributions, so it can contain components that are modulated at frequencies higher than the single molecule term. Because both molecular and II polarizabilities are sensitive to orientational fluctuations, it is possible that cross-correlations between the two make significant contributions to the dynamics.

In order to determine which polarizability terms contribute to the isotropic and anisotropic response, Eq. (2-1) can be used to expand Eq. (2-2), which yields^{30,32}

$$\mathbf{\Pi} = \mathbf{\Pi}^{M,\alpha} + \mathbf{\Pi}^{M,\beta} + \mathbf{\Pi}^{II,\alpha\alpha} + \mathbf{\Pi}^{II,\beta\beta} + \mathbf{\Pi}^{II,\alpha\beta+\beta\alpha} \quad (2-6)$$

The explicit time dependence has been left out. The α and β notation indicates contributions from the α^M isotropic or anisotropic terms respectively. For a rigid molecule, the first term is constant in time and is not observed in the intermolecular Raman signal. The second term, corresponding to rotational diffusion, is traceless and can only contribute to the anisotropic polarizability. Likewise, the third term is also traceless since it consists of the product of two scalars with the dipole interaction tensor.³⁷ The two remaining terms can contribute to both the isotropic and anisotropic polarizability.³⁰ Thus, the many-body polarizability can be partitioned

$$\mathbf{\Pi} = \mathbf{\Pi}^{iso} + \mathbf{\Pi}^{aniso} \quad (2-7)$$

where the isotropic (scalar) and anisotropic (traceless) parts of the polarizability contain:

$$\mathbf{\Pi}^{iso} = a_{iso} \mathbf{\Pi}^{II, \alpha\beta + \beta\alpha} + b_{iso} \mathbf{\Pi}^{II, \beta\beta} \quad (2-8)$$

$$\mathbf{\Pi}^{aniso} = \mathbf{\Pi}^{M, \beta} + \mathbf{\Pi}^{II, \alpha\alpha} + a_{aniso} \mathbf{\Pi}^{II, \alpha\beta + \beta\alpha} + b_{aniso} \mathbf{\Pi}^{II, \beta\beta} . \quad (2-9)$$

For the partitioning constants $a_{iso} + a_{aniso} = 1$ and $b_{iso} + b_{aniso} = 1$; expressions for these variables are given by Frenkel and McTague.³⁰ It is important to note that the isotropic polarizability measures purely interaction-induced effects, and that only terms dependent on the anisotropic part of α^M contribute to the total isotropic polarizability. Murry, Fourkas and Keys therefore conclude that the strength of the isotropic response is an indication of the amount of microscopic asymmetry within solvent cavities.²³ Lastly, we note that if the polarizability is expanded beyond first order DID to include three (or more) body interactions, the isotropic polarizability also contains induced contributions from the isotropic single molecule polarizability.

2.2.3 Translational and rotational contributions to the polarizability

Because the correlation between the molecular polarizability and the II component depends on orientation, a more microscopically descriptive way to divide the polarizability is in terms of rotational and translational contributions.^{27,30,35}

$$\mathbf{\Pi}(t) = \mathbf{\Pi}^{rot}(t) + \mathbf{\Pi}^{trans}(t) \quad (2-10)$$

In brief, each component of $\mathbf{\Pi}^{II}(0)$ is projected along $\mathbf{\Pi}^M(0)$ to obtain the fraction of the interaction-induced polarizability that is correlated with molecular orientations, Δ_{mn} . Then,

the rotational polarizability can be written as $\Pi_{ij}^{rot}(t) = (1 + \Delta_{ij})\Pi_{ij}^M(t)$ and the translational contribution as $\Pi_{ij}^{trans}(t) = \Pi_{ij}^H(t) - \Delta_{ij}\Pi_{ij}^M(t)$.

The relationship between the translational/rotational partitioning and the anisotropic and isotropic polarizability is not trivial, but the rotation-translation cross terms are of particular interest. Rotational and translational terms are orthogonal for any instant in time by construction, however they are not necessarily uncorrelated if measured at two different times. Because of the transform relationship between time and frequency, this requires that the rotation-translation cross term must vanish when integrated over all frequencies, although it can have non-zero spectral intensity for a given frequency. It has been found in simulations that the cross term is often negative for low frequencies, as discussed above, but passes through zero and is positive at higher frequencies.³⁰ This has the effect of shifting the spectral center of gravity of liquids to higher frequencies.

2.2.4 Response function

Information about the microscopic liquid dynamics as observed through the polarizability is contained in the material response function. Within the Born-Oppenheimer approximation, the third-order response function may be separated into contributions from electronic and nuclear degrees of freedom $R^{(3)} = R^{(3)el} + R^{(3)nuc}$. For electronically nonresonant transitions, the electronic response function is effectively instantaneous in time⁴⁵

$$R_{ijkl}^{(3)el}(\tau) = \langle \gamma_{ijkl} \rangle \delta(\tau) \quad (2-11)$$

and therefore contains no information about molecular dynamics. The nuclear response function is proportional to the correlation function of the polarizability operator:

$$R_{ijkl}^{(3)nuc}(\tau) = \frac{i}{\hbar} \langle [\Pi_{ij}(\tau), \Pi_{kl}(0)] \rangle. \quad (2-12)$$

Here i, j, k and l indicate the components of Π in the laboratory frame (x, y, z) . When describing intermolecular dynamics, the quantum mechanical response function is often replaced with a classical impulse response function using the fluctuation-dissipation theorem⁴⁶

$$R_{ijkl}^{(3)nuc}(\tau) = \frac{1}{kT} \frac{d}{dt} \langle \Pi_{ij}(\tau) \Pi_{kl}(0) \rangle. \quad (2-13)$$

The response function can also be represented in the frequency domain through a Fourier-transform

$$\chi(\omega) = \int_0^{\infty} R(\tau) e^{i\omega\tau} d\tau \quad (2-14)$$

where $\text{Im}[\chi(\omega)]$ or equivalently χ'' is the susceptibility, a spectral density for polarizability relaxation.

Although the response function is a tensor quantity, which in principle consists of 64 elements, symmetry constraints limit the number of independent elements.⁴⁷ For an isotropic medium, symmetry with respect to inversion and rotations limits the number of independent elements to three, which are related by $R_{zzzz}^{(3)} = R_{zzyy}^{(3)} + R_{zyzy}^{(3)} + R_{zyyz}^{(3)}$. Kleinmann symmetry further allows the interchange of indices that are time-coincident. Thus, the entire electronic response can be described by a single tensor component, $R_{zzzz}^{(3)el}/3 = R_{zzyy}^{(3)el} = R_{zyzy}^{(3)el} = R_{zyyz}^{(3)el}$. Two elements are required to completely describe the third-order nuclear response, since $R_{zyzy}^{(3)nuc} = R_{zyyz}^{(3)nuc}$. For the remainder of this discussion, R will refer to the third-order nuclear response unless indicated otherwise.

The tensor elements of the third-order response can be used to separate the isotropic and anisotropic dynamics of the many body polarizability. Orientational averaging for an isotropic medium allows the response function tensor elements discussed above to be related to the isotropic and anisotropic polarizability response functions.^{12,48}

$$R_{aniso}(\tau) = \frac{1}{2} [R_{zzzz}(\tau) - R_{zzyy}(\tau)] = \frac{1}{2} [R_{zyzy}(\tau) + R_{zyyz}(\tau)] \quad (2-15)$$

$$\approx \frac{1}{15kT} \frac{d}{dt} \langle \Pi^{aniso}(\tau) \Pi^{aniso}(0) \rangle$$

$$R_{iso}(\tau) = \frac{1}{3} [R_{zzzz}(\tau) + 2R_{zzyy}(\tau)] \quad (2-16)$$

$$\approx \frac{1}{kT} \frac{d}{dt} \langle \Pi^{iso}(\tau) \Pi^{iso}(0) \rangle$$

Because the anisotropic polarizability transforms as a second rank tensor and the isotropic as a zero rank tensor, no correlation can exist between the two³⁰ so that $R_{aniso}(\tau)$ and $R_{iso}(\tau)$ represent a complete and independent basis for describing the third order nuclear response. The isotropic response has also been referred to as the R_{zzmm} tensor element, where the index m indicates a projection of the polarizability onto the laboratory frame axis oriented at 54.7° relative to the z axis, i.e. the magic angle.¹²

The anisotropic response contains only depolarized Raman bands in the intramolecular Raman spectra.¹⁹ It is strongly influenced by orientational motion, especially in the intermolecular region of the spectrum where diffusive reorientation contributes significantly. R_{aniso} can be measured directly in the time-domain using optical Kerr effect (or transient birefringence) spectroscopy.⁴ In the frequency domain, anisotropic dynamics are observed using depolarized light scattering or Raman spectroscopy in the I_{VH} geometry. The light scattering spectrum is related to the susceptibility by⁴

$$S_{LS}(\omega) = 2\hbar^2 \text{Im}[\chi''_{\text{aniso}}(\omega)]/[1 - \exp(-\hbar\omega/kT)] \quad (2-17)$$

Note that the strong Rayleigh line in light scattering is a consequence of the occupation factor. It does not exist in the time domain measurement, allowing a more accurate determination of the lowest frequency range of the spectrum.

For intramolecular vibrations, the isotropic response only contains resonances of totally symmetric vibrations.¹⁹ However, the selective nature of the isotropic response for intermolecular motions is not as obvious, since the symmetry around molecules in the liquid is not well-defined. The reorientational dynamics of individual molecules can not directly contribute to R_{iso} because the isotropic polarizability discussed in Eq. (2-8) does not contain the molecular term. Therefore, the isotropic response is entirely due to interaction-induced effects and thereby provides information about fluctuations of relative orientation and distance between molecules. MD simulations indicate that the isotropic response has a larger contribution from density fluctuations than the anisotropic response, however orientational motions arising from intermolecular interactions may still be dominant.⁴⁹ R_{iso} is measured in the frequency domain by a difference of polarized and depolarized spectra, $I_{\text{ISO}} = I_{\text{VV}} - 4I_{\text{VH}}/3$.⁴⁸ Calculating the difference of two spectra leads to difficulties in accurately matching the experimental conditions for both spectra, particularly with a strong Rayleigh wing.⁵⁰ However, the isotropic response can be directly observed in the time domain using a probing field that is polarized at the magic angle relative to the excitation fields.¹² Alternatively, the anisotropic and/or isotropic response can be reconstructed by measuring R_{zzzz} and R_{zzyy} , and using Eqs. (2-15) and (2-16). As with the frequency domain measurement, an accurate determination requires that the two measurements be taken under exactly the same experimental conditions.

2.3 Experiment

2.3.1 Heterodyne detected polarization

The SM-OKE experiment, an electronically nonresonant third-order nonlinear spectroscopy, utilizes a two-beam near-collinear pump-probe geometry in which a weak probe pulse $\mathbf{E}^{pr}(\mathbf{k}_{pr}, t_{pr})$ is delayed by a time τ with respect to a strong pump pulse $\mathbf{E}^{pu}(\mathbf{k}_{pu}, t_{pu})$. The fields are incident at time t_n , where $n = pu$ or pr , with an incident wavevector \mathbf{k}_n . Also, the fields are linearly polarized along the unit vector $\hat{\mathbf{e}}_n$, so that the polarization component of these field along the $j \in \{x, y, z\}$ laboratory axis can be expressed as

$$\mathbf{E}_j^n(\mathbf{k}_n, t_n) = (\hat{\mathbf{j}} \cdot \hat{\mathbf{e}}_n) E_n(t_n) e^{i\mathbf{k}_n \cdot \mathbf{r} - i\omega_n t_n} + c.c. \quad (2-18)$$

Here E_n represents the time-dependent amplitude of the field.

The pump beam impulsively excites vibrational and collective motion through a Raman process, and the probe stimulates radiation of a coherent optical field from the sample. The experimental signal can be expressed in terms of the third-order nonlinear polarization $\mathbf{P}^{(3)}$, which is generated by two field interactions with the pump and one from the probe. For the nonresonant experiment, it is generally assumed that the lifetime in Raman virtual states is extremely short, and that the Raman excitation interaction and the stimulation of the signal by the probe field involve two time-coincident fields. In this limit, the time-evolution of $\mathbf{P}^{(3)}$ is given by a convolution of the incident fields with the third-order material response function.^{45,46}

$$P_{ijkl}^{(3)}(t, \tau) = E_j^{pr}(t - \tau) \int_0^\infty d\tau' R_{ijkl}^{(3)}(\tau') E_k^{pu*}(t - \tau') E_l^{pu}(t - \tau'). \quad (2-19)$$

where $\tau' = t - t_{pu}$. $P_{ijkl}^{(3)}$ represents the component of $\mathbf{P}^{(3)}$ in the i direction of the laboratory frame induced by the j , k , and l components of the incident fields. While the experiment is taken to be nonresonant, $\mathbf{P}^{(3)}$ can generally be expressed in terms of components that oscillate in-phase and in-quadrature with respect to the probe field:

$$P_{ijkl}^{(3)}(t, \tau) = 2 \operatorname{Re} \left[P_{ijkl}^{(3)}(t, \tau) \right] \cos(\omega t) + 2 \operatorname{Im} \left[P_{ijkl}^{(3)}(t, \tau) \right] \sin(\omega t) \quad (2-20)$$

The polarization coherently radiates a signal field in the wavevector-matched direction $\mathbf{k}_{sig} = \pm \mathbf{k}_{pu} \mp \mathbf{k}_{pr}$, which is along the direction of the transmitted probe beam. The phase of the radiated signal is shifted by $\pi / 2$ with respect to the polarization:

$$E_{ijkl}^{sig}(t, \tau) \propto iP_{ijkl}^{(3)}(t, \tau) \quad (2-21a)$$

$$= 2 \operatorname{Re} \left[P_{ijkl}^{(3)}(t, \tau) \right] \sin(\omega t) + 2 \operatorname{Im} \left[P_{ijkl}^{(3)}(t, \tau) \right] \cos(\omega t) \quad (2-21b)$$

$$= E_{ijkl}^{bir}(t, \tau) \sin(\omega t) + E_{ijkl}^{dic}(t, \tau) \cos(\omega t) \quad (2-21c)$$

Here the signal field components that oscillate in-phase ($\varphi^{sig} - \varphi^{pr} = 0$) and in-quadrature ($\varphi^{sig} - \varphi^{pr} = \pi/2$) with respect to the probe field are commonly known as the dichroic and birefringent parts of the nuclear response, respectively.

The dichroic and birefringent parts of the response are derived predominantly from the evolution of the density matrix in the excited and ground states respectively.⁵¹ Therefore, the relative magnitude of the two is dependent on detuning of the excitation frequency from electronic resonance. In a nonresonant pump-probe experiment, the birefringent response is typically 10-100 times stronger than the dichroic response.

In order to detect a signal that is linear in the radiated field, a local oscillator (LO) is introduced to achieve optical heterodyning, and the interference between the signal and LO is

observed.⁴⁶ If the phase of the LO is well-defined and able to be varied with respect to that of the probe field, the dichroic and birefringent contributions can be measured separately.⁴⁶

In general, the heterodyne detected signal is:

$$S_{ijkl}(\tau) \propto |E_i^{LO}| \left(E_{ijkl}^{bir}(\tau) \sin(\varphi^{LO}) + E_{ijkl}^{dic}(\tau) \cos(\varphi^{LO}) \right) \quad (2-22)$$

Therefore, a LO that is in- or out-of-phase ($\varphi^{LO} = 0, \pi$) with the probe selects the dichroic part of the response (S_{ijkl}^{dic}), while the birefringent response (S_{ijkl}^{bir}) is measured with an in-quadrature LO ($\varphi^{LO} = \pi/2, 3\pi/2$). The latter is preferable for a nonresonant experiment, since the birefringent response dominates.

A local oscillator can be introduced either by mixing the signal with an external LO field or by intrinsic heterodyne detection, in which the LO is derived from the co-propagating transmitted probe field. Traditional optical Kerr effect (OHD-OKE) experiments involve intrinsic heterodyne detection by using a $45^\circ/0^\circ/90^\circ$ polarization geometry for the pump, probe, and analyzer polarizers, and a quarter wave plate in the probe beam.^{1,4} Phase control of the LO is achieved by a small rotation of the polarizer before ($\varphi^{LO} - \varphi^{pr} = \pi/2$) or after ($\varphi^{LO} - \varphi^{pr} = 0$) the sample.⁵² The OHD-OKE experiment is limited by the restriction that only the anisotropic component of the response function can be measured. To achieve direct control over each field, several experimental approaches based on heterodyne detected transient gratings have been reported.^{53,54} An actively stabilized Mach-Zehnder interferometer has been used for transient grating measurements of several independent tensor elements.¹⁵ Diffractive optics have also been used to generate two pulse pairs that are used for a nonresonant transient grating experiment with an additional field that acts as a passively phase-locked external LO.^{17,18,20,55} In these experiments, the phase of the LO is

adjusted by an pulse-envelope-delay introduced tilting a glass plate in the LO beam or with a half-wave plate.

The full tensorial nonresonant response is completely determined by any two independent components, and OHD-OKE experiments are a reliable and straightforward approach to linearly detecting R_{aniso} . Thus, simplified methods of measuring other elements are of interest. In particular, two beam (pump-probe) methods in which the probe acts as an intrinsic LO would be the simplest way to directly measure R_{zzzz} , R_{zzyy} and R_{iso} . The complication is that measurement of the dominant birefringent response requires a LO that is in-quadrature relative to the probe and with the same polarization.

These requirements make it impossible to make transient birefringence measurements in a pump-probe geometry if the incident and radiated fields are treated as plane waves. However, various nonresonant nonlinear phenomena have been described for Gaussian beams in which a radially varying phase applies for the probe (or LO) beam. Such experiments are typically described as transient lens experiments based on radial gradients in temperature or the nonlinear index of refraction.^{56,57} For example, in the Z-scan method, an intense focused optical field induces a nonlinear lens in a sample. The effective focal length of this lens is determined by measuring the intensity of the field transmitted through a partially closed iris after the sample as the position of the sample is moved relative to the waist of the beam. This measures the time-integrated nonresonant response.⁵⁷

Characterizing the time-dependence of the nonlinear transient lens phenomena allows isotropic elements of the nonlinear response to be determined. In analogy to transient thermal lens experiments, a two-beam technique was developed by Simon and co-workers in which the induced polarization acts as a lens to change the focusing of the probe beam.^{14,16}

Another two-beam technique, implemented by Ziegler and co-workers, involves either dispersing the overlapped probe and signal or using a cut-off filter to collect only certain frequency components.²¹

2.3.2 SM-OKE spectroscopy

We have introduced an additional technique that is capable of observing multiple components of the response function by using an iris to spatially mask the transmitted probe beam as a way of introducing a LO field with an in-quadrature component.¹⁹ It utilizes the principle that, for focused Gaussian beams, the difference in Guoy phase shift and radius of curvature between the signal and LO fields are nonzero at finite differences from the sample. Thus, symmetrically aperturing the axial part of the probe allows for heterodyne detection of the birefringent response. Spatially masked optical Kerr effect (SM-OKE) spectroscopy has been demonstrated using the intramolecular modes of CCl_4 by experimentally discriminating against the symmetric and asymmetric vibrations in the anisotropic and isotropic responses respectively. Recently, Ziegler and co-workers have elaborated on this type of method, discussing in detail the similarity between position-sensitive Kerr lens spectroscopy and Z-scan experiments.⁵⁸

The SM-OKE experiment can be explained phenomenologically as a nonlinear lensing effect. In the presence of intense light, a material's complex index of refraction is written $n = n_0 + n_2 I + \dots$, where I is the intensity of the radiation. For a Gaussian beam, the radially varying intensity profile induces a radially varying index of refraction, which in turn acts to focus or defocus the probe. Therefore, the SM-OKE experiment can also be described as a pump-induced lens that modulates the amount of probe transmitted through an aperture

in the far field. This is fundamentally the same as the third-order polarization description presented in the previous section, since n_2 is directly proportional to the susceptibility.^{16,59,60}

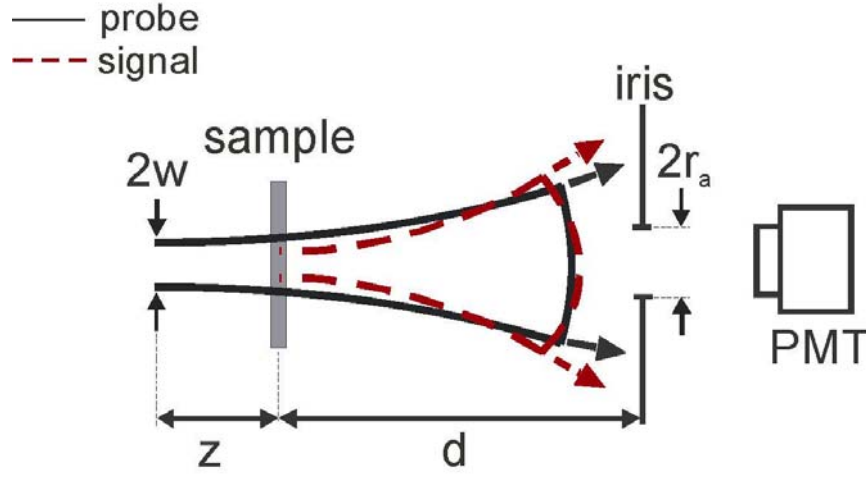


Figure 2-1. (Color) Schematic representation of the SM-OKE experimental arrangement (beam propagation is from left to right). The distances z , d , and r_a are defined in the text.

In a SM-OKE experiment, the focused pump and probe beams are crossed in a thin sample at a distance z from the waist of the beams (See Fig. 2-1). The incident probe beam is assumed to have a Gaussian profile:

$$E^{pr} = E_{pr}(t_{pr}) \frac{w \exp[-i\phi(z)]}{w_{pr}(z)} \exp\left[-\frac{r^2}{w_{pr}^2(z)} - i\frac{kr^2}{2R_{pr}(z)}\right] \quad (2-23)$$

where w is the waist spot size, $k = 2\pi/\lambda$, and $z_0 = kw^2/2$ is the Rayleigh range. The position-dependent spot size of the beam is $w_{pr}^2(z) = w^2(1 + z^2/z_0^2)$ and the radius of curvature is $R_{pr}(z) = z(1 + z^2/z_0^2)$. In Eq. (2-23), $\phi(z)$ is the linear phase, which is radially symmetric. An iris is centered on the probe beam at a distance d from the sample, and is closed to a diameter of $2r_a$. As the probe beam passes through the sample, it stimulates the emission of the coherent nonlinear field in the direction of the transmitted probe. However, the spatial amplitude and phase characteristics of the radiated signal differ from that of the

probe beam. The waist of the radiated signal field is roughly $\sqrt{3}$ smaller than the radius of the incident fields at the sample because the third-order polarization is created by the overlap of three incident light fields at the sample. As the probe and signal propagate away from the sample, spatial variations in the relative phase exist which allow the probe beam to serve as a local oscillator for both the birefringent and dichroic responses. The physical origin of the relative phase shift at finite distances from the sample is the spot size difference, which leads to a shorter Rayleigh range for the third-order signal. Therefore, the axial phase shift and radius of curvature of the probe and third-order signal differ at the iris position, creating a radially varying phase shift between the two (Fig. 2-1). By spatially selecting a portion of the overlapping beams with the iris, one can detect the part of the beams that have the largest integral phase shift. When the iris is removed the integrated radial phase shift between E^{bir} and E^{LO} is $\pi/2$, as expected in the plane wave limit.

The relationship between probe and signal beams may be expressed quantitatively by utilizing a Gaussian decomposition of the input beam.^{57,61} In this treatment, the nonlinear signal is treated as a spatially varying perturbation of the input beam. The total complex electric field at the sample is expressed as a Taylor series expansion of the radially varying nonlinear phase, so that each term can be easily propagated through space to the iris position. The probe is represented as the zero order term ($m = 0$) and the third-order radiated signal as the first order correction term ($m = 1$). The expression for the measured interference signal after passing through the iris has been given by Gardecki, et al.:⁵⁸

$$S_{ijkl}^{OHD}(r_a, z, \tau) = \frac{2w_{00}w_{10}kL}{w_0w_1[1+z^2/z_o^2]^2} \int_0^{r_a} \exp\left[-r^2\left(\frac{1}{w_0^2} + \frac{1}{w_1^2}\right)\right] \times \left\{ \sin\theta_{LO}(r, z)S_{ijkl}^{bir}(\tau) + \cos\theta_{LO}(r, z)S_{ijkl}^{dic}(\tau) \right\} r dr \quad (2-24)$$

where $w_{m0}^2 = w_{pr}^2(z)/(2m+1)$ is the focused spot size of the m^{th} order expansion term, $w_m^2 = w_{m0}^2 [g^2 + d^2/d_m^2]$ is the beam radius at the iris, $d_m = kw_{m0}^2/2$ and $g = 1 + d/R_{pr}(z)$.

The spatially varying LO phase is

$$\theta_{LO}(r, z) = (\theta_1 - \theta_0) - \frac{kr^2}{2} \left(\frac{1}{R_1} - \frac{1}{R_0} \right), \quad (2-25)$$

where the axial phase of the probe and signal are given by

$$\theta_m = \tan^{-1} \left[\left[\frac{d}{gd_m} \right] \right] \quad (2-26)$$

and the axially varying radii of curvature are

$$R_m = d \left[1 - \frac{g}{g^2 + d^2/d_m^2} \right]. \quad (2-27)$$

Therefore, the phase of the local oscillator depends on the sum of contributions from a radially uniform term, $\theta_1 - \theta_0$, which is a scaled Guoy phase shift, and a term of opposite sign which does not contribute on axis but increases in magnitude with radial distance. The total signal magnitude is greatest on axis ($r = 0$) and decreases radially, as one would expect from a Gaussian beam.

The dependence of Eq. (2-24) on r_a and z has been discussed by Gardecki, *et. al.* for both dichroic and birefringent responses. Because birefringence is much larger than dichroism for excitation that is far from electronic resonance, we limit this discussion to the birefringent part of the response. The dependence of the signal on the size of the iris opening is determined by both the radial amplitude profile of the beams and the radially varying phase difference. A plot of the phase difference as a function of radius exhibits an extremum on axis but changes sign when the second term in θ_{LO} dominates the phase. Therefore, the

birefringent signal is largest when the iris is closed just far enough to block the portion of the beam for which the second term in the phase is significant, but opened far enough to collect a measurable fraction of the beam. The signal vanishes for large r_a , since the unapertured probe pulse can not serve as a local oscillator for a birefringent response.

The dependence of the signal on the axial position of the sample relative to the beam waist, z , is determined mostly by the relative amount of Guoy phase shift acquired by each beam as it propagates from the sample to the far field. A plot of the birefringent signal as a function of z is antisymmetric with respect to the beam waist, containing a maximum and minimum on either side of the origin and tending towards zero for large $|z|$. Thus, there is an optimal distance a sample should be placed from the beam waist in order to achieve the maximal SM-OKE signal, which was found to be $\sim 0.8 z_0$ by Gardecki *et. al.*

The final result is that by placing an iris in the probe beam path and moving the sample away from the beam waist, the self-heterodyned pump-probe signal may be detected. Note that the only restriction placed on the light field polarizations in this method is that both pump field interactions are from the same beam and that the signal must have a polarization component along the probe polarization, which allows detection of R_{zzzz} , R_{zzyy} and R_{iso} .

2.3.3 Methods

The experimental setup used for the SM-OKE experiments is a modified version of the standard pump-probe interferometer, in which a single pulse is split into two replicas that travel nearly equal path lengths and are crossed at a small angle ($5-6^\circ$) in the sample. The relative delay between pump and probe is adjusted via a motorized stepper translation stage (Newport UTMPP0.1). For the Z-scan experiments, mica zero-order half-wave plates (CVI)

and Glan-Laser polarizers (CVI) are placed in each arm of the interferometer to allow independent rotation of the linear polarization of each beam. An additional polarizer centered on the probe beam immediately after the sample is adjusted parallel to the incident probe polarization, so that the R_{zzzz} , R_{zzyy} and R_{iso} ($=R_{zzmm}$) tensor components can be measured by rotation of the pump beam polarizer only. The pump and probe are focused to a spot of $2w = 45 \mu\text{m}$ by a 10 cm achromatic doublet (CVI), and crossed $\sim 1/2$ Rayleigh range (1 mm) from the focus. An iris centered on the probe beam is typically placed ~ 20 cm from the sample and opened to a radius which maximizes the experimental signal. While the distance of the sample from the beam waist and iris opening varied between samples, they were always kept constant between measurements of a set of tensor components.

Direct measurements of the anisotropic response function are recorded in a typical OHD-OKE experiment. The main difference between the OHD-OKE and SM-OKE setups is that the half wave plate in the pump arm is replaced by a quarter wave plate placed after the polarizer. The probe and analyzing polarizers are crossed, while the pump polarization is 45° with respect to the probe. An in-quadrature local oscillator is introduced by rotating the probe polarizer by a small angle ($\Delta\phi$), and the homodyne contribution is removed by the subtraction of scans recorded with opposite polarizer rotations ($\pm\Delta\phi$).⁵²

The experiments are performed using the output of a home-built cavity-dumped Ti:sapphire oscillator producing a train of pulses at 500 kHz with a center wavelength of 800 nm. Following pre-compensation in a pair of fused silica prisms and propagation through the experimental interferometer, second harmonic cross correlation in a $10 \mu\text{m}$ BBO crystal typically yields pulsewidths of 16-18 fs FWHM. Pulse energies are typically 10 nJ for the pump and 1 nJ for the probe, which is well within the linear detection regime. Signal

intensity is detected using a photomultiplier tube, and recorded using a lock-in amplifier referenced to the 2 kHz frequency of a chopper placed in the pump arm of the interferometer.

Acetonitrile, carbon disulfide and methanol were obtained from Sigma (all with at least 99.9% purity), deionized water with resistivity $> 1.8 \times 10^6 \Omega/\text{cm}$ was obtained from RICCA, and all liquids were used without further purification. Because of significant signal contribution from the fused quartz cell walls to the isotropic spectrum, a 0.5 mm thick flowing jet was used to obtain measurements for methanol and water. For these samples, the noise floor is dictated by the surface quality of the jet, so great care is needed in adjusting the flow rate and in centering the beam on the smoothest portion of the jet. It was not possible to obtain an optical quality jet for acetonitrile, however it was possible to greatly reduce the cell wall contribution by using a 1 cm path length fused silica cell, and compressing the pulse using the electronic signal contribution. A jet of CS_2 was not attempted for safety considerations, and because the signal was distorted in a long path length cell, a 1 mm path length cell was used for CS_2 .

2.3.4 Data analysis

Small variations in the relative amplitudes and zero delay times ($\tau = 0$) of the signals measured in different polarization geometries with the SM-OKE and OHD-OKE experiments are corrected for using the $R^{(3)}$ symmetry relationships. After recording the time domain data in all four polarization configurations, a self-consistent reconstruction of the data is performed by varying the amplitude and delay times of each tensor component, holding one amplitude and delay time constant, and numerically minimizing the least squares function:

$$\begin{aligned} & \left| \frac{1}{2} [A_{zzzz} S'_{zzzz} - A_{zzyy} S'_{zzyy}] - A_{aniso} S'_{aniso} \right| + \\ & \left| \frac{1}{3} [A_{zzzz} S'_{zzzz} + 2A_{zzyy} S'_{zzyy}] - A_{iso} S'_{iso} \right| \end{aligned} \quad (2-28)$$

The signal components in Eq. (2-28) are experimentally measured nuclear signals, denoted by a prime to differentiate them from the resulting self-consistently fit data. The fit is performed for $\tau > 100$ fs to minimize contributions from the nonresonant electronic response. Because S'_{zzzz} , S'_{zzyy} and S'_{iso} are all measured using the SM-OKE method, it is expected that their scaling amplitudes should be approximately equal. The experimentally observed scaling amplitudes are typically within 10-15% of each other, indicating that the relative signal amplitude varies slightly between measurements due to displacements of pump beam pointing when the polarizer is rotated. Because the strength of the local oscillator in the OHD-OKE setup is different from that in the SM-OKE experiment, the amplitude of the S'_{aniso} component relative to the others is treated as an unknown and is determined completely by the self-consistent fit. Fig. 2-2 provides an example of the utility of this method, where the reconstructed anisotropic and isotropic signals of acetonitrile are compared with the scaled S_{aniso} and experimentally measured S_{iso} . The reconstructed quantities are nearly indistinguishable from those measured directly, as is the case for carbon disulfide and methanol as well. It should be stressed that experimental amplitude and timing uncertainty is greatly reduced by independently measuring all four tensor components, allowing an accurate determination of the two independent response function components.

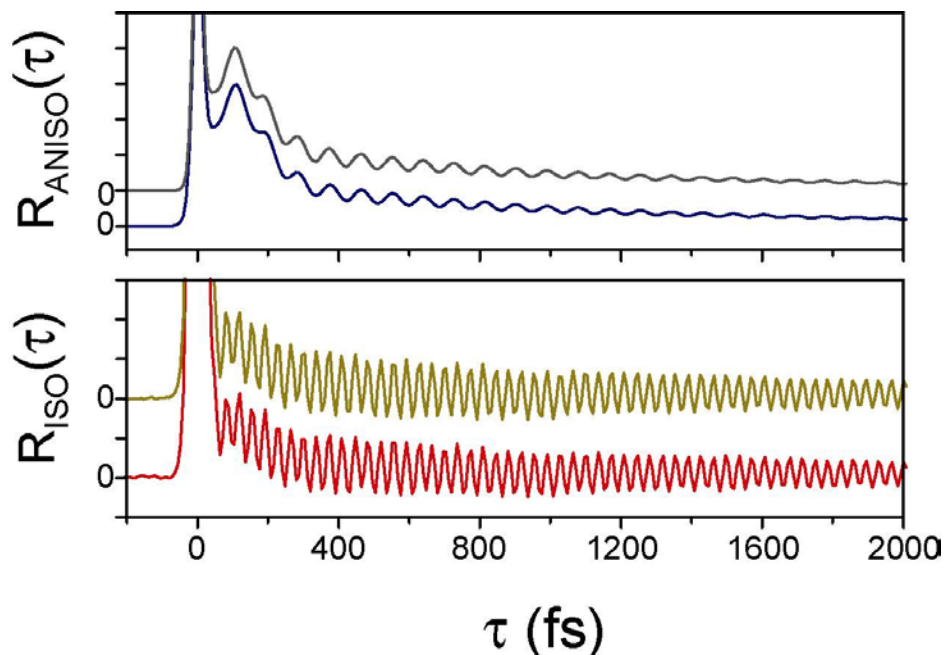


Figure 2-2. (Color) Comparison of the directly measured anisotropic (upper panel) and isotropic (lower panel) acetonitrile signals with their respective reconstructed signals. In each panel, directly measured data is displayed with a positive offset with respect to reconstructed data. The relative phase and amplitude of each scan was determined by a self-consistent fit of the data according to Eq. (2-28). In the case of acetonitrile, $A_{zzzz} = 0.98$ and $A_{zzyy} = 0.96$, where $A = 1$ for both under perfect experimental conditions.

The time-domain data is also presented as a spectral density χ'' , the imaginary part of the Fourier transform (sine transform) of the time-domain response. As described above, this quantity is closely related to the traditional Raman spectrum. However, due to convolution of the material response with the finite duration of the laser pulses, the amplitude of each Fourier component is scaled by the pulse spectral bandwidth. For a heterodyne detected experiment, the impulsive limit is recovered by deconvolution with the second harmonic autocorrelation, which amounts to division of the experimental signal by the autocorrelation in the Fourier domain.⁵² In addition, the contribution of the nonresonant electronic response may be separated from the nuclear portion by considering only the imaginary part of the transform.

2.4 Results and Discussion

2.4.1 Acetonitrile, carbon disulfide and methanol

The heterodyne detected time domain signals for acetonitrile are plotted in Fig. 2-3. The inset shows the nonresonant electronic responses, which follow the predicted intensity ratios, $R_{zzzz} : R_{zzyy} : R_{aniso} : R_{iso} \cong 3 : 1 : 1 : 5/3$. Each signal contains high frequency underdamped oscillations attributed to intramolecular vibrations superimposed on slowly varying damped responses characteristic of the collective liquid response. The amplitude of the polarized (R_{zzzz}) response is greatest and most similar to R_{aniso} , while R_{iso} is much weaker. R_{zzyy} has many of the same features as R_{zzzz} , but with roughly half the amplitude and opposite sign. It is therefore clear that the collective response is predominantly anisotropic. Two Raman active intramolecular modes lie within the laser bandwidth, a symmetric C–C stretch at 918 cm^{-1} and an antisymmetric C–C \equiv N bend at 380 cm^{-1} . Both modes contribute significantly to the parallel and perpendicular response, however the anisotropic and isotropic signals each decay with a single underdamped oscillation.

We demonstrate the polarization selectivity of the measurement in the deconvolved Fourier transform spectra of acetonitrile plotted in Fig. 2-4. Only the antisymmetric mode contributes to the anisotropic signal and only the symmetric mode appears in the isotropic response. Such polarization selectivity for intramolecular modes has been observed for CCl_4 , and explained in terms of the projection of the lab-frame polarizations onto the molecular symmetry axes.¹⁹ The spectral region below 200 cm^{-1} is due to the intermolecular response of the liquid. The spectra indicate that the intermolecular modes are largely depolarized,

since χ''_{zzzz} is almost indistinguishable from χ''_{aniso} in this region, and the amplitude of $\chi''_{aniso} \gg \chi''_{iso}$.

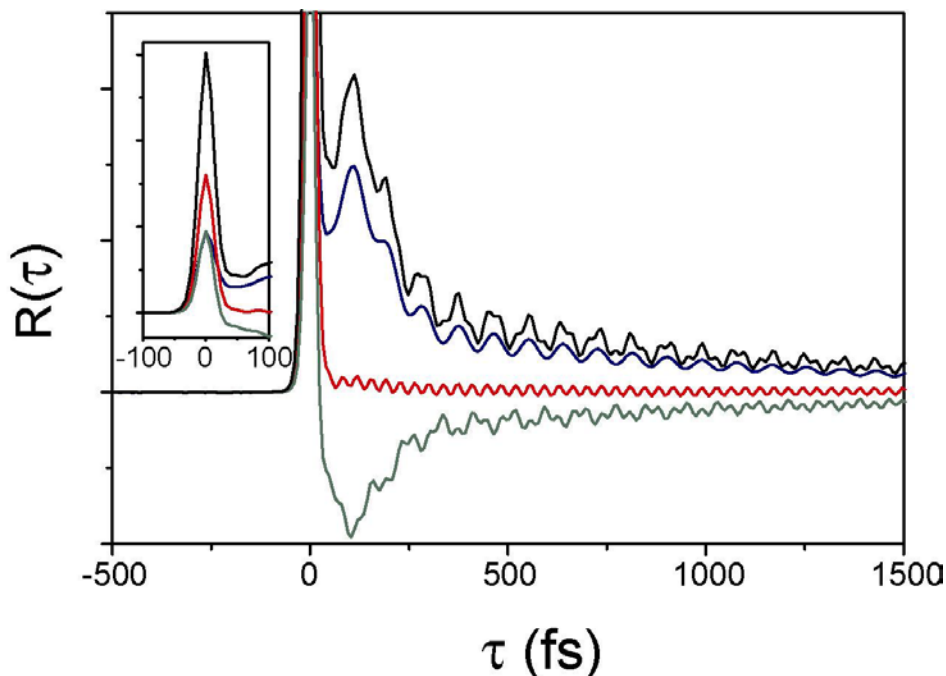


Figure 2-3. (Color) Self-consistent, polarization-selective acetonitrile OKE signals. In the main figure, from top to bottom are plotted R_{zzzz} , R_{aniso} , R_{iso} , and R_{zzyy} . The inset shows the relative amplitudes of the electronic response $R_{zzzz}:R_{iso}:R_{zzyy}:R_{aniso} = 1:0.53:0.31:0.31$.

The deconvolved low-frequency anisotropic and isotropic Raman spectral density for acetonitrile, CS_2 and methanol are compared in Fig. 2-5. For all liquids, the anisotropic response is much stronger than the isotropic. The overall spectral profile for the isotropic and anisotropic response are generally similar, except at frequencies $<10 \text{ cm}^{-1}$ and, for methanol, at frequencies $>300 \text{ cm}^{-1}$. Noise is apparent in the isotropic spectrum of methanol, due to small jitters of the flowing jet combined with a weak nuclear response. In addition, the isotropic CS_2 has a constant non-zero background that extends to 500 cm^{-1} , which we attribute to the wall of the fused silica cell. We have found the cell wall response to be strongly polarized and fairly flat over the region $100\text{-}500 \text{ cm}^{-1}$. Thus, it is not possible to

quantitatively compare the isotropic and anisotropic intermolecular spectral profile on the high frequency edge of CS₂.

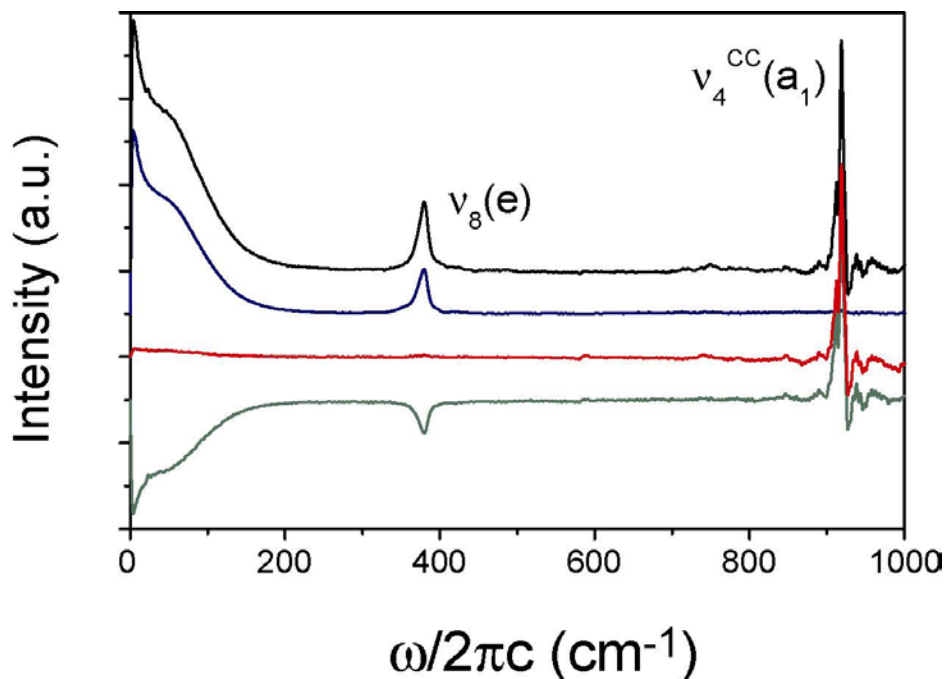


Figure 2-4. (Color) Polarization-selective Fourier transform Raman spectra of acetonitrile. Offset spectra from top to bottom are R_{zzzz} , R_{aniso} , R_{iso} , and R_{zzyy} . The assignment and symmetry of intramolecular vibrations are indicated.

The anisotropic spectra of acetonitrile and CS₂ agree well with previously reported OHD-OKE spectra.^{4,7,52,62} Whereas the spectrum appears to show only two distinct features, a sharp peak at low frequency (≤ 10 cm⁻¹) and broad band extending to ~ 150 cm⁻¹, the time-domain decay here and elsewhere consist of three distinct time scales.⁶³ The low frequency peak is due to the long time exponential tail of the time-domain response, which is attributed to diffusive reorientation of molecules. An intermediate exponential relaxation process on a sub-picosecond time scale contributes weakly to the 20-30 cm⁻¹ region of the spectrum.⁶³ The higher frequency part of the intermolecular spectra is not understood as well. It is often attributed to DID effects because it can be reproduced rather well by MD and INM simulations of atomic fluids and simple liquids.^{31,36,64} When translational and rotational

degrees of freedom are projected from the DID spectral density, librations usually contribute at higher frequencies, although there is significant overlap.^{27,29}

The anisotropic response of methanol contains the low frequency rotational diffusion peak, but it is clearly different from the other two liquids at higher frequencies. Most striking is that it extends to frequencies that are twice as high as acetonitrile or CS₂. In addition, the contour of the high frequency edge is not smooth, but rather undergoes an abrupt change in slope around 200 cm⁻¹. Our measurement differs slightly from previous measurements in the high frequency wing,^{4,65} but high frequency components have been predicted in both MD simulations⁶⁶ and INM calculations²⁹. Chelli and co-workers⁶⁶ believe the intensity between 200–350 cm⁻¹ corresponds primarily to librations about the C-O axis of non-hydrogen bound molecules, while Garberoglio and co-workers²⁹ have attributed it to hydrogen bond stretching. In both studies, this region contains significant amounts of both translational and rotational contributions, suggesting the motion could involve a combination of librational and stretching motions. Both studies also predict a distinct feature at frequencies higher than 350 cm⁻¹ due to librations of hydrogen bonded molecules about the C-O axis, which is absent in our spectrum and in frequency domain depolarized Raman spectra.

In Fig. 2-6, we compare the low frequency anisotropic and isotropic spectra for acetonitrile, CS₂, and methanol on a log frequency plot. For all three liquids, the amplitude of the intermolecular anisotropic response is much larger than the isotropic response, by a factor of >10 in CS₂ and methanol and >20 in acetonitrile. The relative isotropic to anisotropic amplitude ratio agrees well with the 1:15 integrated intensity ratio³⁵ and 1:12 intensity ratio at the peak of the time domain response³⁶ found in MD simulations of CS₂.

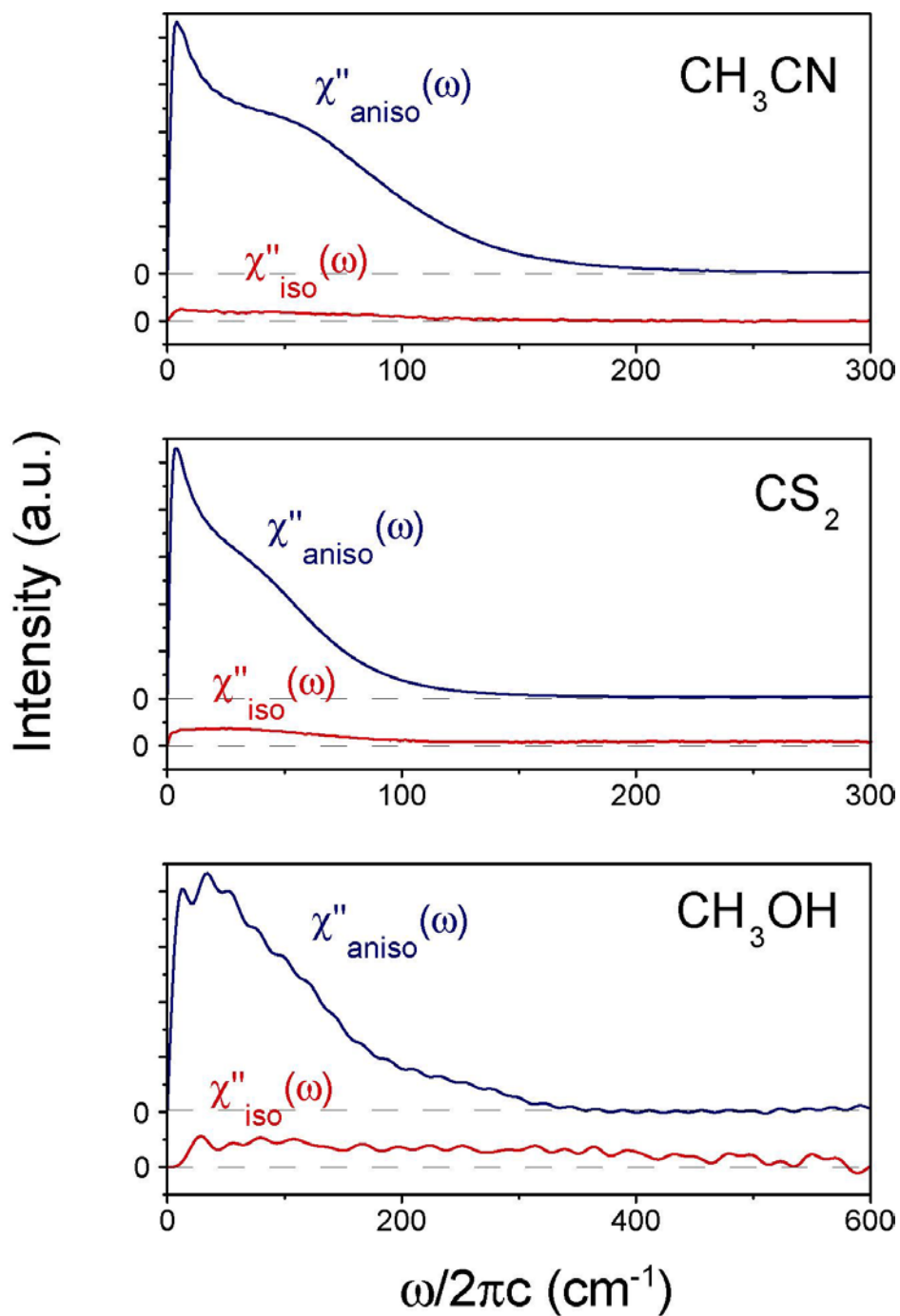


Figure 2-5. (Color) Low-frequency anisotropic and isotropic Fourier transform Raman spectra of acetonitrile, CS_2 and methanol. Intensities are consistent within each panel but are scaled differently for each liquid.

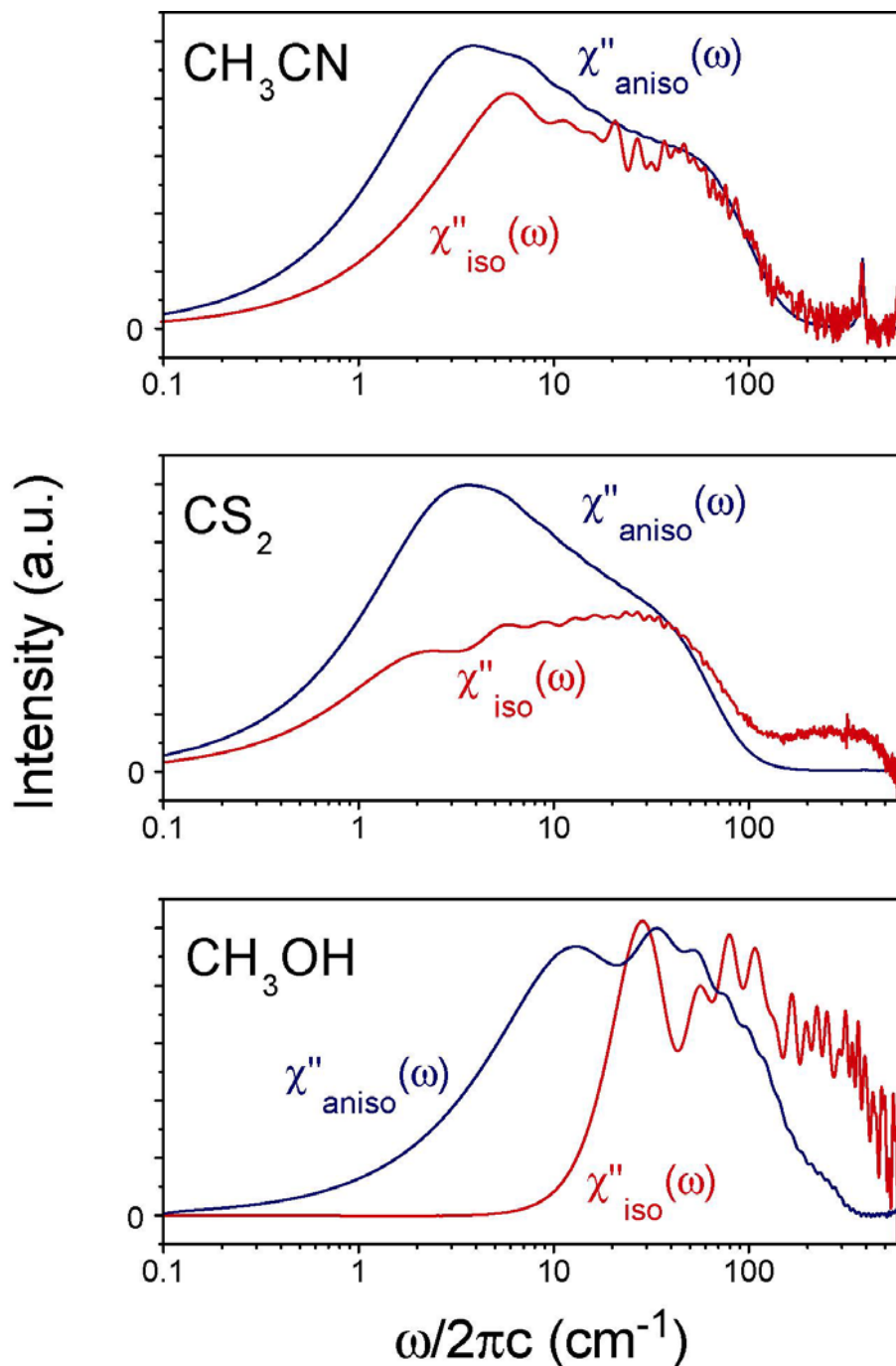


Figure 2-6. (Color) A comparison of the low frequency anisotropic and isotropic lineshapes for acetonitrile, CS₂ and methanol. Isotropic spectra are scaled for the purpose of comparison. Time domain data were zero padded to approximately ten times their original length to demonstrate how each curve slopes toward zero. The isotropic acetonitrile spectrum is the average of three separate scans. Intensities are consistent within each panel but are scaled differently for each liquid.

Equally important to the magnitude is the frequency dependence of each response. In order to make a better comparison, the isotropic response is scaled to compare the high frequency edge. Qualitatively, the high frequency wings of the isotropic and anisotropic spectra for acetonitrile and CS₂ are very similar, but the isotropic response for both liquids differ from that of the anisotropic at frequencies below ~50 cm⁻¹, where the anisotropic response is dominated by contributions from rotational diffusion. For both liquids the same frequency components are present in the isotropic and anisotropic spectra, yet the amplitudes of the lowest frequency contributions are suppressed in the isotropic. Suppression of the lowest frequency components is even more dramatic in the isotropic response of methanol where the response is zero within error for the region below 10 cm⁻¹. We therefore conclude that molecular rotational diffusion is greatly suppressed, or perhaps eliminated entirely in the isotropic signal.

Suppression of the long time decay in the isotropic response has been noted in other experimental investigations. Khalil²⁰ and Constantine²¹ have both observed that the isotropic dichroic response of CS₂ is dominated by processes that decay with intermediate time scales and contain almost no long time decay components. However, Chang¹⁶ reports depolarization ratios for benzene, toluene and benzonitrile which are mostly depolarized but constant for frequencies less than 100 cm⁻¹, indicating that while the isotropic response is greatly suppressed with respect to the anisotropic response, the lowest frequency components are not preferentially eliminated in the isotropic spectrum.

A weak low frequency isotropic component has been observed in computational investigations of CS₂.^{23,36} Based on a decomposition of the polarization according to M and II terms, it may appear surprising that the isotropic response contains dynamics on the time

scale of molecular diffusion. However, it has been demonstrated that the effective isotropic polarizability is larger for molecules that are aligned than for those that are randomly oriented, allowing for an interaction-induced contribution on a time scale corresponding to rotationally diffusive motion.^{36,49} This phenomenon may be alternatively described as a M-II cross term, as discussed by Keyes, Kivelson and McTague who postulated that the timescale for cross-correlations should resemble that of rotational diffusion.⁶⁷ Their argument was based on the assumption that preferential molecular alignment within the liquid would act to reduce the gas phase anisotropy, making the many-body polarizability more isotropic. Thus, while the cross-term is negative for the anisotropic dynamics, it is positive in the isotropic response.

The behavior of the isotropic spectra at frequencies above those corresponding to rotational diffusion is different for methanol, as compared with CS₂ and acetonitrile. While the latter two exhibit isotropic lineshapes that are similar to their anisotropic counterparts, the isotropic spectrum of methanol is significantly different from the depolarized spectrum. After peaking near 25 cm⁻¹, it maintains a constant slope towards baseline with nonzero intensity beyond 500 cm⁻¹. It is possible that the lineshapes of the anisotropic and isotropic are similar at low frequencies, however it is clear that the two differ greatly at the higher frequencies. As discussed above, simulations have predicted that librations about the C-O bond occur at frequencies as high as 600 cm⁻¹,^{29,66} but such motions should be predominantly molecular in nature and should be preferentially eliminated from the isotropic spectrum. Even if librations were to contribute through the $\Pi^{II,\beta\beta}$ term, they should also lend intensity to the anisotropic spectrum at high frequencies.

The differences observed for methanol may be related to the Raman noncoincidence effect, which is a frequency difference in the first and second moments of the isotropic and anisotropic components of an intramolecular vibration. The effect has been explained as a manifestation of transition dipole coupling and is often associated local ordering within a liquid.^{68,69} The intramolecular modes of methanol are known to have a large Raman noncoincidence,⁷⁰ and the results presented here bring into question the applicability of the effect for intermolecular vibrations. There are clear differences since the usual effect involves a perturbation of the observed frequencies for a localized vibration, while the intermolecular spectrum is derived from the motions of less ordered liquid “structures”. Nonetheless, noncoincidence requires that the strong intermolecular coupling is observed differently in the isotropic and anisotropic spectra, which is likely to have a large impact on lineshapes in the intermolecular part of the spectrum, as has been measured for methanol. While we note that Raman noncoincidence may be important for methanol, we do not exclude other possible explanations, such as those discussed below.

Although numerous theoretical investigations have attempted to dissect the third-order responses of CS₂, acetonitrile, and methanol, little has been said about the isotropic spectrum. Some insight into possible contributions to the isotropic spectrum can be gained by discussing contributions to the anisotropic spectrum. As has been stated, II effects have been found to contribute to all portions of the spectrum for a given liquid, although hindered rotations generally dominate the anisotropic spectrum and contribute at higher frequencies than translations. The frequency dependence of the interaction induced terms in Eq. (2-9) is not straightforward, as has been demonstrated in a recent simulation of CS₂³² in which contributions were separated according to the number and order of α and β interactions.

While the response arising from $\Pi^{II,\beta\beta}$ interactions contribute at the highest frequencies, those arising from purely translational fluctuations in the $\Pi^{II,\alpha\alpha}$ tensor are not necessarily found at the lowest frequencies. It has been argued that cancellation effects between second-, third- and higher-order DID interactions are more important in dictating the time scale of a particular contribution than the translational or rotational symmetry of the motions that give rise to them. This result may be used to explain why we do not observe differences between the non-diffusive components of the isotropic and anisotropic spectra for CS₂ and acetonitrile: even though the isotropic spectrum does not contain contributions from all of the terms in Eq. (2-6), the II terms have overlapping time scales so that weak or missing contributions do not change the lineshape appreciably (as compared to the anisotropic spectrum). It is not clear whether such an argument would apply for methanol due to the presence of hydrogen bonds, and it is also possible that the isotropic spectrum of methanol is dominated by a mechanism other than DID (as discussed for below).

MD simulations are generally able to reproduce experimental anisotropic intermolecular lineshapes with a high degree of accuracy, however it is interesting to note areas where difficulty has been encountered. In particular, several studies have had trouble reproducing the high frequency wing of the intermolecular feature, even in CS₂ and acetonitrile.^{31,71} The authors have suggested that poor fits may be due to the importance of higher order terms in the multipole expansion or short range interactions, both of which were neglected in these simulations. Similar difficulties have been encountered in light scattering studies of other simple systems,^{43,44} in which it was found that the same considerations are even more important in reproducing the isotropic lineshape than the anisotropic spectrum. We believe that both higher order multipole terms and short range interactions will be

important for simulating the isotropic spectra for liquids as simple as CS₂, acetonitrile and especially methanol.

2.4.2 Water

It has been well established that the intermolecular Raman spectrum of liquid water is different from that of other liquids. The primary difference is that the intermolecular interactions are known to contribute to the spectral density at frequencies as high as 800 cm⁻¹. The anisotropic response of water has been characterized using both frequency and time domain techniques.⁷²⁻⁷⁶ The depolarized spectrum contains three prominent features (in addition to low frequency rotational diffusion), which are often referred to by assignments based on their similarity with the spectrum of ice.^{72,73} The intermolecular region consists of distinct peaks centered at 60 and 175 cm⁻¹; the former is assigned to a transverse, or bending mode and the latter to a longitudinal, or translational mode. X-ray scattering experiments on liquid water have identified these modes as second and fourth nearest neighbor interactions respectively, emphasizing the collective nature of the motions.⁷⁷ In contrast, the region between 400-1000 cm⁻¹ contains an extremely broad band that arises because of hindered rotations of single water molecules. The breadth of the band has been attributed to librations about different molecular axes,⁷³ with small amplitude motions of the light hydrogen atoms undergoing oscillations in less than 50 fs. It is because of these extremely fast librations that water is able to accommodate changes in the electrostatic charge distributions of solutes more quickly and efficiently than any other liquid.

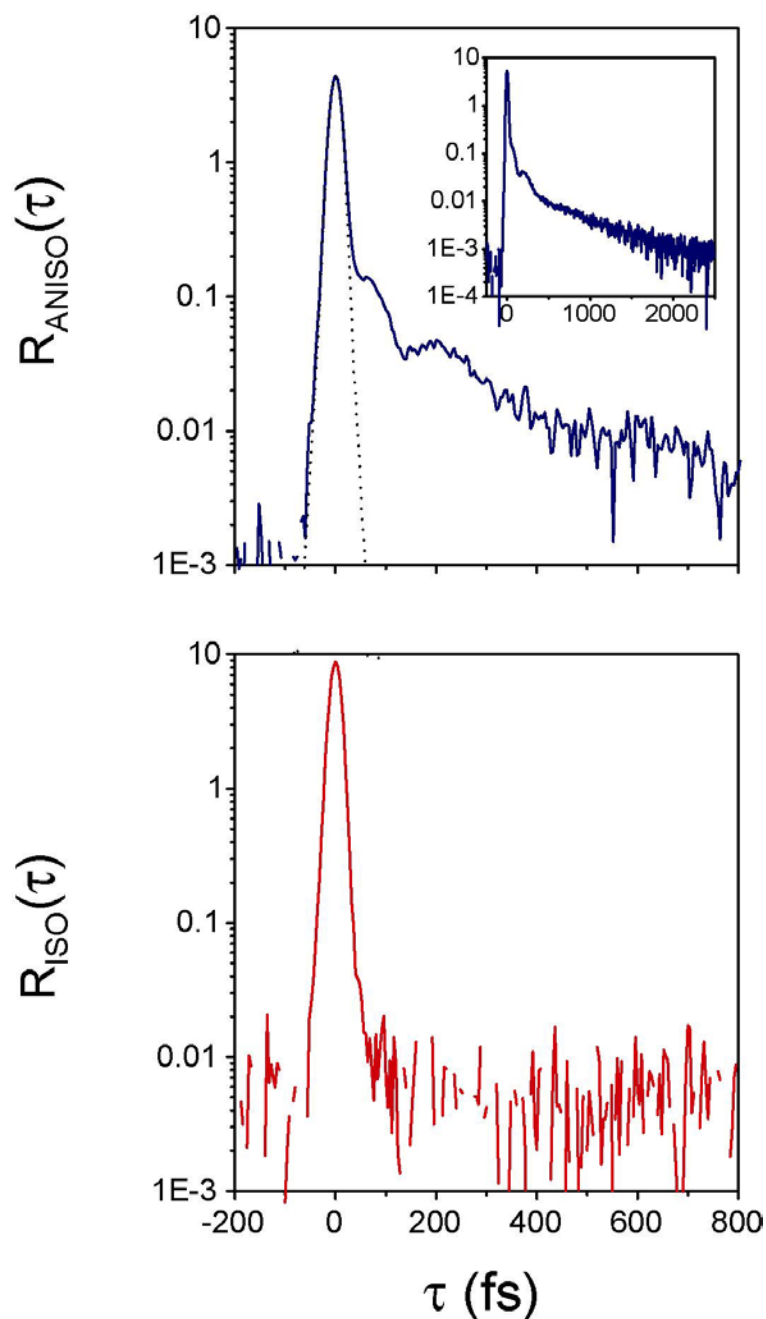


Figure 2-7. (Color) Self-consistent anisotropic and isotropic OKE signals for water. The anisotropic signal shown in the inset was taken using a static cell and may contain unwanted signal from the cell walls at short times, while the anisotropic and isotropic signals in the main panels were taken in the jet and are valid for all times.

The 16 fs pulses utilized in our experiment are sufficient to excite the entire intermolecular band, however data analysis requires extra precautions to ensure quantitative

agreement between the fast and slow time scales. As for the other liquids, all four tensor components were measured experimentally. However, instead of performing a self-consistent least-squares fit using Eq. (2-28) in the time-domain, each data set was first Fourier transformed and then fit in the frequency domain. This procedure is needed because the dynamics on the time scale of the experiment (16 fs) make it unreliable to fit to nuclear dynamics at delay times longer than 100 fs. Because the nonresonant electronic response does not contribute to the imaginary part of the transform, the frequency-domain fit is equivalent to the time-domain fit, as long as the phase of one component can be determined accurately. The depolarized Raman spectrum of water, for which the phase is not an experimental variable, has previously been recorded by Walrafen⁷⁷ and has been used here to phase the experimental anisotropic response. This phase choice has consequences with respect to the intensity of the isotropic response at high frequency, as will be discussed below.

The experimental time-domain anisotropic and isotropic responses are plotted in Fig. 2-7. The anisotropic time domain response is plotted for both the flowing jet and static cell (inset) samples. While the cell data is unreliable at short times due to signal from the walls, the long time diffusive peak is entirely due to water and can be measured more accurately with less noise. The jet data contains a sharp peak at 65 fs and a slightly broader peak near 200 fs. The former is predominantly due to the critically damped oscillation of the intermolecular longitudinal mode, and the latter to that of the transverse mode. Contributions from the librations appear as an asymmetry in the nonresonant electronic spike, which is not easily discernable from the time domain data.

The self-consistent Fourier transform spectra for S_{aniso} , S_{iso} , S_{zzzz} and S_{zzyy} are shown in Fig. 2-8. The frequency-domain anisotropic spectrum agrees quite well with previously reported spectra in both the frequency and relative intensity of all features. It contains all three intermolecular modes discussed above, with bands peaked at 45, 160 and ~ 450 cm^{-1} . The transverse mode peak is shifted to lower frequencies due to overlap with the rotational diffusion response. The spectra plotted in Fig. 2-8 show the direct Fourier transform of the time-domain data. The spectra are still convolved with the pulse bandwidth, which is also shown as a dotted curve in the top panel. However, the behavior of the deconvolved spectrum is clear, and it can be seen that the anisotropic signal decreases to baseline in the region between 800-1000 cm^{-1} , while the isotropic spectrum still has significant amplitude.

The isotropic response of water is entirely different from the anisotropic response. It contains almost no low frequency components, and therefore appears in the time domain predominantly as an asymmetry of the nonresonant electronic spike. Only a hint of a low-frequency decay can be detected at the positive time base of the electronic spike in the isotropic response of Fig. 2-7. The data can be observed much better in the frequency-domain, where the most notable feature is the broad peak extending from 250 cm^{-1} to higher frequencies. The high frequency tail of the broad peak follows the intensity of the pulse spectrum, indicating that the feature extends beyond the experimental bandwidth. The high frequency isotropic response is also observed as a broad positive contribution to the S_{zzzz} and S_{zzyy} spectra.

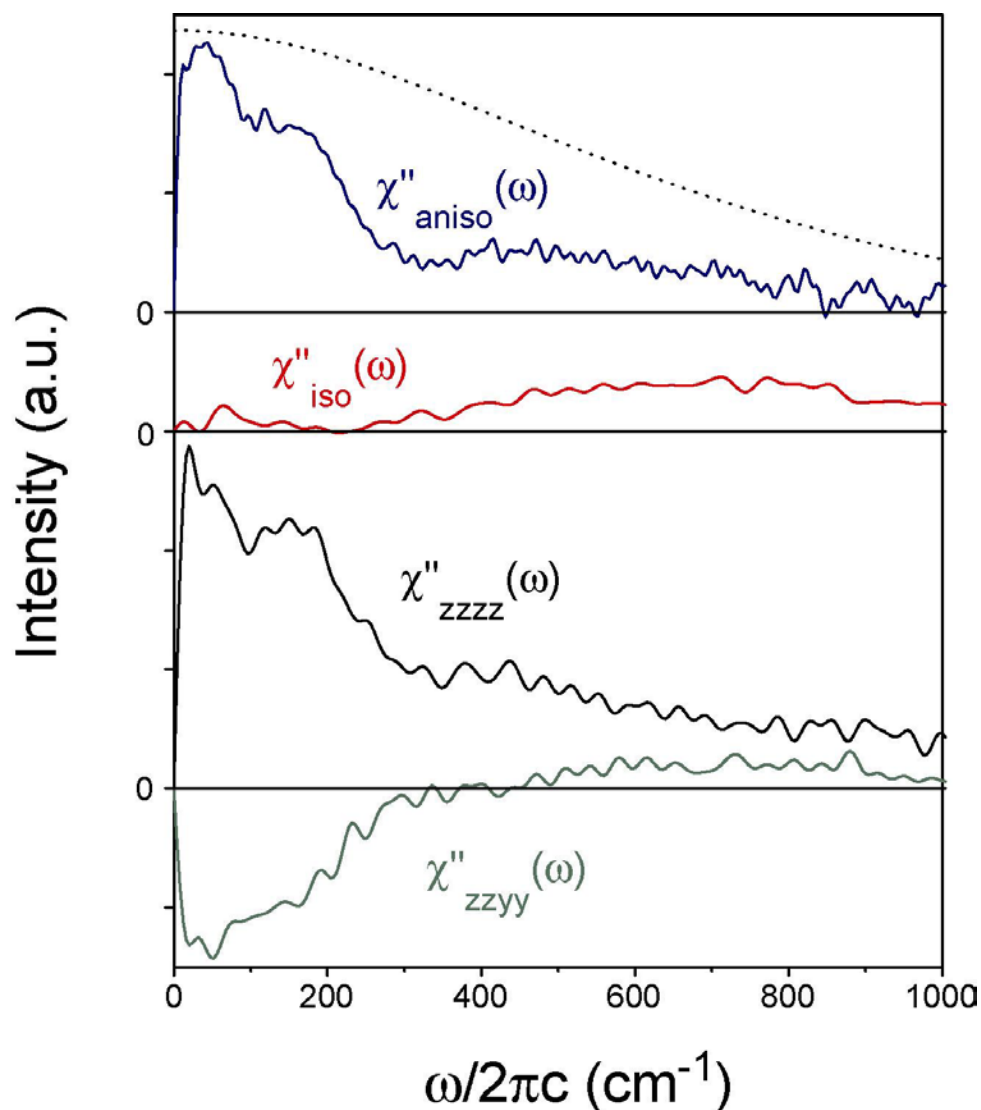


Figure 2-8. (Color) Fourier transform anisotropic, isotropic, parallel and crossed convolved Raman spectra of water. The pulse bandwidth is represented as a dotted line, and has the same zero level as the anisotropic spectrum. The isotropic spectrum represents the average of ten independent datasets, to reduce noise and ensure accuracy. 95% confidence limits are typically $\pm 30\%$.

The magnitude of the isotropic response of water indicates that intermolecular interactions are unusually large in water. Its amplitude is substantially larger than would be predicted based on a first-order DID model (Eq. (2-8)) since the polarizability of an isolated water molecule is nearly isotropic.⁷⁸ A similar conclusion has been reached for the anisotropic response in MD simulations employing first- and higher-order DID methods: the

zero-order molecular polarizability must have significantly more anisotropy than the gas phase value in order to reproduce experimental results.^{34,79,80} This is one indication that the DID approximation is inadequate to describe water, since modifying the isolated polarizability violates the perturbative nature of the approach.

At this point we note the consequence of phasing our data with respect to that of Walrafen. After subtracting background, Walrafen's anisotropic water spectrum drops to near-zero intensity at high frequencies (800–1000 cm^{-1}), however there have been more recent reports which indicate that the spectral intensity is non-zero up to the bending region ($\sim 1600 \text{ cm}^{-1}$).^{38,81,82} The consequence of this discrepancy is that our data represents a lower bound for the intensity of both the anisotropic and isotropic data in the high frequency region. However, because of the self-consistent data collection method, the phases of the two spectra are not independent; phasing the anisotropic data so that the spectral intensity at high frequencies is non-zero would require a corresponding rephasing of the isotropic data to increase its spectral intensity at high frequencies. In any case, it is clear that the intensity of the isotropic component is greater than that of the anisotropic component at high ($>800 \text{ cm}^{-1}$) frequencies.

The presence of a broad feature at high frequencies in the isotropic water spectrum was reported previously by Moskovits, et. al.,⁸¹ and by De Santis, et. al.,³⁸ who reconstructed the spectrum from frequency domain I_{VV} and I_{VH} measurements. These studies observe a broad band similar to Fig. 2-8 that merges with a peak at the OH bending frequency. The frequency of the maximum intensity and width of the band agree well with the Fourier transform isotropic Raman spectrum plotted in Fig. 2-8. Since all three experiments utilize different laser frequencies (488, 514 and 800 nm) yet observe the same feature, and since all

are far from electronic resonance, it is highly unlikely that that the band is due to a dichroic response. Benassi and co-workers also report that as the temperature is increased, the integrated intensity of the high frequency isotropic feature decreases and the maximum intensity shifts to lower frequencies.⁸²

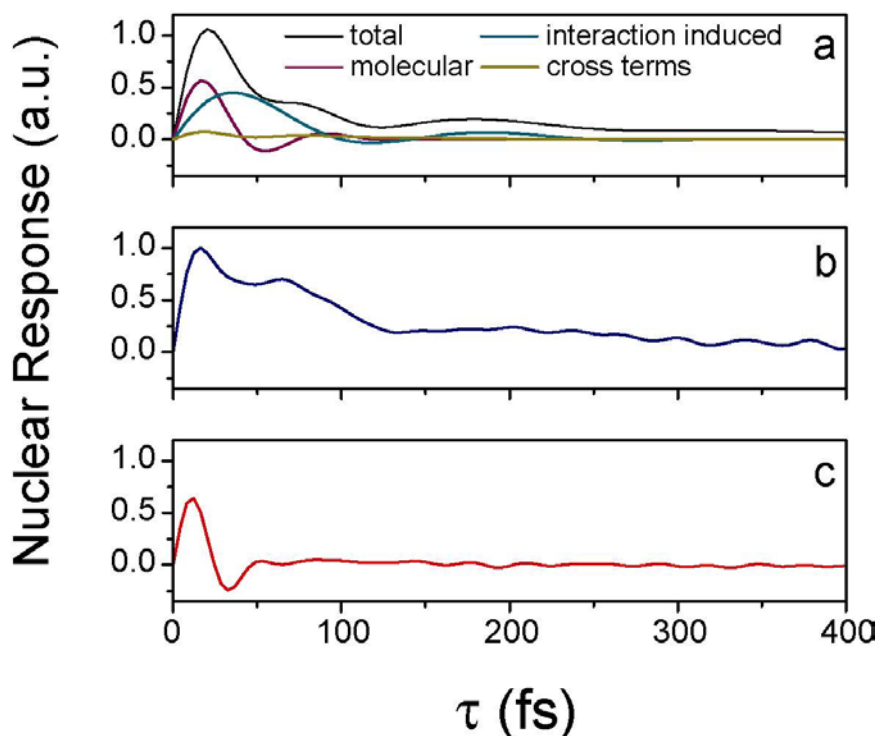


Figure 2-9. (Color) (a) Anisotropic nuclear response of water simulated by Saito and Ohmine.²⁷ Molecular, interaction-induced and cross terms have been projected from the total response. (b) Experimental anisotropic nuclear response of water obtained by inverse Fourier transform of the spectrum. (c) Experimental isotropic nuclear response of water.

There has been debate with regards to the depolarization ratio in the translational region ($<250\text{ cm}^{-1}$) of the spectrum. Walrafen originally reported that this region is entirely depolarized ($\rho = 0.75$), but later found $\rho < 0.75$ and used this as evidence for the existence of C_{2v} symmetry clusters within liquid water.^{72,73} Moscovitz and Michaelian⁸¹ later measured complete depolarization, which was again disputed by DeSantis and co-workers³⁸ who found constant depolarization ratio of $\rho \sim 0.72$ below 250 cm^{-1} . None of the studies indicated

structure to the depolarization ratio in the translational region. We find that the depolarization ratio remains between 0.70 and 0.75 from 10 - 250 cm^{-1} , and that around 60 cm^{-1} it is less than 0.75.

A comparison of the anisotropic and isotropic spectra reveals few similarities, as opposed to the other liquids observed in this investigation. At low frequencies, the only region where the response is non-zero is near 60 cm^{-1} , corresponding to the transverse mode of the anisotropic spectrum. However, the intensity is so low in comparison to the anisotropic intensity that the mode is still almost entirely depolarized. At higher frequencies, the shape of the isotropic band is distinct from the libration band in the anisotropic spectrum. While librations are peaked near 450 cm^{-1} and have zero intensity by about 1000 cm^{-1} , the isotropic feature rises to at least 750 cm^{-1} , and may become more intense or plateau at frequencies higher than the bandwidth of the experiment permits observation. Additionally, if the anisotropic band is properly assigned to arise from pure hindered rotations, one would expect these motions to be suppressed or eliminated entirely from the isotropic spectrum based on symmetry arguments. Therefore, the microscopic origin of the isotropic spectrum of water in the intermolecular region must be different from that which gives rise to the anisotropic spectrum.

In order to gain insight into the relevant time scales the molecular and interaction induced terms contribute to the Raman spectrum of water, Fig. 2-9 compares our nuclear response functions to the anisotropic response calculated by Saito and Ohmine in a MD simulation.³⁴ The experimental nuclear response functions were obtained by back transforming the nuclear spectral densities of Fig. 2-8. Saito and Ohmine have decomposed the response into contributions from the molecular and interaction-induced parts of the

polarizability and from the cross term. The molecular contribution is dominated by librations, and undergoes a critically damped oscillation on an 80 fs time scale, while the II term contributes on a time scale approximately twice as long. It can be seen that the total calculated response matches the experimental anisotropic response quite well. The maxima of the experimental response occur on a slightly faster time scale and with a different height ratio, both of which can be attributed to slight differences in the librational frequency and intensity, however the overall agreement is remarkable. On the other hand, it is nearly impossible to attribute the oscillation of the isotropic nuclear response, shown in Fig. 2-9c, to any of the components of the MD simulation. The isotropic response is clearly faster than even the molecular part of the anisotropic response.

2.4.3 Isotropic spectra of hydrogen bonding liquids

An interpretation of the high frequency features found in the isotropic Raman spectra of water and methanol is not straightforward, since there has been little attention paid to the isotropic response in previous molecular dynamics simulations of liquids. Based on what is available in the literature, we exclude several possibilities and further suggest plausible assignments. The explanations we offer focus on proton effects that may either be quantum mechanical in nature or have to do with a localized proton motion.

It has been suggested that isotropic spectral intensity in the 800-1000 cm^{-1} region of water is the overtone of the water librational band. A similar band has been observed in the IR spectrum of water and assigned as an overtone band.⁸³ Although it is possible for a depolarized intermolecular vibration to have a partially polarized overtone, the intensity of the fundamental relative to that at higher frequencies is not consistent with an assignment as

an overtone band, even for a highly anharmonic mode. In addition, the temperature dependence of the high frequency intensity is opposite that which would be predicted for an overtone band.⁸²

Another explanation for a polarized intermolecular band at high frequencies is that higher order terms in the multipole expansion are significant and contribute at high frequencies. The importance of higher order terms has been suggested by Sampoli and co-workers for both H₂S and for water.^{38,82,84} MD simulations using a TIP4P potential were performed using an induced polarizability that included interactions between the permanent dipole moment and the first hyperpolarizability, and interactions of the molecular polarizability with the dipole-quadrupole polarizability.⁸² While these effects were found to be important to achieve a non-zero isotropic spectral intensity in the 300-700 cm⁻¹ region, the long range induced polarizability model found no spectral density at frequencies greater than 700 cm⁻¹, so it is unlikely that these terms contribute to the observed isotropic response.

Results similar to those presented here have been found for the case of the isotropic component of Raman scattering by atomic gasses^{43,44} and liquids⁸⁵, ionic metal melts^{86,87} and other simple molecules⁸⁸. In general, these studies have measured a depolarization ratio which is a maximum for the lowest frequency components measured, but which drops with increasing frequency, eventually tending towards zero for the highest frequencies measured. For example, a study of He₂ revealed that scattering that is completely polarized beyond ~500 cm⁻¹.⁴⁴ Numerous models have been used to reproduce the depolarization ratios; while a multipole expansion may reproduce the data for low or intermediate frequencies, it consistently fails on the high frequency wing. The authors of these studies have concluded that it is important to take into consideration short range interactions, such as exchange,

induction and dispersion, which may generally contribute to both the anisotropic and isotropic response. It has been suggested that such effects may be taken into account using an analytical model that utilizes non-local polarizability density,⁴² or by means of *ab initio* calculations that can account for these quantum mechanical properties directly.⁸⁹ By using *ab initio* methods, it has been found that these calculations differ substantially from classical models, especially for light atoms such as He where quantum effects are important.

It would be a logical extension to assume that the light hydrogen atoms of water and methanol are greatly affected by these same quantum mechanical interactions and therefore need to be treated as quantum particles. Such a treatment is almost certainly not needed at low frequencies, for which classical simulations adequately approximate the center of mass intermolecular motions, as has been proven by numerous simulations. However, quantum mechanical effects would be expected to contribute significantly for spectral contributions at frequencies higher than kT , as are present in both hydrogen bonding liquids.

Another possible assignment of the isotropic spectrum of water and methanol, which is not necessarily exclusive from the quantum mechanical effects, is a modulation of the polarizability due to low amplitude motions of individual hydrogen atoms, possibly even involving proton mobility. A related idea has been suggested in the form of hydrogen bond dynamics by Nardone and co-workers, although few specifics were proposed.⁸² It is hard to ignore the fact that the broad isotropic band in water is continuous from frequencies corresponding to the anisotropic librations around $400\text{-}500\text{ cm}^{-1}$ to the intramolecular bends near 1600 cm^{-1} . A similar broad background has been observed in the spectroscopy of acidic media and attributed to the strong electronic polarization of collective motions coupled to the excess proton.^{90,91} Simulations and normal mode calculations have been used to assign

features in the 950-1200 cm^{-1} range to collective motions involved in a Zundel-like $\text{O}-\text{H}^+-\text{O}$ stretch.^{92,93} The assignment of our isotropic band would not necessarily have to include excess protons, but could involve a motion localized to hydrogen atoms, which are known to have an unusually large polarizability when involved in a hydrogen bond.⁹⁴

Simulation of this type of motion requires a flexible molecular potential, and calculation of the Raman spectrum depends heavily on the model used to calculate the polarizability. Most MD simulations of water thus far have utilized rigid potentials such as the MCY,⁹⁵ SPC,^{79,96} TIPS2,^{26,34} TIP4P,⁹⁷ and other rigid models,⁹⁸ most in conjunction with point molecular polarizabilities. The fastest dynamics which can be captured by these simulations are librations, which is the reason that the spectral density for each drops to zero by $\sim 800 \text{ cm}^{-1}$. However, simulations of the IR spectrum of neutral water^{28,99,100} and of the hydrated proton^{92,93} in which a flexible potential (flexible SPC) is employed contain a region of non-zero intensity between the librations and intermolecular bends (1000-1600 cm^{-1}). Although the Raman spectrum is not presented, the results indicate that there exists dynamics occurring on a time scale between librations and bends, and it seems likely that a distributed polarizability model would contain Raman spectral density in this region. A Carr-Parinello MD (CPMD) calculation of the IR spectrum of water also contains spectral intensity in this region.¹⁰¹ The CPMD simulation also treats electrons quantum mechanically, so the induction, exchange and dispersion effects discussed above would also be included therein.

Further calculations are needed to investigate the possibility that short-range electronic properties and/or mechanical motions contribute to the high frequency feature we observe in the isotropic spectra. Such a determination should now be possible based on current classical and CPMD simulation techniques. One additional possibility includes the

quantum effects of proton motion, however it is not clear that such a detailed study is needed until the possibilities listed above are explored.

2.5 Conclusions

We have measured the isotropic and anisotropic response functions for several neat liquids in the frequency range 0-1000 cm^{-1} . These results demonstrate the utility of the SM-OKE method for the determination of the low frequency isotropic Raman spectrum, and for the accurate scaling of the spectrum with respect to the depolarized spectrum by a self-consistent fit of multiple data sets. Because the nuclear portion of the third-order susceptibility has only two independent components, our measurements contain all of the information that can be derived from a one-dimensional Raman experiment. We believe the isotropic/anisotropic representation is the clearest separation of the Raman active intermolecular dynamics that can be measured directly.

The isotropic response is less intense than the anisotropic response by about an order of magnitude for CS_2 , acetonitrile and methanol, however the isotropic response of water is unusually strong. In all cases, the lowest frequency components, attributed largely to the rotational diffusion of single molecules, are preferentially suppressed or eliminated from the isotropic spectrum as would be expected from a decomposition of the system polarizability into molecular and induced contributions. At higher frequencies, the isotropic lineshapes for CS_2 and acetonitrile are similar to their anisotropic counterparts, however this is not the case for methanol and water. The high frequency wing of the isotropic spectrum for both of the hydrogen bonding liquids extends farther than the depolarized spectrum, exceeding our instrument sensitivity ($\sim 1000 \text{ cm}^{-1}$) in the case of water.

It is not surprising that the scattering characteristics in the intermolecular frequency range of the spectrum for the nonpolar (CS₂) and polar aprotic (acetonitrile) liquids differ from the strongly associating hydrogen-bonding liquids (methanol and water). However, the particular mechanism that can account for the differences in isotropic scattering is not entirely clear. While a DID interaction mechanism has been widely used to account for anisotropic scattering in simple liquids, we do not believe it will be sufficient to reproduce the entire isotropic response, even for the non-associating liquids. Short-range interactions will be needed to model the interaction-induced effects, especially for methanol and water. It is obvious that quantum effects should be important for these liquids since the bulk of the isotropic scattering occurs above kT , and because light atoms such as hydrogen are especially susceptible to induction and exchange processes. In addition, it is also possible that the observed spectra correspond to motion localized on individual hydrogen atoms. Simulations of liquids that take into account these mechanisms will be essential to gain an understanding of the interactions that give rise to the isotropic spectra presented here.

References

- (1) McMorow, D.; Lotshaw, W. T.; Kenney-Wallace, G. A. *IEEE J. Quantum Electron.* **1988**, *QE-24*, 443.
- (2) Deeg, F. W.; Fayer, M. D. *J. Chem. Phys.* **1989**, *91*, 2269.
- (3) Nelson, K. A. *J. Lumin.* **1990**, *45*, 120.
- (4) Cho, M.; Du, M.; Scherer, N. F.; Fleming, G. R.; Mukamel, S. *J. Chem. Phys.* **1993**, *99*, 2410.
- (5) Righini, R. *Science* **1993**, *262*, 1386.

- (6) Hinze, G.; Brace, D. D.; Gottke, S. D.; Fayer, M. D. *J. Chem. Phys.* **2000**, *113*, 3723.
- (7) Fourkas, J. T. Nonresonant Intermolecular Spectroscopy of Liquids. In *Ultrafast Infrared and Raman Spectroscopy*, 2001; Vol. 26; pp 473.
- (8) Shirota, H.; Castner, E. W. *J. Am. Chem. Soc.* **2001**, *123*, 12877.
- (9) *Phenomena Induced by Intermolecular Interactions*; Birnbaum, G., Ed.; Plenum Publishing Corporation: New York, 1985; Vol. Ser. B, 127.
- (10) Dick, B. *Chem. Phys.* **1987**, *113*, 131.
- (11) Li, W.; Purucker, H.-G.; Laubereau, A. *Opt. Commun.* **1992**, *94*, 300.
- (12) Tokmakoff, A. *J. Chem. Phys.* **1996**, *105*, 1.
- (13) Cummins, H. Z.; Li, G.; Du, W.; Pick, R. M.; Dreyfus, C. *Phys. Rev. E* **1996**, *53*, 896.
- (14) Cong, P.; Chang, Y. J.; Simon, J. D. *J. Phys. Chem.* **1996**, *100*, 8613.
- (15) Matsuo, S.; Tahara, T. *Chem. Phys. Lett.* **1997**, *264*, 636.
- (16) Chang, Y. J.; Cong, P.; Simon, J. D. *J. Chem. Phys.* **1997**, *106*, 8639.
- (17) Goodno, G. D.; Dadusc, G.; Miller, R. J. D. *J. Opt. Soc. Am. B* **1998**, *15*, 1791.
- (18) Maznev, A. A.; Nelson, K. A.; Rogers, J. A. *Opt. Lett.* **1998**, *23*, 1319.
- (19) Khalil, M.; Golonzka, O.; Demirdöven, N.; Fecko, C. J.; Tokmakoff, A. *Chem. Phys. Lett.* **2000**, *321*, 231.
- (20) Khalil, M.; Demirdöven, N.; Golonzka, O.; Fecko, C. J.; Tokmakoff, A. *J. Phys. Chem. A* **2000**, *104*, 5211.
- (21) Constantine, S.; Gardecki, J. A.; Zhou, Y.; Ziegler, L. D.; Ji, X.; Space, B. *J. Phys. Chem. A* **2001**, *105*, 9851.
- (22) Murry, R. L.; Fourkas, J. T. *J. Chem. Phys.* **1997**, *107*, 9726.
- (23) Murry, R. L.; Fourkas, J. T.; Keyes, T. *J. Chem. Phys.* **1998**, *109*, 2814.

- (24) Stratt, R. M. *Acc. Chem. Res.* **1995**, *28*, 201.
- (25) Keyes, T. *J. Phys. Chem. A* **1997**, *101*, 2921.
- (26) Cho, M.; Fleming, G. R.; Saito, S.; Ohmine, I.; Stratt, R. M. *J. Chem. Phys.* **1994**, *100*, 6672.
- (27) Ladanyi, B. M.; Klein, S. J. *J. Chem. Phys.* **1996**, *105*, 1552.
- (28) Ahlborn, H.; Ji, X.; Space, B.; Moore, P. B. *J. Chem. Phys.* **1999**, *111*, 10622.
- (29) Garberoglio, G.; Vallauri, R. *J. Chem. Phys.* **2001**, *115*, 395.
- (30) Frenkel, D.; McTague, J. P. *J. Chem. Phys.* **1980**, *72*, 2801.
- (31) Geiger, L. C.; Ladanyi, B. M. *J. Chem. Phys.* **1987**, *87*, 191.
- (32) Stassen, H.; Steele, W. A. *J. Chem. Phys.* **1995**, *103*, 4408.
- (33) Ladanyi, B. M.; Liang, Y. Q. *J. Chem. Phys.* **1995**, *103*, 6325.
- (34) Saito, S.; Ohmine, I. *J. Chem. Phys.* **1996**, *106*, 4889.
- (35) Kiyohara, K.; Kamada, K.; Ohta, K. *J. Chem. Phys.* **2000**, *112*, 6338.
- (36) Jansen, T. I. C.; Snijders, J. G.; Duppen, K. *J. Chem. Phys.* **2001**, *114*, 10910.
- (37) Buckingham, A. D. Permanent and Induced Molecular Moments and Long-Range Intermolecular Forces. In *Intermolecular Forces*; Hirschfelder, J. O., Ed., 1967; Vol. 12; pp 107.
- (38) De Santis, A.; Frattini, R.; Sampoli, M.; Mazzacurati, V.; Nardone, M.; Ricci, M. A.; Ruocco, G. *Mol. Phys.* **1987**, *61*, 1199.
- (39) Kivelson, D.; Madden, P. A. Light Scattering Studies of Molecular Liquids. In *Ann. Rev. Phys. Chem.*; Rabinovitch, B. S., Schurr, J. M., Strauss, H. L., Eds., 1980; Vol. 31; pp 523.
- (40) Madden, P. A.; Tildesley, D. J. *Mol. Phys.* **1985**, *55*, 969.

- (41) Cao, J.; Wu, J.; Yang, S. *J. Chem. Phys.* **2002**, *116*, 3739.
- (42) Hunt, K. L. C. *J. Chem. Phys.* **1984**, *80*, 393.
- (43) Gaye, O.; Chrysos, M.; Teboul, V.; Le Duff, Y. *Phys. Rev. A* **1997**, *55*, 3484.
- (44) Rachet, F.; Chrysos, M.; Guillot-Noel, C.; Le Duff, Y. *Phys. Rev. Lett.* **2000**, *84*, 2120.
- (45) Hellwarth, R. W. *Prog. Quant. Electr.* **1977**, *5*, 1.
- (46) Mukamel, S. *Principles of Nonlinear Optical Spectroscopy*; Oxford University Press: New York, 1995.
- (47) Butcher, P. N.; Cotter, D. *The Elements of Nonlinear Optics*; Cambridge University Press: Cambridge, 1990.
- (48) Berne, B. J.; Pecora, R. *Dynamic Light Scattering*; R. E. Krieger Publishing Co.: Malabar, FL, 1990.
- (49) Murry, R. L.; Fourkas, J. T.; Li, W.-X.; Keyes, T. *Phys. Rev. Lett.* **1999**, *83*, 3550.
- (50) Zhao, X.; Kivelson, D. *J. Phys. Chem* **1995**, *99*, 6721.
- (51) Ziegler, L. D.; Fan, R.; Desrosiers, A. E.; Scherer, N. F. *J. Chem. Phys.* **1994**, *100*, 1823.
- (52) Lotshaw, W. T.; McMorow, D.; Thantu, N.; Melinger, J. S.; Kitchenham, R. *J. Raman Spectros.* **1995**, *26*, 571.
- (53) Vöhringer, P.; Scherer, N. F. *J. Phys. Chem.* **1995**, *99*, 2684.
- (54) Chang, Y. J.; Cong, P.; Simon, J. D. *J. Phys. Chem.* **1995**, *99*, 7857.
- (55) Xu, Q. H.; Ma, Y. Z.; Fleming, G. R. *Chem. Phys. Lett.* **2001**, *338*, 254.
- (56) Franko, M.; Tran, C. D. *Rev. Sci. Instrum.* **1996**, *67*, 1.

- (57) Sheik-Bahae, M.; Wei, A. A. T.-H.; Hagan, D. J.; van Stryland, E. W. *IEEE J. Quant. Electron.* **1990**, *26*, 760.
- (58) Gardecki, J. A.; Yu, G.; Constantine, S.; Peng, J.; Zhou, Y.; Ziegler, L. D. *J. Chem. Phys.* **2001**, *114*.
- (59) Owyong, A. *IEEE J. Quantum Electron.* **1973**, *QE-9*, 1064.
- (60) Levenson, M. D. *IEEE J. Quantum Electron.* **1974**, *QE-10*, 110.
- (61) Weaire, D.; Wherrett, B. S.; Miller, D. A. B.; Smith, S. D. *Opt. Lett.* **1979**, *4*, 331.
- (62) McMorrow, D.; Lotshaw, W. T. *J. Phys. Chem.* **1991**, *95*, 10395.
- (63) Loughnane, B. J.; Scodinu, A.; Farrer, R.; Fourkas, J. T.; Mohanty, U. *J. Chem. Phys.* **1999**, *111*, 2686.
- (64) Ji, X.; Alhborn, H.; Space, B.; Moore, P. B.; Zhou, Y.; Constantine, S.; Ziegler, L. D. *J. Chem. Phys.* **2000**, *112*, 4186.
- (65) Smith, N. A.; Meech, S. R. *Faraday Discuss.* **1997**, *108*, 35.
- (66) Chelli, R.; Ciabatti, S.; Cardini, G.; Righini, R.; Procacci, P. *J. Chem. Phys.* **1999**, *111*, 4218.
- (67) Keyes, T.; Kivelson, D.; McTague, J. P. *J. Chem. Phys.* **1971**, *55*, 4096.
- (68) McHale, J. L. *J. Chem. Phys.* **1981**, *75*, 30.
- (69) Logan, D. E. *Chem. Phys.* **1986**, *103*, 215.
- (70) Torii, H.; Tasumi, M. *J. Chem. Phys.* **1993**, *99*, 8459.
- (71) Steffen, T.; Meinders, N. A. C. M.; Duppen, K. *J. Phys. Chem. A* **1998**, *102*, 4213.
- (72) Walrafen, G. E. *J. Chem. Phys.* **1964**, *40*, 3249.

- (73) Walrafen, G. E. Raman and Infrared spectral investigations of water structure. In *Water: A Comprehensive Treatise*; Franks, F., Ed.; Plenum: New York, 1972; Vol. 1; pp 151.
- (74) Palese, S.; Schilling, L.; Miller, R. J. D.; Staver, P. R.; Lotshaw, W. T. *J. Phys. Chem.* **1994**, *98*, 6308.
- (75) Castner, E. W., Jr.; Chang, Y. J.; Chu, Y. C.; Walrafen, G. E. *J. Chem. Phys.* **1995**, *102*, 653.
- (76) Carey, D. M.; Korenowski, G. M. *J. Chem. Phys.* **1998**, *108*, 2669.
- (77) Walrafen, G. E. *J. Phys. Chem.* **1990**, *94*, 2237.
- (78) Murphy, W. F. *J. Chem. Phys.* **1977**, *67*, 5877.
- (79) Bosma, W. B.; Fried, L. E.; Mukamel, S. *J. Chem. Phys.* **1993**, *98*, 4413.
- (80) Bursulaya, B. D.; Kim, H. J. *J. Phys. Chem. B* **1997**, *101*, 10994.
- (81) Moskovits, M.; Michaelian, K. H. *J. Chem. Phys.* **1978**, *69*, 2306.
- (82) Benassi, P.; Mazzacurati, V.; Nardone, M.; Ricci, M. A.; Ruocco, G.; De Santis, A.; Frattini, R.; Sampoli, M. *Mol. Phys.* **1987**, *62*, 1467.
- (83) Oder, R.; Goring, D. A. I. *Spectrochim. Acta* **1971**, *27A*, 2285.
- (84) De Santis, A.; Sampoli, M. *Chem. Phys. Lett.* **1983**, *102*, 425.
- (85) Teboul, V.; Le Duff, Y. *J. Chem. Phys.* **1997**, *107*, 10415.
- (86) Madden, P. A.; Board, J. A. *J. Chem. Soc., Faraday Trans. 2* **1987**, *83*, 1891.
- (87) Ribeiro, M. C. C.; Wilson, M.; Madden, P. A. *J. Chem. Phys.* **1999**, *110*, 4803.
- (88) Elliasmine, A.; Godet, J.-L.; Le Duff, Y.; Bancewicz, T. *Phys. Rev. A* **1997**, *55*, 4230.
- (89) Dacre, P. D. *Mol. Phys.* **1982**, *45*, 1.

- (90) Zundel, G. In *The Hydrogen Bond: Recent Developments in Theory and Experiment, Vol. II*; Schuster, P., Zundel, G., Sandorfy, C., Eds.; North Holland: Amsterdam, 1976; pp 683.
- (91) Kim, J.; Schmitt, U.; Greutzmacher, J.; Voth, G. A.; Scherer, N. E. *J. Chem. Phys.* **2002**, *116*, 737.
- (92) Vuilleumier, R. *J. Chem. Phys.* **1999**, *111*, 4251.
- (93) Schmitt, U. W.; Voth, G. A. *J. Chem. Phys.* **1999**, *111*, 9361.
- (94) Janoschek, R.; Weidemann, E. G.; Pfeiffer, H.; Zundel, G. *J. Am. Chem. Soc.* **1972**, *94*, 2387.
- (95) Impey, R. W.; Madden, P. A.; McDonald, I. R. *Mol. Phys.* **1982**, *46*, 513.
- (96) Saito, S.; Ohmine, I. *J. Chem. Phys.* **1995**, *102*, 3566.
- (97) Frattini, R.; Sampoli, M.; Ricci, M. A.; Ruocco, G. *Chem. Phys. Lett.* **1987**, *141*, 297.
- (98) Bursulaya, B. D.; Kim, H. J. *J. Chem. Phys.* **1998**, *109*, 4911.
- (99) Marti, J.; Guardia, E.; Padro, J. A. *J. Chem. Phys.* **1994**, *101*, 10883.
- (100) Marti, J.; Padro, J. A.; Guardia, E. *J. Chem. Phys.* **1996**, *105*, 639.
- (101) Silvestrelli, P. L.; Bernasconi, M.; Parrinello, M. *Chem. Phys. Lett.* **1997**, *277*, 478.

Chapter 3

Theory and modeling of time-resolved IR experiments

3.1 Introduction

Time-dependent resonant spectroscopies probe the dynamic behavior of specific eigenstates, but may provide a wealth of information about a large number of degrees of freedom within a sample. For example, numerous investigations with short visible or near-IR pulses have exploited time-dependent techniques to measure fluctuations in the optical properties a chromophore in solution and interpreted the results in terms of the intermolecular dynamics required to solvate the chromophore.¹⁻⁴ Analogous techniques with mid-IR light measure vibrational dynamics of a specific oscillator, which may likewise be related to intermolecular dynamics.⁵⁻⁷ However, the mid-IR experiments have the advantage that they can observe neat liquids, unperturbed by the presence of a bulky solute that can obscure the most interesting behavior.

The extraction of useful information about the vibrational dynamics of an oscillator from the signals measured in time-resolved IR experiments requires a theory to relate the

experimental observables to microscopic degrees of freedom. This theoretical framework must take into account interactions between the input light fields and the resonant vibrational oscillator (henceforth referred to as the system), as well as interactions between the oscillator and the surrounding degrees of freedom (i.e. the bath). The Brownian oscillator model for four wave mixing experiments developed by Yan and Mukamel describes energy fluctuations in a two level system coupled to a stochastic bath with arbitrary timescales and incorporates field-matter interactions as a perturbative expansion of the density matrix.^{8,9} Their theory has been successfully applied to model a multitude of optical experiments, such as photon echo, transient grating, pump-probe and Raman spectroscopies,^{1,10-14} however the limitation imposed by a two level system precludes its application to resonant IR spectroscopies, which excite a manifold of intramolecular vibrational states. Recently, Sung and Silbey (SS) have extended the Brownian oscillator model to describe four wave mixing spectroscopies for a multilevel system coupled to a bath with arbitrary timescales.^{15,16} Their theory includes both cross- and autocorrelation functions of the energy fluctuations between different states, which are important to describe four wave mixing experiments in vibrational systems and in electronic systems that include specific vibrational sublevels.

In this chapter, the SS theory is applied to frequency fluctuations in the specific case of a three level anharmonic oscillator, which will be used to interpret the results of various types of IR four wave mixing spectroscopies of water in Chapters 5 and 6. Population relaxation is included in the theory phenomenologically, and rotations are treated with an orientational diffusion model. To extract the most meaningful microscopic data possible, the experiments in later chapters are modeled numerically using finite duration input pulses that match those used in the experiments. In some cases, the electric fields used for the

calculations are those actually utilized in the experiment, as measured by a second order frequency resolved optically gated autocorrelation at the time of the experiment. This chapter will provide details on the theory used to model the experiments as well as a description of the numerical calculations, while the results of the calculations are presented with the experimental data in later chapters. The C++ code that implements the numerical calculations is included in the Appendix.

3.2 Theoretical framework

3.2.1 Third order polarization for a multilevel system

In a four wave mixing experiment, the three input electromagnetic fields create a macroscopic polarization within the sample, which subsequently radiates a signal field according to Maxwell's equations. The specific relationship between the input fields and the polarization is governed by the material response function, which is dependent on the microscopic properties of the sample and thus contains all of the information that can be extracted from the spectroscopic measurement. This section first outlines Sung and Silbey's derivation of the nonlinear response function for a multilevel system, which is then used to calculate the polarization and radiated signal field for the particular system and experimental geometry utilized for the majority of the IR four wave mixing experiments in the remainder of this work.

We consider a liquid sample that couples to external electromagnetic fields through dipolar interactions. Following SS,¹⁵ the total Hamiltonian can be separated into a

contribution from the liquid in the absence of the external field H_{liquid} , and a part that describes the field-matter interaction H_{int} :

$$H_{total} = H_{liquid} + H_{int} \quad (3-1)$$

H_{int} takes the form:

$$H_{int} = -\boldsymbol{\mu}(\mathbf{Q}) \cdot \mathbf{E}(\mathbf{r}, t) \quad (3-2)$$

where the transition dipole operator $\boldsymbol{\mu}(\mathbf{Q})$ depends on the system coordinates and $\mathbf{E}(\mathbf{r}, t)$ is the external electric field. The liquid consists of the system, which is defined by those degrees of freedom that directly interact with the radiation field, and the bath, which encompasses the rest of the liquid's degrees of freedom. The liquid Hamiltonian is thus partitioned into contributions from the system H_S , the bath H_B , and the coupling between the system and bath H_{SB} :

$$H_{liquid} = H_S(\mathbf{P}, \mathbf{Q}) + H_B(\mathbf{p}, \mathbf{q}) + H_{SB}(\mathbf{P}, \mathbf{Q}, \mathbf{p}, \mathbf{q}) \quad (3-3)$$

\mathbf{P} and \mathbf{Q} represent the momenta and coordinates of the system, while \mathbf{p} and \mathbf{q} refer to those of the bath.

SS do not make assumptions about the form of H_S , allowing a generalization of their results to four wave mixing on a variety of systems, although they do utilize the system eigenstates as a basis to describe the state of the system. They assume that the bath is comprised of harmonic oscillators:

$$H_B(\mathbf{p}, \mathbf{q}) = \frac{1}{2} \sum_v (p_v^2 + \omega_v^2 q_v^2) \quad (3-4)$$

and that the system couples to the v th bath oscillator with a strength that is linear in the bath coordinate:

$$H_{SB} = \sum_v \chi_v(\mathbf{P}, \mathbf{Q}) q_v. \quad (3-5)$$

χ_v is an operator in the system degrees of freedom that quantifies the strength with which the system couples to the v th bath oscillator. System-bath coupling introduces dephasing and relaxation processes between eigenstates of the system in the absence of the radiation field, although the relaxation processes are neglected in the present treatment and will be included phenomenologically in the final expressions used to model the four wave mixing experiments.

The macroscopic polarization of the sample $\mathbf{P}(\mathbf{r}, t)$ is the expectation value of the dipole operator:

$$\mathbf{P}(\mathbf{r}, t) = \text{Tr}[\boldsymbol{\mu}(\mathbf{Q})\rho(\mathbf{r}, t)]. \quad (3-6)$$

Here, $\rho(\mathbf{r}, t)$ is the total density matrix of the system whose diagonal elements ρ_{nn} describe populations of the system eigenstates and off-diagonal elements ρ_{nm} are coherent superpositions of the eigenstates (henceforth referred to as coherences). Tr indicates a sum over all degrees of freedom. The density matrix evolves according to the Liouville equation:

$$\frac{\partial \rho(\mathbf{r}, t)}{\partial t} = \frac{1}{i\hbar} [H_{total}, \rho(\mathbf{r}, t)] \quad (3-7)$$

where the square brackets in Eq. (3-7) denote a quantum mechanical commutator. By integrating both sides of this equation with respect to time and iteratively substituting the resulting expression for $\rho(\mathbf{r}, t)$ into itself, the density matrix can be expressed as a power series in the number of interactions with the external field. Substitution of this solution into Eq. (3-6) likewise expands the polarization as a power series in the electric field:

$$\mathbf{P}(\mathbf{r}, t) = \sum_{n=1}^{\infty} \mathbf{P}^{(n)}(\mathbf{r}, t). \quad (3-8)$$

$\mathbf{P}^{(1)}(\mathbf{r}, t)$ determines the linear optical properties of the sample, while higher order terms are related to the nonlinear optical properties. For isotropic samples, symmetry arguments dictate that the even terms ($n = 2, 4, \dots$) in the polarization expansion vanish,¹⁷ making the lowest order nonlinear term the third order polarization $\mathbf{P}^{(3)}(\mathbf{r}, t)$. Since four wave mixing spectroscopies probe the third order response of the sample, the remainder of this discussion will focus on the calculation of $P^{(3)}$.

The third order polarization can be expressed as a convolution of the material response function with the input electric fields:¹⁸

$$\begin{aligned} \mathbf{P}^{(3)}(\mathbf{r}, t) = & \int_0^{\infty} dt_3 \int_0^{\infty} dt_2 \int_0^{\infty} dt_1 \mathbf{R}(t_3, t_2, t_1) \\ & \mathbf{E}(\mathbf{r}, t - t_3) \mathbf{E}(\mathbf{r}, t - t_3 - t_2) \mathbf{E}(\mathbf{r}, t - t_3 - t_2 - t_1) \end{aligned} \quad (3-9)$$

where t_1 and t_2 are the positive valued time periods that separate the three field-matter interactions and t_3 is the time between the last interaction and detection of the polarization.

The nonlinear response function $\mathbf{R}(t_3, t_2, t_1)$, calculated according to the procedure described in the preceding paragraph is a thrice-nested commutator of the system transition dipole evaluated at times differences corresponding to those between the field matter interactions:

$$\mathbf{R}(t_3, t_2, t_1) = \left(\frac{i}{\hbar}\right)^3 \left\langle \left[\left[\left[\boldsymbol{\mu}(t_3 + t_2 + t_1), \boldsymbol{\mu}(t_2 + t_1) \right], \boldsymbol{\mu}(t_1) \right], \boldsymbol{\mu}(0) \right] \right\rangle. \quad (3-10)$$

The time dependence of the dipole is $\boldsymbol{\mu}(t) = \exp(iH_{\text{liquid}}t/\hbar)\boldsymbol{\mu}(\mathbf{Q})\exp(-iH_{\text{liquid}}t/\hbar)$ and the angular brackets denote a trace over the liquid degrees of freedom at equilibrium.

Sung and Silbey have evaluated Eq. (3-10) within the second Cumulant approximation in terms of the energy gap correlation function:

$$C_{pq}(\tau - \tau') = \left\langle \delta\omega_{pa}(\tau) \delta\omega_{qa}(\tau') \right\rangle_B \quad (3-11)$$

where $\omega_{xa}(t)$ denotes the energy difference (scaled by \hbar) between the system eigenstates x and a reference state a at time t , and $\delta\omega_{xa}(t)$ is the difference between $\omega_{xa}(t)$ and its time-averaged value. The trace in Eq. (3-11) is evaluated over the bath degrees of freedom. This correlation function is analogous to the frequency autocorrelation function for a vibrational system discussed in Chapter 1 when p and q are the $v=1$ vibrational states ($p = q = 1$). Sung and Silbey find that the response function can be written:¹⁵

$$\begin{aligned} \mathbf{R}(t_3, t_2, t_1) = & \left(\frac{i}{\hbar} \right)^3 \sum_{abcd} P_a \{ \\ & \left[\boldsymbol{\mu}^{ab} \boldsymbol{\mu}^{bc} \boldsymbol{\mu}^{cd} \boldsymbol{\mu}^{da} \exp(-i\omega_{ba}t_3 - i\omega_{ca}t_2 - i\omega_{da}t_1) F_{abcd}^{(1)}(t_3, t_2, t_1) \right. \\ & + \boldsymbol{\mu}^{ab} \boldsymbol{\mu}^{bc} \boldsymbol{\mu}^{cd} \boldsymbol{\mu}^{da} \exp(-i\omega_{dc}t_3 - i\omega_{db}t_2 - i\omega_{da}t_1) F_{abcd}^{(2)}(t_3, t_2, t_1) \\ & + \boldsymbol{\mu}^{ad} \boldsymbol{\mu}^{dc} \boldsymbol{\mu}^{cb} \boldsymbol{\mu}^{ba} \exp(-i\omega_{bc}t_3 + i\omega_{ca}t_2 + i\omega_{da}t_1) F_{abcd}^{(3)}(t_3, t_2, t_1) \\ & \left. + \boldsymbol{\mu}^{ad} \boldsymbol{\mu}^{dc} \boldsymbol{\mu}^{cb} \boldsymbol{\mu}^{ba} \exp(-i\omega_{bc}t_3 + i\omega_{db}t_2 + i\omega_{da}t_1) F_{abcd}^{(4)}(t_3, t_2, t_1) \right] \\ & - c.c. \} \end{aligned} \quad (3-12)$$

where P_a is the probability of beginning in state a , $\boldsymbol{\mu}^{xy}$ is the transition dipole vector between states x and y in the molecular frame and the dephasing functions $F_{abcd}^{(j)}$ are:

$$\begin{aligned} -\ln F_{abcd}^{(1)}(t_3, t_2, t_1) = & h_{bb}(t_3) + h_{cc}(t_2) + h_{dd}(t_1) + h_{bc}^+(t_3, t_2) \\ & + h_{cd}^+(t_2, t_1) + f_{bd}^+(t_3, t_1; t_2) \end{aligned} \quad (3-13)$$

$$\begin{aligned} -\ln F_{abcd}^{(2)}(t_3, t_2, t_1) = & [h_{cc}(t_3)]^* + [h_{bb}(t_2)]^* + h_{dd}(t_1 + t_2 + t_3) + [h_{bc}^+(t_3, t_2)]^* \\ & + h_{cd}^-(t_1 + t_2 + t_3, t_3) + [f_{bd}^-(t_2, t_1 + t_2 + t_3; t_3)]^* \end{aligned} \quad (3-14)$$

$$\begin{aligned} -\ln [F_{abcd}^{(3)}(t_3, t_2, t_1)]^* = & [h_{bb}(t_3)]^* + h_{cc}(t_2 + t_3) + h_{dd}(t_1) + h_{cd}^+(t_2 + t_3, t_1) \\ & - f_{bc}^-(t_3, t_2 + t_3; t_2) - f_{bd}^+(t_3, t_1; t_2) \end{aligned} \quad (3-15)$$

$$-\ln \left[F_{abcd}^{(4)}(t_3, t_2, t_1) \right]^* = h_{cc}(t_3) + h_{dd}(t_1 + t_2) + \left[h_{bb}(t_2 + t_3) \right]^* - h_{bc}^-(t_3, t_2 + t_3) + h_{cd}^+(t_1 + t_2, t_3) - f_{bd}^-(t_1 + t_2, t_2 + t_3; t_3) \quad (3-16)$$

with:

$$h_{xy}(t) = \int_0^t d\tau_2 \int_0^{\tau_2} d\tau_1 C_{xy}(\tau_2 - \tau_1) \quad (3-17)$$

$$h_{xy}^\pm(t_2, t_1) = \int_0^{t_2} d\tau_2 \int_0^{t_1} d\tau_1 C_{xy}(\tau_2 \pm \tau_1) \quad (3-18)$$

$$f_{xy}^\pm(t_2, t_1; t_3) = \int_0^{t_2} d\tau_2 \int_0^{t_1} d\tau_1 C_{xy}(\tau_2 \pm \tau_1 + t_3). \quad (3-19)$$

¹⁹Fig. 3-1 plots Feynman diagrams that represent the time evolution of the density matrix for each of the terms in Eq. (3-12).

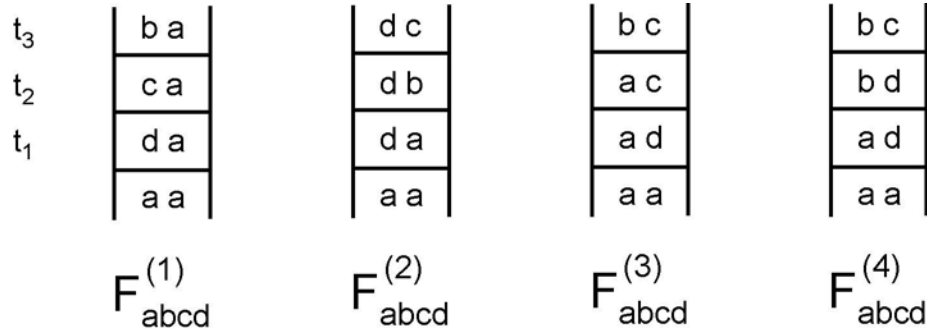


Figure 3-1. Feynman diagrams that represent the evolution of the density matrix corresponding to each of the terms in Eq. (3-12). Time progresses from the bottom to the top of each diagram, with field-matter interactions represented by horizontal lines. a, b, c and d are the eigenstates of the system.

The third order polarization is a vector quantity that can have components in each of the lab frame directions. Orientational dynamics of the system are encoded in the response function tensor, as is indicated by transition dipole products in (3-12), and can be measured using polarized laser pulses. The calculation and interpretation of the polarization is greatly simplified by assuming that vibrational degrees of freedom are independent of the reorientations.²⁰ The basis for decoupling these dynamics in many systems is that the

timescale for reorientational motion is much longer than that on which vibrational dynamics persist. As will be demonstrated in later chapters, this separation of timescales is not as large in water as for other liquids, calling into question the validity of this approximation. Nonetheless, we will proceed by separating vibrational and orientational dynamics because a reasonable theory that treats the coupling of vibrations and rotations in water has not yet been developed. To separate these degrees of freedom, the response function is decomposed into a product of vibrational R_{vib}^{ijkl} and orientational Y_{IJKL}^{ijkl} contributions in the expression for the polarization:

$$\mathbf{P}^{(3)}(\mathbf{r}, t) = \sum_{ijkl=1}^3 \sum_{JKL=1}^3 \hat{\mathbf{X}}_I \int_0^\infty dt_3 \int_0^\infty dt_2 \int_0^\infty dt_1 R_{vib}^{ijkl}(t_3, t_2, t_1) Y_{IJKL}^{ijkl}(t_3, t_2, t_1) E_J(\mathbf{r}, t - t_3) E_K(\mathbf{r}, t - t_3 - t_2) E_L(\mathbf{r}, t - t_3 - t_2 - t_1) \quad (3-20)$$

In this expression, the subscripts I, J, K and L refer to directional unit vectors in the laboratory frame and the superscripts i, j, k and l refer to unit vectors in the molecular body fixed frame. $\hat{\mathbf{X}}_I$ is a unit vector in the laboratory frame. The vibrational contribution is:

$$R_{vib}^{ijkl}(t_3, t_2, t_1) = \left(\frac{i}{\hbar}\right)^3 \sum_{abcd} P_a \left\{ \begin{aligned} & \left[\mu_i^{ab} \mu_j^{bc} \mu_k^{cd} \mu_l^{da} \exp(-i\omega_{ba}t_3 - i\omega_{ca}t_2 - i\omega_{da}t_1) F_{abcd}^{(1)}(t_3, t_2, t_1) \right. \\ & + \mu_i^{ab} \mu_j^{bc} \mu_k^{cd} \mu_l^{da} \exp(-i\omega_{dc}t_3 - i\omega_{db}t_2 - i\omega_{da}t_1) F_{abcd}^{(2)}(t_3, t_2, t_1) \\ & + \mu_i^{ad} \mu_j^{dc} \mu_k^{cb} \mu_l^{ba} \exp(-i\omega_{bc}t_3 + i\omega_{ca}t_2 + i\omega_{da}t_1) F_{abcd}^{(3)}(t_3, t_2, t_1) \\ & \left. + \mu_i^{ad} \mu_j^{dc} \mu_k^{cb} \mu_l^{ba} \exp(-i\omega_{bc}t_3 + i\omega_{db}t_2 + i\omega_{da}t_1) F_{abcd}^{(4)}(t_3, t_2, t_1) \right] \\ & -c.c. \}. \end{aligned} \right. \quad (3-21)$$

The orientational response function $Y_{IJKL}^{ijkl}(t_3, t_2, t_1)$ is a tensor that relates the laboratory coordinates to the molecular body fixed coordinates sequentially projecting the laboratory coordinates on to the molecular coordinates at the time of each field-matter interaction,

allowing molecular reorientation between interactions. The experiments we intend to model probe transitions of a single oscillator, namely the OH stretch of HOD, whose transition dipole in the molecular frame points in the same direction regardless of the initial and final state. Therefore, we choose the molecular coordinates along the OH transition dipole and eliminate the sum over i, j, k and l . Analytical expressions for the orientational response function have been derived for this case by assuming molecular reorientation occurs via isotropic orientational diffusion of spherical rotors.^{21,22} The results, written in terms of the coefficients:

$$c_\ell(t_n) = \exp[-\ell(\ell+1)D_{or}t_n] \quad (3-22)$$

where D_{or} is the orientational diffusion coefficient, are summarized in Table 3-1.

Designation	Tensor Element	Oriental Contribution
parallel	$Y_{ZZZZ}(t_3, t_2, t_1)$	$\frac{1}{9}c_1(t_1)[1 + \frac{4}{5}c_2(t_2)]c_1(t_3)$
perpendicular	$Y_{ZZYY}(t_3, t_2, t_1)$	$\frac{1}{9}c_1(t_1)[1 - \frac{2}{5}c_2(t_2)]c_1(t_3)$
anisotropic	$Y_{ZYZY}(t_3, t_2, t_1) = Y_{ZYZZ}(t_3, t_2, t_1)$	$\frac{1}{15}c_1(t_1)c_2(t_2)c_1(t_3)$

Table 3-1. Nonvanishing tensor components for the orientational contribution of the response function for parallel transition moments.

At this point, it is useful to introduce a notation that is capable of properly keeping track of differences between pulse orderings and interaction orderings.^{23,24} The time variables are defined by Fig. 3-2 and the accompanying caption. The definitions of t_1, t_2 and t_3 match those that have been used thus far, but the additional variables t_α, t_β and t_γ as well as $\tau_\alpha, \tau_\beta,$ and τ_γ are required to define pulse and interaction timings when the characteristics of each pulse become distinct. The relationship between the pulse delay timings $t_\alpha/t_\beta/t_\gamma$ and $\tau_1/\tau_2/t$ are relatively simple because pulses α and β are never scanned past pulse γ in the

experiment. The relationship between the interaction timings $t_1/t_2/t_3$ and $\tau_\alpha/\tau_\beta/\tau_\gamma$ depends on the interaction ordering, which is not controlled experimentally and may thus occur in any order allowed by pulse overlap. It is presented in Table 3-2. Both sets of interaction time variables will be used, since the use of the timings $t_1/t_2/t_3$ simplify expressions for the response function, while the timings $\tau_\alpha/\tau_\beta/\tau_\gamma$ are needed to keep track of interaction order in the polarization.

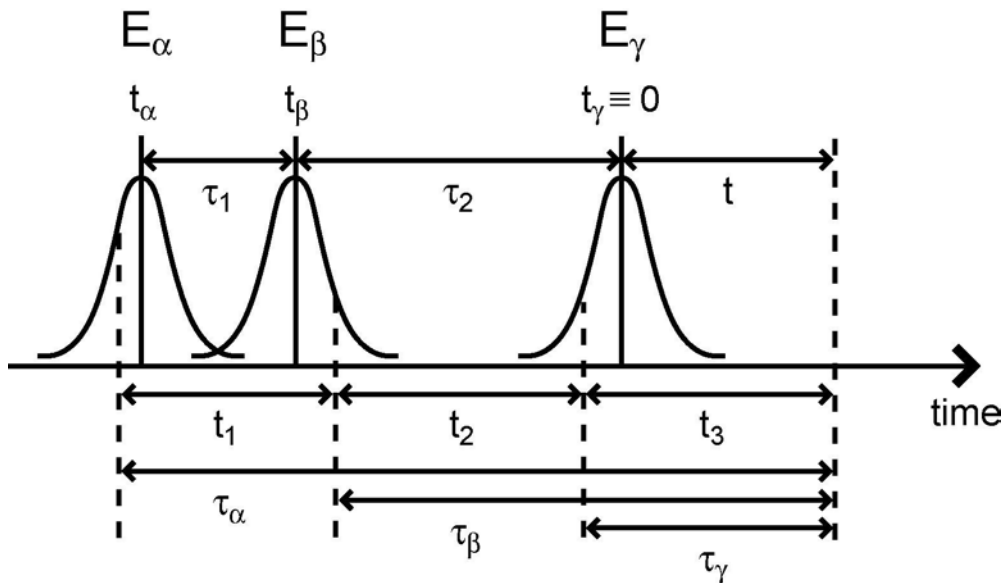


Figure 3-2. Illustration of the time variables used in the calculation of the nonlinear polarization for pulses with labels α , β and γ . Events that occur to the left in this diagram arrive at the sample earlier than those farther to the right. t_α , t_β , and t_γ are the times at which the center of each pulse arrives at the sample. The polarization is detected a time t after the third pulse. t_γ is defined as the time origin so that t_α and t_β are both negative and t is positive as shown. The pulse delay times are defined by $\tau_1 = t_\beta - t_\alpha$ and $\tau_2 = t_\gamma - \max(t_\beta - t_\alpha)$. Dashed vertical lines indicate interaction times within each pulse, which occur at the positive valued times τ_α , τ_β , and τ_γ before the detection of the polarization. t_1 , t_2 and t_3 are the positive valued time periods between the interactions and are always numbered consecutively, regardless of pulse ordering.

To obtain a computationally tractable expression for the polarization the input electric fields are written:

$$\mathbf{E}_\alpha(\mathbf{r}, t) = \frac{1}{2} \hat{\mathbf{e}}_\alpha^J G_\alpha(t - t_\alpha) \varepsilon_\alpha(\mathbf{r}) \exp\left[i(\mathbf{k}_\alpha \cdot \mathbf{r} - \omega_\alpha(t - t_\alpha))\right] + c.c. \quad (3-23)$$

where $\hat{\mathbf{e}}_\alpha^J$ is a unit vector in the laboratory frame in the electric field direction, \mathbf{k}_α and ω_α are the wave vector and frequency of pulse α , $G_\alpha(t - t_\alpha)$ denotes its temporal envelope including the time dependent phase, and $\varepsilon_\alpha(\mathbf{r})$ is its spatial envelope function. This form of the electric field is appropriate when pulse delays are generated by changing the path length traversed by the pulse, as is the case for the experiments.²⁵ Substitution of Eq. (3-23) into the expression for the third order polarization with the pulse associated timing variables yields:

$$\begin{aligned} \mathbf{P}^{(3)}(\mathbf{r}, t, t_\beta, t_\alpha) = & \frac{1}{8} \sum_{IJKL} \hat{\mathbf{X}}_I \int_0^\infty d\tau_\gamma \int_0^\infty d\tau_\beta \int_0^\infty d\tau_\alpha R_{\text{vib}}(\tau_\gamma, \tau_\beta, \tau_\alpha) Y_{IJKL'}(\tau_\gamma, \tau_\beta, \tau_\alpha) \\ & \left\{ \hat{\mathbf{e}}_\alpha^I G_\alpha(t - t_\alpha - \tau_\alpha) \varepsilon_\alpha(\mathbf{r}) \exp\left[i(\mathbf{k}_\alpha \cdot \mathbf{r} - \omega_\alpha(t - t_\alpha - \tau_\alpha))\right] + c.c. \right\} \\ & \left\{ \hat{\mathbf{e}}_\beta^K G_\beta(t - t_\beta - \tau_\beta) \varepsilon_\beta(\mathbf{r}) \exp\left[i(\mathbf{k}_\beta \cdot \mathbf{r} - \omega_\beta(t - t_\beta - \tau_\beta))\right] + c.c. \right\} \\ & \left\{ \hat{\mathbf{e}}_\gamma^J G_\gamma(t - t_\gamma - \tau_\gamma) \varepsilon_\gamma(\mathbf{r}) \exp\left[i(\mathbf{k}_\gamma \cdot \mathbf{r} - \omega_\gamma(t - t_\gamma - \tau_\gamma))\right] + c.c. \right\} \end{aligned} \quad (3-24)$$

Note that this equation does not specify which of the three electric fields interact with the sample first, second or third, as in earlier expressions of the polarization, since the order of the field-matter interactions does not necessarily follow the order in which the pulses arrive at the sample when the temporal pulse envelopes overlap in time. $R_{\text{vib}}(\tau_\gamma, \tau_\beta, \tau_\alpha)$ and $Y_{IJKL'}(\tau_\gamma, \tau_\beta, \tau_\alpha)$ involve a change of variables from $t_1/t_2/t_3$ to $\tau_\alpha/\tau_\beta/\tau_\gamma$ that is dependent on the pulse ordering (see Table 3-2).

3.2.2 Nonlinear spectroscopy of an anharmonic oscillator

The nonlinear IR experiments presented here probe vibrational transitions, so the system is a weakly anharmonic oscillator, whose eigenstates are denoted by the labels

$\nu = 0, 1, 2, \dots$ The energy difference between the fundamental ($|1\rangle \leftarrow |0\rangle$) and overtone ($|2\rangle \leftarrow |1\rangle$) transitions is the anharmonicity Δ , which is small compared with the energy spacings by definition.

The polarization created by the interaction of three input fields with the system is entirely determined by Eq. (3-24) along with the response function (Eq. (3-21)) and dephasing functions (Eqs. (3-13) through (3-16)). However, for numerical calculations involving non-canonical energy gap correlation functions and input pulses that have a finite duration, the integrals required to compute the polarization become computationally expensive, even for electric fields that are resonant with the vibrational transition of interest. The reason is that both the response function and the combination of the (resonant) input fields have terms which oscillate at frequencies of $\pm\omega$, $\pm 2\omega$ and $\pm 3\omega$ during various time periods, and thus the product of the response function and the fields have terms that are nearly resonant as well as quickly oscillating terms. (The response function may, in principal, have terms that oscillate at even higher frequencies, because the indices a , b , c and d can be any eigenstate of the system.) The quickly oscillating terms in the product require evaluation of the integrand on a three dimensional grid that has finely spaced time steps in τ_α , τ_β and τ_γ , but also extends to long enough times in all three dimensions that the contribution neglected by the finite upper bounds is negligible. However, these terms contribute little to the integral by virtue of the fact that they oscillate so quickly. Therefore, the inclusion of all of the terms in Eq. (3-24) wastes computational time for several reasons. Rather, it is prudent to retain only terms for which oscillations in the response function are approximately canceled by oscillations in the field factors, which is known as the rotating wave approximation (RWA).⁹

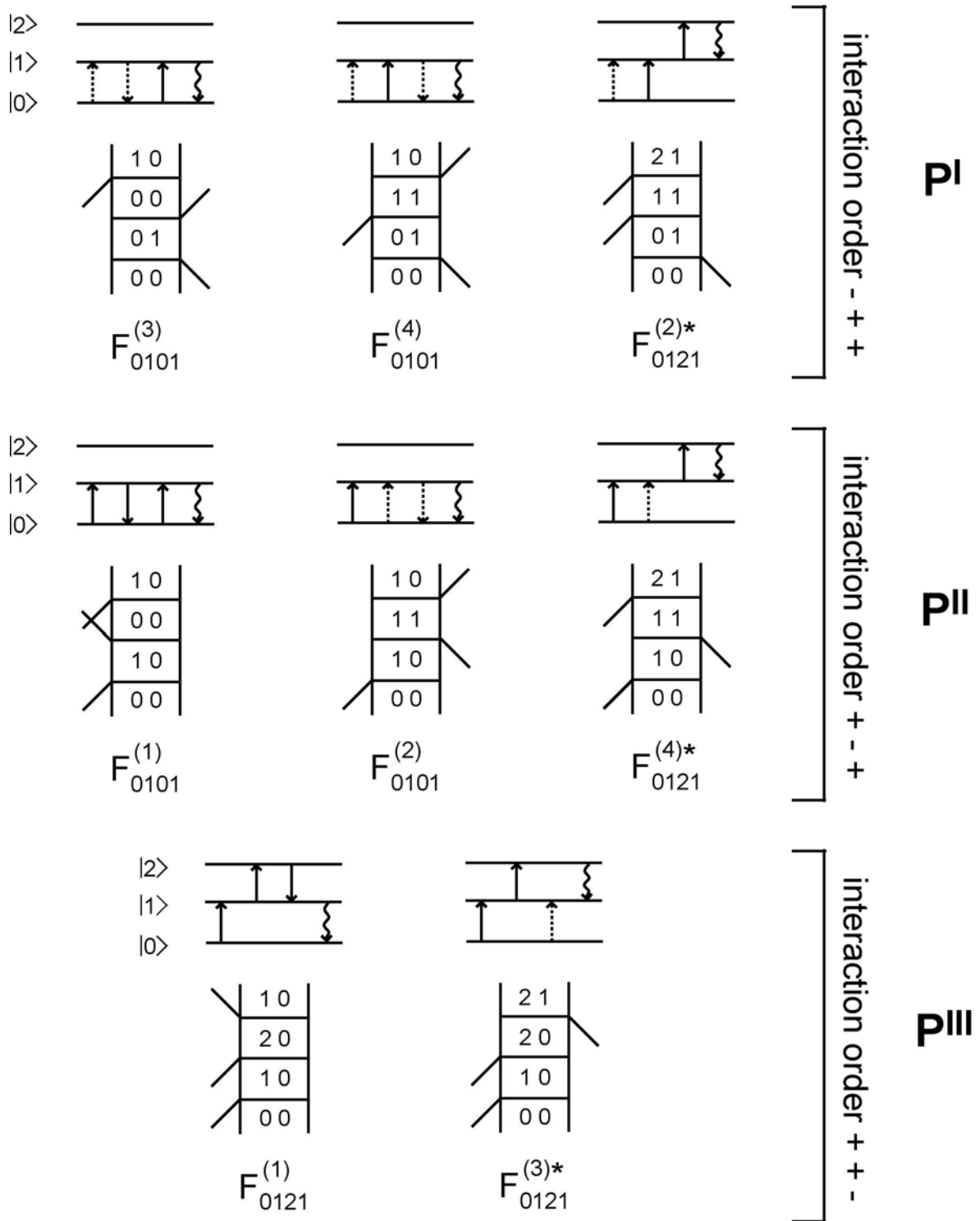


Figure 3-3. Feynman and associated ladder diagrams that represent the evolution of the density matrix for each of the terms from Eq. (3-21) that survive the RWA for a three level system in the phase-matching direction $\mathbf{k}_{sig} = -\mathbf{k}_\alpha + \mathbf{k}_\beta + \mathbf{k}_\gamma$. Each row contributes only when the interaction order satisfies the conditions listed on the right hand side of the row.

Interaction Time	Vibrational Response	Orientalional Response	t1	t2	t3
$\tau_\alpha > \tau_\beta \geq \tau_\gamma$	\tilde{R}_{vib}^I	Y_{IJKL}	$\tau_\alpha - \tau_\beta$	$\tau_\beta - \tau_\gamma$	τ_γ
$\tau_\alpha \geq \tau_\gamma > \tau_\beta$	\tilde{R}_{vib}^I	Y_{IKJL}	$\tau_\alpha - \tau_\gamma$	$\tau_\gamma - \tau_\beta$	τ_β
$\tau_\beta \geq \tau_\alpha \geq \tau_\gamma$	\tilde{R}_{vib}^{II}	Y_{IJLK}	$\tau_\beta - \tau_\alpha$	$\tau_\alpha - \tau_\gamma$	τ_γ
$\tau_\beta > \tau_\gamma > \tau_\alpha$	\tilde{R}_{vib}^{III}	Y_{ILJK}	$\tau_\beta - \tau_\gamma$	$\tau_\gamma - \tau_\alpha$	τ_α
$\tau_\gamma > \tau_\alpha \geq \tau_\beta$	\tilde{R}_{vib}^{II}	Y_{IKLJ}	$\tau_\gamma - \tau_\alpha$	$\tau_\alpha - \tau_\beta$	τ_β
$\tau_\gamma \geq \tau_\beta > \tau_\alpha$	\tilde{R}_{vib}^{III}	Y_{ILKJ}	$\tau_\gamma - \tau_\beta$	$\tau_\beta - \tau_\alpha$	τ_α

Table 3-2. Density matrix pathways that contribute to the phase matched signal in the direction $\mathbf{k}_{sig} = -\mathbf{k}_\alpha + \mathbf{k}_\beta + \mathbf{k}_\gamma$ within the rotating-wave approximation. Pathways are classified according to the relative behavior of the coherences during the three time periods. Also tabulated are the relationship between the timings $t_1/t_2/t_3$ and $\tau_\alpha/\tau_\beta/\tau_\gamma$ for each interaction ordering.

When modeling four wave mixing experiments, an additional simplification in the evaluation of the polarization results because the input fields have well defined wave vectors, which further limits the number of terms that contribute in the RWA. The experiments discussed in later chapters utilize a boxcar or triangle geometry, in which the signal is detected in the $\mathbf{k}_{sig} = -\mathbf{k}_\alpha + \mathbf{k}_\beta + \mathbf{k}_\gamma$ wave vector direction. The specific pathways by which the density matrix evolves that contribute to the experimental signal are identified by first selecting the electric field terms from Eq. (3-24) that contribute in this phase-matching direction, and then applying the RWA, retaining only terms in the response function which oscillate at frequencies that approximately cancel those in the field terms. For input pulses that are nearly resonant with the fundamental and overtone transitions, eight terms contribute to the polarization in the \mathbf{k}_{sig} direction. Feynman diagrams that illustrate the time evolution of the density matrix for each of these terms are plotted in Fig. 3-3.

These density matrix pathways that survive the RWA in the phase-matched direction can be divided into three categories according to their pulse interaction orderings. These

three contributions, denoted $\tilde{\mathbf{P}}^I$, $\tilde{\mathbf{P}}^{II}$, and $\tilde{\mathbf{P}}^{III}$, are complex valued as a result of the RWA, although the total polarization remains real valued:

$$\mathbf{P}^{(3)}(\mathbf{k}_{sig}, t, t_\beta, t_\alpha) = \left\{ \left[\tilde{\mathbf{P}}^I(\mathbf{k}_{sig}, t, t_\beta, t_\alpha) + \tilde{\mathbf{P}}^{II}(\mathbf{k}_{sig}, t, t_\beta, t_\alpha) + \tilde{\mathbf{P}}^{III}(\mathbf{k}_{sig}, t, t_\beta, t_\alpha) \right] \exp \left[i(\mathbf{k}_{sig} \cdot \mathbf{r} - \omega(t + t_\alpha - t_\beta)) \right] \right\} + c.c. \quad (3-25)$$

Common terms that oscillate quickly in the pulse delay timings have been factored out of the individual contributions, so that $\tilde{\mathbf{P}}^I$, $\tilde{\mathbf{P}}^{II}$, and $\tilde{\mathbf{P}}^{III}$ are envelope functions that vary slowly in t, t_β, t_α . $\tilde{\mathbf{P}}^I$ contains terms that contribute when the first field-matter interaction comes from the pulse with wave vector $-\mathbf{k}_\alpha$, followed by interactions from the pulses with wave vectors $+\mathbf{k}_\beta$ and $+\mathbf{k}_\gamma$ (the latter two interactions can come in either order). The terms in $\tilde{\mathbf{P}}^{II}$ and $\tilde{\mathbf{P}}^{III}$ contribute when the interaction from the pulse with wave vector $-\mathbf{k}_\alpha$ come second and third, respectively. Table 3-2 summarizes these criterion as well as the specific orientational response functions that match the vibrational contributions to $\tilde{\mathbf{P}}^I$, $\tilde{\mathbf{P}}^{II}$ and $\tilde{\mathbf{P}}^{III}$. The three polarization contributions can therefore be written:

$$\tilde{\mathbf{P}}^I(\mathbf{k}_{sig}, t, t_\beta, t_\alpha) = \frac{1}{8} \sum_{IJKL} \hat{\mathbf{X}}_I \int_0^\infty d\tau_\gamma \int_0^\infty d\tau_\beta \int_0^\infty d\tau_\alpha \tilde{R}_{vib}^I(\mathbf{k}_{sig}, \tau_\gamma, \tau_\beta, \tau_\alpha) \hat{\mathbf{e}}_\alpha^J G_\alpha^*(t - t_\alpha - \tau_\alpha) \hat{\mathbf{e}}_\beta^K G_\beta(t - t_\beta - \tau_\beta) \hat{\mathbf{e}}_\gamma^L G_\gamma(t - t_\gamma - \tau_\gamma) \quad (3-26)$$

$$\tilde{\mathbf{P}}^{II}(\mathbf{k}_{sig}, t, t_\beta, t_\alpha) = \frac{1}{8} \sum_{IJKL} \hat{\mathbf{X}}_I \int_0^\infty d\tau_\gamma \int_0^\infty d\tau_\beta \int_0^\infty d\tau_\alpha \tilde{R}_{vib}^{II}(\mathbf{k}_{sig}, \tau_\gamma, \tau_\beta, \tau_\alpha) \hat{\mathbf{e}}_\alpha^J G_\alpha^*(t - t_\alpha - \tau_\alpha) \hat{\mathbf{e}}_\beta^K G_\beta(t - t_\beta - \tau_\beta) \hat{\mathbf{e}}_\gamma^L G_\gamma(t - t_\gamma - \tau_\gamma) \quad (3-27)$$

$$\tilde{\mathbf{P}}^{III}(\mathbf{k}_{sig}, t, t_\beta, t_\alpha) = \frac{1}{8} \sum_{IJKL} \hat{\mathbf{X}}_I \int_0^\infty d\tau_\gamma \int_0^\infty d\tau_\beta \int_0^\infty d\tau_\alpha \tilde{R}_{vib}^{III}(\mathbf{k}_{sig}, \tau_\gamma, \tau_\beta, \tau_\alpha) \exp \left[-2i\omega \cdot \min(|t_\alpha|, |t_\beta|) \right] \hat{\mathbf{e}}_\alpha^J G_\alpha^*(t - t_\alpha - \tau_\alpha) \hat{\mathbf{e}}_\beta^K G_\beta(t - t_\beta - \tau_\beta) \hat{\mathbf{e}}_\gamma^L G_\gamma(t - t_\gamma - \tau_\gamma) \quad (3-28)$$

with the RWA modified response functions:

$$\begin{aligned}\tilde{R}'_{vib}(\mathbf{k}_{sig}, t_3, t_2, t_1) &= \left(\frac{i}{\hbar}\right)^3 \left\{ |\mu_{10}|^4 [F_{0101}^{(3)}(t_3, t_2, t_1) + F_{0101}^{(4)}(t_3, t_2, t_1)] \right. \\ &\quad \left. - |\mu_{10}|^2 |\mu_{21}|^2 \exp[-i(\omega_{21} - \omega_{10})t_3] [F_{0121}^{(2)}(t_3, t_2, t_1)]^* \right\} \\ &\quad \exp(i(\omega - \omega_{10})t_3 - i(\omega - \omega_{10})t_1)\end{aligned}\quad (3-29)$$

$$\begin{aligned}\tilde{R}''_{vib}(\mathbf{k}_{sig}, t_3, t_2, t_1) &= \left(\frac{i}{\hbar}\right)^3 \left\{ |\mu_{10}|^4 [F_{0101}^{(1)}(t_3, t_2, t_1) + F_{0101}^{(2)}(t_3, t_2, t_1)] \right. \\ &\quad \left. - |\mu_{10}|^2 |\mu_{21}|^2 \exp[-i(\omega_{21} - \omega_{10})t_3] [F_{0121}^{(4)}(t_3, t_2, t_1)]^* \right\} \\ &\quad \exp(i(\omega - \omega_{10})t_3 + i(\omega - \omega_{10})t_1)\end{aligned}\quad (3-30)$$

$$\begin{aligned}\tilde{R}'''_{vib}(\mathbf{k}_{sig}, t_3, t_2, t_1) &= \left(\frac{i}{\hbar}\right)^3 \left\{ |\mu_{10}|^2 |\mu_{21}|^2 [F_{0121}^{(1)}(t_3, t_2, t_1)] \right. \\ &\quad \left. - |\mu_{10}|^2 |\mu_{21}|^2 \exp[-i(\omega_{21} - \omega_{10})t_3] [F_{0121}^{(3)}(t_3, t_2, t_1)]^* \right\} \\ &\quad \exp(i(\omega - \omega_{10})t_3 + i(2\omega - \omega_{20})t_2 + i(\omega - \omega_{10})t_1).\end{aligned}\quad (3-31)$$

where the center frequency of all input fields has been set equal ($\omega_\alpha = \omega_\beta = \omega_\gamma \equiv \omega$), and their spatial dependence $\varepsilon(\mathbf{r})$ has been neglected. In the above expressions, it has been assumed that the level spacing is greater than kT , so that the system resides in the ground state at equilibrium ($P_0 = 1$). This also implies that the ground state is the reference state for the evaluation of the energy gap correlation function and thus the dephasing functions. Of the dephasing functions required for the evaluation of the response functions, four involve only the ground and first excited state ($abcd = 0101$):

$$\begin{aligned}-\ln F_{0101}^{(1)}(t_3, t_2, t_1) &= h_{11}(t_1) + h_{11}(t_2) + h_{11}(t_3) - h_{11}(t_1 + t_2) - h_{11}(t_2 + t_3) \\ &\quad + h_{11}(t_1 + t_2 + t_3)\end{aligned}\quad (3-32)$$

$$\begin{aligned}-\ln F_{0101}^{(2)}(t_3, t_2, t_1) &= h_{11}(t_1) + h_{11}^*(t_2) + h_{11}^*(t_3) - h_{11}(t_1 + t_2) - h_{11}^*(t_2 + t_3) \\ &\quad + h_{11}(t_1 + t_2 + t_3)\end{aligned}\quad (3-33)$$

$$-\ln \left[F_{0101}^{(3)}(t_3, t_2, t_1) \right]^* = h_{11}(t_1) - h_{11}(t_2) + h_{11}^*(t_3) + h_{11}(t_1 + t_2) + h_{11}(t_2 + t_3) - h_{11}(t_1 + t_2 + t_3) \quad (3-34)$$

$$-\ln \left[F_{0101}^{(4)}(t_3, t_2, t_1) \right]^* = h_{11}(t_1) - h_{11}^*(t_2) + h_{11}(t_3) + h_{11}(t_1 + t_2) + h_{11}^*(t_2 + t_3) - h_{11}(t_1 + t_2 + t_3) \quad (3-35)$$

and four involve the second excited state ($abcd = 0121$):

$$-\ln F_{0121}^{(1)}(t_3, t_2, t_1) = h_{11}(t_1) - h_{21}(t_1) + h_{11}(t_2) - h_{12}(t_2) - h_{21}(t_2) + h_{22}(t_2) + h_{11}(t_3) - h_{12}(t_3) - h_{11}(t_1 + t_2) + h_{21}(t_1 + t_2) - h_{11}(t_2 + t_3) + h_{12}(t_2 + t_3) + h_{11}(t_1 + t_2 + t_3) \quad (3-36)$$

$$-\ln F_{0121}^{(2)}(t_3, t_2, t_1) = h_{11}(t_1) + h_{11}^*(t_2) - h_{12}^*(t_2) + h_{11}^*(t_3) - h_{12}^*(t_3) - h_{21}^*(t_3) + h_{22}^*(t_3) - h_{11}(t_1 + t_2) + h_{21}(t_1 + t_2) - h_{11}^*(t_2 + t_3) + h_{12}^*(t_2 + t_3) + h_{11}(t_1 + t_2 + t_3) - h_{21}(t_1 + t_2 + t_3) \quad (3-37)$$

$$-\ln \left[F_{0121}^{(3)}(t_3, t_2, t_1) \right]^* = h_{11}(t_1) - h_{21}(t_1) - h_{11}(t_2) + h_{12}(t_2) + h_{11}^*(t_3) - h_{12}^*(t_3) + h_{11}(t_1 + t_2) + h_{11}(t_2 + t_3) - h_{12}(t_2 + t_3) - h_{21}(t_2 + t_3) + h_{22}(t_2 + t_3) - h_{11}(t_1 + t_2 + t_3) + h_{21}(t_1 + t_2 + t_3) \quad (3-38)$$

$$-\ln \left[F_{0121}^{(4)}(t_3, t_2, t_1) \right]^* = h_{11}(t_1) - h_{11}^*(t_2) + h_{12}^*(t_2) + h_{11}(t_3) - h_{12}(t_3) - h_{21}(t_3) + h_{22}(t_3) + h_{11}(t_1 + t_2) - h_{21}(t_1 + t_2) + h_{11}^*(t_2 + t_3) - h_{12}^*(t_2 + t_3) - h_{11}(t_1 + t_2 + t_3) + h_{21}(t_1 + t_2 + t_3). \quad (3-39)$$

Carrier frequency terms from the input fields have been included in the modified response functions to emphasize the benefit of the RWA for numerical calculations of the polarization. Phase modulations in the modified response functions occur on timescales equal to the detuning of the input pulses from resonance, $\omega - \omega_{10}$ (and $2\omega - \omega_{20}$), and the frequency difference between the overtone and fundamental transitions, $\omega_{21} - \omega_{10}$. These

oscillations occur at considerably lower frequencies than the vibrational transitions themselves.

Differences in the time behavior of $\tilde{\mathbf{P}}^I$, $\tilde{\mathbf{P}}^{II}$, and $\tilde{\mathbf{P}}^{III}$ are primarily determined by the density matrix pathways that contribute to each.²⁶ The most important characteristic that distinguishes $\tilde{\mathbf{P}}^I$ pathways from the others is that the phase acquired by coherences during t_1 is approximately conjugate of that acquired during t_3 . Under certain conditions, this means that the phase relationships created by the first field-matter interaction, but subsequently destroyed by system-bath interactions, can be reestablished after all three pulses have interacted with the sample. This process is often referred to as the creation of a vibrational echo, and is analogous to the photon echo in electronic spectroscopy and the Hahn echo in NMR.²⁷ $\tilde{\mathbf{P}}^{II}$ and $\tilde{\mathbf{P}}^{III}$ evolve with the same coherence during the first and third time periods and can not form an echo. For this reason, the density matrix pathways that contribute to $\tilde{\mathbf{P}}^I$ are classified as rephasing and those of $\tilde{\mathbf{P}}^{II}$ and $\tilde{\mathbf{P}}^{III}$ are nonrephasing.

Comparison of the polarization expressions obtained for the three level vibrational system with the analogous expressions for a two level system reveal several important differences. First, the existence of $\tilde{\mathbf{P}}^{III}$ is unique to the vibrational system, where it is possible to have a coherence between the ground and second excited state during t_2 . In fact, the absence of density matrix pathways involving a second excited state in electronic spectroscopy has important consequences for the behavior of four wave mixing signals when all pulses are overlapped in time, since there is a discontinuity in the response function at the time origin.^{1,24} There is no such problem in vibrational spectroscopy. A second important difference is the behavior of the polarization during t_3 , since the four wave mixing signal of a vibrational system is modulated by interference between the overtone and fundamental

transitions, while the electronic transition is smooth. In fact, deviation from harmonic behavior is required to prevent perfect interference between these two contributions for all times.²⁸⁻³⁰ This is especially apparent at early t_3 times, where the polarization increases from a value of 0 at $t_3 = 0$ for the vibrational system due to perfect interference (regardless of the aforementioned deviations).

Recall that in the derivation of the lineshape functions, Eqs. (3-13) - (3-16) from the system Hamiltonian, Eq. (3-3), system-bath coupling terms leading to relaxation processes between the system eigenstates (in this case, vibrational relaxation) were neglected in favor of those which describe dephasing. Because the experimental signals are strongly influenced by vibrational relaxation, this process must be reinserted into the theory used to model the experiments. To account for population relaxation, we introduce a phenomenological model based on results for a multilevel Markovian system, in which population relaxation from the n^{th} eigenstate occurs at a rate $T_{1,n}$.^{31,32} For n - m coherences of the density matrix, population relaxation occurs at a rate $T_{1,n-m} = T_{1,m-n}$. The response functions, including population relaxation, are:

$$\begin{aligned}
\tilde{R}_{vib/pop}^I(\mathbf{k}_{sig}, t_3, t_2, t_1) = & \left(\frac{i}{\hbar}\right)^3 \left\{ |\mu_{10}|^4 \exp\left[-\frac{t_3 + t_1}{2T_{1,1-0}}\right] \right. \\
& \left[\exp\left[-\frac{t_2}{T_{1,0}}\right] F_{0101}^{(3)}(t_3, t_2, t_1) + \exp\left[-\frac{t_2}{T_{1,1}}\right] F_{0101}^{(4)}(t_3, t_2, t_1) \right] \\
& - |\mu_{10}|^2 |\mu_{21}|^2 \exp\left[-\frac{t_3}{2T_{1,2-1}} - \frac{t_2}{T_{1,1}} - \frac{t_1}{2T_{1,1-0}}\right] \\
& \exp\left[-i(\omega_{21} - \omega_{10})t_3\right] \left[F_{0121}^{(2)}(t_3, t_2, t_1) \right]^* \left. \right\} \\
& \exp\left(i(\omega - \omega_{10})t_3 - i(\omega - \omega_{10})t_1\right)
\end{aligned} \tag{3-40}$$

$$\begin{aligned}
\tilde{R}_{vib/pop}^{II}(\mathbf{k}_{sig}, t_3, t_2, t_1) &= \left(\frac{i}{\hbar}\right)^3 \left\{ |\mu_{10}|^4 \exp\left[-\frac{t_3 + t_1}{2T_{1,1-0}}\right] \right. \\
&\quad \left[\exp\left[-\frac{t_2}{T_{1,0}}\right] F_{0101}^{(1)}(t_3, t_2, t_1) + \exp\left[-\frac{t_2}{T_{1,1}}\right] F_{0101}^{(2)}(t_3, t_2, t_1) \right] \\
&\quad - |\mu_{10}|^2 |\mu_{21}|^2 \exp\left[-\frac{t_3}{2T_{1,2-1}} - \frac{t_2}{T_{1,1}} - \frac{t_1}{2T_{1,1-0}}\right] \\
&\quad \left. \exp\left[-i(\omega_{21} - \omega_{10})t_3\right] \left[F_{0121}^{(4)}(t_3, t_2, t_1) \right]^* \right\} \\
&\quad \exp\left(i(\omega - \omega_{10})t_3 + i(\omega - \omega_{10})t_1\right)
\end{aligned} \tag{3-41}$$

$$\begin{aligned}
\tilde{R}_{vib/pop}^{III}(\mathbf{k}_{sig}, t_3, t_2, t_1) &= \left(\frac{i}{\hbar}\right)^3 \exp\left[-\frac{t_2}{2T_{1,2-0}} - \frac{t_1}{2T_{1,1-0}}\right] \\
&\quad \left\{ |\mu_{10}|^2 |\mu_{21}|^2 \exp\left[-\frac{t_3}{2T_{1,1-0}}\right] \left[F_{0121}^{(1)}(t_3, t_2, t_1) \right] \right. \\
&\quad \left. - |\mu_{10}|^2 |\mu_{21}|^2 \exp\left[-\frac{t_3}{2T_{1,2-1}}\right] \right. \\
&\quad \left. \exp\left[-i(\omega_{21} - \omega_{10})t_3\right] \left[F_{0121}^{(3)}(t_3, t_2, t_1) \right]^* \right\} \\
&\quad \exp\left(i(\omega - \omega_{10})t_3 + i(2\omega - \omega_{20})t_2 + i(\omega - \omega_{10})t_1\right).
\end{aligned} \tag{3-42}$$

These response functions can be substituted directly into Eqs. (3-26) - (3-28) to obtain the total polarization, Eq. (3-25). This is the final expression for the polarization which radiates in the phase-matched direction \mathbf{k}_{sig} , calculated within the RWA, and accounts for vibrational dephasing and population relaxation of a three level system, as well as molecular reorientation.

3.2.3 Calculation of experimental signals

The nonlinear polarization acts as a source to emit electromagnetic radiation into the phase-matched direction, which is subsequently detected in the experiments.^{9,33} The

relationship between the polarization and signal field is provided by Maxwell's equations. By assuming an infinite plane wave whose envelope varies slowly as compared with the carrier frequency, Faeder and Jonas have found the following relationship between the inverse Fourier transform of the polarization, $\mathbf{P}^{(3)}(\omega) \equiv \int_{-\infty}^{\infty} \mathbf{P}^{(3)}(t) \exp(i\omega t) dt$ and the radiated field $\mathbf{E}_{rad}(\omega)$.²⁴

$$\mathbf{E}_{rad}(\omega) = \frac{2\pi l}{n(\omega)c} i\omega \mathbf{P}^{(3)}(\omega) \text{sinc}\left(\frac{\Delta kl}{2}\right) \exp\left(\frac{i\Delta kl}{2}\right). \quad (3-43)$$

where l is the sample length, $n(\omega)$ is the index of refraction of the sample, c is the speed of light and Δk is the phase mismatch between the four fields. Although not strictly true for all experiments, we assume perfect phase-matching conditions ($\Delta kl = 0$). Since the index of refraction is not strongly dependent on frequency in the mid-IR, Eq. (3-43) is Fourier transformed to express the field radiated by the sample due to the nonlinear polarization:

$$\mathbf{E}_{rad}(\mathbf{k}_{sig}, t, t_{\beta}, t_{\alpha}) = -\frac{2\pi l}{nc} \frac{\partial \mathbf{P}^{(3)}(\mathbf{k}_{sig}, t, t_{\beta}, t_{\alpha})}{\partial t} \quad (3-44)$$

The nonlinear polarization expressed in Eq. (3-25), is a product of the envelope functions $\tilde{\mathbf{P}}^I$, $\tilde{\mathbf{P}}^{II}$, and $\tilde{\mathbf{P}}^{III}$, which vary slowly in t , and the carrier term that oscillates at ωt . Therefore, the t dependence of the radiated field closely follows that of the polarization with a $\pi/2$ phase shift ($i\mathbf{P}^{(3)}$), as others have calculated. However, for short input pulse envelopes (and particularly for envelopes derived from experimental measurements, which are not necessarily smooth), the derivative of the envelope functions may not be negligible.

The nonlinear IR experiments performed in this work may be classified according to those that detect the radiated field directly (homodyne), and those that are mixed with a reference field (i.e. local oscillator) before detection (heterodyne). The detectors measure the

intensity of the incident radiation, $|E(t)|^2$. However, because the electric field and polarization envelope functions have characteristic timescales of tens of femtoseconds to several picoseconds, the detectors are not fast enough to resolve the t dependence of the radiated field. Therefore, the signal detected in a homodyne measurement S_{hom} is calculated as:

$$S_{hom}(\mathbf{k}_{sig}, t_\beta, t_\alpha) = \int_{-\infty}^{\infty} |E_{rad}(\mathbf{k}_{sig}, t, t_\beta, t_\alpha)|^2 dt \quad (3-45)$$

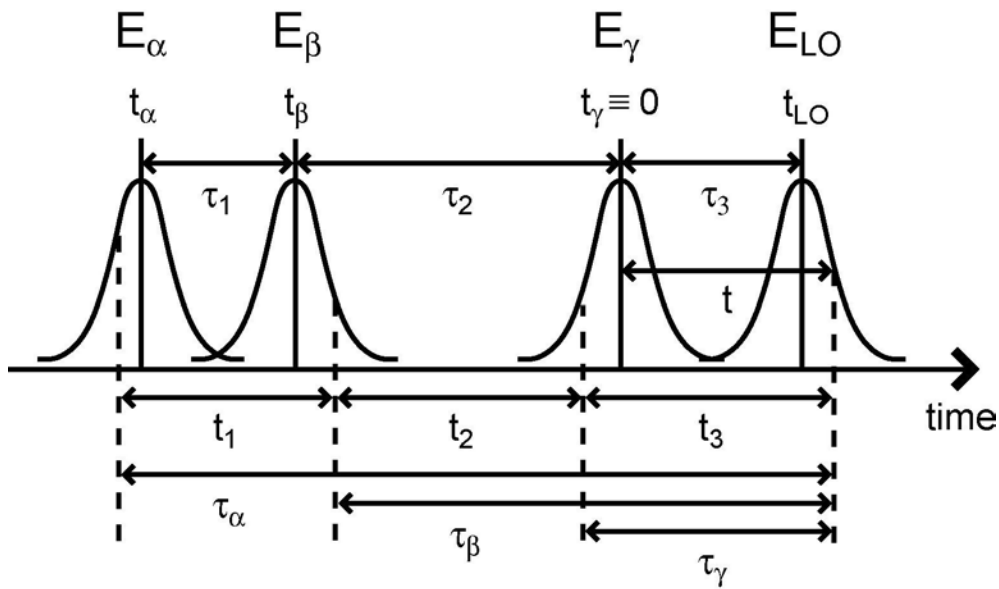


Figure 3-4. Illustration of the time variables used in the calculation of the heterodyned detected signal.

In a heterodyne detected experiment, the field radiated by the sample is combined with a local oscillator that is typically at least an order of magnitude more intense than the radiated field. In addition, the signal field is usually chopped via mechanical means so that the contribution due to only the local oscillator is removed. The time delay of the local oscillator

with respect to the three input pulses is then varied, as is illustrated in Figure 3-4. The signal detected in the heterodyned measurement S_{het} is calculated as:

$$S_{het}(\mathbf{k}_{sig}, t_{LO}, t_{\beta}, t_{\alpha}) = \int_{-\infty}^{\infty} \left[\left| E_{rad}(\mathbf{k}_{sig}, t, t_{\beta}, t_{\alpha}) + E_{LO}(\mathbf{k}_{sig}, t) \right|^2 - \left| E_{LO}(\mathbf{k}_{sig}, t) \right|^2 \right] dt \quad (3-46)$$

$$\approx \int_{-\infty}^{\infty} \left| E_{rad}(\mathbf{k}_{sig}, t, t_{\beta}, t_{\alpha}) E_{LO}(\mathbf{k}_{sig}, t) \right|^2 dt$$

3.3 Numerical calculations

Calculation of experimental signals based on the formalism presented above requires knowledge of several characteristics of the system including the fundamental and overtone transition frequencies (ω_{10}, ω_{21}) and dipole moments (μ_{10}, μ_{21}), the characteristic timescales for reorientations D_{or} , as well as the frequency correlation functions and T_I times for the first and second excited states and their cross terms ($C_{11}(t), C_{22}(t), C_{12}(t) = C_{21}(t), T_{1,0}(t), T_{1,1}(t), T_{1,1-0}(t), T_{1,2-1}(t), T_{1,2-0}(t)$). The last correlation function relationship is a result of the system-bath coupling chosen by Sung and Silbey. To simplify the calculation, we assume that the dipole moments, correlation functions, and T_I times are adequately approximated by harmonic scaling rules. The dipole moments are:

$$|\mu_{21}|^2 = 2|\mu_{10}|^2, \quad (3-47)$$

and because the absolute magnitude of the polarization is unimportant (since the experimental signal intensities are not recorded on an absolute scale), the dipole moment of the fundamental transition is set to unity. The correlation function amplitudes are scaled by:

$$C_{22}(t) = 2C_{12}(t) = 4C_{11}(t) \equiv 4C(t), \quad (3-48)$$

so that a single frequency correlation function describes the dynamics of the system. Similarly, the T_I times for each vibrational state scale with the quantum number:²⁸

$$T_{1,n} = T_{1,0} / n, \quad n \neq 0 \quad (3-49)$$

For the coherences, the T_I times are calculated as the average rate ($1/T_I$) of the eigenstates involved in the coherence, so that a single T_I time describes the vibrational relaxation in the system. Calculation of the experiments also involves the center frequency of the input pulses (ω), and their individual envelope functions and polarizations ($G_n(t)$ and $\hat{\mathbf{e}}_n$ where $n = \alpha, \beta, \gamma$).

The fundamental absorption frequency is roughly the peak of the FTIR, taken as 3400 cm^{-1} . The first moment of the FTIR is actually 3415 cm^{-1} , which is reproduced in calculations of the FTIR lineshape when a Stokes shift is included. The anharmonicity reported by Woutersen, *et. al.* is $\sim 250 \text{ cm}^{-1}$, indicating that the overtone transition frequency is 3150 cm^{-1} .³⁴ Guided by physical intuition about the system, the frequency correlation function used in our calculations is the sum of two overdamped and two underdamped Brownian oscillators. The correlation function can be complex valued $C(t) = C'(t) + iC''(t)$, where the real and imaginary parts are given by:⁹

$$C'(t) = \sum_{n=1}^2 A_n \gamma_n \cot(\beta \hbar \gamma_n / 2) \exp(-\gamma_n t) + \sum_{m=3}^4 \frac{A_m}{\zeta_m} \left[\coth(i\varphi'_m \beta \hbar / 2) \exp(-\varphi'_m t) - \coth(i\varphi_m \beta \hbar / 2) \exp(-\varphi_m t) \right] \quad (3-50)$$

$$C''(t) = -\sum_{n=1}^2 A_n \gamma_n \exp(-\gamma_n t) - 2 \sum_{m=3}^4 \frac{A_m}{\zeta_m} \exp(-\gamma_m t / 2) \sin(\zeta_m t) \quad (3-51)$$

with:

$$\varphi_m = \frac{\gamma_m}{2} + i\zeta_m, \quad \varphi'_m = \frac{\gamma_m}{2} - i\zeta_m$$

$$\zeta_m = \sqrt{\omega_m^2 - \gamma_m^2/4}$$

A_n and A_m are amplitudes, γ_n and γ_m are damping constants, and ω_m is the frequency. This form was chosen to allow the transform of the correlation function to resemble the low frequency Raman spectrum of the bath, although the relative amplitudes and most of the damping constants and frequencies were floated to fit the experimental data, as is discussed below.

In the experiments, the center frequency of the pulse spectrum is generally centered between the fundamental and overtone transitions by properly tuning the nonlinear crystals in the optical parametric amplifier, so the pulse frequency is almost always 3275 cm^{-1} . The form of the temporal envelope of the electromagnetic pulses depends on the level of accuracy required of the calculation. The simplest calculations assume that the time duration of the pulses is infinitely short, so that $G(t)$ is a delta function in time. However, nearly all of the calculations presented in this work utilize finite duration pulses. Some assume that the field is unchirped and therefore has a transform limited pulse length Δ_p :

$$G(t) = \frac{4 \ln(2)/\pi}{1.414\Delta_p} \exp\left(\frac{-4 \ln(2)}{(1.414\Delta_p)} t^2\right) \quad (3-52)$$

To determine the effect of pulse chirp on the nonlinear signals, Eq. (3-52) is modified:

$$G(t) = \frac{4 \ln(2)/\pi}{1.414\Delta_p} \exp\left(\frac{-4 \ln(2)}{(1.414\Delta_p)} t^2 \cdot (1 - Bi)\right) \quad (3-53)$$

where the parameter B determines the amount of linear chirp added into the calculation. When the amplitude and phase characteristics of the electric field are measured

experimentally at the time a particular measurement is taken, those are used in the calculations. The calculations using experimentally measured pulses include both amplitude and phase (chirp of all orders) modulations.

C++ code written to calculate the polarization according to Eq. (3-25) and then determine the signal from Eq. (3-45) or (3-46) is included as Appendix I. It takes full advantage of the RWA in the equations above, by utilizing step sizes commensurate with the frequency of modulations expected for the particular quantities being measured. The frequency of the carrier wave of the input pulses, as well as that of the fundamental and overtone transitions is approximately 0.1 cycle/fs. To ensure sampling well within the Nyquist criterion, the final signal has a 2.5 fs point spacing. However, as noted previously the response functions, Eqs. (3-40) - (3-42) do not oscillate at nearly this high of a frequency. (The highest frequencies in the response functions are generally of the anharmonic splitting, corresponding to time periods well over 100 fs.) Therefore, the response function is sampled at 10 fs intervals, and linear interpolation in all three time variables allows smooth interpolation at a finer point spacing when needed.

We impose finite limits to perform the convolutions in the polarization Eqs. (3-26) - (3-28). The limits are chosen to exclude less than 1% of the integrated pulse envelope intensity. When transform limited Gaussian pulses are utilized, the limits are $\pm 2\Delta_p$, but the limits are generally larger than a comparable value (based on the full width at half maximum) when envelopes measured experimentally are used because they typically have more amplitude and phase modulations in the tail of the pulse. The integrations are performed using the gauleg algorithm from Numerical Recipes,³⁵ which is optimized for integrals using Gaussian functions.

To extract the correlation function from the experimental 3PEPS data, we compared 3PEPS signal calculated from a trial correlation function to the experimental result and then repeatedly adjusted the relative amplitudes and timescales of the Brownian oscillators to improve the fit. An iterative minimization algorithm based on the downhill simplex method in multiple dimensions (Numerical Recipe routine AMOEBA³⁵) was employed until convergence was achieved to within 0.001%. We restarted the minimization from the convergence point multiple times to avoid settling into a local minimum. In this process, the frequency and damping time of the highest-frequency component were fixed, but otherwise the amplitudes, damping times and frequencies of all other components were floated. The 3PEPS decay is relatively insensitive to the overall amplitude of the correlation function, so this amplitude was determined by constraining the absorption spectrum calculated from the correlation function to the width of the FTIR spectrum.

An AMD Athlon-based 1.6 GHz PC with 512 MB RAM running Mandrake Linux calculated the nonlinear signals and fit the 3PEPS data. The size of the three dimensional grid to calculate the response functions and pulse delays varied depending on the particular experiment. Likewise, the time required to perform the calculations varied according to the complexity of the calculation, but was typically on the order of 1 minute for single-step (i.e. not 3PEPS fits) calculations. Calculation results will be presented along with the experimental data in Chapters 5 and 6.

References

- (1) Joo, T.; Jia, Y.; Yu, J.-Y.; Lang, M. J.; Fleming, G. R. *J. Chem. Phys.* **1996**, *104*, 6089.

- (2) Lang, M. J.; Jordanides, X. J.; Song, X.; Fleming, G. R. *J. Chem. Phys.* **1999**, *110*, 5884.
- (3) de Boeij, W. P.; Pshenichnikov, M. S.; Wiersma, D. A. *Annu. Rev. Phys. Chem.* **1998**, *49*, 99.
- (4) Horng, M. L.; Gardecki, A.; Papuzayan, A.; Maroncelli, M. *J. Phys. Chem.* **1995**, *99*, 17311.
- (5) Tokmakoff, A.; Fayer, M. D. *Acc. Chem. Res.* **1995**, *28*, 437.
- (6) Hamm, P.; Lim, M.; Hochstrasser, R. M. *Phys. Rev. Lett.* **1998**, *81*, 5326.
- (7) Rector, K. D.; Fayer, M. D. *Int. Rev. Phys. Chem.* **1998**, *17*, 261.
- (8) Yan, Y. J.; Mukamel, S. *J. Chem. Phys.* **1991**, *94*, 179.
- (9) Mukamel, S. *Principles of Nonlinear Optical Spectroscopy*; Oxford University Press: New York, 1995.
- (10) Cho, M.; Du, M.; Scherer, N. F.; Fleming, G. R.; Mukamel, S. *J. Chem. Phys.* **1993**, *99*, 2410.
- (11) Cho, M.; Yu, J.-Y.; Joo, T.; Nagasawa, Y.; Passino, S. A.; Fleming, G. R. *J. Phys. Chem.* **1996**, *100*, 11944.
- (12) de Boeij, W. P.; Pshenichnikov, M. S.; Weirsma, D. A. *J. Phys. Chem.* **1996**, *100*, 11806.
- (13) de Boeij, W.; Pshenichnikov, M. S.; Wiersma, D. A. *Chem. Phys. Lett.* **1996**, *253*, 53.
- (14) Xu, Q. H.; Ma, Y. Z.; Fleming, G. R. *J. Phys. Chem. A* **2002**, *106*, 10755.
- (15) Sung, J.; Silbey, R. J. *J. Chem. Phys.* **2001**, *115*, 9266.
- (16) Sung, J.; Silbey, R. J. *J. Chem. Phys.* **2003**, *118*, 2443.

- (17) Butcher, P. N.; Cotter, D. *The Elements of Nonlinear Optics*; Cambridge University Press: Cambridge, 1990.
- (18) Mukamel, S.; Loring, R. F. *J. Opt. Soc. B* **1986**, *3*, 595.
- (19) Note that the first term on the right hand side of Eq. (3-14) is conjugated, although it was printed incorrectly in the published version of the paper.
- (20) Cho, M.; Fleming, G. R.; Mukamel, S. *J. Chem. Phys.* **1993**, *98*, 5314.
- (21) Dick, B. *Chem. Phys.* **1987**, *113*, 131.
- (22) Tokmakoff, A. *J. Chem. Phys.* **1996**, *105*, 1.
- (23) Gallagher Faeder, S. M.; Jonas, D. M. *J. Phys. Chem. A* **1999**, *103*, 10489.
- (24) Gallagher Faeder, S. M.; Jonas, D. M. *Phys. Rev. A* **2000**, *62*, 033820.
- (25) Albrecht, A. W.; Hybl, J. D.; Gallagher Faeder, S. M.; Jonas, D. M. *J. Chem. Phys.* **1999**, *111*, 10934.
- (26) Khalil, M.; Demirdöven, N.; Tokmakoff, A. *J. Phys. Chem. A* **2003**, *107*, 5258.
- (27) Ernst, R. R.; Bodenhausen, G.; Wokaun, A. *Principles of Nuclear Magnetic Resonance in One and Two Dimensions*; Oxford University Press: Oxford, 1987.
- (28) Fourkas, J. T.; Kawashima, H.; Nelson, K. A. *J. Chem. Phys.* **1995**, *103*, 4393.
- (29) Fourkas, J. T. *Laser Physics* **1995**, *5*, 661.
- (30) Khalil, M.; Tokmakoff, A. *Chem. Phys.* **2001**, *266*, 213.
- (31) Oxtoby, D. W.; Rice, S. A. *Chem. Phys. Lett.* **1976**, *42*, Chem. Phys. Lett.
- (32) Diestler, D. J. *Chem. Phys. Lett.* **1976**, *39*, 39.
- (33) Shen, Y. R. *The Principles of Nonlinear Optics*; Wiley-Interscience: New York, 1984.
- (34) Woutersen, S.; Bakker, H. J. *Phys. Rev. Lett.* **1999**, *83*, 2077.

(35) Press, W. H.; Teukolsky, S. A.; Vetterling, W. T.; Flannery, B. P. *Numerical Recipes in C++*; Cambridge University Press: Cambridge, 2002.

Chapter 4

Mid-IR BBO/KNbO₃ OPA

4.1 Introduction

Time-resolved resonant nonlinear spectroscopy of vibrational transitions requires pulses of infrared light that are both intense and have short pulse durations. Such pulses can be generated in free electron lasers,¹ color-center lasers,² or through difference frequency processes such as parametric amplification or direct difference frequency generation (DFG).³⁻

⁷ Parametric amplification, sometimes coupled with DFG, has emerged as the most ideal option for experiments requiring mid-infrared pulses with femtosecond pulse lengths. Optical parametric oscillators (OPO) and amplifiers (OPA) pumped by the output of Ti:sapphire amplifiers can routinely generate sub-picosecond pulses that span the wavelength range 1 – 20 μm . The 3 μm region is of particular interest to spectroscopists due to the absorption of hydride stretches. Not only are the frequencies of these groups sensitive to their molecular surrounding, but also the vibrations are more localized than other functional groups, making them ideal probes of local structure and dynamics in condensed phase systems.

We investigate microscopic dynamics in water through the vibrational spectroscopy of the OH stretch, which absorbs light at roughly 3400 cm^{-1} . The OH absorption spectrum of a dilute HOD in D_2O sample, plotted in Fig. 4-1, is extremely broad ($\sim 250\text{ cm}^{-1}$). Third-order vibrational spectroscopies are also sensitive to the overtone transition, and recent attempts to probe the overtone spectrum have indicated that the anharmonicity is 250 cm^{-1} and that the transition is even broader than the fundamental absorption ($>400\text{ cm}^{-1}$, Fig. 4-1).⁸ These spectra constrain the mid-IR pulse characteristics required to perform the nonlinear vibrational spectroscopy, since it should have coherent bandwidth to span both the fundamental and overtone transitions.

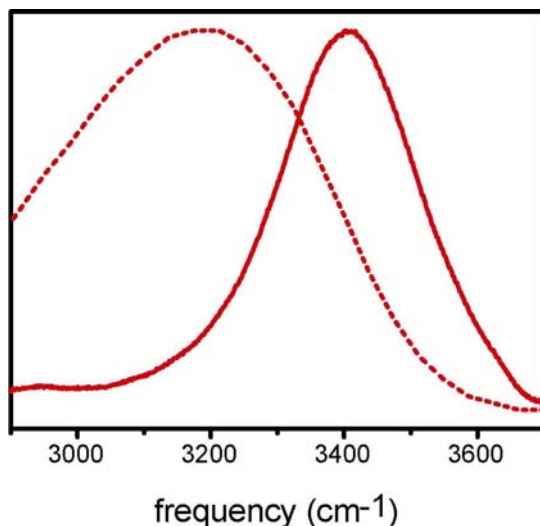


Figure 4-1. (Color) Absorption spectrum for the OH stretch of 1% HOD in D_2O (solid) and the anharmonically shifted $\nu = 2 \leftarrow 1$ overtone absorption (dashed, taken from Ref. 10).

Parametric amplification involves the transfer of power in a nonlinear medium from a relatively intense pump pulse of frequency ω_3 to two weaker pulses of frequencies ω_1 and ω_2 , where $\omega_3 = \omega_1 + \omega_2$. The higher frequency amplified pulse is referred to as the signal and the lower frequency one as the idler. Efficient transfer of power from the pump to the

signal and idler requires that the three waves satisfy the phase matching constraint $\mathbf{k}_3 = \mathbf{k}_1 + \mathbf{k}_2$, which is usually accomplished by a judicious choice of the propagation direction within a birefringent nonlinear crystal.^{9,10}

The most common crystal used in the parametric generation of femtosecond infrared pulses is beta barium borate, β -BaB₂O₄ (BBO), because it supports large bandwidths and has a high damage threshold.¹¹ When pumped by the 800 nm output of a Ti:sapphire amplifier, BBO can generate pulses in the 1.1 – 2.8 μm region.¹² It absorbs at longer wavelengths, sharply decreasing its efficiency and preventing its use to directly produce pulses with wavelengths longer than about 3.2 μm . The 3 – 12 μm region may be accessed by DFG between the signal and idler in another nonlinear crystal, such as silver gallium sulfide, AgGaS₂,^{3,4} or gallium selenide, GaSe.⁶ However the additional nonlinear process reduces the overall efficiency, and group velocity walk-off increases the pulse duration. Neither of these crystals can be used to directly convert 800 nm pulses to the mid-IR because two-photon absorption of the pump is large, leading to a poor efficiency for the generation of mid-IR pulses.

A limited number of crystals are both transparent beyond 3 μm and have a UV band edge that does not permit two-photon absorption of strong 800 nm pulses. Of those, potassium niobate, KNbO₃ (KNB), shows the most promise for short mid-IR pulse generation, because its nonlinearity is the largest, allowing for short crystal lengths, and its steep phase-matching curve near 3 μm results in a large acceptance bandwidth.¹³⁻¹⁹ It has the additional advantage of a high damage threshold, allowing its use for the generation of pulses energetic enough to perform nonlinear experiments. Several previous studies have demonstrated the generation of mid-IR pulses in KNB under various conditions, and most

notably sub-100 fs pulses were achieved in two OPAs involving a single pass through KNB. Kafka and Watts generated 3-4 μJ pulses near 3 μm , which were reported to have a 50 fs duration but were not well characterized.¹⁵ Gruetzmacher and Scherer generated weak pulses (a few nJ), which were thoroughly analyzed by cross-correlating them with the pump, finding a duration of just under 50 fs.¹⁸ Building on this earlier work, we have designed and constructed a two-stage BBO/KNB OPA that produces sub-50 fs, 3-4 μJ pulses suitable for performing nonlinear vibrational spectroscopy on the OH stretch. The following provides design and operation details for the OPA, focusing on the selection of the nonlinear crystals and the full characterization of the resulting pulse spectra, time-dependent amplitude and phase and stability.

4.2 Design and fabrication of the 3 μm OPA

In order to perform nonlinear spectroscopic measurements on water, the mid-IR pulses generated by the OPA should have an energy greater than 1 μJ and duration of 50 fs or less after compression. It would be preferable to span the fundamental and overtone transitions of the OH stretch with the coherent bandwidth of the pulses, although to do so within the full width at half maximum would require over 750 cm^{-1} of bandwidth. Such a large bandwidth would be difficult to compress, so a more useful goal is near-transform-limited pulses that are tunable between the center fundamental ($\sim 3400 \text{ cm}^{-1}$) and overtone ($\sim 3150 \text{ cm}^{-1}$) frequencies. Based on the work discussed above, we choose to concentrate on a scheme incorporating KNB to generate these pulses. Design of the OPA then consists of choices relating to crystal orientations and focusing conditions, as well as several options for the production of a seed to be used in the final amplification.

At room temperature, KNB is a negative biaxial material that is optically transparent beyond 4 μm . Its crystals are orthorhombic with point-group symmetry $mm2$, whose smallest refractive index lies along the two-fold rotation symmetry axis.^{13,20} We use the convention $n_x < n_y < n_z$ and consider only propagation within the principal planes. Type I phase-matched propagation of the appropriate wavelengths can be achieved in the xy and xz planes, but the latter maximizes the nonlinear coefficient d_{eff} and is therefore chosen as the propagation direction. The tuning curve for an 800 nm pump beam polarized in the extraordinary direction, assuming the signal and idler are polarized in the ordinary direction, is plotted in Fig. 4-2. Its effective nonlinearity is:

$$d_{\text{eff}} = d_{31} \sin(1 - \theta), \quad (4-1)$$

where θ is measured from the z axis. The process:

$$800 \text{ nm} (e) \rightarrow 3000 \text{ nm} (o) + 1090 \text{ nm} (o) \quad (4-2)$$

is phase-matched at $\theta = 41^\circ$ with $d_{\text{eff}} = 6.7 \text{ pm/V}$. The group velocity mismatch calculated between the pump and idler pulses is significant,¹⁶ limiting crystal lengths to less than 1 mm for the generation of sub-100 fs pulses. Previous experiments have indicated that the temporal walk-off is less severe than calculations predict, prompting the choice of 1 mm crystal lengths for the OPA.^{15,16,18}

The system that pumps the OPA is comprised of commercial lasers from Spectra Physics and Femtolasers (Fig. 4-3). Briefly, a Millennia pumps the Femtolasers Ti:sapphire oscillator, producing 5 nJ, 12 fs pulses at 800 nm. These pulses seed a chirped pulse Femtolasers multi-pass Ti:sapphire amplifier, pumped by an Evolution. The resulting pulses have a duration of 25 fs, as measured with a collinear autocorrelation in BBO. The output

pulse energy of the amplifier is 800 μJ , but only 400 μJ is used to pump the OPA to allow for future expansion of the system.

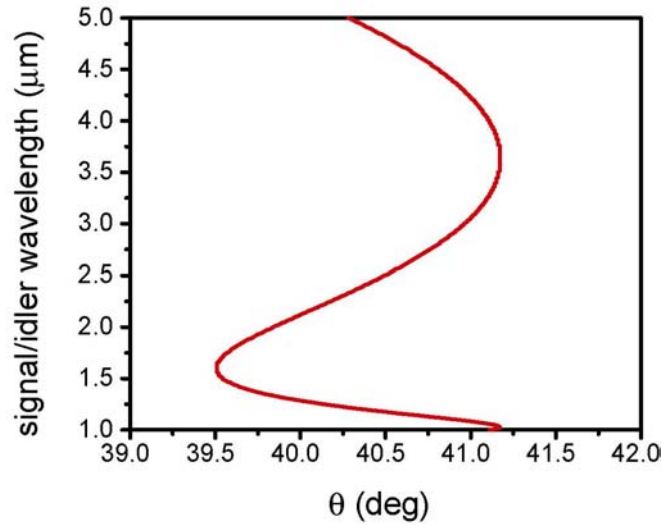


Figure 4-2. (Color) Type I tuning curve for propagation in the xz axis of KNB using an 800 nm pump beam polarized in the extraordinary direction. θ is measured off z towards y .

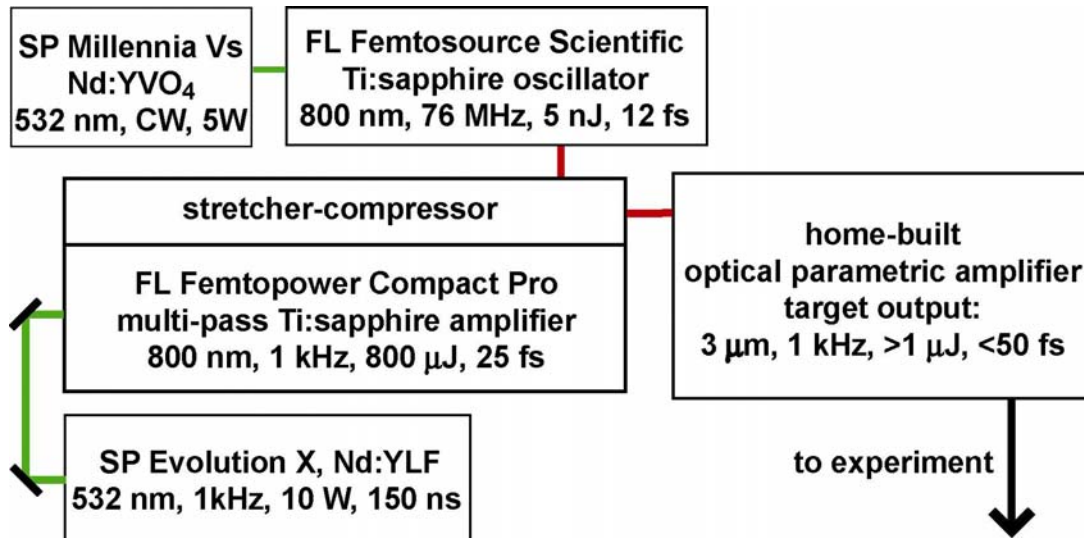


Figure 4-3. (Color) Schematic diagram of the laser system used to pump the home built OPA (SP = Spectra Physics, FL = Femtolasers)

In order to achieve mid-IR pulse energies sufficient to perform nonlinear spectroscopies ($> 1 \mu\text{J}$) from several hundred microjoule pump pulses, we choose a two stage, white light seeded OPA design. In this scheme, the initial signal pulse is derived from the continuum generated by focusing a small amount of the pump pulse into a [0001]-cut sapphire plate. It is parametrically amplified with its corresponding idler pulse in a nonlinear crystal, which is pumped by part of the input pulse and oriented for proper phase-matching. In principal, either the signal or idler (but not both due to parametric interference²¹) can be used as a strong seed for the second stage power amplification. Due to ease of manipulation, we discard the idler (and the residual pump pulse) after the first stage and feed the signal, along with the remaining pump pulse, into the second stage. Therefore, in order to achieve optimal OPA performance, the idler generated in the first stage should be energetic, exhibit good pulse-to-pulse stability, and have a spectrum that is broad and tunable in the $1.1 \mu\text{m}$ region. To satisfy these criteria, we do not restrict the crystal choice in the first stage to KNB, but rather consider BBO as well, since it has exhibited solid performance with respect to these criteria in other systems. (Because the idler beam is discarded in favor of the signal, the absorption properties of BBO in the mid-IR are less of an issue for the first stage than for the second stage.)

The pulse spectra of the signal beam for both crystals are easily tunable in the $1.1 \mu\text{m}$ range and exhibit widths of approximately 600 cm^{-1} in the case of KNB and 400 cm^{-1} for BBO. Due to a wavelength-dependent grating efficiency curve, the spectra cannot be taken as quantitatively correct, however an accurate energy comparison is made in Table 4-1. These energy values are recorded through a bandpass filter whose center wavelength matches that required for the generation of idler pulses at $3 \mu\text{m}$ in the second stage. The pulses

generated in BBO are approximately twice as energetic as those generated in KNB, despite the fact that the effective nonlinearity in BBO is nearly four times smaller than that calculated above for KNB. This discrepancy can be explained in terms of the group velocity mismatch, which is considerably smaller for BBO, allowing more efficient amplification over the length of the crystal. In fact, the BBO signal pulse energy would be even larger if it were not for the coincidence that the angle used to phase-match the generation of 1.1 μm light from an 800 nm pump is nearly that needed to frequency double 1.1 μm light. Therefore, a significant portion (as much as 50%) of the signal is converted to visible light in the 550 – 600 nm range.²²²³

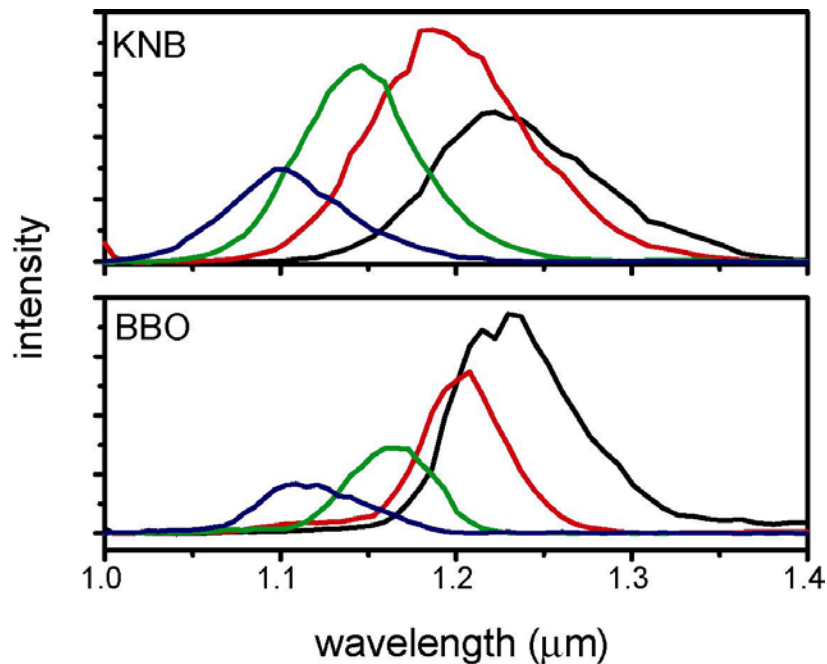


Figure 4-4. (Color) Pulse spectra of the signal beams resulting from angle tuning KNB and BBO. Both are pumped and seeded under the same conditions, as described in the text. Each crystal is tuned to achieve spectra centered at approximately 1120 nm, 1160 nm, 1200 nm and 1240 nm. The spectra have not been corrected for grating efficiency.

We compare the signal beam characteristics of KNB to that of BBO in Figs. 4-4 and 4-5 and in Table 4-1. Type I phase-matching and the same focusing conditions are used for

both crystals. Each is pumped with 50 mJ 800 nm pulses and seeded with white light generated as described above. Surprisingly, we found that the threshold for continuum generation is similar for both crystals, allowing us to operate just under this condition by increasing the pump spot size at the crystal just beyond this threshold (~250 μm diameter). The KNB crystal is 1 mm long and cut as described above. The tuning curve for BBO, which has been presented elsewhere,²² indicates the process described by Eq. (4-2) is phase-matched at $\theta = 21.5^\circ$. We use a 1 mm crystal which is cut at $\theta = 29^\circ$, but is properly rotated in the mount.

Center wavelength	BBO energy at 1.1 μm	KNB energy at 1.1 μm
1240 nm	150 nJ	65 nJ
1200 nm	260 nJ	95 nJ
1160 nm	500 nJ	280 nJ
1120 nm	480 nJ	230 nJ

Table 4-1. Pulse energy of the signal beam at 1.1 μm resulting from angle tuning KNB and BBO under the same conditions. The 800 nm pump energy is 50 μJ . Signal energies are measured through a 1.1 μm bandpass optical filter (1.08-1.14 μm , Spectragon) with a calibrated germanium detector (Coherent).

To compare the stability of signal pulses generated from each crystal, we plot histograms of the pulse energy measured through the 1.1 μm bandpass filter Fig. 4-5. Signal pulses generated from BBO are clearly more stable than those from KNB, and are nearly limited by the amplifier shot stability. The BBO performance is surprising considering that much of the idler is absorbed within the crystal, which is often assumed to degrade the stability of the parametric process, but another recent study also found good performance from a BBO OPA operating near the absorption edge.²⁴

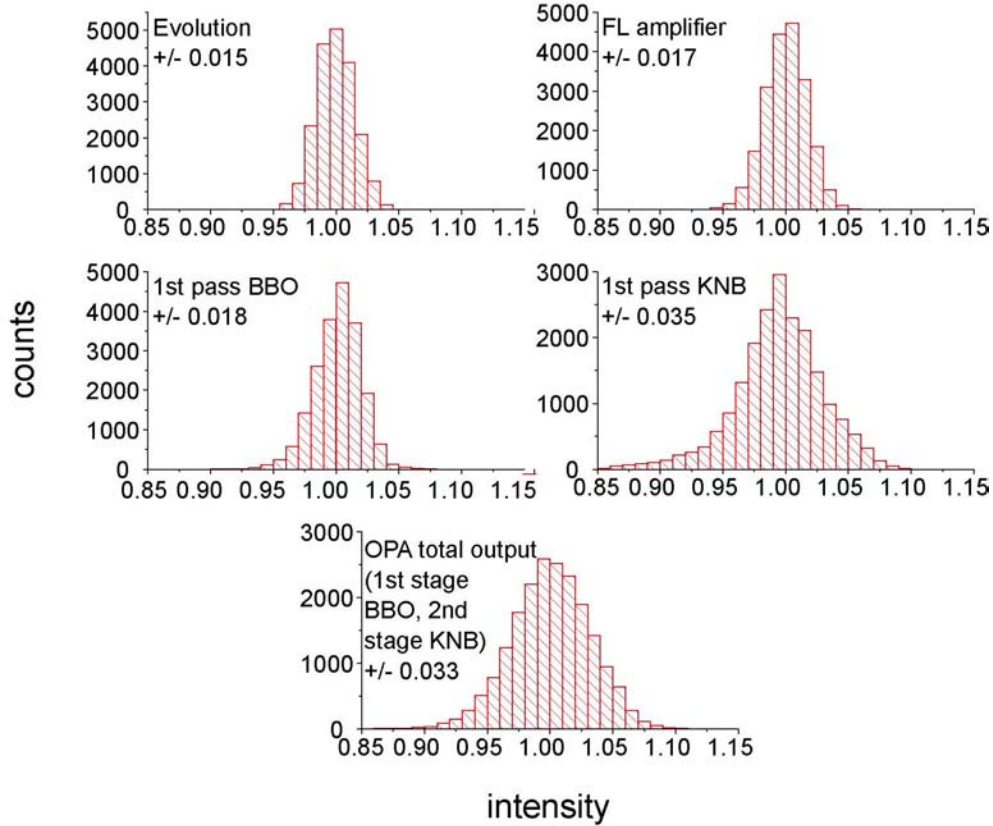


Figure 4-5. (Color) Pulse energy stability histograms for components used to generate mid-IR pulses. The energy of every 50th pulse was recorded for 20 minutes for each component. The mean of each distribution has been normalized to unity, and the reported errors are the standard deviation.

Based on these comparisons, we chose to use BBO in the first stage to generate energetic and stable 1.1 μm pulses for subsequent parametric amplification by KNB in the second stage. Fig. 4-6 is a schematic representation of the OPA. Besides the crystals, other design choices have been made to optimize the device for short-pulse generation. First, the optical elements in each arm have been chosen so as to roughly equalize the amount of pulse broadening caused by passing through dispersive materials. The amplifier compressor is then adjusted to precompensate for this dispersion, resulting in unchirped pulses in each arm. Secondly, we use all reflective optics to manipulate the white light, which is especially prone to pulse broadening due to its broad spectral content. The custom dichroic beamsplitter that

combines the 800 nm pump with the white light is designed to minimize group velocity dispersion for both beams.

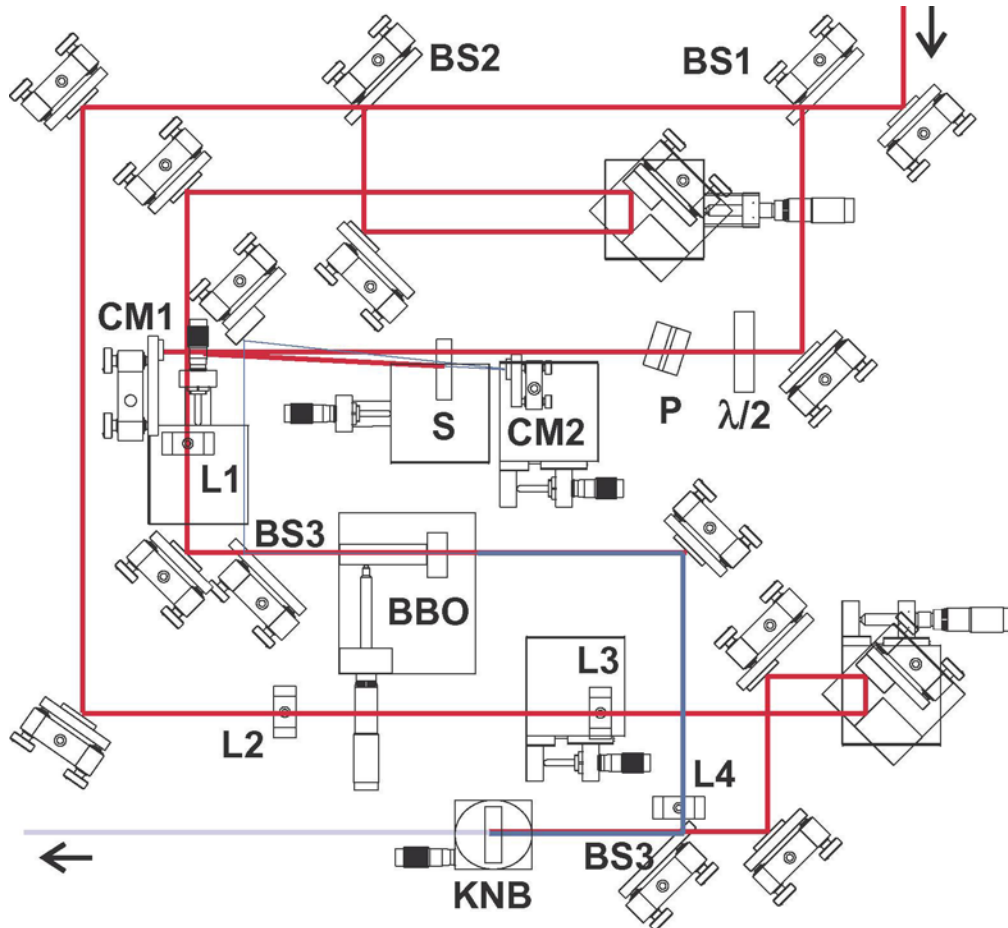


Figure 4-6. (Color) Experimental configuration of the 3 μm BBO/KNB OPA. (T = transmission, R = reflection, FS = fused silica, AR = anti-reflection coating) **BS1** CVI FS window, single-side AR800nm; **BS2** Femtolasers 37%R beamsplitter; **BS3** Cascade Optical custom beamsplitter, T800nm R1100nm, designed to minimize GVD for both beams; **CM1** and **CM2** CVI protected gold concave spherical mirrors, radius of curvatures 30 and 7.5 cm respectively; **L1**, **L2**, **L3** CVI FS plano lenses, focal lengths 28, 34 and -11.3 cm respectively; **L4** Newport BK7 plano lens, focal length 10 cm; $\lambda/2$ CVI quartz zero order half wave plate; **P** Alpine Research Optics thin film polarizer, broadband design; **S** Meller Optics [0001]-cut sapphire disc, 1.5 mm thick; **BBO** Casix BBO crystal, 1 mm thick, $\theta=29.2^\circ$ $\phi=0^\circ$, both sides AR800nm; **KNB** Spectrogen KNB crystal, 1mm thick, $\theta=41^\circ$ (off b towards c) $\phi=0^\circ$, entrance side AR800nm; all unspecified optics are CVI protected gold plane mirrors.

For the experiments described in this work, the OPA is pumped with 400 μJ , 800 nm pulses, collimated to a diameter of ~ 6 mm. A 28 cm lens, placed 25-26 cm from the BBO crystal, focuses the pump beam in the first pass. As with the earlier experiments to choose the crystal, the beam diameter is slightly larger than the size required to generate continuum. (Since the input power is greater than was used previously, the diameter is also larger (~ 400 μm) than was used before.) The spot size of the white light is similar to that of the pump beam, which was found to give the best power and stability characteristics. In the second pass, the pump beam is not focused as tightly, nor is it as convergent at the crystal. Besides the fact that the pump pulses are more energetic, a tight focus would cause the mid-IR idler pulses to diverge quickly, and could lead to spectral broadening due to the steep angular tuning curve. To control the pump beam size, a 3:1 Galilean telescope is adjusted slowly to focus the pump to achieve a spot size of 500-600 μm at the KNB crystal. After the crystal, the pump and near-IR signal beams are dumped using a 800 nm high reflector which is transparent to the idler and a germanium window, anti-reflection coated for 3 μm light. The mid-IR beam is collimated to a diameter of 8 mm with a Galilean telescope employing CaF_2 lenses.

When tuned near 3 μm , the idler power is 3-4 $\mu\text{J}/\text{pulse}$. This power is slightly lower than might be expected based on a double pass configuration with the pulse energies and durations used to pump it. The efficiency can be explained by the relatively poor beam quality of the pump beam as compared with that derived from regenerative amplifiers. The energy stability of the output pulse stability is a factor of two worse than the stability of the pump pulses and the 1.1 μm pulses from the first pass, however it appears that this type of

behavior is typical of KNB since it was also observed when KNB was tested for the first pass behavior.

4.3 Characteristics of the mid-IR pulses

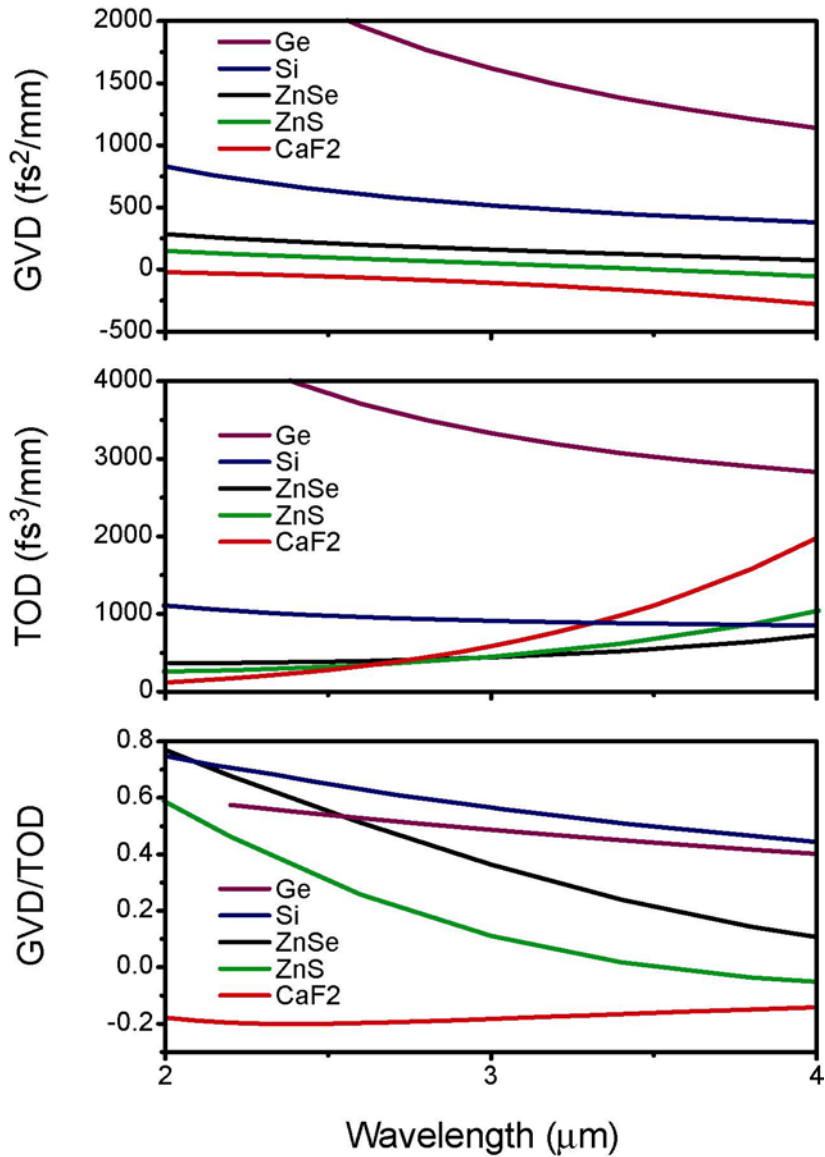


Figure 4-7. (Color) Dispersion characteristics in the 3 μm region of common mid-IR materials; from top to bottom: group velocity dispersion (GVD), third order dispersion (TOD) and the ratio of the two. Note that the GVD is negative for CaF₂ but positive for all other materials, while the TOD is positive for all materials.

The idler pulses exiting the OPA are not transform limited and therefore require compression before use in an experiment. It has recently been shown that pulse compression to second order in the optical phase can be achieved by using materials with GVD of opposite signs in the mid-IR.^{25,26} This technique is not possible for visible pulses, since the sign of the GVD is the same for all materials in that region of the electromagnetic spectrum. However, the sign of GVD changes from positive to negative in the mid-IR for many common materials. At 3 μm , both KNB and CaF_2 have a negative GVD, as can be observed from Fig. 4-7. Therefore, KNB used to generate the mid-IR light in the second stage of the OPA also imparts a large amount of chirp on the pulses, which must be compensated by a material with positive GVD. However, the situation is much more complicated, since the nonlinear experiments require the pulses to traverse a path that passes through lenses, windows, beamsplitters and polarizers. By measuring the pulse duration at the sample as described below, the amounts of these materials have been adjusted to compress the mid-IR pulses as much as possible. In total, after the KNB crystal in the OPA, the pulses travel through 2 mm Ge and 14 mm CaF_2 .

To characterize the mid-IR pulses, we measure the pulse spectrum, as well as the second harmonic background-free autocorrelation and frequency resolved optically gated autocorrelation (FROG).²⁷ The spectral characteristics were measured by dispersing the beam in a 150 mm focal length, f/4 imaging monochromator (Acton, SpectraPro 150) with a 300 groove/mm grating optimized for 2.5 μm (Thermo-RGL, 674-18). The grating has a flat spectral response throughout the 3 μm region, and is also efficient in the 1.5 μm region for the characterization of frequency doubled pulses. All dispersed measurements were recorded with a liquid nitrogen cooled InSb detector (Infrared Associates). The time characteristics

were recorded at the position of the sample, and thus utilized the five-beam interferometer discussed in Chapters 5 and 6. In brief, each mid-IR pulse is split by a custom 3 μm 50/50 beamsplitter, designed to minimize the GVD of the transmitted and reflected beams (Thin Film Lab). The material in each arm of the interferometer is matched using compensation plates. One arm includes a computer-controlled translation stage (Aerotech, ANT-25L) to vary the path length traversed by that beam, and thus the relative timings between the two beams. The beams focused by an off-axis parabolic mirror (Janos) in a background-free autocorrelation geometry. A 300 μm thick silver gallium sulfide (AgGaS_2) crystal, cut for type I phase matching ($\theta = 37.4^\circ$, $\phi = 45^\circ$) generates the second order autocorrelation. The autocorrelation is either detected directly by an InGaAs photodiode (ThorLabs) or directed into the monochromator as discussed above for the FROG.

The set of experimentally measured autocorrelation, spectrum and FROG for IR pulses centered at 3300 cm^{-1} is presented in Fig. 4-8 as an example of the OPA performance. The autocorrelation full width at half maximum is 60 fs and the spectral full width at half maximum is 400 cm^{-1} . The spectral lineshape is primarily determined by the angle tuning of the BBO and KNB crystals, and is affected to a lesser extent by the compression of the input pump pulses and the relative timings between seed and pump pulses. However, when BBO is replaced by KNB in the first stage, we find that the spectrum is much more sensitive to the timing between the 1.1 μm seed and pump in the second stage. This most likely explanation that the spectrum depends on the pulse timing is that the signal pulses generated using KNB in the first stage are significantly chirped (at least relative to those generated using BBO), which is not surprising considering the GVD and TOD curves plotted in Fig. 4-7. In contrast to the spectrum, the autocorrelation width and lineshape are affected by nearly every

parameter in the OPA, such as crystal angles, pulse timings, pump pulse chirp, quality of the white light. It is also dependent on the material that the mid-IR beam passes through after leaving the OPA as discussed above.

The strategy we use to align the OPA (after overlapping all beams and adjusting focusing conditions) begins by tuning the crystals to properly center the spectrum with as little bandwidth as possible. The second criterion assures that the center frequency of the signal beam from the BBO is properly phase-matched in the KNB crystal. (Although it has been suggested that shorter pulses can be generated by slightly detuning the phase-matched frequencies in one crystal with respect to those phase-matched in the second crystal,⁴ we have not been able to compress pulses generated in this manner to shorter durations than those generated by phase-matching the same frequencies in both crystals.) After tuning the crystals, we typically tweak on pulse timings and pump beam compression to simultaneously improve the autocorrelation lineshape (reducing both width and wings) and maintain a steady pulse train. Then, material with different sign GVD (CaF_2 and ZnSe) is inserted into the beam after the OPA in an attempt to further improve the autocorrelation. The last two steps are iterated until the best autocorrelation is achieved while maintaining pulse stability.

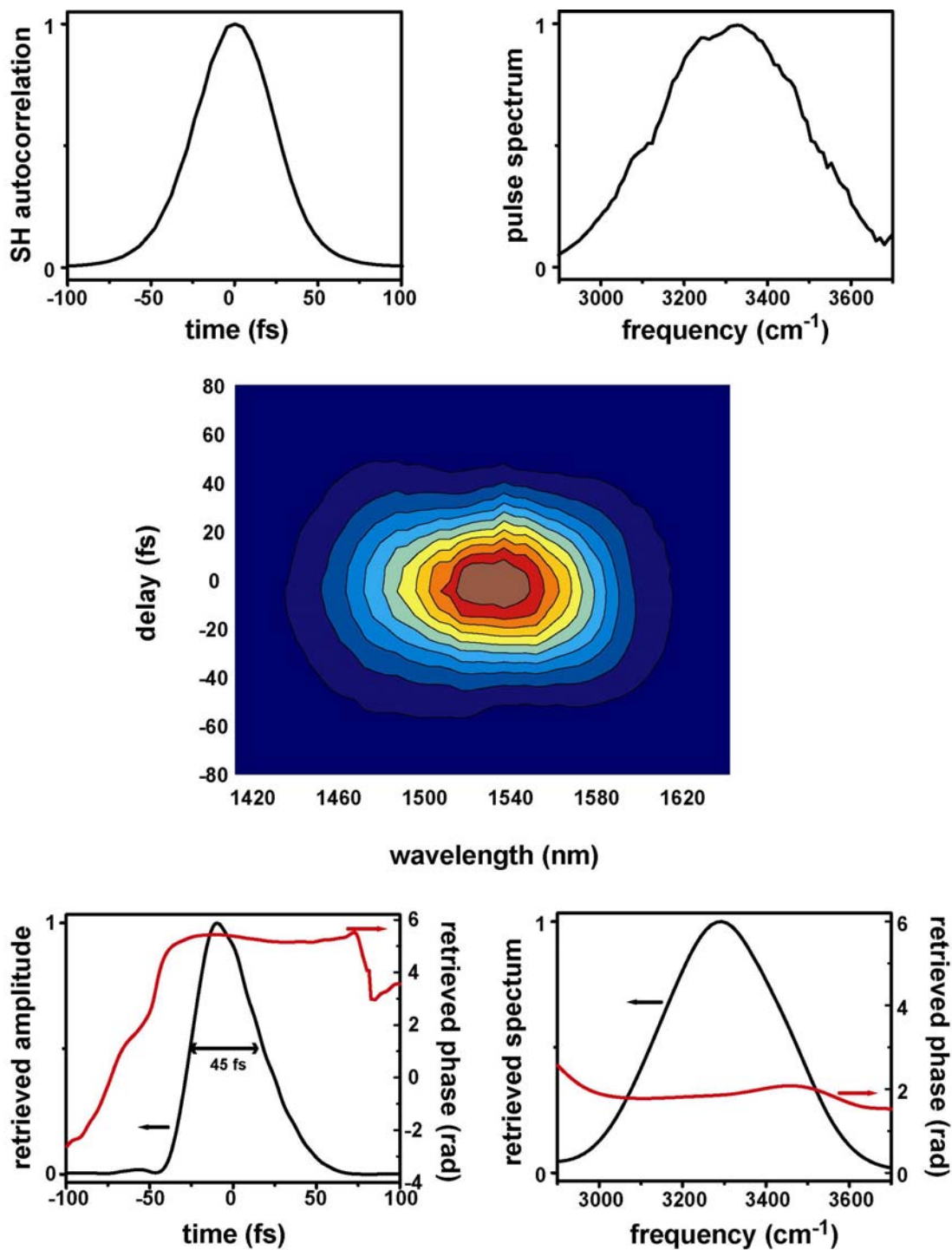


Figure 4-8. (Color) Time and frequency characteristics of the mid-IR pulse generated by the BBO/KNB OPA. (top) Experimentally measured second-harmonic background-free autocorrelation and pulse spectrum centered at 3300 cm^{-1} . (center) Experimentally measured second harmonic FROG and (bottom) retrieved amplitude and phase in time and frequency. The FROG contours are plotted at 10% levels.

The pulse amplitude and phase are extracted from the measured FROG with commercial software (Femtosoft Technologies). For the FROG in Fig 4-8, the error associated with the retrieval was 0.012 on a square 64 element grid. To check the reproducibility of the extracted field, the retrieval was performed numerous times (>10), with random initial guesses for the amplitude and phase. The time duration of the field in Fig. 4-8 is 45 fs, although values ranged from 43-47 fs. The phase is relatively flat over the main portion of the pulse, indicating that it is nearly transform limited. The spectral width is 350 cm^{-1} , which is slightly smaller than the observed spectral indicating that a small portion of the spectrum is incoherent. More importantly, the coherent bandwidth of the pulse is larger than the OH absorption linewidth, ensuring that all dynamical processes can be observed in the spectroscopic measurements. The bandwidth is not enough to span both the fundamental and overtone transitions, however this only results in a spectral filtering of the signal, which is taken into account by the real pulse calculations.

4.4 Conclusion

We have designed and built a two-stage, white light seeded OPA to generate short pulses of 3 μm light. The first stage employs BBO to generate a 1.1 μm seed for subsequent parametric amplification of the 3 μm pulse in KNB. By passing the mid-IR beam through materials chosen to eliminate GVD, the pulses are compressed to a duration less than 50 fs. These pulses are ideal for the third order nonlinear spectroscopic experiments on the OH stretch of HOD in D_2O .

References

- (1) Dlott, D. D.; Fayer, M. D. *IEEE J. Quantum Electron.* **1991**, *27*, 2697.
- (2) Kean, P. N.; Zhu, X.; Crust, D. W.; Grant, R. S.; Langford, N.; Sibbett, W. *Opt. Lett.* **1989**, *14*, 39.
- (3) Seifert, F.; Petrov, V.; Woerner, M. *Opt. Lett.* **1994**, *19*, 2009.
- (4) Wilson, K. R.; Yakovlev, V. V. *J. Opt. Soc. Am. B* **1997**, *14*, 444.
- (5) Emmerichs, U.; Woutersen, S.; Bakker, H. J. *J. Opt. Soc. Am. B* **1997**, *14*, 1480.
- (6) Kaindl, R. A.; Wurm, M.; Reimann, K.; Hamm, P.; Weiner, A. M.; Woerner, M. *J. Opt. Soc. Am. B* **2000**, *17*, 2086.
- (7) Petrov, V.; Rotermund, F.; Noack, F. *J. Opt. A: Pure Appl. Opt.* **2001**, *3*, R1.
- (8) Woutersen, S.; Bakker, H. J. *Phys. Rev. Lett.* **1999**, *83*, 2077.
- (9) Shen, Y. R. *The Principles of Nonlinear Optics*; Wiley-Interscience: New York, 1984.
- (10) Yariv, A. *Optical Electronics in Modern Communications*, Fifth ed.; Oxford University Press: New York, 1997.
- (11) Eimerl, D.; Davis, L.; Velsko, S.; Graham, E. K.; Zalkin, A. *J. Appl. Phys.* **1987**, *62*, 1968.
- (12) Yakovlev, V. V.; Kohler, B.; Wilson, K. R. *Opt. Lett.* **1994**, *19*, 2000.
- (13) Zysset, B.; Biaggio, I.; Gunter, P. *J. Opt. Soc. Am. B* **1992**, *9*, 380.
- (14) Biaggio, I.; Kerkoc, P.; Wu, L.-S.; Gunter, P.; Zysset, B. *J. Opt. Soc. Am. B* **1992**, *9*, 507.

- (15) Kafka, J. D.; Watts, M. L. A potassium niobate OPA pumped by an amplified Ti:sapphire laser. In *Ultrafast Phenomena X*; Barbara, P. F., Fujimoto, J. G., Knox, W. H., Zinth, W., Eds.; Springer-Verlag: Berlin, 1996; Vol. 62.
- (16) Petrov, V.; Noack, F. *Opt. Lett.* **1996**, *21*, 1576.
- (17) Cussat-Blanc, S.; Ivanov, A.; Lupinski, D.; Freysz, E. *Appl. Phys. B* **2000**, *70*, S247.
- (18) Gruetzmacher, J. A.; Scherer, N. F. *Rev. Sci. Inst.* **2002**, *73*, 2227.
- (19) Pack, M. V.; Armstrong, D. J.; Smith, A. V. *J. Opt. Soc. Am. B* **2003**, *20*, 2109.
- (20) Dmitriev, V. G.; Gurzadyan, G. G.; Nikogosyan, D. N. *Handbook of Nonlinear Optical Crystals*, Second ed.; Springer: New York, 1997; Vol. 64.
- (21) Fraser, J. M.; Hall, K. C. *Opt. Express* **1999**, *5*, 21.
- (22) Lopez-Martens, R.; Fournier, S.; Le Blanc, C.; Baubeau, E.; Salin, F. *IEEE J SEL TOP QUANT* **1998**, *4*, 230.
- (23) Type-II BBO was tested in the first stage at a later date, but the overall OPA output was relatively similar to the output with a type-I BBO crystal.
- (24) Zhang, D.; Kong, Y.; Zhang, J.-Y. *Opt. Commun.* **2000**, *184*, 485.
- (25) Demirdöven, N.; Khalil, M.; Golonzka, O.; Tokmakoff, A. *Opt. Lett.* **2002**, *27*, 433.
- (26) Demirdöven, N. *Coherent Two-Dimensional Infrared Spectroscopy: Study of Coupled Vibrations*, Massachusetts Institute of Technology, 2003.
- (27) Trebino, R.; DeLong, K. W.; Fittinghoff, D. N.; Sweetser, J. N.; Krumbugel, M. A.; Richman, B. A.; Kane, D. J. *Rev. Sci. Inst.* **1997**, *68*, 3277.

Chapter 5

Ultrafast hydrogen bond dynamics in the IR spectroscopy of water

5.1 Introduction

Hydrogen bonding has an unusually strong influence on the physical and chemical properties of water, distinguishing it from other liquids. Hydrogen bonds are especially important for water because of its low molecular weight, and because each molecule can interact directly with four neighboring molecules, allowing the formation of an extended network of molecules that are linked together by hydrogen bonds. The connectivity of this network is continuously changing due to molecular motions that break and form individual hydrogen bonds. Because these dynamics impact processes that occur in aqueous solutions, such as chemical reactions or biological proton transfer, it is essential to understand the physical processes that govern them. Despite many decades of experimental and theoretical investigations of hydrogen bonding in water,¹⁻¹⁶ many mysteries remain about the way hydrogen bonds are made and broken. For instance, the influence of collective processes on

the local and large-scale rearrangements of the hydrogen bond network is not well understood.¹⁷

One persistent difficulty in the study of hydrogen bond dynamics in water is that the characteristic timescales of the relevant molecular motions are picoseconds or shorter.¹¹ Traditional probes of molecular structure, such as x-ray scattering, provide time-averaged information, while NMR and dielectric relaxation can measure reorientational correlation times, but still cannot resolve sub-picosecond dynamics. Raman spectroscopy (and optical Kerr effect spectroscopy) can observe fast processes, but it measures dynamics through the many-body polarizability,¹⁸ which is an inherently non-local quantity and thus may not provide direct information about local structural changes. Computer simulations of molecular models have the potential to reveal a great deal about the fast structural reorganizations, but because most water models are parameterized to reproduce thermodynamic data,¹⁹ simulation results require experimental validation to ensure the insights gained from them are based in physical reality.

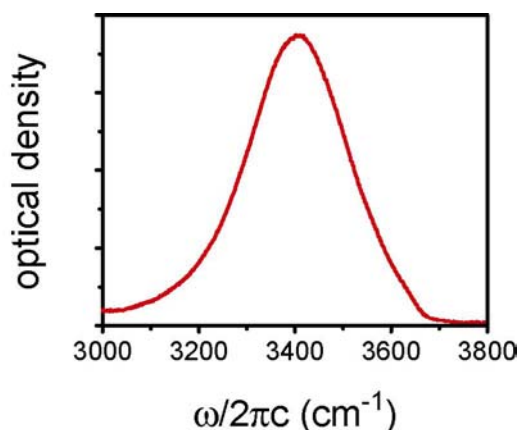


Figure 5-1. (Color) Linear absorption spectrum of ~1% HOD in D₂O in the OH stretching region.

Time-resolved infrared spectroscopy is an ideal experimental technique to study the motions of water molecules because the vibrational frequency of an OH oscillator depends

strongly on its local environment. For example, in a large number of solids containing O-H...O hydrogen bonds, the OH stretching frequency is strongly correlated with the hydrogen bond length, R_{OO} .^{20,21} Because of the distribution of environments that exists within the liquid state, the linear OH absorption spectrum (Fig. 5-1) is extremely broad. By measuring time-dependent OH frequency fluctuations of a dilute solution of HOD in D₂O (to eliminate resonant intermolecular energy transfer), one may infer changes in the configuration of solvent molecules around the oscillator.^{22,23} Measurements with sub-picosecond IR pulses can directly observe dynamics on timescales comparable to those associated with intermolecular structural rearrangements. Most experiments of this type involve the narrowband excitation of a non-equilibrium distribution of OH vibrations with a narrow-band IR pump laser pulse, followed by the time-dependent observation of the distribution as it relaxes to equilibrium with a second IR probe pulse.²⁴⁻³⁸ These time-dependent hole burning measurements have found changes in the initially excited distribution on timescales of 0.5 – 1 ps, and attributed these results to changes in R_{OO} or hydrogen bond making and breaking.^{28,33,36} However, a complete interpretation of the experiments is complicated by other contributions to the signal on similar timescales, including vibrational lifetime, molecular reorientations, a time-dependent Stokes shift and relaxation-induced heating of the bath.^{33,37,39} Some studies have even indicated that a number of these quantities are wavelength-dependent.^{31,32,35,40} In addition, an inherent limitation of the hole burning technique is that the time resolution is limited by the pump pulse duration, which is typically several hundred femtoseconds. Details about these previous investigations are discussed with our results, however it is clear that because simulations predict important processes

faster than have been observed in hole burning experiments, improved experimental time resolution is needed.^{2,8,41-45}

In this chapter, I present the results of time-resolved IR experiments of water with mid-IR pulses short enough to resolve all of the processes that broaden the OH vibrational lineshape. More specifically, polarization-selective broadband pump-probe (PP) and three-pulse vibrational echo peak shift (3PEPS) spectroscopies were used to observe population relaxation and dephasing of OH oscillators, as well as molecular reorientations. (I refer to the combined effect of these three processes generically as vibrational dynamics, due to their influence on the time-resolved IR spectroscopy.) The PP experiments measure pump-induced transmission changes of a weak probe beam as a function of the time delay between the two. Because the pump beam excites a population of OH oscillators, this technique is primarily sensitive to vibrational population relaxation and molecular reorientations. Use of polarized light fields allows the separation of these two contributions. The 3PEPS technique relies on the formation of vibrational echoes, which are IR analogs of photon echoes with visible light and spin echoes in NMR.^{46,47} It involves the measurement of time-integrated vibrational echoes as a function of the time-delays between three input pulses to determine the timescales for spectral diffusion. 3PEPS experiments with visible pulses have successfully measured dephasing dynamics for a variety of electronic systems.⁴⁸⁻⁵⁰

Following the experiments, I develop a unified description of the vibrational dynamics for the OH oscillator of HOD in D₂O by analyzing the PP and 3PEPS results using a comprehensive model to treat the nonlinear spectroscopy. For the sake of simplicity, the model inherently assumes that the vibrational dynamics are independent of frequency. All of our resonant IR experiments can be self-consistently reconstructed from three dynamical

quantities that describe vibrational dephasing, vibrational population lifetime, and molecular orientation. Aside from these, our model requires only four static, scalar quantities that describe the center frequencies of the fundamental and overtone transitions, as well as the frequency shift and change in transition dipole that result from relaxation-induced heating of the bath. By treating the data in this way, each resulting dynamical quantity is free from the influences of the others for the entire range of the experiments – from tens of femtoseconds to several picoseconds. A comparison with previous experimental and theoretical work highlights the utility of this treatment and provides insight into several long-standing disputes.

5.2 Theory

5.2.1 Response function formalism

Four wave mixing (FWM) experiments with IR light measure dephasing and population relaxation between the eigenstates of a vibrational oscillator, which serves as a local probe of microscopic dynamics. They also observe molecular reorientation when polarized light fields are used in the measurement. Vibrational 3PEPS and PP spectroscopies are specific FWM techniques in which the timings and wave vectors of the incident IR pulses are manipulated to separate contributions to the signal from different dynamical processes. However, to extract meaningful information from these experiments, a model that accounts for interactions between the light fields and vibrational oscillator, and for those between the oscillator and the rest of the sample is needed. Building on earlier work by Mukamel and co-workers,^{46,51} Sung and Silbey have recently developed such a theory for FWM experiments of a multilevel system coupled to a bath with arbitrary timescales.^{52,53} Here, we apply and

expand upon their results to develop a framework that will be used to model the experimental results presented in subsequent sections.

In a FWM experiment, three input electromagnetic fields create a macroscopic polarization within the sample, which subsequently radiates a fourth, signal field. We calculate the polarization by perturbatively expanding the total density matrix that describes the liquid and fields in orders of the field-matter interactions. The FWM signal results from the third term in the expansion, $\mathbf{P}^{(3)}$, which is obtained by a triple convolution of the third-order material response function \mathbf{R} with the incident electric fields \mathbf{E} :⁵⁴

$$\mathbf{P}^{(3)}(t) = \int_0^\infty dt_3 \int_0^\infty dt_2 \int_0^\infty dt_1 \mathbf{R}(t_3, t_2, t_1) \mathbf{E}(t-t_3) \mathbf{E}(t-t_3-t_2) \mathbf{E}(t-t_3-t_2-t_1). \quad (5-1)$$

t_1 and t_2 are the positive valued time periods that separate the three field-matter interactions and t_3 is the time between the last interaction and detection of the polarization at time t (Fig 3-2). The polarization and response function are each real-valued tensor quantities and the electric fields are real-valued vector quantities. The response function is a thrice-nested commutator of the transition dipole operator $\boldsymbol{\mu}$ evaluated at times corresponding to each field-matter interaction:

$$\mathbf{R}(t_3, t_2, t_1) = \left(\frac{i}{\hbar}\right)^3 \left\langle \left[\left[\left[\boldsymbol{\mu}(t_3 + t_2 + t_1), \boldsymbol{\mu}(t_2 + t_1) \right], \boldsymbol{\mu}(t_1) \right], \boldsymbol{\mu}(0) \right] \right\rangle. \quad (5-2)$$

Because the dipole operator evolves according to the Hamiltonian of the liquid, the response function contains information about the microscopic dynamics of the sample.

Sung and Silbey evaluate the response function in Eq. (5-2) within the second Cumulant approximation by partitioning the liquid Hamiltonian into terms that depend on system degrees of freedom (those that directly couple to the external field), bath degrees of

freedom, or both.⁵² They treat the bath as a set of harmonic oscillators that are linearly coupled to the system, retaining terms that account for vibrational dephasing but neglecting population relaxation. The form of the system Hamiltonian is general, but here we apply their theory to the vibrational spectroscopy of a weakly anharmonic oscillator, whose eigenstates are denoted $\nu = 0, 1, 2, \dots$. The energy difference between the fundamental ($|1\rangle \leftarrow |0\rangle$) and overtone ($|2\rangle \leftarrow |1\rangle$) transitions (the anharmonicity Δ) is small compared with the energy spacings.

Our experiments are performed with pulses of light that have a finite duration, and well-defined polarization and wave vectors. To account for these characteristics, the electric field is expressed:

$$\mathbf{E}(t) = \tilde{E}_J(\mathbf{k}_\chi, t_\chi, t) + c.c. \quad (5-3)$$

$$\tilde{E}_J(\mathbf{k}_\chi, t_\chi, t) = \frac{1}{2} \hat{\mathbf{J}} \tilde{e}(t - t_\chi) \exp\left[i(\mathbf{k}_\chi \cdot \mathbf{r} - \omega_\chi(t - t_\chi))\right] \quad (5-4)$$

where the χ^{th} pulse is polarized in the $\hat{\mathbf{J}}$ direction and propagates with wave vector \mathbf{k}_χ and frequency ω_χ . The envelope function $\tilde{e}(t - t_\chi)$ can incorporate idealized or experimentally measured amplitude and phase (i.e. chirp) variations.⁵⁵

Vibrational echo experiments detect the signal radiated in the phase-matched direction:

$$\mathbf{k}_{sig} = -\mathbf{k}_\alpha + \mathbf{k}_\beta + \mathbf{k}_\gamma \quad (5-5)$$

where \mathbf{k}_α , \mathbf{k}_β , and \mathbf{k}_γ are the wave vectors of the incident pulses. We assume the input pulses are resonant with the vibrational transition, and therefore apply the rotating wave approximation (RWA) by retaining only those terms in the response function whose phase

modulations approximately cancel the phase modulations in the electric field terms.⁴⁶ The RWA not only reduces the total number of terms in the calculation, but also increases the minimum size of the time steps required for numerical evaluation of the convolution integrals by eliminating quickly oscillating terms. Feynman diagrams representing the evolution of the density matrix for terms that survive the RWA are plotted in Fig 3-3. Note that the order in which pulses with positive and negative wave vector components interact with the sample determines the specific terms that contribute to the response function. The polarization resulting from the RWA, written in terms of pulse-labeled interaction times to simplify the notation (see Fig. 3-2 and caption) is:

$$P_{IJKL}^{(3)}(\mathbf{k}_{sig}, t_\beta, t_\alpha; t) = \int_0^\infty d\tau_\gamma \int_0^\infty d\tau_\beta \int_0^\infty d\tau_\alpha \tilde{R}_{vib}(\mathbf{k}_{sig}, \tau_\gamma, \tau_\beta, \tau_\alpha) Y_{IJKL'}(\tau_\gamma, \tau_\beta, \tau_\alpha) \tilde{E}_J(\mathbf{k}_\gamma, t_\gamma \equiv 0; t - \tau_\gamma) \tilde{E}_K(\mathbf{k}_\beta, t_\beta; t - \tau_\beta) \tilde{E}_L(\mathbf{k}_\alpha, t_\alpha; t - \tau_\alpha) + c.c. \quad (5-6)$$

The subscripts I, J, K, L (and their primed counterparts) are indices for unit vectors in the laboratory frame, while α, β and γ label the incident pulses. In Eq. (5-6), we have decomposed the response function into a product of vibrational \tilde{R}_{vib} and orientational Y_{IJKL} contributions. This separation is exact when the total liquid Hamiltonian is factorable into vibrational and rotational terms (with no cross terms between the two).⁵⁶ The form of the response function depends on the pulse interaction order:

$$\tilde{R}_{vib}(\mathbf{k}_{sig}, \tau_\gamma, \tau_\beta, \tau_\alpha) \times Y_{IJKL'}(\tau_\gamma, \tau_\beta, \tau_\alpha) \left\{ \begin{array}{l} \tilde{R}_{vib}^I(\mathbf{k}_{sig}, \tau_\gamma, \tau_\beta - \tau_\gamma, \tau_\alpha - \tau_\beta) Y_{IJKL}(\tau_\gamma, \tau_\beta - \tau_\gamma, \tau_\alpha - \tau_\beta) \quad \tau_\alpha > \tau_\beta \geq \tau_\gamma \\ \tilde{R}_{vib}^I(\mathbf{k}_{sig}, \tau_\beta, \tau_\gamma - \tau_\beta, \tau_\alpha - \tau_\gamma) Y_{IKJL}(\tau_\beta, \tau_\gamma - \tau_\beta, \tau_\alpha - \tau_\gamma) \quad \tau_\alpha \geq \tau_\gamma > \tau_\beta \\ \tilde{R}_{vib}^{II}(\mathbf{k}_{sig}, \tau_\gamma, \tau_\alpha - \tau_\gamma, \tau_\beta - \tau_\alpha) Y_{IJKL}(\tau_\gamma, \tau_\alpha - \tau_\gamma, \tau_\beta - \tau_\alpha) \quad \tau_\beta \geq \tau_\alpha \geq \tau_\gamma \\ \tilde{R}_{vib}^{II}(\mathbf{k}_{sig}, \tau_\beta, \tau_\alpha - \tau_\beta, \tau_\gamma - \tau_\alpha) Y_{IKLJ}(\tau_\beta, \tau_\alpha - \tau_\beta, \tau_\gamma - \tau_\alpha) \quad \tau_\gamma > \tau_\alpha \geq \tau_\beta \\ \tilde{R}_{vib}^{III}(\mathbf{k}_{sig}, \tau_\alpha, \tau_\gamma - \tau_\alpha, \tau_\beta - \tau_\gamma) Y_{ILJK}(\tau_\alpha, \tau_\gamma - \tau_\alpha, \tau_\beta - \tau_\gamma) \quad \tau_\beta > \tau_\gamma > \tau_\alpha \\ \tilde{R}_{vib}^{III}(\mathbf{k}_{sig}, \tau_\alpha, \tau_\beta - \tau_\alpha, \tau_\gamma - \tau_\beta) Y_{ILKJ}(\tau_\alpha, \tau_\beta - \tau_\alpha, \tau_\gamma - \tau_\beta) \quad \tau_\gamma \geq \tau_\beta > \tau_\alpha \end{array} \right. \quad (5-7)$$

The orientational response function tensor takes into account the effect of molecular reorientation on the nonlinear signal by sequentially projecting the electric field polarizations in the laboratory coordinates onto the distribution of molecular coordinates at the time of each field-matter interaction. For an isotropic medium, it has only four nonvanishing components Y_{ZZZZ} , Y_{ZZYY} , Y_{ZYYZ} and Y_{ZYZY} , three of which are independent $Y_{ZZZZ} = Y_{ZZYY} + Y_{ZYYZ} + Y_{ZYZY}$.⁵⁷ Each of these can be written in terms of the rotational correlation functions of the transition dipole unit vectors $\hat{\mu}$, $p_\ell(t) = \langle P_\ell(\hat{\mu}(t) \cdot \hat{\mu}(0)) \rangle$, where P_ℓ is the ℓ th-order Legendre polynomial. For our model, we apply analytical expressions for $Y_{JKL}(t_3, t_2, t_1)$ derived for isotropic orientational diffusion of spherical rotors,^{58,59} with the implicit assumption that all transition moments lie along the same molecular axis. In this limit, the rotational correlation functions take the form:

$$p_\ell(t_n) = \exp[-\ell(\ell+1)D_{or}t_n] \quad (5-8)$$

where D_{or} is an orientational diffusion coefficients (Table 3-1).

The vibrational response functions \tilde{R}_{vib}^I , \tilde{R}_{vib}^{II} and \tilde{R}_{vib}^{III} are the sum of all density matrix pathways that contribute for a given interaction ordering, corresponding to the diagrams in Fig. 3-3:

$$\begin{aligned} \tilde{R}_{vib}^I(\mathbf{k}_{sig}, t_3, t_2, t_1) = & \left(\frac{i}{\hbar}\right)^3 \\ & \left\{ |\mu_{10}|^4 \exp[-i\omega_{10}t_3 + i\omega_{10}t_1] [F_{0101}^{(3)}(t_3, t_2, t_1) + F_{0101}^{(4)}(t_3, t_2, t_1)] \right. \\ & \left. - |\mu_{10}|^2 |\mu_{21}|^2 \exp[-i\omega_{21}t_3 + i\omega_{10}t_1] [F_{0121}^{(2)}(t_3, t_2, t_1)]^* \right\} \quad (5-9) \end{aligned}$$

$$\begin{aligned} \tilde{R}_{vib}^{II}(\mathbf{k}_{sig}, t_3, t_2, t_1) &= \left(\frac{i}{\hbar}\right)^3 \\ &\left\{ |\mu_{10}|^4 \exp(-i\omega_{10}t_3 - i\omega_{10}t_1) [F_{0101}^{(1)}(t_3, t_2, t_1) + F_{0101}^{(2)}(t_3, t_2, t_1)] \right. \\ &\left. - |\mu_{10}|^2 |\mu_{21}|^2 \exp(-i\omega_{21}t_3 - i\omega_{10}t_1) [F_{0121}^{(4)}(t_3, t_2, t_1)]^* \right\} \end{aligned} \quad (5-10)$$

$$\begin{aligned} \tilde{R}_{vib}^{III}(\mathbf{k}_{sig}, t_3, t_2, t_1) &= \left(\frac{i}{\hbar}\right)^3 |\mu_{10}|^2 |\mu_{21}|^2 \\ &\left\{ \exp(-i\omega_{10}t_3 - i\omega_{20}t_2 - i\omega_{10}t_1) [F_{0121}^{(1)}(t_3, t_2, t_1)] \right. \\ &\left. - \exp(-i\omega_{21}t_3 - i\omega_{20}t_2 - i\omega_{10}t_1) [F_{0121}^{(3)}(t_3, t_2, t_1)]^* \right\} \end{aligned} \quad (5-11)$$

They depend on the time-averaged energy differences (scaled by \hbar) ω_{ba} and transition dipoles μ_{ab} between eigenstates, as well as the nonlinear dephasing functions $F_{abcd}^{(n)}$ ($a, b, c, d \in 0, 1, 2, \dots$). We have assumed that the energy spacing is sufficiently large that the system is initially in the ground state at room temperature, and have neglected direct $|2\rangle \leftarrow |0\rangle$ transitions. Sung and Silbey derived analytical expressions for the dephasing functions in terms of the frequency correlation functions:

$$C_{pq}(\tau - \tau') = \left\langle \delta\omega_{p0}(\tau) \delta\omega_{q0}(\tau') \right\rangle_B \quad (5-12)$$

where $\delta\omega_{a0}(t)$ is the difference between $\omega_{a0}(t)$ and its time averaged value. For the three-level anharmonic oscillator considered here, they are:

$$\begin{aligned} -\ln F_{0101}^{(1)}(t_3, t_2, t_1) &= h_{11}(t_1) + h_{11}(t_2) + h_{11}(t_3) - h_{11}(t_1 + t_2) - h_{11}(t_2 + t_3) \\ &\quad + h_{11}(t_1 + t_2 + t_3) \end{aligned} \quad (5-13)$$

$$\begin{aligned} -\ln F_{0101}^{(2)}(t_3, t_2, t_1) &= h_{11}(t_1) + h_{11}^*(t_2) + h_{11}^*(t_3) - h_{11}(t_1 + t_2) - h_{11}^*(t_2 + t_3) \\ &\quad + h_{11}(t_1 + t_2 + t_3) \end{aligned} \quad (5-14)$$

$$-\ln \left[F_{0101}^{(3)}(t_3, t_2, t_1) \right]^* = h_{11}(t_1) - h_{11}(t_2) + h_{11}^*(t_3) + h_{11}(t_1 + t_2) + h_{11}(t_2 + t_3) - h_{11}(t_1 + t_2 + t_3) \quad (5-15)$$

$$-\ln \left[F_{0101}^{(4)}(t_3, t_2, t_1) \right]^* = h_{11}(t_1) - h_{11}^*(t_2) + h_{11}(t_3) + h_{11}(t_1 + t_2) + h_{11}^*(t_2 + t_3) - h_{11}(t_1 + t_2 + t_3) \quad (5-16)$$

$$-\ln F_{0121}^{(1)}(t_3, t_2, t_1) = h_{11}(t_1) - h_{21}(t_1) + h_{11}(t_2) - h_{12}(t_2) - h_{21}(t_2) + h_{22}(t_2) + h_{11}(t_3) - h_{12}(t_3) - h_{11}(t_1 + t_2) + h_{21}(t_1 + t_2) - h_{11}(t_2 + t_3) + h_{12}(t_2 + t_3) + h_{11}(t_1 + t_2 + t_3) \quad (5-17)$$

$$-\ln F_{0121}^{(2)}(t_3, t_2, t_1) = h_{11}(t_1) + h_{11}^*(t_2) - h_{12}^*(t_2) + h_{11}^*(t_3) - h_{12}^*(t_3) - h_{21}^*(t_3) + h_{22}^*(t_3) - h_{11}(t_1 + t_2) + h_{21}(t_1 + t_2) - h_{11}^*(t_2 + t_3) + h_{12}^*(t_2 + t_3) + h_{11}(t_1 + t_2 + t_3) - h_{21}(t_1 + t_2 + t_3) \quad (5-18)$$

$$-\ln \left[F_{0121}^{(3)}(t_3, t_2, t_1) \right]^* = h_{11}(t_1) - h_{21}(t_1) - h_{11}(t_2) + h_{12}(t_2) + h_{11}^*(t_3) - h_{12}^*(t_3) + h_{11}(t_1 + t_2) + h_{11}(t_2 + t_3) - h_{12}(t_2 + t_3) - h_{21}(t_2 + t_3) + h_{22}(t_2 + t_3) - h_{11}(t_1 + t_2 + t_3) + h_{21}(t_1 + t_2 + t_3) \quad (5-19)$$

$$-\ln \left[F_{0121}^{(4)}(t_3, t_2, t_1) \right]^* = h_{11}(t_1) - h_{11}^*(t_2) + h_{12}^*(t_2) + h_{11}(t_3) - h_{12}(t_3) - h_{21}(t_3) + h_{22}(t_3) + h_{11}(t_1 + t_2) - h_{21}(t_1 + t_2) + h_{11}^*(t_2 + t_3) - h_{12}^*(t_2 + t_3) - h_{11}(t_1 + t_2 + t_3) + h_{21}(t_1 + t_2 + t_3). \quad (5-20)$$

where

$$h_{pq}(t) = \int_0^t d\tau_2 \int_0^{\tau_2} d\tau_1 C_{pq}(\tau_2 - \tau_1). \quad (5-21)$$

The pathways that contribute to \tilde{R}_{vib}^I can oscillate with frequencies during the third time period (t_3) that are conjugate or nearly conjugate to those during the first time period (t_1), allowing the system to rephase, while pathways that contribute to \tilde{R}_{vib}^{II} and \tilde{R}_{vib}^{III} can not rephase because they oscillate with the same frequency during both time periods.⁶⁰

However, the rephasing character of the density matrix for \tilde{R}_{vib}^I relies on the frequency correlation during t_1 and t_3 , which is diminished and eventually lost as the time between the second and third interactions t_2 is increased. This memory loss is the basis for the vibrational 3PEPS experiments discussed below.

The vibrational response functions for an anharmonic oscillator differ from the well-known nonlinear response functions for electronic spectroscopy because they include terms that depend on the overtone transition ($F_{0121}^{(n)}$). The existence of \tilde{R}_{vib}^{III} is unique to a multilevel system, where it is possible to have a coherence between the $|0\rangle$ and $|2\rangle$ eigenstates during t_2 . These pathways only contribute to the experiments simulated here when the pulses overlap. The presence of an overtone transition also introduces oscillations in the FWM signal during t_3 that are characteristic of the anharmonic energy splitting. As expected, the nonlinear response for a classical harmonic system in this model is identically zero due to scaling relations between the energy fluctuations ($C_{22}(t) = 2C_{21}(t) = 2C_{12}(t) = 4C_{11}(t) \equiv 4C(t)$) and matrix elements ($\mu_{10} = \sqrt{2}\mu_{21}$) of the eigenstates.⁶¹ However, we assume these relationships remain valid for our weakly anharmonic system.

The response function in Eq. (5-6) accounts for the influence of vibrational dephasing and molecular reorientation on the FWM signal, but neglects vibrational energy relaxation. To account for population relaxation, we introduce a phenomenological model based on results for a multilevel Markovian system, in which population relaxation occurs with an exponential relaxation rate Γ_{ab} .^{62,63} For a harmonic system, Γ_{aa} scales with the quantum

number and $\Gamma_{ab} = \frac{1}{2}(\Gamma_{aa} + \Gamma_{bb})$, so that all energy relaxation can be described by a single quantity $T_1 = (\Gamma_{11})^{-1}$.⁶¹

In the conventional picture, vibrational relaxation of a set of molecules that have been excited by a laser pulse results in the repopulation of the equilibrium ground state, treating the solvent as a heat bath that absorbs the relatively small amount of excess energy without change. (Experimentally, the sample is circulated to avoid heating effects due to repeated pulses.) However, recent experiments suggest that the excited molecules relax on the time scale of T_1 to a state that is spectroscopically distinct from the equilibrium ground state, probably due to a non-thermal population of low-frequency vibrational states in the local bath molecules.^{39,64} Some have referred to this as a hot ground state (HGS) because it leads to a small temperature change in the bath once the excess energy has diffused. To account for the effect of the HGS on our nonlinear signal, we take an approach similar to Stenger and co-workers by including an additional term in each of \tilde{R}'_{vib} and \tilde{R}''_{vib} that accounts for the additional absorption from the HGS during t_3 (Fig. 5-2).³⁹ These terms increase during t_2 as molecules undergo vibrational relaxation. The HGS model accounts for changes in the average energy spacing ($\Delta\omega$) and transition dipole ($\Delta\mu$) as compared with the equilibrium ground state, but assumes the dynamics that drive dephasing are unchanged.

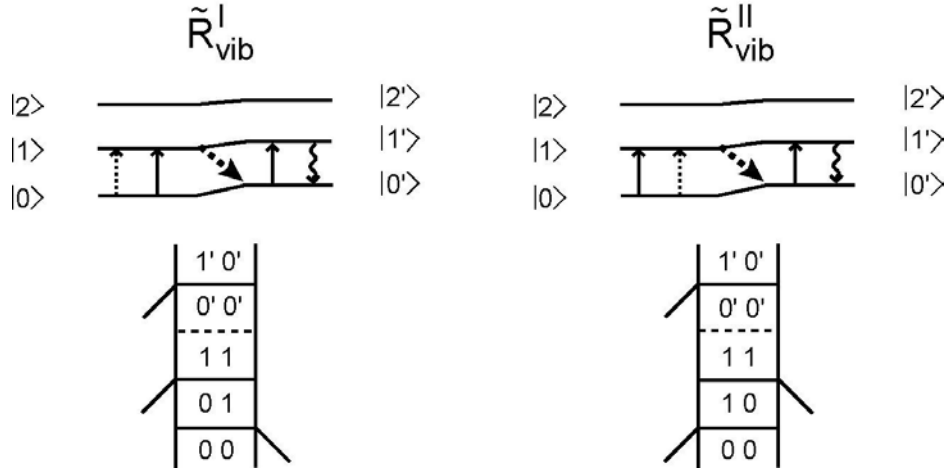


Figure 5-2. Feynman and associated ladder diagrams that represent the evolution of the density matrix for additional terms in the response function that account for the HGS. The dashed horizontal lines in the Feynman diagrams and thick arrows in the ladder diagrams indicate population relaxation during the second time period.

The final expressions for the vibrational contribution to the response function, including the harmonic approximations, population relaxation and the HGS are:

$$\begin{aligned}
 \tilde{R}_{vib}^I(\mathbf{k}_{sig}, t_3, t_2, t_1) &= \left(\frac{i}{\hbar}\right)^3 \exp\left[-i\omega_{10}(t_3 - t_1)\right] \\
 &\left\{ \exp\left[-\frac{t_3}{2T_1} - \frac{t_1}{2T_1}\right] F_{0101}^{(3)}(t_3, t_2, t_1) + \exp\left[-\frac{t_3}{2T_1} - \frac{t_2}{T_1} - \frac{t_1}{2T_1}\right] F_{0101}^{(4)}(t_3, t_2, t_1) - \right. \\
 &2 \exp\left[-\frac{t_3}{2T_1/3} - \frac{t_2}{T_1} - \frac{t_1}{2T_1}\right] \exp\left[-i(\omega_{21} - \omega_{10})t_3\right] \left[F_{0121}^{(2)}(t_3, t_2, t_1)\right]^* - \\
 &\left. |1 - \Delta\mu|^2 \exp\left[-i(\Delta\omega)t_3\right] \exp\left[-\frac{t_3}{2T_1} - \frac{t_1}{2T_1}\right] \left(1 - \exp\left[-\frac{t_2}{T_1}\right]\right) F_{0101}^{(3)}(t_3, t_2, t_1) \right\} \quad (5-22)
 \end{aligned}$$

$$\begin{aligned}
\tilde{R}_{vib}^{II}(\mathbf{k}_{sig}, t_3, t_2, t_1) &= \left(\frac{i}{\hbar}\right)^3 \exp\left[-i\omega_{10}(t_3+t_1)\right] \\
&\left\{ \exp\left[-\frac{t_3}{2T_1} - \frac{t_1}{2T_1}\right] F_{0101}^{(1)}(t_3, t_2, t_1) + \exp\left[-\frac{t_3}{2T_1} - \frac{t_2}{T_1} - \frac{t_1}{2T_1}\right] F_{0101}^{(2)}(t_3, t_2, t_1) - \right. \\
&2 \exp\left[-\frac{t_3}{2T_1/3} - \frac{t_2}{T_1} - \frac{t_1}{2T_1}\right] \exp\left[-i(\omega_{21} - \omega_{10})t_3\right] \left[F_{0121}^{(4)}(t_3, t_2, t_1)\right]^* - \\
&\left. |1-\Delta\mu|^2 \exp\left[-i(\Delta\omega)t_3\right] \exp\left[-\frac{t_3}{2T_1} - \frac{t_1}{2T_1}\right] \left(1 - \exp\left[-\frac{t_2}{T_1}\right] F_{0101}^{(1)}(t_3, t_2, t_1)\right) \right\} \quad (5-23)
\end{aligned}$$

$$\begin{aligned}
\tilde{R}_{vib/pop}^{III}(\mathbf{k}_{sig}, t_3, t_2, t_1) &= \left(\frac{i}{\hbar}\right)^3 \exp\left(-i\omega_{10}(t_3+t_1) - i\omega_{20}t_2\right) \\
&\left\{ 2 \exp\left[-\frac{t_3}{2T_1} - \frac{t_2}{T_1/2} - \frac{t_1}{2T_1}\right] \left[F_{0121}^{(1)}(t_3, t_2, t_1)\right] - \right. \\
&2 \exp\left[-\frac{t_3}{2T_1/3} - \frac{t_2}{T_1/2} - \frac{t_1}{2T_1}\right] \exp\left[-i(\omega_{21} - \omega_{10})t_3\right] \left[F_{0121}^{(3)}(t_3, t_2, t_1)\right]^* \left. \right\} \quad (5-24)
\end{aligned}$$

Substitution of these expressions, along with the orientational correlation functions into Eq. (5-6) yields the final expression for the nonlinear polarization. This polarization then acts as a source to emit electromagnetic radiation into the phase-matched direction, which is detected in the experiments. Maxwell's equations dictate that the radiated field is:⁶⁵

$$\mathbf{E}_{rad}(\mathbf{k}_{sig}, t_\beta, t_\alpha; t) = -\frac{2\pi l}{nc} \frac{\partial \mathbf{P}^{(3)}(\mathbf{k}_{sig}, t_\beta, t_\alpha; t)}{\partial t} \quad (5-25)$$

where l is the sample length, n is the refractive index and c is the speed of light in vacuum.

5.2.2 FWM experiments

A theoretical description of the 3PEPS and PP measurements has been given for optical and vibrational systems,^{45,48,49,66,67} so only the important details will be summarized

here. The 3PEPS experiment is performed with three non-collinear IR input pulses that have well defined pulse separations τ_1 and τ_2 , defined in Fig 3-2. An IR detector collects the radiation emitted into the phase-matched direction (e.g. Eq. (5-5)) as a function of the pulse delays. Because the detector is slow relative to the timescale of the pulses and system dynamics, it integrates the homodyne signal:

$$\mathbf{S}_{IE}(\mathbf{k}_{sig}, t_\beta, t_\alpha) \propto \int_{-\infty}^{\infty} \left| \mathbf{E}_{rad}(\mathbf{k}_{sig}, t_\beta, t_\alpha; t) \right|^2 dt. \quad (5-26)$$

When wave vectors of the incident pulses are ordered $(-, +, +)$ and the second delay period τ_2 is sufficiently short, a large portion of the response is due to the rephasing pathways in \tilde{R}'_{vib} , resulting in the formation of a vibrational echo. As a result, the maximum of the integrated signal occurs at nonzero values of τ_1 , which is called the peak shift and denoted τ_1^* . Numerous calculations have indicated that the peak shift, measured as a function of τ_2 , is sensitive to the details of the frequency correlation function,^{49,66} and therefore provides the most unambiguous experimental determination of the correlation function.

The PP experiment measures pump-induced changes in the transmission of a narrow distribution of frequency components within a probe beam as a function of pulse delay, τ . The signal is calculated within the framework of a FWM experiment in which two interactions are derived from the pump beam and one from the probe beam. The probe beam serves as a phase-locked local oscillator (LO) because the radiated field propagates in the same direction as the probe. They are dispersed by a bandpass filter before detection, resulting in the heterodyne-detected signal:

$$\mathbf{S}_{PP}(\mathbf{k}_{sig}, \tau) \propto \int_{-\infty}^{\infty} d\omega F(\omega) \times \text{Re} \left[\int_{-\infty}^{\infty} dt_{LO} e^{-i\omega t_{LO}} \int_{-\infty}^{\infty} dt \mathbf{E}_{rad}(\mathbf{k}_{sig}, t_\beta = \tau, t_\alpha = \tau; t) \mathbf{E}_{LO}(\mathbf{k}_{sig}, t_{LO}; t) \right] \quad (5-27)$$

where $F(\omega)$ is the bandpass filter spectrum. For the most part, the present work focuses on the time and polarization dependence of the PP signal for a fixed detection frequency, which primarily measures molecular reorientation and population relaxation.

5.2.3 Numerical Calculations

Nonlinear signals were calculated in C++ on a AMD Athlon-based 1.6 GHz PC running Mandrake Linux. The algorithm to calculate the vibrational FWM signals was written in-house, although several decisions were guided by referencing code provided by Jonas,^{68,69} including the use of Numerical Recipes' Gauss-Legendre quadrature routine GAULEG for the convolution integrals.⁷⁰ Calculations used either transform-limited Gaussian pulse envelopes, or envelopes extracted from experimental FROG measurements, as noted in the text (see Experiment section). To calculate the polarization, we imposed finite limits on the integrals, chosen to exclude less than 1% of the integrated field amplitude. Between 6 and 10 quadrature points were used to evaluate each integral. We used a frequency correlation function comprised of two overdamped and two underdamped Brownian oscillators (see Chapter 3), since the inclusion of more terms did not improve comparison to the data. As noted, some calculations used only the real part of the correlation function, while others included the analytical forms of the imaginary components. To extract the correlation function from the experimental 3PEPS data, we compared 3PEPS signal calculated from a trial correlation function to the experimental result and then repeatedly adjust the relative amplitudes and timescales of the Brownian oscillators to improve the fit. An iterative minimization algorithm based on the downhill simplex method in multiple dimensions (Numerical Recipe routine AMOEBA⁷⁰) was employed until convergence was

achieved to within 0.001%. We restarted the minimization from the convergence point multiple times to avoid settling into a local minimum. In this process, the frequency and damping time of the highest-frequency component were fixed, but otherwise the amplitudes, damping times and frequencies of all other components were floated. The 3PEPS decay is relatively insensitive to the overall amplitude of the correlation function, so this amplitude was determined by constraining the absorption spectrum calculated from the correlation function to the width of the FTIR spectrum, which is calculated as:⁴⁶

$$I_{FTIR}(\omega) \propto \text{Re} \left[\int_0^{\infty} dt \exp(i(\omega - \omega_{10})t - h_{11}(t)) \cdot p_1(t) \cdot \exp\left(-\frac{t}{2T_1}\right) \right]. \quad (5-28)$$

5.3 Experiments

A home-built optical parametric amplifier (OPA) pumped by a commercial Ti:sapphire laser system (Femtolasers CompactPro) generates the ultrashort mid-IR pulses required for the nonlinear experiments. This near-IR system includes a chirped-mirror oscillator producing 12 fs pulses which seed a multi-pass amplifier that also uses chirped mirrors to aid in pulse compression. The output is comprised of 800 nm, sub-30 fs pulses at a 1 kHz repetition rate, which are attenuated to 400 μJ to pump the OPA. We employ a white-light seeded two-stage OPA design to produce the 3 μm pulses. In this scheme, the initial 1.1 μm seed is derived from the continuum generated by focusing a small amount (~ 1 μJ) of the pump pulse into a [0001]-cut, 1.5 mm thick sapphire disc (Meller Optics). This seed is parametrically amplified in the first stage with its corresponding 3 μm idler pulse in a 1 mm β -barium borate (BBO) crystal (Casix) oriented for type-I phase matching and pumped

by ~37% of the input 800 nm pulses. Because much of the 3 μm pulse is absorbed by BBO, we discard the remaining idler and feed the strong signal beam, along with the remaining pump pulse, into the second stage. A 1 mm potassium niobate (KNB) crystal (Spectragen) was chosen for the power amplification of the 3 μm pulses because its nonlinear coefficient is large, allowing for a short crystal length, and because its steep phase-matching curve results in a large acceptance bandwidth.⁷¹⁻⁷⁷ The OPA typically produces 3-4 μJ pulse energies in the 3 μm wavelength range, which is sufficient to perform third-order nonlinear experiments on vibrational systems. We characterize the mid-IR pulses in frequency by recording their spectrum (Fig. 4-8), and in time by measuring either a second-order background-free autocorrelation or a frequency-resolved optically gating (FROG),⁷⁸ as discussed below.

The IR beam is expanded in a 2.5:1 Galilean telescope using CaF_2 lenses spaced to collimate the beam to a 8 mm diameter, which allows propagation for several meters without significant divergence. To simplify subsequent alignment, the IR beam is overlapped with a mode-matched He-Ne beam using a 2 mm thick Ge window BBAR coated for mid-IR (Janos). The Ge window also aids in IR pulse compression, which is achieved by adjusting the total amount of group velocity dispersion (GVD) imparted by the materials in the beam path to minimize the pulse duration at the sample.⁷⁹ The main sources of negative GVD for the 3 μm pulse, the 1 mm KNB crystal and approximately 15 mm of CaF_2 (lenses, beamsplitters, compensation plates and polarizers) are approximately balanced by the 2 mm Ge window. Additional negative (positive) dispersion can be introduced by a 3mm thick ZnSe (3 mm thick CaF_2) window placed normal to the beam, to compensate for the small day-to-day compression changes due to alignment of the amplifier or OPA.

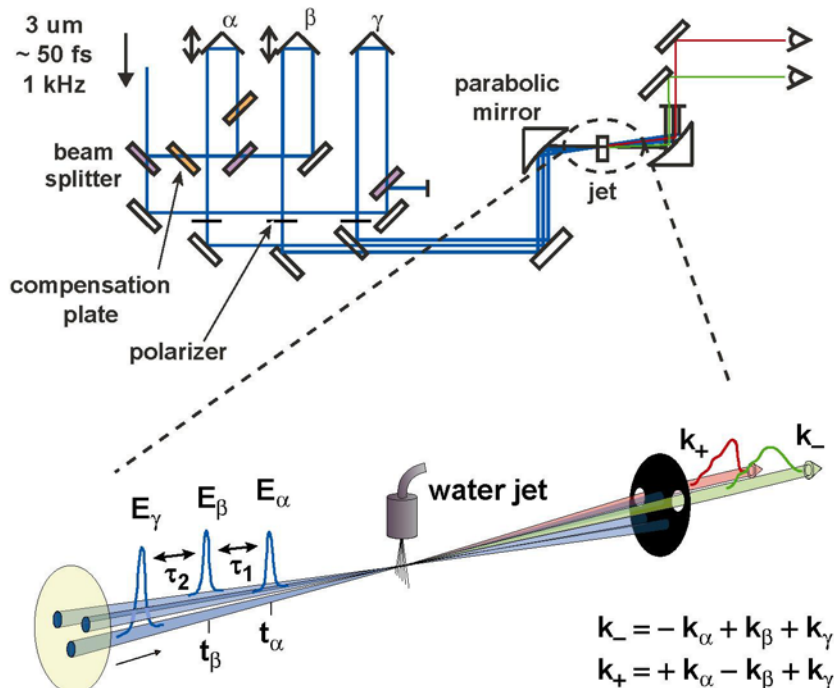


Figure 5-3. (Color) Experimental layout of the IR interferometer for the 3PEPS experiment. The inset details the excitation and detection beam geometry.

Each pulse is split into five replicas of itself in a modified Mach-Zender interferometer similar to those described previously, although only three of the replicas are used for the experiments presented in this Chapter. This interferometer employs custom 3 μm 50/50 CaF_2 beamsplitters that are designed to minimize the GVD of the transmitted and reflected beams (Thin Film Lab). Each arm contains the appropriate number of CaF_2 compensation plates to balance the total amount of material traversed by the beam and a 3 mm thick CaF_2 wire grid polarizer (Optometrics) to control the polarization. Retroreflectors mounted on computer controlled translation stages (Aerotech ANT25-L) vary the relative delay between pulses derived from each arm. Parallel beams arranged in the appropriate geometry (discussed below) exit the interferometer and are focused into the sample by a 100-

mm focal length, off-axis parabolic mirror (Janos) to a spot size ($2w$) of 100 μm . Relative pulse energies of the three beams at the sample are within 20% of each other.

Either a second-order autocorrelation or FROG characterizes the mid-IR pulse duration, and simultaneously determines the relative timings between pulses. Both are measured in a background free geometry, by placing a 300 μm thick silver gallium sulfide (AgGaS_2) crystal, cut for type I phase matching ($\theta = 37.4^\circ$, $\phi = 45^\circ$) at the sample position. The autocorrelation signal is either detected directly by an InGaAs photodiode (ThorLabs) or directed into a monochromator to record the FROG. The same monochromator is used to measure the pulse spectrum and to frequency resolve the autocorrelation. It is a 150 mm focal length, $f/4$ imaging monochromator (Acton, SpectraPro 150) with a 300 groove/mm grating optimized for 2.5 μm (Thermo-RGL, 674-18). The grating has a flat spectral response throughout the 3 μm region, and is also efficient in the 1.5 μm region. All PP measurements were recorded with liquid nitrogen cooled InSb detectors (Infrared Associates).

The experimental set-up for vibrational 3PEPS experiments is similar to those described for the analogous electronic experiments,^{49,66} except optimized for mid-IR radiation. Three of the beams exiting the interferometer are arranged in an equilateral triangle geometry, although the orientation is rotated 90° from that typically presented for visible experiments to minimize the background from light that is scattered preferentially in the horizontal direction by the lathe-turned parabolas. The polarization direction and approximate pulse energies of all three beams are equivalent. Liquid nitrogen cooled InSb detectors record the integrated echo signal simultaneously in the two phase-matched directions $\mathbf{k}_- = -\mathbf{k}_\alpha + \mathbf{k}_\beta + \mathbf{k}_\gamma$ and $\mathbf{k}_+ = +\mathbf{k}_\alpha - \mathbf{k}_\beta + \mathbf{k}_\gamma$, where the subscripts α , β and γ label

the incident beams but do not necessarily indicate the relative time orderings. A mechanical chopper placed in one arm of the interferometer blocks every other pulse, permitting lock-in detection to reduce experimental noise.

The integrated echoes are recorded as a function of the delay between pulses α and β , τ_1 , for fixed values of the waiting time, τ_2 (see Fig 5-4). Because echoes in the \mathbf{k}_+ and \mathbf{k}_- directions are equivalent under exchange of the α and β indices, their time profiles are symmetric about $\tau_1=0$. The peak shift is half of the time period between the two maxima, which reduces the influence of errors on the determination of τ_1^* due to inexact knowledge of pulse timings. We measure a FROG immediately following each 3PEPS dataset, to account for the pulse amplitude and phase characteristics in calculations to extract the correlation function.

To record the PP decay, a mechanical chopper is placed in one of the three beams, which acts as the pump, so that lock-in detection can be used to separate the PP signal from the constant probe background. After the sample, the pump beam is blocked and the remaining two beams both pass through a bandpass filter (Spectragon) centered at 3400 cm^{-1} , with a 50 cm^{-1} full-width at half-maximum (see Fig. 5-12). Liquid nitrogen cooled InSb detectors measure the intensity of each beam, and the laser noise is partially removed from by normalizing the PP signal by the intensity of the third beam, I_R :

$$S_{PP}(\tau) = \ln\left(\frac{I'_{pu}}{I_R}\right) - \ln\left(\frac{I_{pu}}{I_R}\right) \quad (5-29)$$

where I_{pr} (I_{pr}) is the intensity of the probe beam in the presence (absence) of the pump beam. In this notation, an induced absorption is negative and a bleach is positive. As opposed to the 3PEPS measurements, the polarization of the pump and probe are varied independently, and

the probe beam passes through an additional wire-grid polarizer after the sample. Because waveplates are not included in our interferometer, energy balanced PP decays needed to calculate the anisotropy were recorded by rotating the polarizer in the probe arm of the interferometer to 45° with respect to the pump polarization, then rotating the analyzing polarizer to 0° or 90° .³² The relative scaling of the PP signals for different polarization conditions were checked carefully by averaging the $\tau = 0$ signal

The sample, a dilute solution of HOD in D_2O , is flowed continuously as a $50\ \mu\text{m}$ path length jet. The concentration was adjusted to produce a peak optical density (OD) in the range of 0.3-0.4 at the outset of the experiment, and was tested at the end of each dataset to ensure that the change in OD did not exceed 0.05. This concentration range assures that OH oscillators are not close enough to resonantly transfer vibrational energy.⁸⁰ By using a free-flowing jet instead of a sample cell, we avoid any signal contribution from the sample cell walls (see Discussion) and further prevent long term heating effects due to repeated laser shots interacting the same molecules.

5.4 Results

A typical set of autocorrelation, spectrum and FROG for IR pulses centered at $3300\ \text{cm}^{-1}$ is presented in Fig. 4-8.⁸¹ The autocorrelation full width at half maximum is 60 fs and the spectral full width at half maximum is $400\ \text{cm}^{-1}$. The pulse amplitude and phase are extracted from the measured FROG with commercial software (Femtosoft Technologies). For the FROG in Fig 4-8, the error associated with the retrieval was 0.012 on a square 64 element grid. To check the reproducibility of the extracted field, the retrieval was performed numerous times (>10), with random initial guesses for the amplitude and phase. The time

duration of the retrieved field is 45 fs, although values ranged from 43-47 fs for the FROG in Fig. 4-8. Its phase is relatively flat over the main portion of the pulse, indicating that it is nearly transform limited. The retrieved spectral width is 350 cm^{-1} , which is slightly smaller than the experimental spectrum. However, the coherent bandwidth of the pulse is larger than the OH absorption linewidth, ensuring that all dynamical processes can be observed in the spectroscopic measurements. The bandwidth is not enough to span both the fundamental and overtone transitions within the full width at half maximum, however this only results in a spectral filtering of the signal, which is taken into account by the real pulse calculations, and therefore does not affect the results extracted from the measurements.

Typical experimentally measured integrated echoes are plotted in Fig. 5-4 for several waiting times. Peak shift values were determined by fitting both integrated echo profiles with Gaussian functions for times $\tau_1 = \tau_{1,\text{max}} \pm 50 \text{ fs}$, where $\tau_{1,\text{max}}$ is the maximum signal. This procedure reduces the influence of experimental noise and provides a consistent determination of the peak shift for all waiting times. As other studies have noted, the integrated echoes exhibit a slight asymmetry at waiting times less than the pulse duration ($\tau_2 < 50 \text{ fs}$), causing the peak of the signal to deviate slightly from the center of the Gaussian fit.⁸² However, the asymmetry is largely reproduced in the calculation, so a consistent treatment is achieved by fitting the calculated integrated echoes in exactly the same way as the experimental data. The 3PEPS signal resulting from this fit (Fig. 5-4) decays from an initial value of $\tau_1^* = 28 \text{ fs}$ with characteristic timescales of 75 fs and 1.2 ps, but exhibits a weak recurrence that peaks at 150 fs. As we have noticed previously, the amplitudes and timescales of the short time features depend on the pulse characteristics, but the differences

are reproduced by including the experimentally determined pulse characteristics in the numerical calculations.⁴⁵

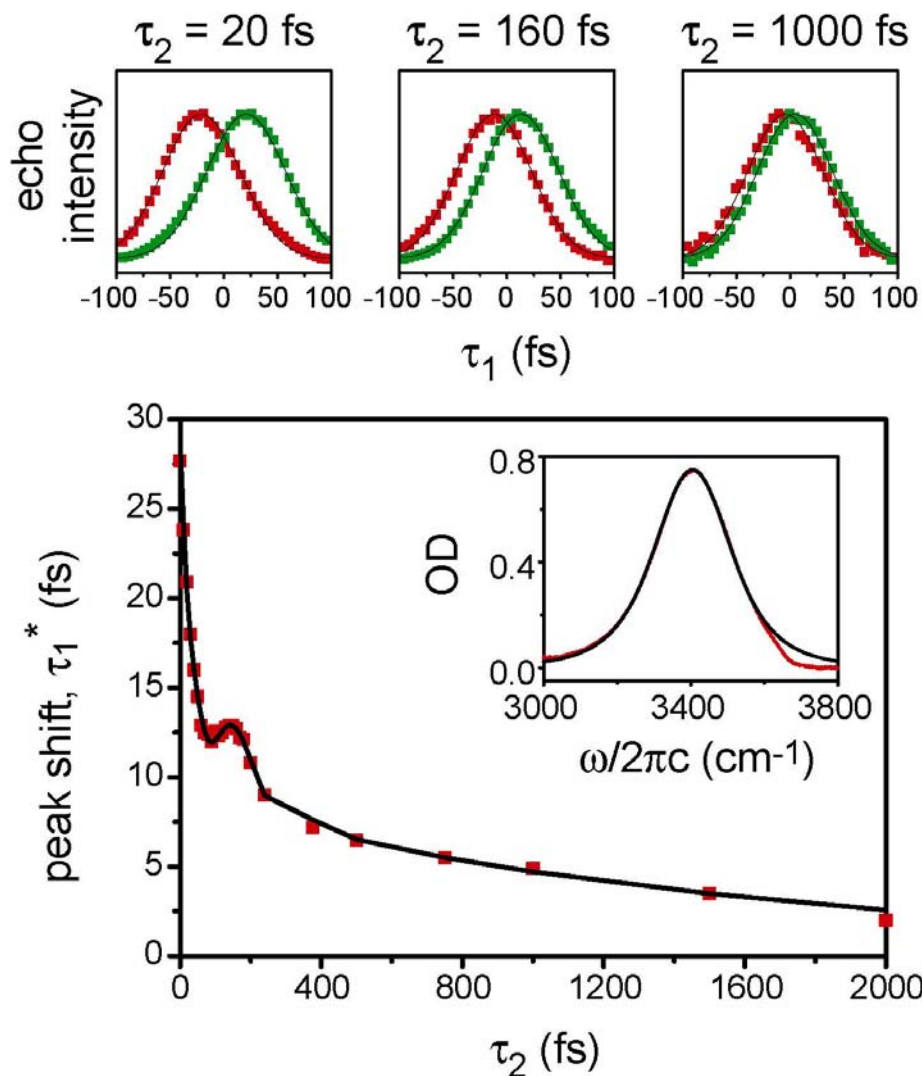


Figure 5-4. (Color) Top: Examples of experimentally measured normalized vibrational echoes of HOD in the \mathbf{k}_+ (red squares) and \mathbf{k}_- (green squares) wave vector geometries for the indicated waiting times. For each τ_2 , the value of τ_1^* is obtained by fitting both echoes with Gaussian functions (black lines) to determine the time interval between peak positions. Bottom: The 3PEPS decay (red squares) is plotted along with the best fit (black line) according to the procedure described in the text. In the inset, the absorption spectrum simulated from the extracted dynamical quantities (black line) is superimposed on the experimental IR absorption spectrum (red line) of HOD in D_2O .

Fig. 5-5 presents the PP signals for experiments in which the polarizer in the pump beam is oriented parallel (0° , S_{ZZZZ}), perpendicular (90° , S_{ZZYY}) or at the magic angle (54.7° , S_{ZZMM}) with respect to the polarizers along the probe beam. All three signals contain non-exponential behavior at short pulse delay times ($\tau_2 > 400$ fs), single- or bi-exponential behavior for intermediate times (400 fs $< \tau_2 < 4$ ps), and a 3.5% offset that remains constant to at least $\tau_2 = 50$ ps. Of these, the intermediate timescale contains the most useful information, namely the dynamics of vibrational population relaxation and molecular reorientation. Differences in the intermediate decay times of the three polarization conditions, highlighted by a semilog plot of the normalized signals (from which the long time offset has been removed by subtraction), are due to the amplitude that molecular reorientations contribute to each. The magic angle signal (MA-PP), which is free from the effects of reorientations,⁵⁹ exhibits a single exponential decay at long times ($\tau_2 > 400$ fs), indicating a OH population lifetime of $T_1=700$ fs.

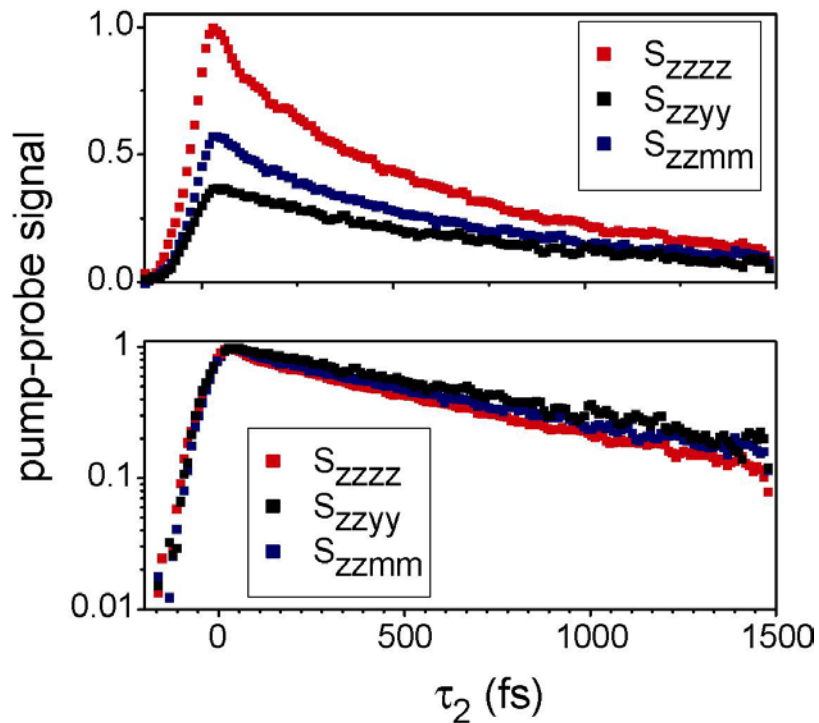


Figure 5-5. (Color) Experimentally measured pump-probe signals in parallel, perpendicular and magic angle geometries. The top panel displays relative intensities as measured in the experiment, while the bottom panel is a semilog plot of the normalized signals to highlight the relative decay rates.⁸³⁸⁴

To determine the effects of reorientations, the time-dependent anisotropy $r(t)$ (Fig. 5-6) was calculated from the parallel and perpendicular experimental signals as:

$$r(\tau_2) = \frac{S_{zzzz}(\tau_2) - S_{zzyy}(\tau_2)}{S_{zzzz}(\tau_2) + 2S_{zzyy}(\tau_2)}. \quad (5-30)$$

Its initial value $r(0)$ is 0.38, approaching the limiting value of 0.4 and indicating that our measurement captures nearly all of the molecular reorientational dynamics. It is fit well by the biexponential function:

$$r(\tau_2) = 0.08 \exp(-\tau_2/60) + 0.32 \exp(-\tau_2/3000), \quad (5-31)$$

where times are given in units of fs.

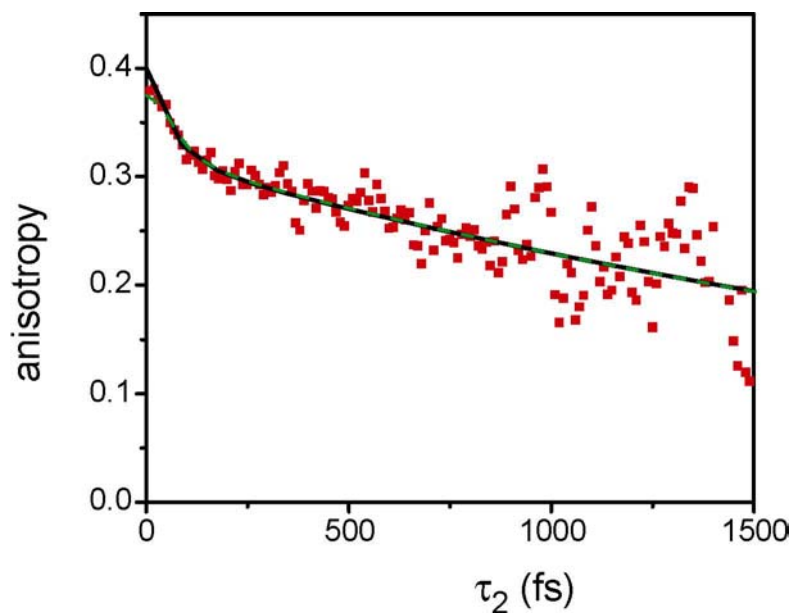


Figure 5-6. (Color) Decay of the anisotropy determined from the parallel and perpendicular pump-probe signals (red squares). The black line is a fit according to Eq. (5-31), and the green dashed line is the anisotropy simulated from the extracted dynamical quantities.

5.5 Self-consistent data modeling

One goal of the present work is to experimentally separate contributions to the OH vibrational spectroscopy, to determine the timescales for pure vibrational dephasing, population relaxation and molecular reorientation. This description lends itself to the clearest interpretation in terms of molecular-level dynamics through a direct comparison with simulation results, and serves as a basis for future investigations of deviations from the simple vibrational dynamics studied here. The formalism developed in Section 5.2 defines the framework for this process by describing the nonlinear spectroscopy with the smallest physically reasonable number of independent parameters. Scaling relations reduce the number of functions describing dynamical quantities to three: the OH frequency correlation

function $C(t)$ measures vibrational dephasing, the second Legendre polynomial of the OH dipole $p_2(t)$ measures molecular reorientation, and the population relaxation time T_1 determines the exponential population relaxation rate. Aside from these, only four static, scalar quantities enter into calculation of the material response functions: the center frequencies of the fundamental ω_{10} and overtone ω_{21} transitions, as well as the frequency shift $\Delta\omega$ and change in transition dipole $\Delta\mu$ of the HGS relative to the fundamental transition. Extraction of the dynamical quantities from the nonlinear experiments is not extremely sensitive to the values of the static quantities, but our effort to model the data self-consistently begins by determining their values.

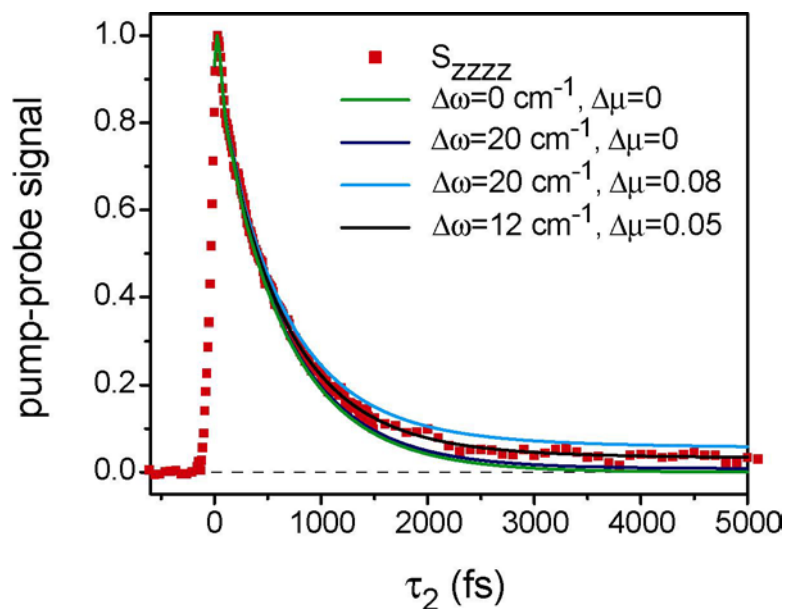


Figure 5-7. (Color) Experimentally measured parallel pump-probe (red squares), which decays to a constant offset of $\sim 3.5\%$ of the maximum value. Solid lines are pump-probes simulated from the extracted dynamical quantities, with HGS parameters as listed.

The frequency of the fundamental transition is determined from the peak of the linear FTIR absorption spectrum of HOD in D_2O (Fig. 5-4), which is $\omega_{10} = 3400 \text{ cm}^{-1}$ at room

temperature.^{11,85} (NOTE: Strictly speaking, the transition frequency differs from the peak of the absorption spectrum for a quantum mechanical correlation function, prompting us to choose a frequency that is slightly below the peak.) We take the frequency of the overtone transition $\omega_{21} = 3150 \text{ cm}^{-1}$ from previous determinations of the anharmonicity.³⁰

To evaluate quantities relating to the HGS, we examine the behavior of the PP signal for pulse delay times that are long compared with the vibrational dynamics, where it exhibits a positive offset as compared to the signal level at when the probe pulse precedes the pump pulse. The absolute magnitude of this offset, approximately 3.5% of the maximum of the parallel signal, is the same for the parallel, crossed and magic angle decays detected with the 3400 cm^{-1} filter. It remains constant for delays at least as long as 50 ps. An offset at long times has been observed in previous pump-probe and transient grating experiments on water, and attributed to changes in the bath due to the energy resulting from vibrational relaxation of the OH stretch (as discussed in Section 5.2). Stenger and co-workers postulated that the effect could be modeled with a HGS transition that is distinct from the equilibrium fundamental transition only in a small frequency shift ($\Delta\omega = 20 \text{ cm}^{-1}$, $\Delta\mu = 0$) to the blue.³⁹ However, our nonlinear signals calculated with these values disagree with the experimental results; the calculated magnitude of the offset in the aforementioned pump probe signal is too small by nearly a factor of 10 (Fig. 5-7), while the 3PEPS signal exhibits an offset that is too large (~ 6 fs, data not shown). The discrepancy results from the dependence of the response functions ((5-22) and (5-23)) on the detection frequency. For sufficiently long t_2 delays, the nonlinear signal reflects the difference in the absorption spectra between the equilibrium and HGS fundamental transitions. Because the frequency at which the PP measurement is detected is near the peak of the equilibrium absorption spectrum, this absorption difference is

small for shifts that are small compared with the linewidth. However, the 3PEPS is sensitive to changes in the entire absorption line due to the broadband nature of the detection.

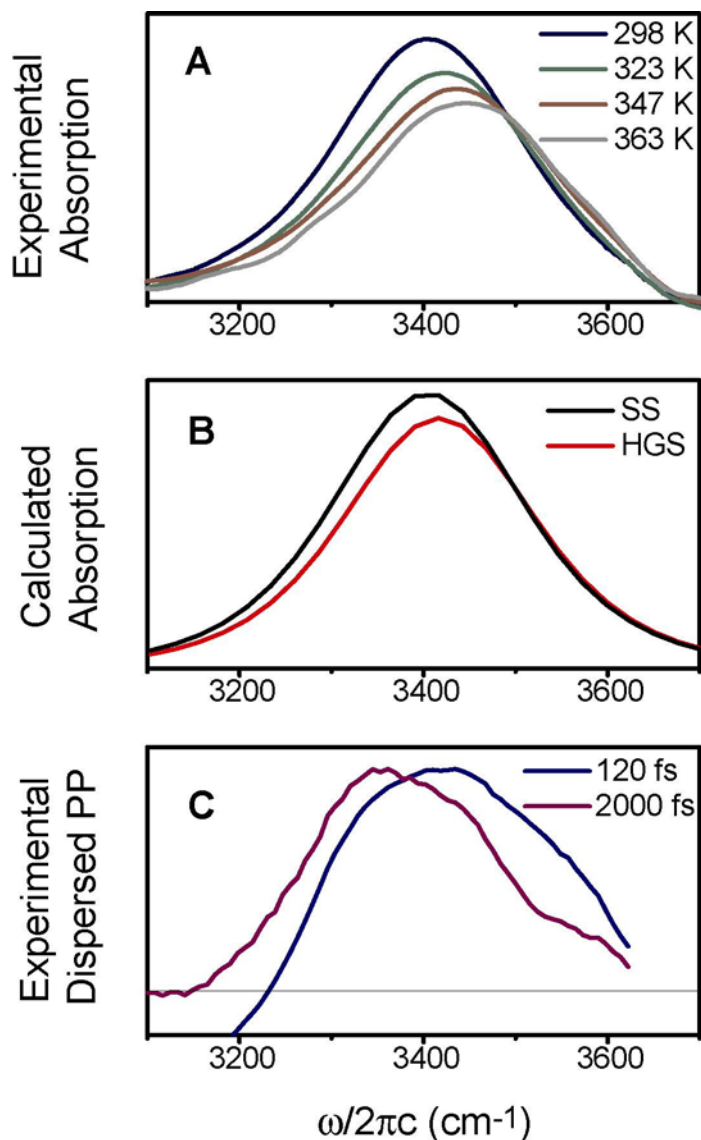


Figure 5-8. (Color) (A) Experimental temperature-dependent FTIR of 1% HOD in D₂O in the OH stretching region. (B) The steady-state (SS) and hot ground state (HGS) absorption spectra simulated from our model with the extracted dynamical quantities. The HGS spectrum is simulated with $\Delta\omega = 12$ cm⁻¹, $\Delta\mu = 0.05$. (C) Experimentally measured dispersed pump-probe spectra for waiting times of $\tau_2 = 120$ fs and 2000 fs.

To model the HGS more carefully, we note that the vibrational energy deposited into the solvent results in a small temperature change after the energy has diffused, and make use

of the temperature dependence of the linear OH absorption spectrum (Fig. 5-8A) to aid in modeling the HGS absorption.⁸⁶ As the temperature is increased, the lineshape shifts to higher frequencies and decreases in intensity without broadening significantly. These changes are due to weakened hydrogen bonds. The spectra loosely justify our assumption that absorption from the HGS can be modeled with frequency and transition dipole changes without significantly affecting dephasing dynamics. The absorption change and frequency shift scale approximately linearly with each other, $\Delta OD \propto 0.0075\Delta\omega$ where frequency is measured in cm^{-1} . We use this empirical relationship, valid for the thermalized system, to constrain the values of $\Delta\mu$ and $\Delta\omega$ for the inherently non-thermalized HGS. The calculated PP signals in Fig. 5-7 demonstrate that the appropriate frequency shift and associated change in dipole to model the experimental data are $\Delta\omega = 12 \text{ cm}^{-1}$, $\Delta\mu = 0.05$. The calculated equilibrium and HGS spectra (using the dynamical quantities discussed below) are plotted in Fig 5-8B. A comparison of the frequency dependence of the PP for short and long pulse delay times (Fig 5-8C) provides experimental evidence supporting the application of the thermalized quantities to model the HGS. The small τ behavior primarily follows the bleach of the (equilibrium) $|1\rangle \leftarrow |0\rangle$ transition (although it is slightly shifted to higher frequencies due to pump-induced $|2\rangle \leftarrow |1\rangle$ absorption), while the large τ spectrum is the difference between the equilibrium and HGS spectra, which is shifted to lower frequencies as expected from Fig. 5-8B.

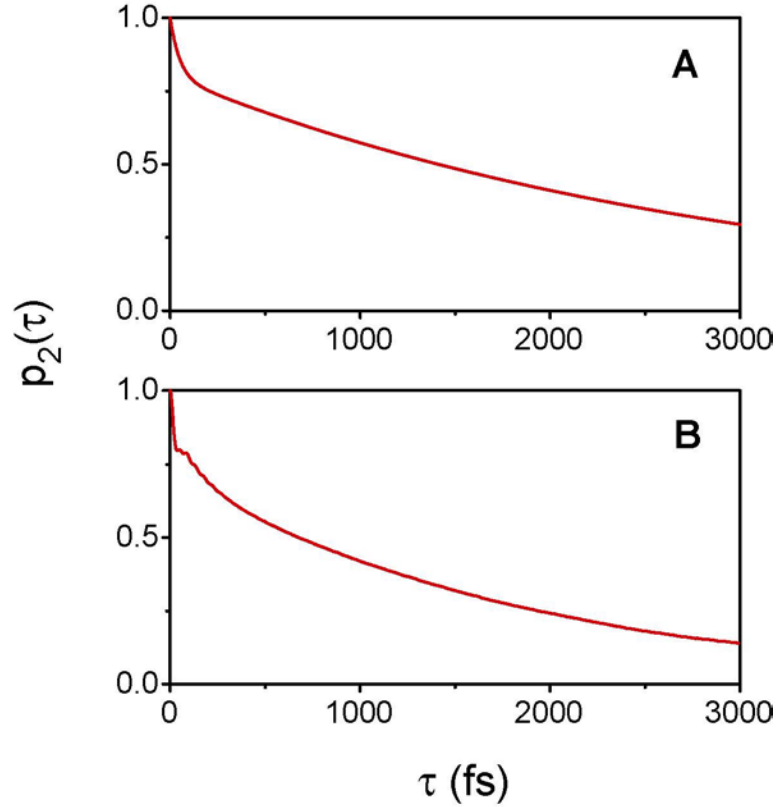


Figure 5-9. (Color) Rotational correlation function extracted from the PP and 3PEPS measurements (A) compared with the rotational correlation function from the computer simulation of Eaves and Geissler (B).

Extraction of the dynamical quantities proceeded by fixing the values of the scalar, static quantities described above and then iteratively fitting the experimental 3PEPS, MA-PP and anisotropy decays to self-consistently determine $C(t)$, T_1 and $p_2(t)$ respectively. Few iterations were needed, since the MA-PP is a good measure of T_1 for intermediate decay times and the anisotropy is only sensitive to $p_2(t)$ for all times (aside from pulse overlap effects at very short times). The most challenging aspect of this scheme was the extraction of $C(t)$ from the 3PEPS decay, for which we used a more rigorous iterative procedure (described in Section 5.2) based on a downhill simplex minimization method. The initial

timescales and relative amplitudes for the Brownian oscillators in $C(t)$ were chosen to match those in the peak shift, while those for $p_2(t)$ were taken from $r(t)$.

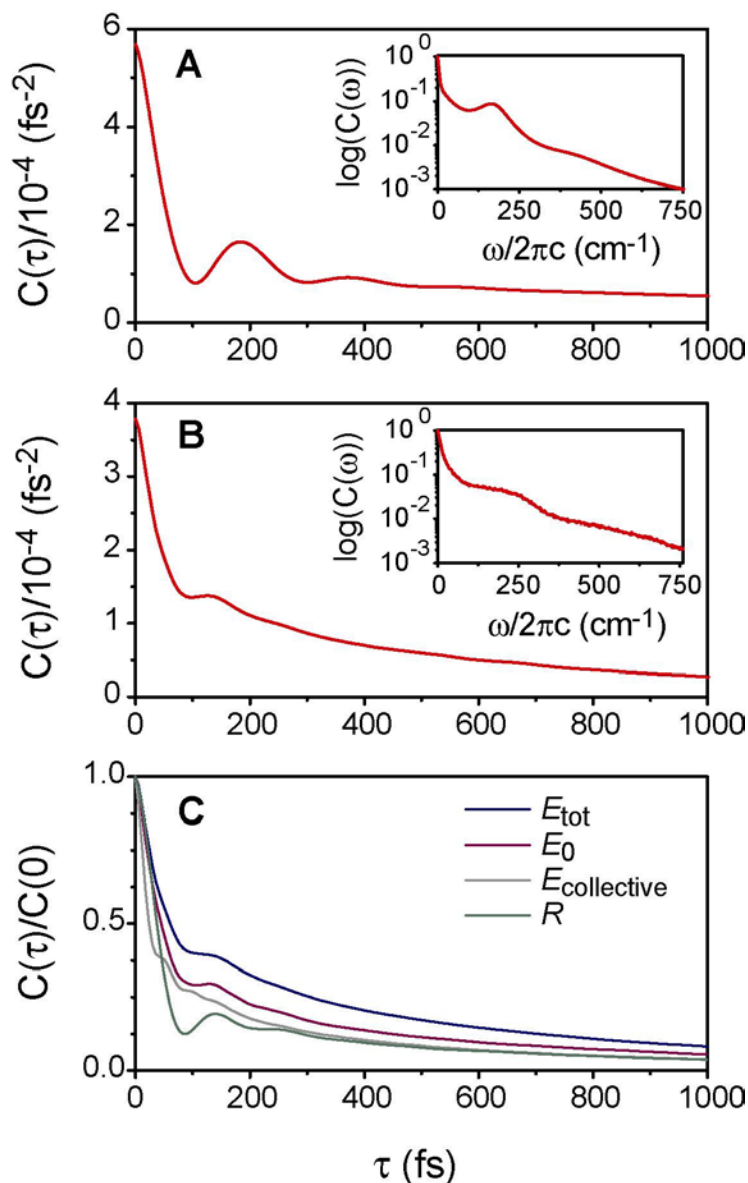


Figure 5-10. (Color) OH frequency correlation function extracted from the 3PEPS and PP measurements (A) compared with the OH frequency correlation function from the computer simulation of Eaves and Geissler (B). The inset in each displays a cosine transform of the respective correlation function. Panel (C) shows normalized correlation functions of some of the order parameters examined in Fig. 5-15 and of the collective electric field (excluding the contributions from the hydrogen-bonding partner, $E_{\text{collective}} = E_{\text{tot}} - E_0$). (computer simulation results reproduced from Ref. 45)

The experimental signals were evaluated with Eqs. (5-26) and (5-27), including finite duration pulses. Calculation of the 3PEPS decay included the amplitude and phase of the electric field envelopes that were used to make the measurement, as extracted from the FROG taken immediately afterwards. In both experiments and calculations, we found that pulse characteristics strongly influence the early time decay of the 3PEPS signal, which is in agreement with observations made by others.⁸⁷ Calculation of the PP experiments, in which we were less concerned about the early time behavior of the nonlinear signals, employed transform limited pulses whose duration matches that of an autocorrelation taken before or after the experiment.

The final nonlinear signals, calculated from the best fits values of $C(t)$, T_1 and $p_2(t)$ are plotted as solid curves on the experimental data in Figs. 5-4, 5-6 and 5-7. Not surprisingly, the value of T_1 resulting from our analysis, 700 ± 50 fs, matches the original fit to the MA-PP. Similarly, the resulting form of $p_2(t)$ (Fig. 5-9A) resembles the anisotropy in Eq. (5-31) except the timescale of the fast component is slightly shorter (50 ± 20 fs and 3.0 ± 0.5 ps). The extracted OH frequency correlation function $C(t)$ (Fig. 5-10A) has the same qualitative features as the 3PEPS decay, although the relative amplitudes and timescales are different. Its initial decay is faster (50 ± 20 fs), while the oscillation period of the underdamped component (180 ± 20 fs) is slightly longer. The amplitudes of both features are enhanced in the correlation function relative to the 3PEPS decay. The slow component of $C(t)$ is 1.4 ± 0.2 ps. Table 5-2 lists the best-fit parameters for the frequency correlation function. A graphical comparison of the timescales we have measured in this global analysis is presented in Fig. 5-14 by normalizing all three dynamical quantities in our model.

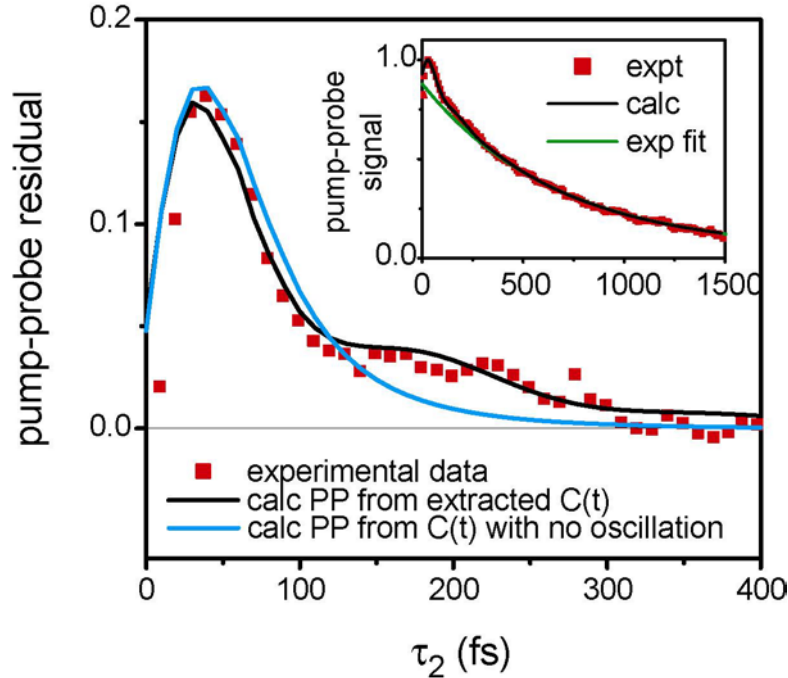


Figure 5-11. (Color) Residuals that result from subtracting an exponential function whose timescale and amplitude reproduce the long time tail from the experimental and simulated parallel pump-probe decays. In the inset, the exponential function (exp fit) is plotted with the pump-probe decays from the experiment (expt) and simulated with the extracted dynamical quantities (calc). In the main figure, the residuals are plotted from the experimental data (expt), pump-probe simulated with the extracted dynamical quantities (calc), and pump-probe simulated with a frequency correlation function that excludes an oscillation (but otherwise matches the timescales present in the extracted correlation function).

We have assigned error bars based on the quality of our data and the sensitivity of our fits to each parameter. Because the fast decay components in both $C(t)$ and $p_2(t)$ occur on the timescale of the pulse duration, the sensitivity of the fits to their precise values is decreased, resulting in an uncertainty that is significant relative to their values. At long times, the nonlinear signal is reduced by population relaxation, which particularly affects the 3PEPS decay since it is a homodyne measurement. (At $\tau_2 = 2$ ps, the peak vibrational echo intensity is reduced by a factor of $[\exp(-2000/700)]^{-2} \approx 300$.) However, since the anisotropy is a difference between the parallel and perpendicular PP signals, it also suffers

from noise for long pulse delays. In addition, extraction of data from both measurements is sensitive to the HGS model. Therefore, we assign the smallest error bars to dynamical quantities associated with times where the pulse overlap is negligible ($\tau_2 > 100$ fs) but the signal remains strong ($\tau_2 < 1.5$ ps).

Before proceeding to a discussion and interpretation of the results, we mention two last results that were not included in the global analysis to extract the dynamical information, but that confirm the results nonetheless. At short delay times, the PP signals contain weak contributions from frequency fluctuations, often referred to as coherent transients,^{49,88,89} in addition to those from lifetime and reorientations. This can be most easily observed in the residual that results from subtracting the lifetime and reorientation decays from a set of experimental data that has been averaged to reduce experimental noise. This residual is plotted with one that results from the calculated signal, treated in the same way, in Fig 5-11. The peak at early times ($\tau_2 \sim 40$ fs) is due to the fast decay in the correlation function. Both residuals also exhibit a feature for $\tau_2 > 100$ fs that is due to the presence of the 180 fs oscillation in the correlation function (as demonstrated by the absence of this feature in a calculation of the same residual using a correlation function that is equivalent to the extracted $C(t)$ except without the oscillation). Note that $C(t)$ was extracted entirely from the 3PEPS results, but still reproduces the early time transient present in the PP data.

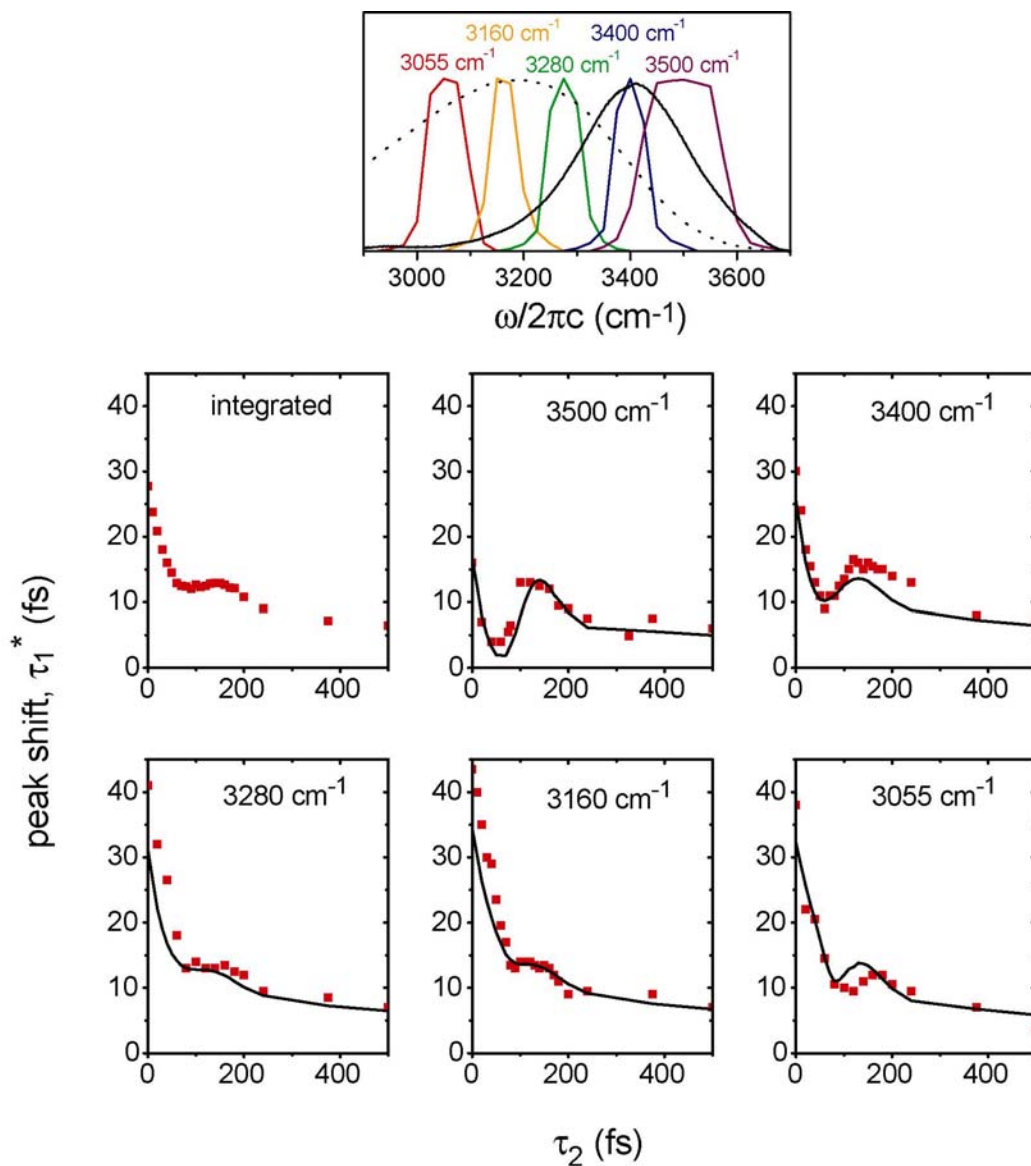


Figure 5-12. (Color) (Top) Transmission spectra of the bandpass filters used to collect the PP and dispersed 3PEPS superimposed on the OH fundamental (solid black) and projected overtone³⁰ (dotted black) spectra. (Bottom) Experimentally measured dispersed 3PEPS decays of HOD in D₂O (red squares) and simulated dispersed 3PEPS signals with the dynamical quantities extracted from the frequency-integrated measurements.

We also measured a set of dispersed vibrational echoes to examine the information contained in their 3PEPS decays. The data were recorded by inserting bandpass filters directly after the sample, so that the echo signals in both phase matching directions were spectrally filtered. The center frequencies of the filters spanned the fundamental and

overtone transition frequencies. The dispersed 3PEPS decays (Fig. 5-12) differ greatly in their initial values and initial decay rates, but the frequency and amplitude of the oscillation are relatively similar. Using the same formalism presented in the Theory section, and the same dynamical and static quantities extracted from the earlier experiments, we calculated dispersed 3PEPS traces. The results, also plotted in Fig. 5-12, are remarkably similar to the experimental data, lending further experimental support to the data treatment as well as the extracted values of $C(t)$, T_1 and $p_2(t)$. There are small discrepancies between the experimental and calculated decays, particularly in the oscillation frequency, which could be due to the spectral heterogeneities discussed in Chapter 6.

5.6 Discussion

The experimental results presented here access a new time regime in the IR spectroscopy of hydrogen-bonded systems by measuring sub-200 fs decays in the 3PEPS signal and anisotropy. The observation of fast processes is only attainable with ultrashort duration mid-IR pulses, highlighting the importance of our novel OPA and subsequent steps taken to compress and characterize the pulses. However, the application of short pulses alone does not guarantee an accurate measurement of these fast dynamics. In a set of preliminary experiments, we found that the early time behavior of both the 3PEPS and PP was obscured by contributions to the signal from the CaF₂ cell that was being used at the time to hold the HOD in D₂O sample. The problem is illustrated in Fig. 5-13 by comparing the PP signal of a sample held in a cell with one recorded in the jet, scaled to match the long time decay. A number of observations support the assignment of this feature to a nonresonant response (dispersive shape in time, dependence on the overlap of all three pulses

in a boxcar geometry), which is unusual because the PP is most sensitive to resonant contributions to the signal.^{49,90} The presence of a strong CaF₂ contribution is even more disruptive to the interpretation of vibrational echo experiments, which led us to perform all experiments on a water jet to avoid complications associated with the extra signal contribution. This greatly enhanced our ability to detect and interpret the early time behavior of the nonlinear signals.

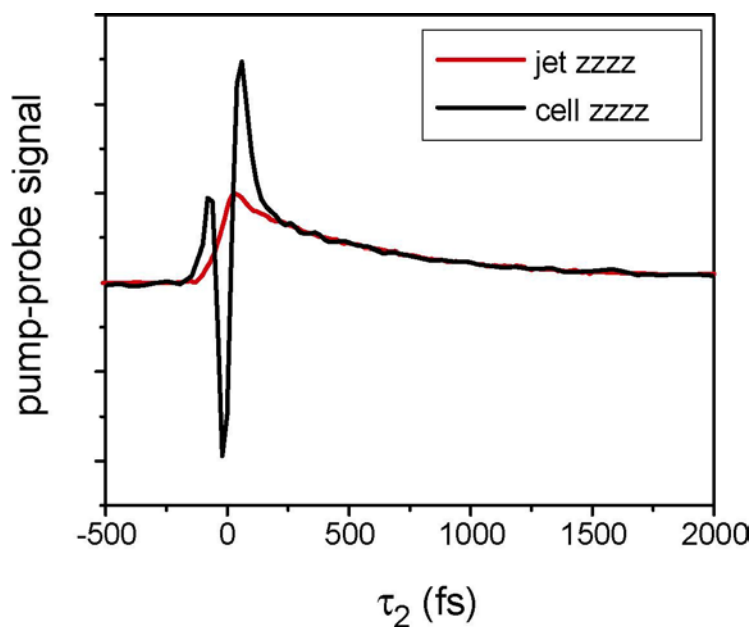


Figure 5-13. (Color) Comparison of the experimentally measured parallel pump-probe signals when the HOD/D₂O sample is held in a sample cell with 3 mm thick CaF₂ walls, or flowed as a jet. The sample thickness is 50 μ m and optical density is \sim 0.4 for both. The data were scaled to match the long time decay.

The unified treatment presented here to analyze results from multiple nonlinear experiments provides an independent determination of vibrational dephasing, population relaxation and molecular reorientation on timescales from 50 fs to several ps. Aside from time resolution issues, which dictate the use of calculations involving real pulses to extract meaningful information about dynamics on timescales comparable to the pulse duration, this approach is required to observe pure dephasing. Polarization-selective PP measures

population relaxation and reorientations with relatively little influence from dephasing, but there are no experiments that observe pure vibrational dephasing directly. The 3PEPS decay is most sensitive to dephasing because it measures time shifts rather than amplitude changes of the integrated vibrational echoes, however other processes that take place on timescales similar to dephasing can complicate the experimental results. For example, inclusion of population relaxation and molecular reorientations in our model causes the long time decay of the correlation function to differ from the 3PEPS decay, in contrast to predictions from more simple models.^{91,92} Contributions from the HGS also influence 3PEPS at long τ_2 delay times. The effect that these processes have on $C(t)$ is made most evident by comparing the results of the present treatment with the correlation function we derived earlier,⁴⁵ which neglected them. The two are similar, agreeing quantitatively in the timescale and relative amplitudes of all features to within about 20%. The largest two differences are the timescale of the long time component, which has increased from 1.2 to 1.4 ps, and a decrease in the overall amplitude. Nonetheless, the present form of $C(t)$ provides the best determination of pure vibrational dephasing and is most appropriate to compare with the wealth of theoretical results available in the literature. Before making a comparison to theory and interpreting the vibrational dynamics in terms of molecular quantities, we place our results in the context of other recent experiments.

Table 5-1 (at the end of this chapter) summarizes the dynamical information obtained by several groups that study the OH vibrational dynamics of HOD in D₂O using time-resolved IR spectroscopy. A similar comparison made just over two years ago highlighted similarities and differences in the results of hole-burning experiments,²⁸ but the more recent experiments using echo techniques (including the present study) and combined IR excitation

and Raman detection provide additional data.^{39,40,45,93,94} The hole burning and IR/Raman experiments involve a trade-off between time and frequency resolution, limiting their sensitivity to fast processes but allowing measurement of frequency-dependent dynamics. The echo measurements have primarily focused on achieving high time resolution at the expense of frequency resolution. In cases where multiple values were reported, Table 5-1 lists the values most relevant to the present study.

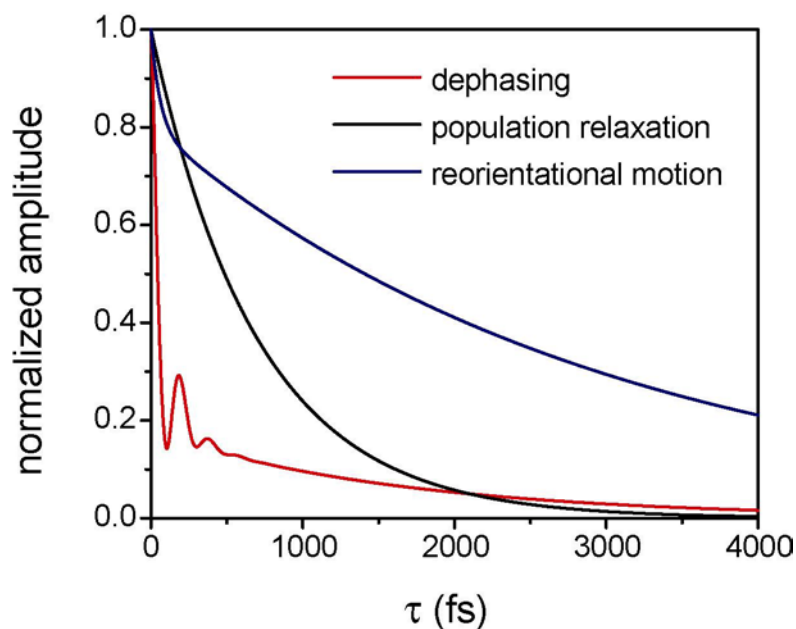


Figure 5-14. (Color) Plots of the normalized OH frequency correlation function $C(\tau)$, orientational correlation function $p_2(\tau)$, and vibrational lifetime decay.

The population lifetime that we extract from our measurements agrees well with those measured by the Bakker and Gale groups (although the latter has published conflicting values), and is slightly shorter than those of Laubereau and Dlott who use longer IR pulse durations. The lifetime values have historically decreased as the experiments have progressively shorter pulses, however the current T_1 of ~ 700 fs has resulted with a range of pulse durations. With respect to reorientational data, the long time component of our anisotropy also matches earlier values, but no experiment had resolved a fast time component

in the anisotropy. There have also been reports of a >10 ps contribution to the anisotropy,²⁸ which is well beyond the noise sensitivity of our measurement.

There has been much debate about the OH frequency correlation function, and the best way to extract it from time-resolved measurements. As with the lifetime, timescales for the correlation function have decreased with the duration of the IR pulses used in the experiments. Echo experiments, which have employed the shortest pulses to date, agree that $C(t)$ exhibits a fast (~ 100 fs) and a slow (~ 1 ps) component, and in one case, a 5-15 ps component was also suggested. The time resolution achieved in hole burning experiments is not enough to observe the short component, but may reflect the longer decay or a mixture of the two. Two of the previous echo investigations involved two-pulse techniques, from which extraction of a correlation function is not as straightforward as 3PEPS.^{93,94}

Stenger and co-workers did use 3PEPS to extract a correlation function taking into account their pulse duration and population relaxation,³⁹ but not the effects of molecular reorientation. Unfortunately, their pulse length was 2-3 times longer than those used in our measurement, so the fastest dynamics were not captured. Instead, the authors focused on the long time vibrational dynamics, because they found a large recurrence in the 3PEPS for pulses centered on the red side of the OH absorption line, but not on the blue (which is possible to observe because the spectral bandwidth of their pulses is significantly less than our pulses). We do not observe this long time recurrence in our data, which could be due to the broadband nature of our experiments, lessening the overall effect on the 3PEPS decay below our signal to noise level at long waiting times. They attributed the rise in signal to absorption from the HGS, and were able to reproduce it on the blue side of the band with proper choice of $\Delta\omega$, assuming $\Delta\mu = 0$. However, the signal calculated on the red side of

the line also exhibited a recurrence that was stronger than they observed experimentally. We believe that their results could be reproduced globally by assuming a similar in both $\Delta\omega$ and $\Delta\mu$, as in our modeling. We also note that their 3PEPS measurement extends to significantly longer τ_2 than we were able to achieve, so a full modeling of the data at long times could reveal a more accurate determination of the longest timescales in $C(t)$.

The HGS model deserves some comment because it has received considerable attention in the literature. As it was introduced in Sec. 5.2, the nonlinear signals measured in several experiments indicate that the absorption characteristics of molecules that undergo vibrational population relaxation differ from their initial state. The physical basis is almost certainly energy transfer from the system (OH oscillator) to the bath, which in turn affects the subsequent OH vibrational dynamics. This process, however, is inherently non-equilibrium because over 3000 cm^{-1} is transferred to a small group of solvent molecules in a short period of time. Therefore, the vibrational dynamics on timescales relevant to the HGS ($>1\text{-}2\text{ ps}$) should not be interpreted in terms of equilibrium hydrogen bond dynamics unless a linear response argument is invoked (the validity of which may be questionable). However, these dynamics may be interesting in the context non-equilibrium energy flow. As for the specific model we have chosen for the HGS, we do not claim that it is rigorously correct, but just that it reproduces our data and may well reproduce data others have published.³⁹ It is known, for instance, that the dominant energy relaxation mechanism of the OH stretch is to the bend of HOD and of the D_2O solvent molecules,^{40,95} which is not present in our model. Besides other questions of treating the non-equilibrium process with parameters from equilibrium, the assumption that $C(t)$ is independent of temperature is only approximate.⁹⁶

Other experimental techniques are sensitive to molecular reorientations and the intermolecular dynamics that influence the correlation function. In particular, Raman spectroscopy, NMR and dielectric relaxation all observe reorientational motion. Heterodyne-detected optical Kerr effect (OKE) experiments have measured a 1.2 ps component in the correlation function of D₂O,^{97,98}. Values from NMR and dielectric relaxation vary between 3-8 ps,⁹⁹⁻¹⁰¹ although they are sensitive to $p_1(t)$ so the decay values should be multiplied by a third for comparison to the Raman and IR work.^{102, Winkler, 2000 #1817} Discrepancies in these results are probably due to the collective nature of many of the other experiments, as opposed to IR spectroscopy that directly probes the OH dipole on individual molecules.¹⁰³ For example, Raman spectroscopy measures a correlation function of the many body polarizability, which includes terms from single molecules as well as interaction-induced terms that depend on an arbitrarily large number of molecules.¹⁰⁴

Comparison of the correlation function extracted from our data modeling to results from OKE or Raman experiments is even more interesting.^{10,85,104-106} The spectral density of $C(t)$ (inset in Fig. 5-10A) exhibits a pronounced peak at 170 cm⁻¹, a feature which is also present in the low frequency Raman spectrum of D₂O. Comparisons to the spectroscopy of ice and x-ray scattering, as well as numerous computer simulation studies indicate that the Raman feature is predominantly due to motion of the center of mass of water molecules along the OH coordinate. It is not surprising that time-resolved IR spectroscopy measures this type of motion, considering the strong correlation between the OH vibrational frequency and hydrogen bond distance in solids. A further comparison of the IR and Raman spectral densities indicates that $C(t)$ is not particularly sensitive to librations, as evidenced by its small amplitude at 400 cm⁻¹.

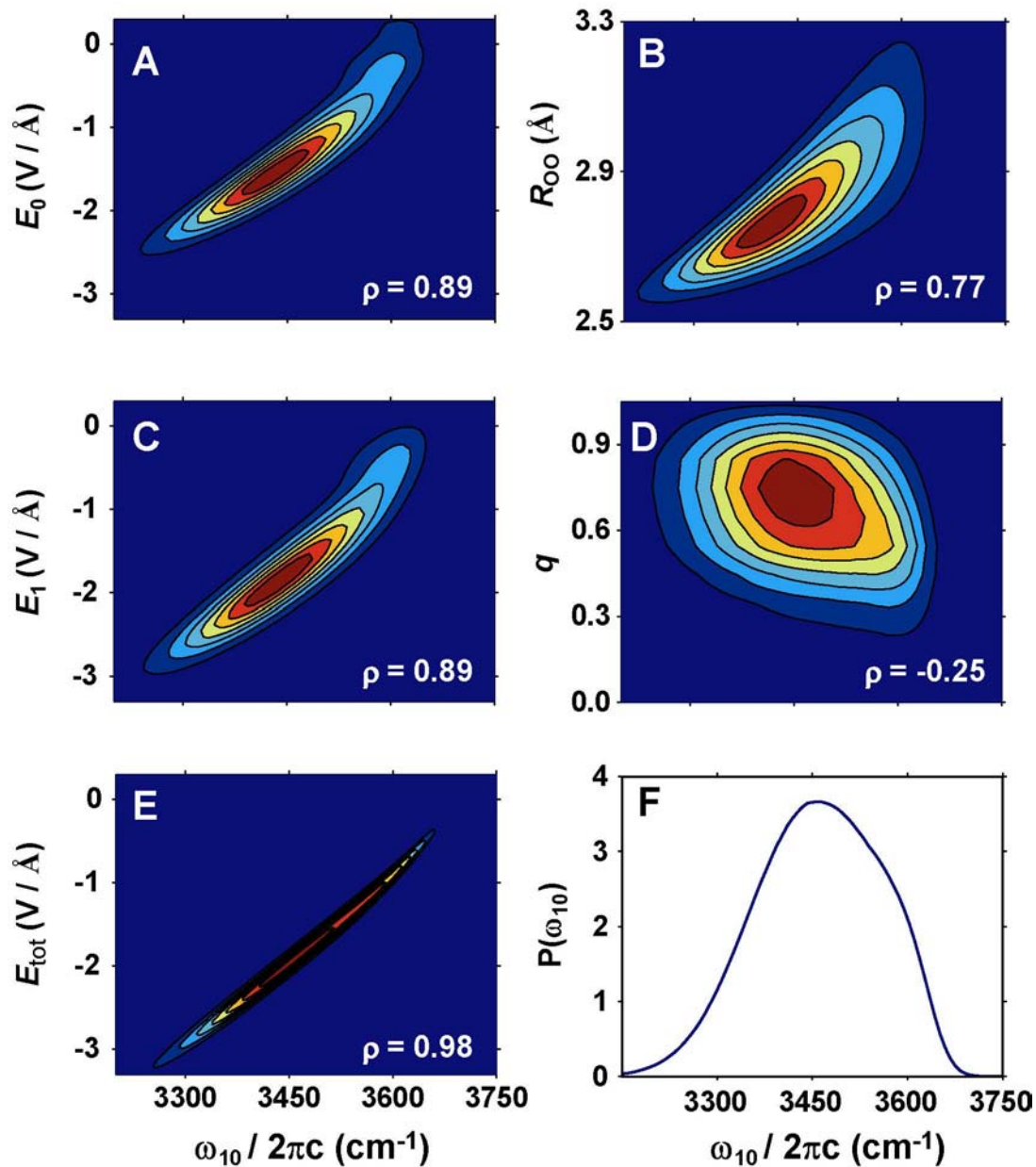


Figure 5-15. (Color) Joint probability distributions of OH vibrational frequency (ω_{10}) and order parameters describing local (A-B), first solvation shell (C-D), and collective (E) environments. Left panels show correlations of ω_{10} with the electric field experienced by the proton, projected onto the OH bond vector. E_0 , E_1 , and E_{tot} are the contribution to this field from the hydrogen bond partner, first solvation shell and all of the molecules in the simulation. Panels B and D show correlations of ω_{10} with structural variables, namely the hydrogen bond distance, R_{OO} , and the degree of tetrahedrality in the first solvation shell, q . Panel F plots the OH frequency probability density for the model. (reproduced from Ref. 45)

While comparison to other experiments is useful, computer simulations provide the clearest interpretation of our results in terms of molecular quantities. Water has been the subject of numerous theoretical and simulation studies, but there has been considerable debate about the validity of various models and simulation strategies. The dynamical quantities we have measured will aid in answering these questions by establishing a set of experimentally determined standards for vibrational dephasing, population relaxation and molecular rotations to which simulation results can be compared. Here, we use results of recent simulations performed by several groups to interpret the dephasing and reorientational dynamics measured with time-resolved IR experiments,⁴¹⁻⁴⁵ but focus mostly on the work of Eaves and Geissler (EG).⁹⁶

To simulate the liquid dynamics, EG chose a model based on the rigid SPC/E potential, in which the OH oscillator is treated as a single quantum mechanical degree of freedom. By assuming an adiabatic separation of timescales, molecular translations and rotations of the rigid molecules evolved classically, but the OH vibrational frequency was calculated at each time step for fixed configurations of the surrounding solvent. The frequency correlation function calculated from their model (Fig 5-10B) exhibits the same qualitative features as the experimentally determined $C(t)$: a fast decay, an oscillation at intermediate times and a long time component. The amplitudes and timescales of the simulated correlation function differ slightly from the experimental values, particularly for the oscillation and slow decay components, but the agreement is sufficient to proceed with an investigation of the molecular origins of dephasing. We also note that OH frequency correlation functions calculated by Hynes and co-workers and Lawrence and Skinner are nearly identical to $C(t)$ in Fig 5-10B.

Guided by chemical intuition as well as earlier results, EG investigated the relationship between OH frequency shifts and molecular order parameters that describe specific distances and angles within the liquid.⁴⁵ The results are presented as joint probability distributions between the OH frequency (whose static distribution is in Fig 5-15F) and individual order parameters, and are quantified by a correlation coefficient ρ that varies from -1 to 1 . The hydrogen bond length, R_{OO} , significantly influences the frequency of an OH oscillator (Fig 5-15B). This result indicates that the experimental correlation between frequency and distance for hydrogen bonding solids holds, at least partially, for liquids. The correlation is not perfect ($\rho = 0.77$) because disorder in the liquid causes a large distribution of hydrogen bond angles. EG found a much better correlation ($\rho = 0.89$) between frequency and the force exerted on the OH oscillator by the electric field due to the hydrogen-bonding partner, E_0 (Fig 5-15A). In fact, inclusion of the force exerted by all of the molecules in the simulation (and their periodic images), E_{tot} , yielded the best correlation ($\rho = 0.98$), leading EG to conclude that frequency shifts are dominated by molecular Stark shifts. Surprisingly little influence on the OH frequency was imparted by molecules in the first solvation shell which did not directly bond to the OH oscillator.

The molecular origins of vibrational dephasing are revealed in the dynamics of these order parameters, illustrated in Fig 5-10C by their time correlation functions. The frequency correlation function is best reproduced by the total electric field correlation function for all times. However, at short times, the local electric field E_0 autocorrelation function also resembles $C(t)$, and reproduces the oscillation particularly well. This feature appears to be a signature of local relaxation. It is also observed in the dynamics of R_{OO} , indicating that dephasing of hydrogen bond stretching is an important component of frequency relaxation at

short times. Not surprisingly, the relaxation of collective electrostatic contributions (excluding E_0) mirrors the dielectric dispersion of water, with a beat around 60 fs typically assigned to librations. All of the time correlation functions presented in Fig. 4 decay asymptotically on the same timescale. As a consequence, the long-time decay of frequency correlations cannot be associated with a single specific motion of individual molecules. Instead, it reflects a variety of relaxation mechanisms, including collective rearrangement of the hydrogen bond network, as well as density and polarization fields, on length scales greater than a molecular diameter.

Molecular reorientational dynamics measured by our experiments have been examined by EG (see Fig. 5-9),⁹⁶ as well as other investigators.^{2,107} The rotational time correlation functions $p_\ell(t)$, which exhibit little dependence on the particular model used for the calculation, decay on a sub-60 fs timescale, oscillate near 60 fs, and then decay on a long timescale. The initial decay time and oscillation period are relatively independent of the order of the Legendre polynomial, ℓ , as opposed to Eq. (5-8) which predicts a scale factor of $\ell(\ell+1)$ for rotational diffusion. Deviation from the diffusion prediction are not surprising at short times, when atomic interactions are still important. The short time decay has been universally assigned to fast librations (low amplitude hindered rotations) of the water molecules, which is clearly non-diffusive due to a restoring force imposed by the relatively static configuration of surrounding solvent molecules on the libration timescale. Our experiment is the first to directly observe this fast motion in the IR region of the spectrum, however we do not find evidence for an oscillation in $p_2(t)$ as the simulations predict. A strong contribution from librations has been observed low-frequency Raman and optical Kerr effect experiments.^{10,85,104-106} The calculations we have performed to model the experimental

data assumed a scale factor of 3 between the first and second Legendre polynomials, however performing the calculations without scaling the short time component produces a very similar result. For the long time component, the computer simulations predict that the Legendre polynomials roughly scales with $\ell(\ell+1)$, indicating the motion more closely resembles rotational diffusion. The long time decay of $p_2(t)$ calculated by EG decays on a 1.8 ps timescale.

The vibrational dephasing and molecular reorientational dynamics measured in our experiments both exhibit a clear separation of fast and slow timescales, which are conveniently divided by the correlation time, which is calculated as $\tau_c = C(0)^{-1} \int C(\tau) d\tau$. For the experimental correlation function, $\tau_c \sim 350$ fs. In both cases, simulations indicated that the intermolecular dynamics that contribute to the observable for times shorter than τ_c are characteristic of local processes – low amplitude motions that occur on molecular length scales. The longer timescale processes involve the corresponding large-scale motions, such as large translational and rotational displacements, that lead to reorganizations of the hydrogen bond network. These dynamics fit well within the energy landscape picture discussed earlier for water, where the system samples local minima of the global potential energy on short timescales, but undergoes larger structural changes on longer timescales that correspond to transitions between basins of attraction in the surface.

5.7 Conclusions

We have presented a comprehensive investigation of the vibrational dynamics of the OH stretch of HOD in D₂O, in which multiple experiments and a unified theoretical

treatment allowed the separation of pure dephasing dynamics, reorientational dynamics and vibrational population relaxation. By using sub-50 fs mid-IR pulses and avoiding unwanted signal contributions from a sample cell, the time resolution of the experiments is sufficient to capture all of the dynamical processes in water that lead to linebroadening. We observe a vibrational lifetime (700 fs) consistent with earlier studies, but measure dephasing and reorientational dynamics on sub-200 fs timescales that had eluded most previous time-resolved IR studies. The fast dynamics mainly correspond to local dynamics, namely hydrogen bond oscillations and hindered rotational motion, respectively. On timescales longer than the correlation time, dephasing and reorientations reflect larger-scale motions that cause reorganization of the hydrogen bond network. However, we note that the experiments presented here used broadband pulses to excite the entire distribution of OH frequencies, and therefore the dynamics that they measure are averaged over all solvent configurations. Others have noted that the intermolecular dynamics in water may depend on local environment due to the strong influence of hydrogen bonds, leading to a distribution of timescales for local and structural reorganizations. However, the experiments performed here are not sensitive to this behavior and our theoretical modeling has correspondingly assumed that the frequency fluctuations follow Gaussian statistics. The averaged treatment here is not to diminish the importance of configuration-dependent dynamics, but to develop a solid foundation that will become a point of departure for future investigations of spectrally heterogeneous dynamics.

	Tokmakoff	Bakker ^{29,30,32}	Gale ^{34,35}	Laubereau ²⁸	Dlott ⁴⁰	Elsaesser ^{39,93}	Wiersma ⁹⁴
Pop. Lifetime, T_1	700 fs	740 fs	650 fs @ 3400 cm ⁻¹	1.0 ± 0.2 ps	~1 ps	-	-
Anisotropy decay, $r(t)$	50 fs & 3 ps	2.6 ps (v=0); 4.2 ps (v=1)	-	3 ps 3500 cm ⁻¹ 10 ps 3350 cm ⁻¹	-	-	-
Correlation Function, $C(t)$	50 fs, 1.4 ps & 180 fs osc.	500 fs	700 fs	1.0 ps	0-2 ps	90 fs, 700 fs & 5-15 ps	130 & 900 fs
Stoke's Shift	-	70 cm ⁻¹	-	-	100 cm ⁻¹	-	-
Techniques	IR 3PEPS & PP	IR HB	IR HB	IR HB	IR-Raman	IR 2 & 3 pulse echoes	IR HD 2 pulse echoes
Pulse length & Bandwidth	45 fs 400 cm ⁻¹	200 fs 70 cm ⁻¹	150 fs 65 cm ⁻¹	500 fs 35 cm ⁻¹	1.2 ps 55 cm ⁻¹	130 fs 100 cm ⁻¹	70 fs 300 cm ⁻¹

Table 5-1. Summary of experimental techniques and results from this and previously published investigations of HOD in D₂O. PP, broadband pump-probe; HB, narrowband hole burning; HD, heterodyne-detected.

$A_1 = 2.62 \times 10^{-3} \text{ fs}^{-2}$	$\gamma_1 = 9.31 \times 10^{-3} \text{ fs}^{-1}$	
$A_2 = 1.31 \times 10^{-3} \text{ fs}^{-2}$	$\gamma_2 = 7.07 \times 10^{-4} \text{ fs}^{-1}$	
$A_3 = 1.75 \times 10^{-6} \text{ fs}^{-2}$	$\gamma_3 = 1.92 \times 10^{-2} \text{ fs}^{-1}$	$\omega_3 = 3.42 \times 10^{-2} \text{ fs}^{-1}$
$A_4 = 8.29 \times 10^{-7} \text{ fs}^{-2}$	$\gamma_4 = 5.00 \times 10^{-2} \text{ fs}^{-2}$	$\omega_4 = 8.00 \times 10^{-2} \text{ fs}^{-1}$

Table 5-2. Best-fit parameters for the Brownian oscillator functions that comprise the extracted OH frequency correlation function $C(t)$ (the Brownian oscillator functions are defined in Eqs. 3-50 and 3-51).

References

- (1) Pauling, L. The Structure of Water. In *Hydrogen Bonding: Papers Presented at the Symposium on Hydrogen Bonding (1957; Slovenia)*; Hadzi, D., Ed.; Pergamon Press: New York, 1959; pp 1.
- (2) Rahman, A.; Stillinger, F. H. *J. Chem. Phys.* **1971**, *55*, 3336.
- (3) Stillinger, F. H. *Adv. Chem. Phys.* **1975**, *31*, 1.
- (4) Sceats, M. G.; Stavola, M.; Rice, S. A. *J. Chem. Phys.* **1979**, *70*, 3927.
- (5) Stanley, H. E. *J. Phys. A* **1979**, *12*, L329.
- (6) Stillinger, F. H.; Weber, T. A. *J. Phys. Chem.* **1983**, *87*, 2833.
- (7) Ohmine, I.; Tanaka, H. *Chem. Rev.* **1993**, *93*, 2545.
- (8) Luzar, A.; Chandler, D. *Nature* **1996**, *379*, 55.
- (9) Errington, J. R.; Debenedetti, P. G. *Nature* **2001**, *409*, 318.
- (10) Walrafen, G. E. *J. Chem. Phys.* **1964**, *40*, 3249.
- (11) Eisenberg, D.; Kauzmann, W. *The Structure and Properties of Water*; Clarendon Press: Oxford, 1969.
- (12) *The Physics and Physical Chemistry of Water*; Franks, F., Ed.; Plenum Press: New York, 1975; Vol. 1.
- (13) Jarzeba, W.; Walker, G. C.; Johnson, A. E.; Kahlow, M. A.; Barbara, P. F. *J. Phys. Chem.* **1988**, *92*, 7039.
- (14) Jimenez, R.; Fleming, G. R.; Kumar, P. V.; Maroncelli, M. *Nature* **1994**, *369*, 471.
- (15) Cunsolo, A.; Ruocco, G.; Sette, F.; Masciovecchio, C.; Mermet, A.; Monaco, G.; Sampoli, M.; Verbeni, R. *Phys. Rev. Lett.* **1999**, *82*, 775.
- (16) Keutsch, F. N.; Saykally, R. J. *PNAS* **2001**, *98*, 10533.

- (17) Ohmine, I.; Tanaka, H.; Wolynes, P. G. *J. Chem. Phys.* **1988**, *89*, 5852.
- (18) See Chapter 2 and references therein.
- (19) Robinson, G. W.; Zhu, S.-B.; Singh, S.; Evans, M. W. *Water in Biology, Chemistry and Physics*; World Scientific: New Jersey, 1996; Vol. 9.
- (20) Novak, A. Hydrogen bonding in solids. Correlation of spectroscopic and crystallographic data. In *Structure and Bonding*; Dunitz, J. D., Hemmerich, P., Holm, R. H., Ibers, J. A., Jorgenson, C. K., Neilands, J. B., Reinen, D., Williams, R. J. P., Eds.; Springer-Verlag: New York, 1974; Vol. 18; pp 177.
- (21) Mikenda, W. *J. Mol. Struct.* **1986**, *147*, 1.
- (22) Bratos, S.; Leicknam, J.-C. *J. Chem. Phys.* **1994**, *101*, 4536.
- (23) Bratos, S.; Leicknam, J.-C. *J. Mol. Liquids* **1995**, *64*, 151.
- (24) Graener, H.; Seifert, G.; Laubereau, A. *Phys. Rev. Lett.* **1991**, *66*, 2092.
- (25) Laenen, R.; Rauscher, C.; Laubereau, A. *Phys. Rev. Lett.* **1998**, *80*, 2622.
- (26) Laenen, R.; Rauscher, C.; Laubereau, A. *J. Phys. Chem. B* **1998**, *102*, 9304.
- (27) Laenen, R.; Simeonidis, K.; Laubereau, A. *J. Phys. Chem. B* **2002**, *106*.
- (28) Laenen, R.; Simeonidis, K.; Laubereau, A. *Bull. Chem. Soc. Jpn.* **2002**, *75*, 925.
- (29) Woutersen, S.; Emmerichs, U.; Nienhuys, H.-K.; Bakker, H. J. *Phys. Rev. Lett.* **1998**, *81*, 1106.
- (30) Woutersen, S.; Bakker, H. J. *Phys. Rev. Lett.* **1999**, *83*, 2077.
- (31) Nienhuys, H. K.; Woutersen, S.; Santen, R. A. v.; Bakker, H. J. *J. Chem. Phys.* **1999**, *111*, 1494.
- (32) Nienhuys, H.-K.; van Santen, R. A.; Bakker, H. J. *J. Chem. Phys.* **2000**, *112*, 8487.

- (33) Bakker, H. J.; Nienhuys, H.-K.; Gallot, G.; Lascoux, N.; Gale, G. M.; Leicknam, J.-C.; Bratos, S. *J. Chem. Phys.* **2002**, *116*, 2592.
- (34) Gale, G. M.; Gallot, G.; Hache, F.; Lascoux, N.; Bratos, S.; Leicknam, J.-C. *Phys. Rev. Lett.* **1999**, 1068.
- (35) Gale, G. M.; Gallot, G.; Lascoux, N. *Chem. Phys. Lett.* **1999**, *311*, 123.
- (36) Bratos, S.; Gale, G. M.; Gallot, G.; Hache, F.; Lascoux, N.; Leicknam, J.-C. *Phys. Rev. E* **2000**, *61*, 5211.
- (37) Gallot, G.; Lascoux, N.; Gale, G. M.; Leicknam, J.-C.; Bratos, S.; Pommeret, S. *Chem. Phys. Lett.* **2001**, *341*, 535.
- (38) Gallot, G.; Bratos, S.; Pommeret, S.; Lascoux, N.; Leicknam, J.-C.; Kozinski, M.; Amir, W.; Gale, G. M. *J. Chem. Phys.* **2002**, *117*, 11301.
- (39) Stenger, J.; Madsen, D.; Hamm, P.; Nibbering, E. T. J.; Elsaesser, T. *J. Phys. Chem. A* **2002**, *106*, 2341.
- (40) Deak, J. C.; Rhea, S. T.; Iwaki, L. K.; Dlott, D. D. *J. Phys. Chem. A* **2000**, *104*, 4866.
- (41) Rey, R.; Moller, K. B.; Hynes, J. T. *J. Phys. Chem. A* **2002**, *106*, 11993.
- (42) Moller, K. B.; Rey, R.; Hynes, J. T. *J. Phys. Chem. A* **2004**, *108*, 1275.
- (43) Lawrence, C. P.; Skinner, J. L. *J. Chem. Phys.* **2002**, *117*, 5827.
- (44) Lawrence, C. P.; Skinner, J. L. *J. Chem. Phys.* **2003**, *118*, 264.
- (45) Fecko, C. J.; Eaves, J. D.; Loparo, J. J.; Tokmakoff, A.; Geissler, P. L. *Science* **2003**, *301*, 1698.
- (46) Mukamel, S. *Principles of Nonlinear Optical Spectroscopy*; Oxford University Press: New York, 1995.

- (47) Ernst, R. R.; Bodenhausen, G.; Wokaun, A. *Principles of Nuclear Magnetic Resonance in One and Two Dimensions*; Oxford University Press: Oxford, 1987.
- (48) Weiner, A. M.; Silvestri, S. D.; Ippen, E. P. *J. Opt. Soc. Am. B* **1985**, *2*, 654.
- (49) Joo, T.; Jia, Y.; Yu, J.-Y.; Lang, M. J.; Fleming, G. R. *J. Chem. Phys.* **1996**, *104*, 6089.
- (50) de Boeij, W. P.; Pshenichnikov, M. S.; Wiersma, D. A. *Chem. Phys.* **1998**, *233*, 287.
- (51) Yan, Y. J.; Mukamel, S. *J. Chem. Phys.* **1991**, *94*, 179.
- (52) Sung, J.; Silbey, R. J. *J. Chem. Phys.* **2001**, *115*, 9266.
- (53) Sung, J.; Silbey, R. J. *J. Chem. Phys.* **2003**, *118*, 2443.
- (54) Mukamel, S.; Loring, R. F. *J. Opt. Soc. B* **1986**, *3*, 595.
- (55) Albrecht, A. W.; Hybl, J. D.; Gallagher Faeder, S. M.; Jonas, D. M. *J. Chem. Phys.* **1999**, *111*, 10934.
- (56) Cho, M.; Fleming, G. R.; Mukamel, S. *J. Chem. Phys.* **1993**, *98*, 5314.
- (57) Butcher, P. N.; Cotter, D. *The Elements of Nonlinear Optics*; Cambridge University Press: Cambridge, 1990.
- (58) Dick, B. *Chem. Phys.* **1987**, *113*, 131.
- (59) Tokmakoff, A. *J. Chem. Phys.* **1996**, *105*, 1.
- (60) Khalil, M.; Demirdöven, N.; Tokmakoff, A. *J. Phys. Chem. A* **2003**, *107*, 5258.
- (61) Fourkas, J. T.; Kawashima, H.; Nelson, K. A. *J. Chem. Phys.* **1995**, *103*, 4393.
- (62) Oxtoby, D. W.; Rice, S. A. *Chem. Phys. Lett.* **1976**, *42*, Chem. Phys. Lett.
- (63) Diestler, D. J. *Chem. Phys. Lett.* **1976**, *39*, 39.
- (64) Asbury, J. B.; Steinel, T.; Stromberg, C.; Corcelli, S. A.; Lawrence, C. P.; Skinner, J. L.; Fayer, M. D. *J. Phys. Chem. A* **2004**, *108*, 1107.

- (65) Gallagher Faeder, S. M.; Jonas, D. M. *Phys. Rev. A* **2000**, *62*, 033820.
- (66) de Boeij, W. P.; Pshenichnikov, M. S.; Wiersma, D. A. *Annu. Rev. Phys. Chem.* **1998**, *49*, 99.
- (67) Hamm, P.; Lim, M.; Hochstrasser, R. M. *Phys. Rev. Lett.* **1998**, *81*, 5326.
- (68) Gallagher Faeder, S. A 2d FT spectroscopic study of the non-equilibrium solvation dynamics of ir44 in methanol, University of Colorado, 1999.
- (69) Jonas, D. M.
- (70) Press, W. H.; Teukolsky, S. A.; Vetterling, W. T.; Flannery, B. P. *Numerical Recipes in C++*; Cambridge University Press: Cambridge, 2002.
- (71) Zysset, B.; Biaggio, I.; Gunter, P. *J. Opt. Soc. Am. B* **1992**, *9*, 380.
- (72) Biaggio, I.; Kerkoc, P.; Wu, L.-S.; Gunter, P.; Zysset, B. *J. Opt. Soc. Am. B* **1992**, *9*, 507.
- (73) Kafka, J. D.; Watts, M. L. A potassium niobate OPA pumped by an amplified Ti:sapphire laser. In *Ultrafast Phenomena X*; Barbara, P. F., Fujimoto, J. G., Knox, W. H., Zinth, W., Eds.; Springer-Verlag: Berlin, 1996; Vol. 62.
- (74) Petrov, V.; Noack, F. *Opt. Lett.* **1996**, *21*, 1576.
- (75) Cussat-Blanc, S.; Ivanov, A.; Lupinski, D.; Freysz, E. *Appl. Phys. B* **2000**, *70*, S247.
- (76) Gruetzmacher, J. A.; Scherer, N. F. *Rev. Sci. Inst.* **2002**, *73*, 2227.
- (77) Pack, M. V.; Armstrong, D. J.; Smith, A. V. *J. Opt. Soc. Am. B* **2003**, *20*, 2109.
- (78) Trebino, R.; DeLong, K. W.; Fittinghoff, D. N.; Sweetser, J. N.; Krumbugel, M. A.; Richman, B. A.; Kane, D. J. *Rev. Sci. Inst.* **1997**, *68*, 3277.
- (79) Demirdöven, N.; Khalil, M.; Golonzka, O.; Tokmakoff, A. *Opt. Lett.* **2002**, *27*, 433.
- (80) Woutersen, S.; Bakker, H. J. *Nature* **1999**, *402*, 507.

- (81) The pulse characteristics are typical of those used in the PP measurements, while the pulses used for the 3PEPS experiments were slightly longer in duration (50 - 55 fs).
- (82) Larsen, D. S.; Ohta, K.; Xu, Q.-H.; Cyrier, M.; Fleming, G. R. *J. Chem. Phys.* **2001**, *114*, 8008.
- (83) Loparo, J. J.; Fecko, C. J.; Eaves, J. D.; Roberts, S. T.; Tokmakoff, A. *Phys. Rev. Lett.* **2004**, submitted.
- (84) The pump-probe data in Figures 5-5 were recorded by Joe Loparo and Sean Roberts after I had permanently left the lab, so I am grateful to be able to use it in my analysis.
- (85) Walrafen, G. E. Raman and Infrared spectral investigations of water structure. In *Water: A Comprehensive Treatise*; Franks, F., Ed.; Plenum: New York, 1972; Vol. 1; pp 151.
- (86) Although the final temperature change due to relaxation-induced heating of the bath is small, the energy is initially deposited into a small number of bath degrees of freedom. To model this non-equilibrium distribution, we must consider the effect of large temperature changes on the thermalized absorption spectrum.
- (87) Ohta, K.; Larsen, D. S.; Yang, M.; Fleming, G. R. *J. Chem. Phys.* **2001**, *114*, 8020.
- (88) Balk, M. W.; Fleming, G. R. *JCP* **1985**, *83*, 4300.
- (89) Farrow, D. A.; Yu, A.; Jonas, D. M. *J. Chem. Phys.* **2003**, *118*, 9348.
- (90) Xu, Q. H.; Ma, Y. Z.; Fleming, G. R. *J. Phys. Chem. A* **2002**, *106*, 10755.
- (91) Cho, M.; Yu, J.-Y.; Joo, T.; Nagasawa, Y.; Passino, S. A.; Fleming, G. R. *J. Phys. Chem.* **1996**, *100*, 11944.
- (92) de Boeij, W. P.; Pshenichnikov, M. S.; Weirisma, D. A. *J. Phys. Chem.* **1996**, *100*, 11806.

- (93) Stenger, J.; Madsen, D.; Hamm, P.; Nibbering, E. T. J.; Elsaesser, T. *Phys. Rev. Lett.* **2001**, *87*, 027401.
- (94) Yeremenko, S.; Pshenichnikov, M. S.; Wiersma, D. A. *Chem. Phys. Lett.* **2003**, *369*, 107.
- (95) Lawrence, C. P.; Skinner, J. L. *J. Chem. Phys.* **2003**, *119*, 1623.
- (96) Eaves, J. D. *Vibrational dynamics from the molecule's perspective*, Massachusetts Institute of Technology, 2004.
- (97) Vöhringer, P.; Scherer, N. F. **1996**, unpublished results.
- (98) Winkler, K.; Lindner, J.; Bürsing, H.; Vöhringer, P. *J. Chem. Phys.* **2000**, *113*, 4674.
- (99) Fung, B. M.; McGaughey, T. W. *J. Chem. Phys.* **1976**, *65*, 2970.
- (100) Barthel, J.; Bachhuber, K.; Buchner, R.; Hetzenauer, H. *Chem. Phys. Lett.* **1990**, *165*, 369.
- (101) Buchner, R.; Barthel, J.; Stauber, J. *Chem. Phys. Lett.* **1999**, *306*, 57.
- (102) Berne, B. J.; Pecora, R. *Dynamic Light Scattering*; R. E. Krieger Publishing Co.: Malabar, FL, 1990.
- (103) Rothschild, W. G. *Dynamics of Molecular Liquids*; John Wiley and Sons: New York, 1984.
- (104) Fecko, C. J.; Eaves, J. D.; Tokmakoff, A. *J. Chem. Phys.* **2002**, *117*, 1139.
- (105) Castner, E. W., Jr.; Chang, Y. J.; Chu, Y. C.; Walrafen, G. E. *J. Chem. Phys.* **1995**, *102*, 653.
- (106) Palese, S.; Schilling, L.; Miller, R. J. D.; Staver, P. R.; Lotshaw, W. T. *J. Phys. Chem.* **1994**, *98*, 6308.
- (107) Impey, R. W.; Madden, P. A.; McDonald, I. R. *Mol. Phys.* **1982**, *46*, 513.

Chapter 6

Heterogeneous dynamics in water revealed by 2DIR spectroscopy

6.1 Introduction

Although it is widely believed that the average local ordering around water molecules in the liquid resembles the tetrahedral packing present in ice, thermal fluctuations cause transient departures from this behavior that prevent long-range order.¹⁻⁷ As a result, there is a broad distribution of intermolecular distances and angles, and because interactions between molecules strongly depend on these variables, a correspondingly large range of energetic barriers for structural reorganization. Therefore, the rate that characterizes molecular rearrangements varies according to the initial environment, leading to a distribution of dynamical timescales within the liquid.⁷⁻¹⁰ This type of behavior, termed heterogeneous dynamics, is common in glasses and supercooled liquids, but is not significant for most normal liquids under ambient conditions.¹¹⁻¹³

In analogy to the formalism used to describe these more classically heterogeneous systems, Stillinger and Weber framed the intermolecular dynamics of water in the energy landscape picture, as transitions between minima of the potential energy surface, referred to

as inherent structures.^{6,14} A number of interpretations of structures within the liquid have emerged,^{7,8,15-18} but these structural details (i.e. ideas about well-defined geometrical structures that exist within the liquid) are secondary in the present investigation of intermolecular dynamics to the actual transitions that take place between these potential energy minima, which necessarily involve hydrogen bond making and breaking events. By experimentally observing heterogeneous dynamics, one may be able to infer details about these hydrogen bond dynamics, greatly augmenting the insight gained from our earlier measurements of the composite dynamics.

Infrared spectroscopy is an ideal technique to probe the heterogeneous nature of intermolecular dynamics due to the correlation between the OH absorption frequency and local structure around a particular molecule.¹⁹⁻²³ By selecting a narrow distribution of initial frequencies (and therefore a sub-ensemble of initial environments), and observing the subsequent evolution of this distribution, IR experiments can measure frequency-dependent vibrational dynamics. In this way, hole burning experiments are particularly intuitive to interpret in terms of heterogeneous dynamics, but they cannot access the fastest timescales, for which heterogeneous behavior should be most evident. Two-dimensional infrared (2DIR) spectroscopy is a broadband technique capable of frequency-resolving ultrafast vibrational dynamics, and thereby measuring heterogeneous dynamics.²⁴⁻³³ However, much like the 3PEPS experiments discussed in Chapter 5, the interpretation of 2DIR experiments is complicated by other frequency-dependent relaxation processes. For example, the vibrational population lifetime depends on the energy difference between the OH stretch and other states involved in the relaxation pathways, such as the bend overtone, which varies across the band.^{34,35}

This chapter is focused on our initial attempts to explore the heterogeneous character of the intermolecular dynamics of liquid water (HOD in D₂O) with 2DIR spectroscopy. The composite dynamics measured with frequency-integrated techniques in Chapter 5 result from an average over all initial environments within the liquid, and thus serve as a point of departure for our treatment of frequency-dependent dynamics. Although these investigations are still underway, we have made significant progress in overcoming experimental obstacles to quantitatively measure the 2DIR spectrum of liquid water and interpret the experimental results. As with our earlier time-resolved IR investigations of intermolecular dynamics in water, this study relies on a close collaboration between experiments and computer simulations to connect observables with molecular details.

6.2 IR signatures of heterogeneous dynamics

The OH vibrational frequency of an HOD molecule is governed by forces exerted on the oscillator by other molecules within the liquid. Simulations indicate that the nearest neighbor contribution is dominant,²³ resulting in the approximation that oscillators which absorb on the red side of the line take part in stronger hydrogen bonds than those that absorb to the blue side. It is reasonable to assume that the extreme blue edge of the linear absorption spectrum contains contributions from oscillators that are not involved in a hydrogen bond. Absorption by non-bonded oscillators has been proposed to explain the asymmetry observed in the static OH frequency distribution from recent computer simulations, and tested by decomposing the distribution according to molecules that are hydrogen-bonded and non-hydrogen-bonded (defined by imposing geometrical cut-offs for a hydrogen bond).^{22,36} The

results, plotted in Fig. 6-1, demonstrate that the two distributions overlap but that non-bonded oscillators are indeed a dominant contribution at the highest frequencies.

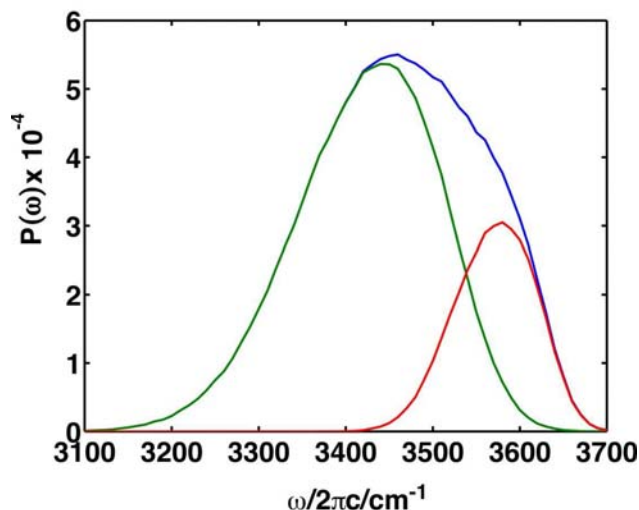


Figure 6-1. (Color) Contributions to the static OH vibrational frequency distribution (blue) from oscillators that are involved in a hydrogen bond (green) and those which are not hydrogen bonded (red), as calculated by EG from a computer simulation of a single HOD molecule in a bath of D₂O.

To investigate the effect of initial hydrogen bonding environment on vibrational dephasing dynamics, Eaves and Geissler (EG) simulated the time evolution of sub-ensembles having a narrow initial frequency distribution.³⁶ They characterized the time-dependence of these distributions by the dynamic Stokes shift, defined by:

$$S(\tau) = \frac{\overline{\omega(\tau)} - \overline{\omega(\infty)}}{\overline{\omega(0)} - \overline{\omega(\infty)}} \quad (6-1)$$

where $\overline{\omega(\tau)}$ is the first moment of the frequency distribution at time τ , and $\tau = 0$ and ∞ are the initial and long time limits. Linear response theory predicts that the relaxation of the initial non-equilibrium distribution of frequencies reflects the frequency fluctuations at equilibrium, and therefore $S(\tau) = C(\tau)/C(0)$. Within this limit, the dynamic Stokes shift is independent of the center frequency of the initial distribution.

The simulation results exhibit behavior contrary to the predictions of linear response (Fig. 6-2), as $S(t)$ calculated from a distribution initially centered on the far red side of the band differs from that calculated on the blue side, both of which are distinct from the normalized correlation function. In particular, relaxation from a population chosen from the red side of the band exhibits a faster decay and more pronounced oscillation at 150 fs than the distribution on the blue side, which shows an additional weak feature at the oscillation frequency of the libration. These vibrational dynamics clearly reflect heterogeneities in the intermolecular dynamics. Dephasing signatures of strong hydrogen-bonded molecules, such as a prominent 150 fs hydrogen-bond oscillation, are dominant on the red side of the line, and the blue side shows features expected of non-hydrogen-bonded molecules, such as a large amplitude libration. The long time behavior of the dynamic Stokes shift is less intuitive, but an analysis beyond the first moment of the frequency fluctuations reveals behavior characteristic of a barrier crossing in the initial blue-side distribution, while this behavior is mostly absent from the initial red-side distribution. These results will be discussed in more detail elsewhere. Moller and co-workers have noted similar spectrally heterogeneous behavior.³⁷ We stress that the dynamics predicted by these simulations depend on the water model and method of calculation, and thus require experimental verification.

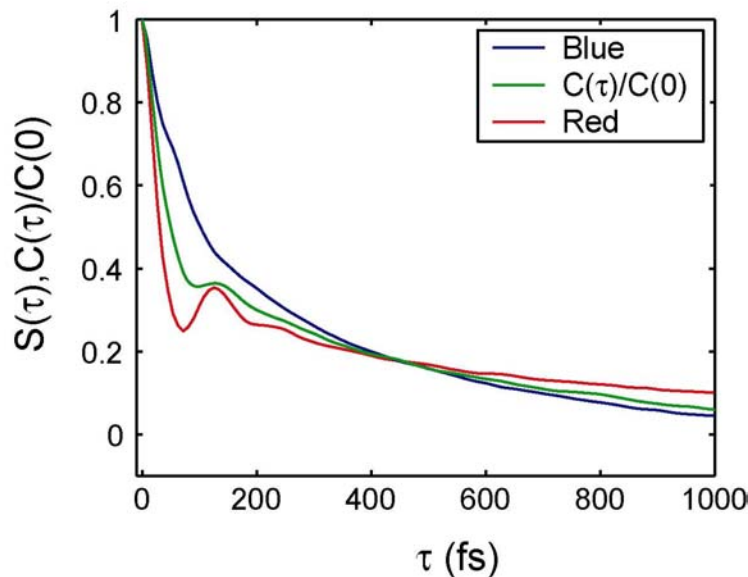


Figure 6-2. (Color) Normalized time-dependent vibrational Stokes shifts and frequency correlation function for the OH oscillator of a single HOD molecule in a bath of D_2O , as calculated from the simulations of EG. The time-dependent Stokes shifts are obtained by observing the time dependent relaxation of a distribution of molecules whose initial OH frequencies are greater than (blue) or less than (red) 150 cm^{-1} from the static distribution.

6.3 2DIR spectroscopy

2DIR spectroscopy is a resonant four wave mixing experiment that incorporates a local oscillator (LO) field to heterodyne-detect the nonlinear signal.²⁶ The fundamental physics of this technique are analogous to the theory and experiments discussed in Chapters 3 and 5, but the introduction of a LO tracks the time evolution of the third-order polarization, revealing more information about the system, bath and system-bath couplings than is available from conventional FWM spectroscopies. In its most general form, the 2D experiment is performed as a function of all three time delays (or their conjugate frequencies) between the input and LO pulses, defined in Fig. 6-3 as the evolution (τ_1), waiting (τ_2), and detection (τ_3) periods. However, the results are often plotted as a 2D function of the

evolution and detection variables for fixed waiting times, since it is most useful to compare the state of the system during periods in which it oscillates in coherent superpositions of the vibrational eigenstates (ignoring \tilde{R}_{vib}^{III} , which is only important when all three input pulses overlap in time)³⁸. Much of the literature has focused on interpreting the Fourier transform (FT) 2D spectrum (as a function of ω_1 and ω_3 , the conjugate variables to τ_1 and τ_3) due to the simple physical picture associated with this representation of the results,^{26,39} but the time-domain representation has advantages when the field envelope is extracted from the signal.

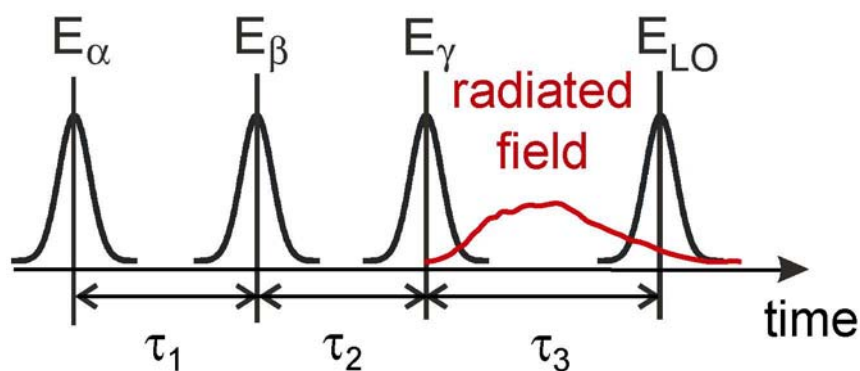


Figure 6-3. (Color) Time-ordering of pulses in a 2DIR experiment.

The majority of published 2DIR experiments are aimed at measuring structural information about model protein systems or small polypeptides,^{26,39-43} rather than the revealing bath dynamics through system-bath interactions. Nonetheless, the intuition built from these studies is helpful to understand the spectra presented here. A FT-2DIR surface is a map of the probability amplitudes that the system oscillates at a frequency ω_1 during the evolution period, and a frequency ω_3 during the detection period. The spectrum of a single anharmonic vibrational oscillator exhibits two peaks: a diagonal peak that corresponds to oscillation at the fundamental transition frequency during both time periods (centered at

$\omega_1 \approx \omega_3 \approx \omega_{10}$), and an oppositely signed peak below the diagonal that corresponds to oscillation at the fundamental and anharmonically shifted overtone frequencies during the evolution and detection periods, respectively (centered at $\omega_1 \approx \omega_{10}$, $\omega_3 \approx \omega_{21}$). The quantum mechanical origin of these two features is the evolution of the system density matrix due to interactions with the input fields, as represented by the Feynman diagrams in Fig. 3-3. When the system consists of multiple oscillators that are well separated in frequency (e.g. ω_{10a} and ω_{10b}), each contributes a set of peaks to the FT-2DIR spectrum, but additional off-diagonal features can arise due to oscillation at one frequency during the evolution and another during detection (centered at $\omega_1 \approx \omega_{10a}$, $\omega_3 \approx \omega_{10b}$, etc.). The presence and amplitude of these cross-peaks depends on the couplings between the oscillators (a and b in this case).²⁶

The 2D lineshape of each peak reflects the timescales for broadening relative to the experimental timescale. Fig. 6-4 presents an illustration of linear FTIR and 2D lineshapes in the slow and fast modulation limits (in traditional terms, inhomogeneous and homogeneous broadening).^{44,45} The former case corresponds to a collection of oscillators, each of which has a slightly different absorption frequency (i.e. a continuous distribution for macroscopic samples). Because the frequency of a given oscillator is constant over the timescale of the experiment, the 2D lineshape is composed of a superposition of diagonal peaks (and corresponding overtone peaks). However, when the dominant broadening mechanism is fast compared to the experimental timescale, the 2D lineshape is more symmetric. The linear absorption spectra for these two cases are quite similar, making it extremely difficult to differentiate between the two on the basis of an FTIR lineshape, which highlights the advantage of a 2DIR experiment.

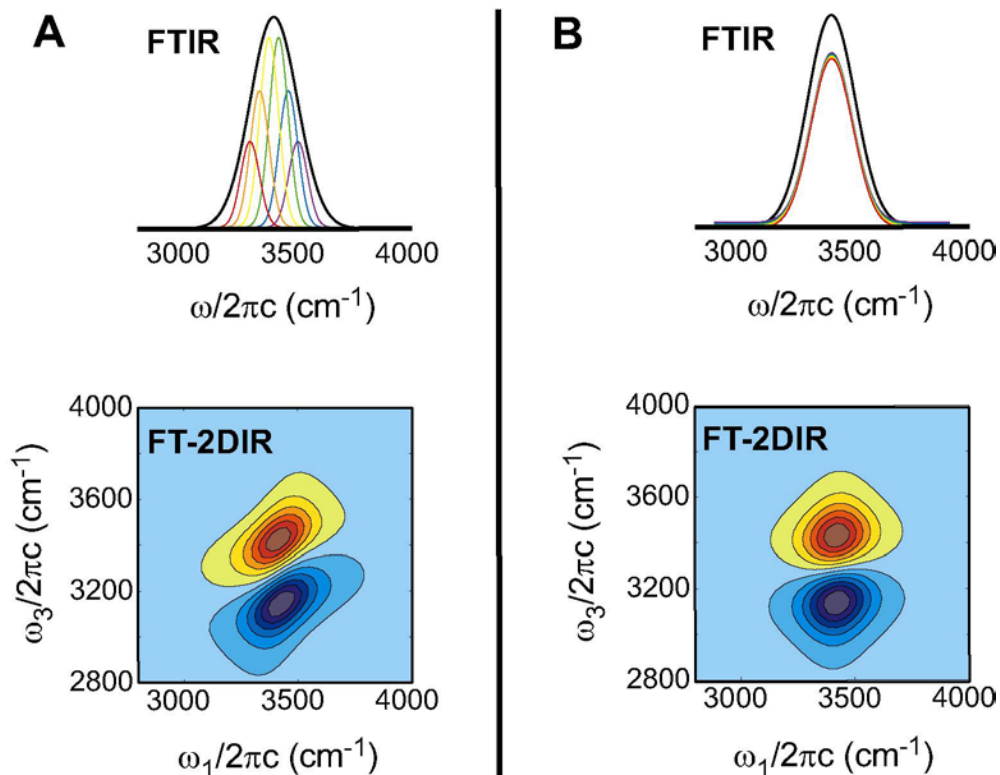


Figure 6-4. (Color) A cartoon of the 1D and 2D vibrational lineshapes in the slow (A) and fast (B) modulation limits. The thin, colored lines in the top panels represent the absorption spectra for individual molecules in each case.

While it is possible to extract dynamical information from 2D lineshapes for a single waiting time, a relaxation experiment, in which 2D surfaces are collected as a function of the waiting time, is a much better indicator of the timescales for vibrational dynamics. Varying the time between pulse pairs effectively changes the characteristic timescale of the experiment. Therefore, a relaxation experiment measures the time-dependent evolution of the 2D features from the slow to fast modulation limits (assuming the IR pulses and characteristics of the vibrational transition(s) are sufficiently fast to observe the slow modulation limit for $\tau_2 = 0$). The relaxation experiment is somewhat analogous to a 3PEPS experiment, in which the waiting time dependence of the integrated echoes are recorded,

except that the 2D surfaces provide much more detailed information about the system than the 1D integrated echoes.

The relaxation experiment follows the time-dependent interactions between system states through the waiting time dependence of the peak amplitudes in the spectrum. For the present case, the time-dependences of the off-diagonal cross peaks are particularly important, since they indicate bath-induced couplings between the system states. In fact, the broadening of individual peaks discussed in the preceding paragraph is a subset of this behavior: peaks initially elongated along the diagonal are due to a distribution of environments, and the τ_2 -dependent broadening results from the bath-induced “transitions” between environments. This picture connects the idea of heterogeneous dynamics to the 2DIR experiments, because the frequency distribution arises from the distribution of intermolecular distances and angles around OH oscillators, and the “transitions” correspond to the structural reorganization of local environments. In the case of homogeneous dynamics, where the energetic barrier to structural reorganization is independent of environment, the 2D lineshape should broaden symmetrically. However, in the case of spectrally heterogeneous dynamics, the time-dependent line broadening should be frequency-dependent. These qualitative ideas are explicated by quantitative modeling in the Discussion section.

6.4 Experimental methods

Many of the experimental details to record the 2DIR relaxation experiment on water are equivalent to those presented for other experiments in earlier chapters, and will only be discussed briefly here. A two-stage BBO/KNbO₃ pumped by a Ti:sapphire multi-pass amplifier generated mid-IR pulses at a 1 kHz repetition rate. The pulses had a center

wavelength of $\sim 3 \mu\text{m}$ and bandwidth sufficient to excite the fundamental and most of overtone OH vibrational transitions of the sample. We adjusted the amount and type of IR materials in the beam path to compress the pulses at the sample, which typically resulted in sub-50 fs pulse durations as characterized by SHG-FROG. After collimation by a telescope, and overlap with a mode-matched visible tracer, the beam traversed a five-beam Mach-Zender interferometer (Fig. 6-5). The interferometer is equivalent to the one described in Chapter 5, except that all five beams are needed for the 2DIR experiment. The linear polarizations of all five beams were parallel.

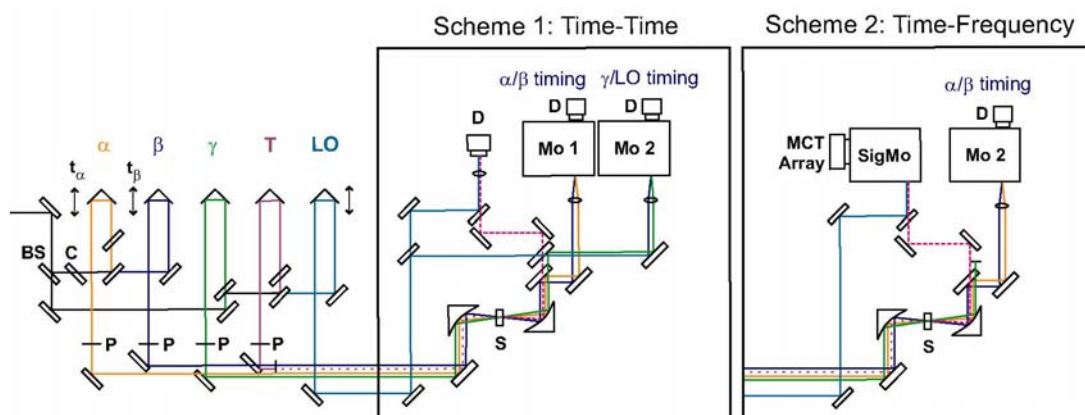


Figure 6-5. (Color) Experimental layout of the IR interferometer and detection geometries for the 2DIR experiment. Details of optical components are provided in Chapter 5. BS: 50/50 IR beamsplitter; C: compensation plate; P: polarizer; S: water jet sample; Mo: monochromator; D: liquid nitrogen cooled InSb detector.

Four of the beams exiting the interferometer, arranged in a traditional boxcar geometry, were focused into the sample by an off-axis parabolic mirror. Three of the beams, which had similar pulse energies, were used as the excitation pulses, while the fourth beam was a tracer for alignment and timing purposes and was therefore blocked during the experiment. The peak of a second order autocorrelation in a AgGaAs crystal placed at the sample position set the temporal overlap between pulse pairs to within ± 5 fs.

An additional 50/50 beamsplitter after the sample combined nonlinear field radiated into the $\mathbf{k}_{sig} = -\mathbf{k}_\alpha + \mathbf{k}_\beta + \mathbf{k}_\gamma$ phase-matched direction with the LO (the fifth beam created in the interferometer). We carefully overlapped the two beams in space with two sets of iris and detector pairs placed ~ 4 m apart. The LO zero timing was determined by the most intense fringe of an interferogram between the LO and tracer (with the signal blocked). Although the error in this measurement is less than the fringe spacing (± 10 fs), the radiated field does not necessarily follow the exact path of the tracer, making the error in the zero timing of the LO relative to the signal much larger (about ± 40 fs). The LO intensity was adjusted relative to the signal intensity to achieve the best experimental signal to noise ratio.

We measured the heterodyne signal for a fixed waiting time in one of two ways (Fig. 6-5): by detecting the frequency-integrated interference between the signal and LO as a function of the τ_1 and τ_3 pulse delays (scheme 1), or by detecting the frequency-dispersed interference between the signal and LO as a function of τ_1 for fixed τ_3 (scheme 2). The former case used a liquid nitrogen cooled InSb single element detector, while the latter employed a spectrometer and liquid nitrogen cooled 64-element MCT array detector. All pulse delays were stepped in 2 fs increments (the oscillation period is 10 fs) to limiting values for which the signal was indiscernible after a single scan. The spectral resolution of the array was ~ 8 cm^{-1} . In scheme 1, we collected the time-time surface by scanning the τ_3 delay for each fixed τ_1 delay. For scheme 2, the array recorded an entire spectrum for each τ_1 delay. To reduce experimental noise, a mechanical chopper placed in one of the excitation arms of the interferometer blocked every other pulse, allowing lock-in or differential detection in schemes 1 and 2, respectively.

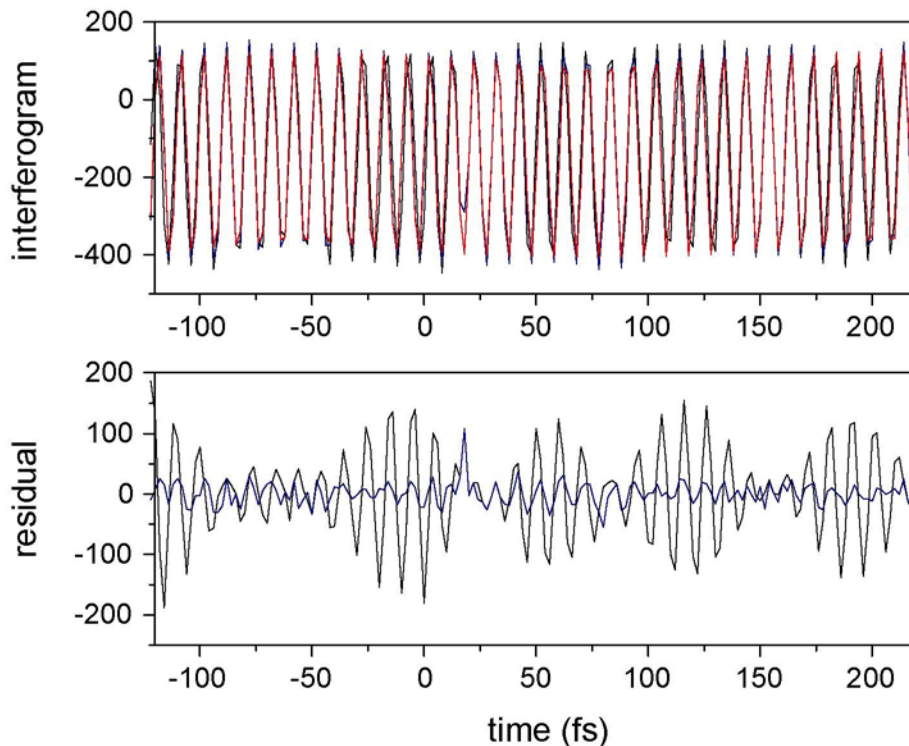


Figure 6-6. (Color) (Top) Experimentally measured interferogram between pulses α and β plotted as a function of encoder-determined timings (black), along with a sinusoidal fit to the data (red) as described in the text. The interpolated interferogram is also shown (blue). (Bottom) The difference between the original interferogram and the fit (black) and between the interpolated interferogram and the fit (blue).

The signal measured in the two schemes are related by a Fourier transform in the detection variables (τ_3 and ω_3). Many of the advantages of one over the other follow standard frequency verses time arguments, so the optimal detection scheme depends on the dynamical timescales of the sample and noise characteristics of the IR source. However, scheme 2 has the added advantage that the array detector collects the entire ω_3 frequency axis simultaneously. All of the 2DIR experiments reported to date have utilized a time-frequency detection method similar to scheme 2, mostly because proteins lend themselves better to this technique. The vibrational dynamics in water are fast compared to most other systems, but we have found that time-frequency detection still requires a shorter amount of data collection time (typically 20 min/surface) than the time-time scheme (typically 40 min/surface) to

achieve similar signal to noise levels (due to the use of an array detector). However, the experimental data presented in this Chapter was all recorded using the time-time method of scheme 1, although comparisons to data collected by scheme 2 were used to evaluate the quality and repeatability of the 2D surfaces.

Interferometric detection requires path length stability and knowledge of all pulse delays to within a fraction of a wavelength. To satisfy these conditions, we performed the experiment on floating optical tables using extremely stable pedestals/mounts for all optics, and enclosed the entire experiment to prevent unwanted air currents. Retroreflectors mounted on high resolution (10 nm) computer controlled translation stages (Aerotech ANT-25L) introduced pulse delays. Nonetheless, we observed distorted lineshapes in the FT-2DIR spectrum due to small step size inaccuracies. To eliminate these timing errors, relative delays were monitored experimentally by dispersing spatially overlapped beams in a monochromator after the sample (Fig. 6-5), and measuring their interference at a single frequency. We fit the resulting interferograms (Fig. 6-6) to single sinusoidal curves, from which we determined the experimentally measured delay times by projecting the measured intensity onto the fit. A cubic spline interpolation corrected the resulting data points to an evenly spaced time grid for data manipulation with fast Fourier transform algorithms. The interferogram between the α and β beams measured the τ_1 timing (schemes 1 and 2), while an interferogram between the γ and LO beams measured the τ_3 timing (scheme 1 only, data not shown). We did not experimentally monitor the τ_2 timing, since it is fixed for each surface. The stage position errors were often systematic – it typically took smaller steps than requested for a few microns, then took larger steps for the next few microns. Step errors

were as large as ± 1 fs. It is important to note that this procedure does not aid in determining the zero (absolute) timing between pulse pairs.

The sample consisted of a dilute solution of HOD in D₂O to avoid interactions between individual OH oscillators.⁴⁶ We used a particularly low optical density (< 0.2 at 3400 cm^{-1}) for the 2D experiments to avoid spectral filtering due to reabsorption of the signal. As with earlier studies, the sample was flowed as a $50 \text{ }\mu\text{m}$ path length jet to prevent accumulated heating effects from absorption of multiple shots, and to eliminate signal contributions from sample cell walls.

6.5 Treatment of the data

In the limit that the LO is much more intense than the field radiated by the third order polarization, $|E_{LO}|^2 \gg |E_{rad}|^2$, the signal measured by scheme 1 is:

$$S(\mathbf{k}_{sig}, t_{LO}, t_{\beta}, t_{\alpha}) = \int_{-\infty}^{\infty} \left| E_{rad}(\mathbf{k}_{sig}, t_{\beta}, t_{\alpha}; t) E_{LO}(\mathbf{k}_{sig}, t_{LO}; t) \right|^2 dt \quad (6-2)$$

where we have used pulse-labeled delay times (defined in Fig. 3-4) for clarity. The traditional pulse delay times are $\tau_1 = t_{\beta} - t_{\alpha}$ and $\tau_2 = t_{\gamma} - \max(t_{\beta} - t_{\alpha})$. When $t_{\alpha} > t_{\beta}$ ($\tau_1 > 0$),

\tilde{R}^I density matrix pathways tend to dominate the signal, while \tilde{R}^{II} pathways dominate for $t_{\beta} > t_{\alpha}$ ($\tau_1 < 0$); we refer to these as the rephasing and nonrephasing signals, respectively.

To obtain absorptive lineshapes, contributions from both of these signals must be included in the FT-2DIR spectrum.^{26,39,47} In principal, this could be accomplished by collecting the entire surface (for a fixed τ_2 delay) as a continuous function of the τ_1 delay by decreasing t_{β} from its largest value (most negative τ_1) until $t_{\beta} = t_{\alpha}$ ($\tau_1=0$), then increasing t_{α} to its largest

value (most positive τ_1), scanning τ_3 at each τ_1 as described above. The FT-2DIR spectrum would be the 2D Fourier transform of this surface. The experimental difficulty, however, is that it is nearly impossible to determine the exact point at which $t_\beta = t_\alpha$. Timing errors of this type distort the FT lineshapes due to a discontinuity of the signal phase along τ_1 . Therefore, the rephasing and nonrephasing half-surfaces are collected and transformed separately so that the τ_1 timing error in each can be adjusted independently (as discussed below), then added together to obtain the complete FT-2DIR spectrum. For both half-surfaces, the α and β pulses are scanned beyond the $\tau_1 = 0$ defined by the autocorrelation to ensure that each includes the actual $t_\beta = t_\alpha$ pulse overlap.

There are three zero timing errors in the time-time spectra recorded according to the experimental procedure in the preceding paragraph, which we define by $\Delta\tau_{1R}$, $\Delta\tau_{1N}$ and $\Delta\tau_3$. The first two correspond to the zero timing error between the α and β pulses in the rephasing and nonrephasing half-surfaces, and the last is the error between the γ and LO pulses, which is common to both. Before discussing the transform and phasing procedure, we note the projection-slice theorem,⁴⁸ which relates the 2D signal to the dispersed pump-probe signal (PP) at the same τ_2 pulse delay:

$$PP(\omega_3, \tau_2) \approx \text{Re} \left[\int_{-\infty}^{\infty} S(\omega_3, \tau_2, \omega_1) d\omega_1 \right] = \text{Re} \left[S(\omega_3, \tau_2, \tau_1 = 0) \right]. \quad (6-3)$$

We have neglected the spectral filtering of the LO in the PP. Therefore, the τ_1 step closest to the actual $t_\beta = t_\alpha$ pulse overlap was determined independently for the rephasing and nonrephasing surfaces by Fourier transforming each slice in the detection period and finding the slice for each within the τ_1 zero timing uncertainty that most closely matched the PP. Each half-surface was truncated at that τ_1 step, and both were then Fourier transformed along

the evolution period. The resulting rephasing and nonrephasing surfaces were summed, and the ω_1 projection of the FT-2DIR spectrum was compared to the PP spectrum according to (6-3). Small changes to the three linear phase values to improve the comparison phased the FT-2DIR spectrum.

6.6 Results and Discussion

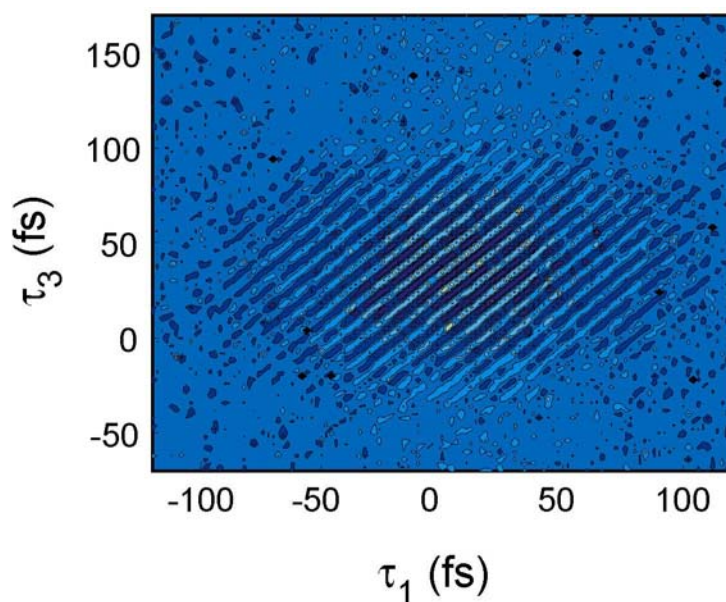


Figure 6-7. (Color) Filled contour plot of a typical experimentally measured 2D time-time surface of HOD in D₂O for a waiting time of $\tau_2 = 160$ fs. Twelve equally spaced contours separate the minimum and maximum values.

Fig. 6-7 displays a typical time-time 2D surface for $\tau_2 = 160$ fs (the rephasing and nonrephasing surfaces have been joined at $\tau_1 = 0$ for plotting). It oscillates as a function of both the τ_1 and τ_3 pulse delays, as expected from Eq. 3-25, and the maximum of the envelope is centered at positive τ_1 , which is consistent with the peak shift value at this waiting time. Although the influence of the LO on the 2D signal complicates a direct comparison of the results to the integrated echo results, a projection of the absolute value of the 2D surface onto

the τ_1 axis serves as a qualitative comparison of the two sets of experiments. A Gaussian function centered at $\tau_1 = 14$ fs fits the projection for the $\tau_2 = 160$ fs surface (Fig. 6-8), which is close to the 12.7 fs value obtained in the 3PEPS experiment of Chapter 5. To further this comparison, as well as investigate the possibility of spectrally heterogeneous dynamics, 2D surfaces were typically recorded at values of τ_2 corresponding to features in the 3PEPS decay, such as the origin (0 fs), trough (80 fs) and peak (160 fs) of the oscillation and the long time decay (240 fs, 500 fs, etc.), to investigate the effect of dynamical heterogeneities on these features. Fig. 6-8 compares the projected echoes from the 2D surfaces at these waiting times with the 3PEPS results. Other than the $\tau_2 = 0$ fs waiting time, which is strongly influenced by the solvent non-resonant response in the 2D experiments,⁴⁹ the two quantities agree rather well.

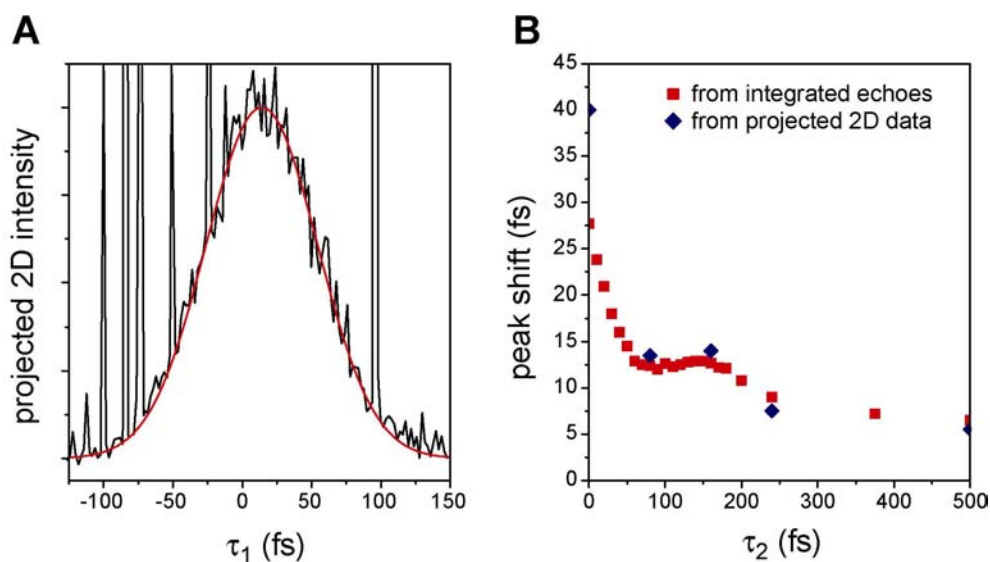


Figure 6-8. (Color) Comparison to projections of the 2D data to the experimentally measured integrated echo data from Chapter 5. (Left) Projection of the absolute value of the $\tau_2 = 160$ fs surface onto the τ_1 axis (black) and the Gaussian function that fits the data (red). (Right) Comparison of the time-center of the 2D projections with the 3PEPS data.

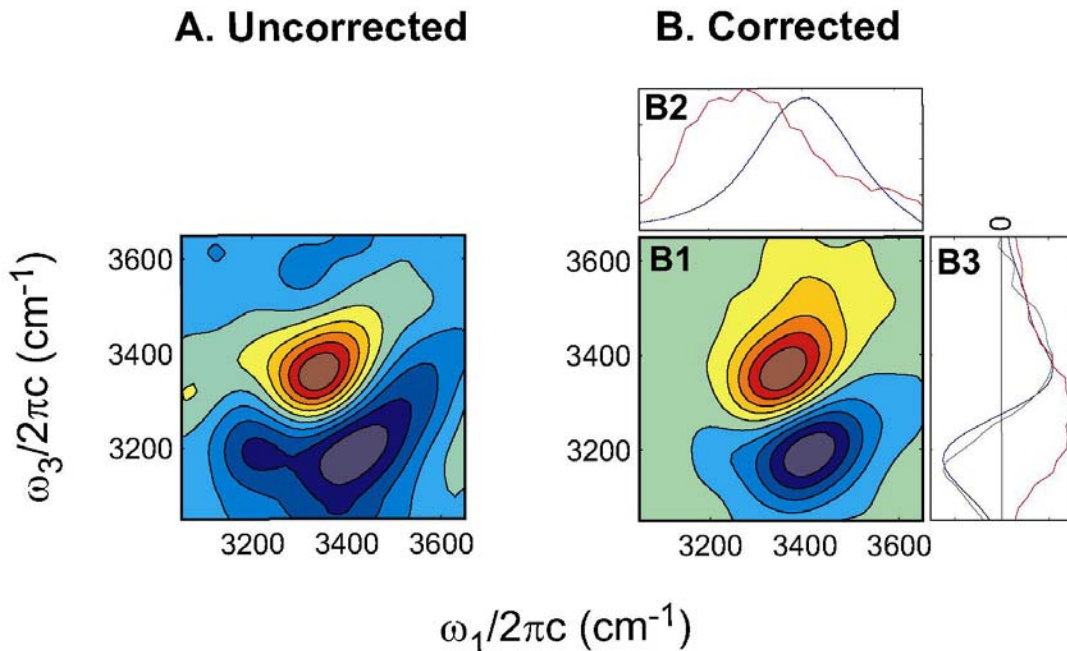


Figure 6-9. (Color) FT-2DIR surfaces for $\tau_2 = 160$ fs. Both surfaces are for the same time-time dataset, except that the time axes were not corrected with the interferograms in A. The corrected surface (B1) is centered at a slightly lower frequency than the peak of the linear absorption spectrum (B2, blue) in ω_1 due to the OPA tuning (pulse spectrum B2, red). The projection of the 2D surface on to the ω_3 axis (B3, blue) is compared with the dispersed pump-probe (B3, green). The pulse spectrum (B3, red) influences the shape of the surface and pump-probe.

The τ_1 and τ_3 time axes for each surface were corrected from the interferograms as described above. The signal to noise of the τ_1 interferogram was usually sufficient to determine the actual stage delays because it was scanned slowly relative to the data collection rate, permitting a significant amount of signal averaging on each point. In contrast, the τ_3 axis was scanned quickly, resulting in relatively noisy interferograms. However, we have determined that the step size errors are reproducible for each stage, so a well-averaged τ_3 interferogram guided the determination of actual stage delays along this axis. After performing the cubic spline interpolation to an evenly spaced grid of time points, each surface was transformed and phased to the corresponding dispersed pump-probe as discussed above. We found that the dispersed pump-probes did not change significantly from day to

day (as long as the pulse spectrum did not change significantly), so dispersed pump-probes for only one or two of the waiting times were normally recorded to check consistency with well averaged scans taken at another time.

A set of FT-2DIR surfaces for several waiting times is plotted in Fig. 6-10b. Each surface is the average of two datasets to reduce experimental noise, and the contour levels in each surface have been normalized for the sake of comparison. The fundamental and anharmonically shifted overtone features are clearly discernable as the positive (yellow/red) and negative (blue) peaks. They are centered at $\sim 3375 \text{ cm}^{-1}$ in the ω_1 dimension, which is a slightly lower frequency than the peak of the linear FTIR ($\sim 3415 \text{ cm}^{-1}$) because the pulse is centered near 3275 cm^{-1} to ensure sufficient overlap with the overtone transition (see Fig. 4-8). The fundamental feature lies just above the diagonal, as expected for broad lines because destructive interference with the overtone feature shifts the peak to slightly higher frequencies in the ω_3 dimension. The peak frequencies in the $\tau_2 = 0 \text{ fs}$ surface are slightly different from the other three due to weak contributions from the nonresonant response of the solvent and from \tilde{R}_{vib}^{III} , both of which contribute only when all pulses are overlapped.

As expected, peaks in the early τ_2 surfaces are elongated along the diagonal, demonstrating that there is significant broadening on timescales longer than the experiment. The lineshapes generally become more symmetric and rotate towards the horizontal as the waiting time is increased, indicating a transition to the fast modulation limit in the later surfaces. The qualitative broadening timescales are consistent with the composite vibrational dynamics measured in Chapter 5, but a wealth of additional information about the dynamics is available from the frequency dependence of the broadening. The broadening in the relaxation experiment does not follow a simple model, so we have used calculations and

computer simulations to aid in the analysis. Before discussing these comparisons, we comment briefly on the reproducibility of the experimental data.

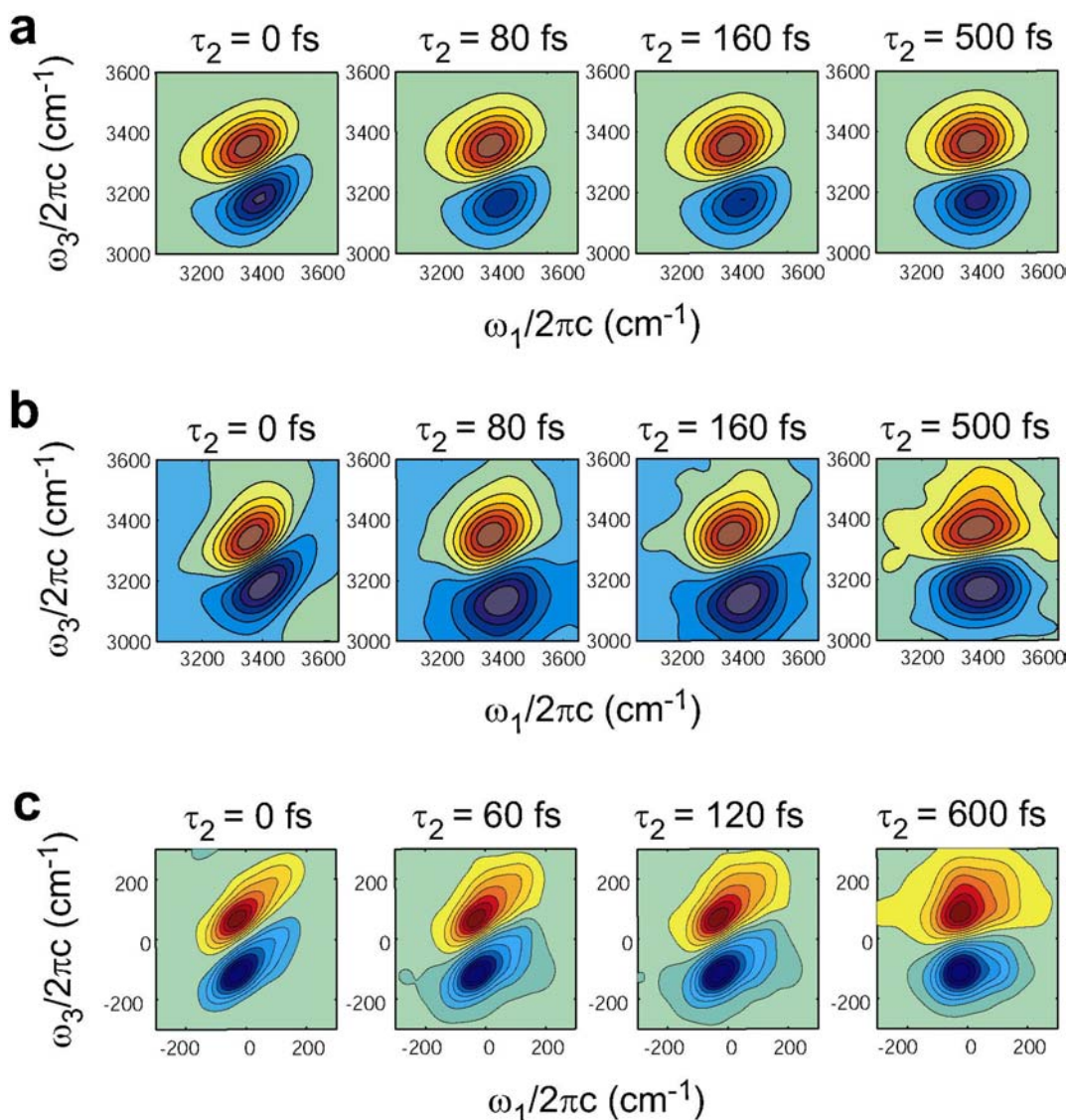


Figure 6-10. (Color) FT-2DIR relaxation spectra for the waiting times indicated. Twelve equally spaced contour levels from the minimum to the maximum of the signal are plotted for each surface. (a) Surfaces in the top row calculated from a response function treatment that assumes spectrally homogeneous dynamics. (b) The middle row is experimental data, as described in the text. (c) Surfaces in the bottom row are from the computer simulation results of EG, which exhibit spectrally heterogeneous dynamics. The axes are shifted by the mean of the transition frequency.

We repeated the relaxation experiment several times to determine the effect of experimental conditions and reproducibility on the FT-2DIR surfaces. Although surfaces of the same waiting time taken on a particular day were largely reproducible, surfaces recorded on different days exhibited clear variations, especially at the lowest contour levels. Pulse characteristics, which were not taken into account for the 2D experiments, certainly influence the lineshapes, however we attribute the largest source of error to continued difficulties with the determination and correction of pulse delays and phase drifts. By employing time-frequency detection of the 2D surface, as in scheme 2 (Fig. 6-5), more recent experiments have eliminated translation stage errors in the τ_3 dimension, but continue to experience problems measuring highly reproducible surfaces. Nonetheless, by recording a large number of surfaces, clear trends have emerged. The surfaces plotted in Fig. 6-10b were chosen to highlight the reproducible aspects of the data.

Spectrally heterogeneous dynamics, in which the vibrational dynamics of an oscillator depend on its initial frequency, causes the 2D lineshapes to broaden asymmetrically in the relaxation experiment. To better understand how heterogeneous dynamics could be manifested in the results we compare and contrast the 2D lineshapes of two sets of calculations, one of which is based on the response function formalism in Chapters 2 and 5 and the other based on the computer simulations of EG. The response function treatment assumes the OH oscillators are linearly coupled to a set of harmonic oscillators, and therefore truncates the Cumulant expansion after the second term to express the vibrational dynamics in terms of a two-point correlation function. This approach inherently assumes spectrally homogeneous dynamics. We calculated the 2D surfaces using this formalism (assuming 50 fs transform-limited pulses), along with the frequency

correlation function, reorientational correlation function, and population lifetime that resulted from our analysis in Chapter 5. These results, presented in Fig. 6-10a, model the relaxation experiment for a system that exhibits spectrally homogeneous dynamics equivalent to those measured in Chapter 5.

On the other hand, we have already introduced results from the simulations of EG that suggest the dynamics are spectrally heterogeneous. They have explicitly calculated the full four-point frequency correlation from their simulation to model the relaxation experiment.³⁶ The surfaces, presented in Fig. 6-10c, assume the IR pulses are delta functions in time and do not take into account reorientations or population relaxation. They therefore represent an idealized case for the detection of spectrally heterogeneous dynamics with a 2DIR relaxation experiment. We have presented surfaces from slightly different waiting times for a better comparison because the timescales in the simulation differ slightly from the experimentally measured timescales (Chapter 5).

There are similarities, but also many clear differences between the two sets of calculated surfaces. Both are initially elongated along the diagonal, but become more symmetric as the waiting time as increased. The $\tau_2 = 0$ fs surface in Fig. 6-10c is more elongated than its counterpart in Fig. 6-10a, mostly because the former calculation assumes infinitely short IR excitation and LO pulses. However, the striking difference between the two sets is the off-diagonal structure resulting from the simulation. We interpret these lobes as cross peaks between the hydrogen bonded and non-hydrogen-bonded species that result when molecules which are initially non-bonded form hydrogen bonds and visa versa. These cross peaks appear in the $\tau_2 = 0$ fs surface, even for infinitely short pulses, due to hydrogen bonds that are made and broken on the relaxation timescale of the experiment, but become

much more prominent as the waiting time is increased. They are a clear indication that the 2D lineshapes are sensitive to initial environment. The behavior of the diagonal and cross peaks as a function of waiting time reveals the heterogeneous dynamics of molecules that are initially hydrogen bonded and those that are not initially bonded, as well as their interconversion.

The experimentally measured 2D lineshapes in Fig. 6-10b have some of the character of the bimodal distribution and heterogeneous dynamics predicted by the simulation, but the deviations from the homogeneous case are not as prominent. In fact, the early waiting time behavior more closely follows the surfaces calculated within the response function formalism, while the lineshapes exhibit distortions reminiscent of the simulation results at later waiting times. In particular, the slight elongation of the fundamental peak in the ω_3 dimension is especially apparent in the experimental results. It is not surprising that the heterogeneous character is not as large as the surfaces in Fig. 6-10c, since they were calculated assuming infinitely short pulses, and did not account for other vibrational dynamics that cause relaxation in FWM experiments. Additionally, the slowest timescales in the simulation, which correspond to large-scale structural rearrangements (such as hydrogen bond making and breaking), are significantly faster than the experimentally measured decay of the correlation function. Therefore, these rearrangements are more significant in the simulation results as the system relaxes during τ_1 and τ_3 , and thereby influence individual 2D surfaces calculated from the simulations more than those from experiments.

A quantitative comparison of the experimentally measured relaxation experiment to the two sets of calculations requires more highly reproducible data because the heterogeneous dynamics most affect the lowest few contours in the 2D lineshapes. Efforts

are currently underway to perfect the experimental measurements, including time-frequency detection of the nonlinear signal and active phase stabilization. Nonetheless, the preliminary results clearly indicate that the 2D relaxation experiment exhibits signatures of spectrally heterogeneous dynamics expected of hydrogen bond making and breaking events.

References

- (1) Walrafen, G. E. *J. Chem. Phys.* **1964**, *40*, 3249.
- (2) Eisenberg, D.; Kauzmann, W. *The Structure and Properties of Water*; Clarendon Press: Oxford, 1969.
- (3) *The Physics and Physical Chemistry of Water*; Franks, F., Ed.; Plenum Press: New York, 1975; Vol. 1.
- (4) Sceats, M. G.; Stavola, M.; Rice, S. A. *J. Chem. Phys.* **1979**, *70*, 3927.
- (5) Stanley, H. E. *J. Phys. A* **1979**, *12*, L329.
- (6) Stillinger, F. H.; Weber, T. A. *J. Phys. Chem.* **1983**, *87*, 2833.
- (7) Ohmine, I.; Tanaka, H. *Chem. Rev.* **1993**, *93*, 2545.
- (8) Ohmine, I. *J. Phys. Chem.* **1995**, *99*, 6767.
- (9) Luzar, A.; Chandler, D. *Nature* **1996**, *379*, 55.
- (10) Luzar, A.; Chandler, D. *Phys. Rev. Lett.* **1996**, *76*, 928.
- (11) Richert, R. *J. Phys. : Condens. Matter* **2002**, *14*, R703.
- (12) Giovambattista, N.; Starr, F. W.; Sciortino, F.; Buldyrev, S. V.; Stanley, H. E. *Phys. Rev. E* **2002**, *65*, 041502.
- (13) Giovambattista, N.; Mazza, M. G.; Buldyrev, S. V.; Starr, F. W.; Stanley, H. E. *J. Phys. Chem. B* **2004**, *ASAP Article*.

- (14) Stillinger, F. H.; Weber, T. A. *Science* **1984**, *225*, 983.
- (15) Belch, A. C.; Rice, S. A. *J. Chem. Phys.* **1987**, *86*, 5676.
- (16) Jedlovszky, P.; Brodholt, J. P.; Bruni, F.; Ricci, M. A.; Soper, A. K.; Vallauri, R. *J. Chem. Phys.* **1998**, *108*, 8528.
- (17) Ludwig, R. *Angew. Chem. Int. Ed.* **2001**, *40*, 1808.
- (18) Laenen, R.; Simeonidis, K.; Laubereau, A. *Bull. Chem. Soc. Jpn.* **2002**, *75*, 925.
- (19) Novak, A. Hydrogen bonding in solids. Correlation of spectroscopic and crystallographic data. In *Structure and Bonding*; Dunitz, J. D., Hemmerich, P., Holm, R. H., Ibers, J. A., Jorgenson, C. K., Neilands, J. B., Reinen, D., Williams, R. J. P., Eds.; Springer-Verlag: New York, 1974; Vol. 18; pp 177.
- (20) Mikenda, W. *J. Mol. Struct.* **1986**, *147*, 1.
- (21) Rey, R.; Moller, K. B.; Hynes, J. T. *J. Phys. Chem. A* **2002**, *106*, 11993.
- (22) Lawrence, C. P.; Skinner, J. L. *J. Chem. Phys.* **2003**, *118*, 264.
- (23) Fecko, C. J.; Eaves, J. D.; Loparo, J. J.; Tokmakoff, A.; Geissler, P. L. *Science* **2003**, *301*, 1698.
- (24) Demirdöven, N.; Khalil, M.; Golonzka, O.; Tokmakoff, A. *J. Phys. Chem. A* **2001**, *105*, 8025.
- (25) Demirdöven, N.; Khalil, M.; Tokmakoff, A. *Phys. Rev. Lett.* **2002**, *89*, 237401.
- (26) Khalil, M.; Demirdöven, N.; Tokmakoff, A. *J. Phys. Chem. A* **2003**, *107*, 5258.
- (27) Zanni, M. T.; Asplund, M. C.; Hochstrasser, R. M. *J. Chem. Phys.* **2001**, *114*, 4579.
- (28) Zanni, M. T.; Stenger, J.; Asplund, M. C.; Hochstrasser, R. M. *Biophysical Journal* **2001**, *80*, 38.
- (29) Woutersen, S.; Mu, Y.; Stock, G.; Hamm, P. *Proc. Natl. Acad. Sci.* **2001**, *98*, 11254.

- (30) Woutersen, S.; Hamm, P. *J. Chem. Phys.* **2001**, *115*, 7737.
- (31) Thompson, D. E.; Merchant, K. A.; Fayer, M. D. *J. Chem. Phys.* **2001**, *115*, 317.
- (32) Asbury, J. B.; Steinel, T.; Stromberg, C.; Gaffney, K. J.; Piletic, I. R.; Fayer, M. D. *J. Chem. Phys.* **2003**, *119*, 12981.
- (33) Asbury, J. B.; Steinel, T.; Stromberg, C.; Corcelli, S. A.; Lawrence, C. P.; Skinner, J. L.; Fayer, M. D. *J. Phys. Chem. A* **2004**, *108*, 1107.
- (34) Gale, G. M.; Gallot, G.; Lascoux, N. *Chem. Phys. Lett.* **1999**, *311*, 123.
- (35) Deak, J. C.; Rhea, S. T.; Iwaki, L. K.; Dlott, D. D. *J. Phys. Chem. A* **2000**, *104*, 4866.
- (36) Eaves, J. D. *Vibrational dynamics from the molecule's perspective*, Massachusetts Institute of Technology, 2004.
- (37) Moller, K. B.; Rey, R.; Hynes, J. T. *J. Phys. Chem. A* **2004**, *108*, 1275.
- (38) The evolution of the density matrix for the 2DIR pulse sequence is represented by Feynman diagrams in Fig. 3-3.
- (39) Khalil, M. *A Tale of Coupled Vibrations in Solutions Told by Coherent Two-Dimensional Infrared Spectroscopy*, Massachusetts Institute of Technology, 2004.
- (40) Demirdöven, N. *Coherent Two-Dimensional Infrared Spectroscopy: Study of Coupled Vibrations*, Massachusetts Institute of Technology, 2003.
- (41) Hamm, P.; Lim, M.; DeGrado, W. F.; Hochstrasser, R. M. *Proc. Natl. Acad. Sci. USA* **1999**, *96*, 2036.
- (42) Zanni, M.; Ge, N.-H.; Kim, Y. S.; Hochstrasser, R. M. *Proc. Natl. Acad. Sci. USA* **2001**, *98*, 11265.
- (43) Zanni, M. T.; Hochstrasser, R. M. *Curr. Opin. Struct. Biol.* **2001**, *11*, 516.
- (44) Okumura, K.; Tokmakoff, A.; Tanimura, Y. *Chem. Phys. Lett.* **1999**, *314*, 488.

- (45) Tokmakoff, A. *J. Phys. Chem. A* **2000**, *104*, 4247.
- (46) Woutersen, S.; Bakker, H. J. *Nature* **1999**, *402*, 507.
- (47) Khalil, M.; Demirdöven, N.; Tokmakoff, A. *Phys. Rev. Lett.* **2003**, *90*, 47401.
- (48) Hybl, J. D.; Ferro, A. A.; Jonas, D. M. *J. Chem. Phys.* **2001**, *115*, 6606.
- (49) The 2D surfaces were recorded at a much lower optical density than the 3PEPS experiments to avoid spectral filtering. Therefore, the nonresonant response of the solvent is stronger relative to the OH resonant signal for short waiting times in the 2D experiment.

Appendix

C++ code for numerical calculation of FWM signals for water

A.1 Introduction

This appendix provides the C++ code that numerically calculates FWM signals (and the linear absorption lineshape) for HOD/D₂O based on parameters for a (real or complex valued) frequency correlation function, reorientational correlation function, population relaxation time, and pulse characteristics. More specifically, the code calculates vibrational echo profiles, 3PEPS decays, pump-probe signals, and 2DIR surfaces in time or frequency. It is also optimized to fit a 3PEPS decay by varying amplitudes and timescales in a frequency correlation function using a multi-dimensional downhill simplex method.

The primary user interface is `main.cc` (Section A.3), which allows the user to define the FWM signal to be calculated (or fit), as well as the timescales and amplitudes of the frequency correlation function. Functions in `Functions.cc` (Section A.4) calculate the response functions, convolve them with the electric fields to determine the nonlinear polarization, and then output experimental signals. `Amoeba.cc` and `Amotry.cc` (Sections A.5)

are for fitting 3PEPS data. Lastly, the calculations require the complex class `Complex.h` (Section A.6).

A.2 Header

Header.h

```
// header file
#ifndef HEADER_H
#define HEADER_H

#include <iostream>
#include <fstream>
#include <iomanip>
#include <cmath>
#include <time.h>
#include <exception>
#include "Complex.h"
#include "ABCVector.h"
#include "Vector.h"
#include "Plot2D.h"
#include "nr.h"
#include "nrtypes.h"
#include "nrutil.h"
#include "Functions.h"
#include "Integrals.h"
#include "amoeba.h"
#include "amotry.h"

//removed typedef statements 1/16/04 because the compiler on Macha had a problem with the
vector typedef

const double pi = 4.0*atan(1.0);
const double w10 = 2*pi*3e-5*3400;
const double w21 = 2*pi*3e-5*3150;
const double w20 = w10+w21;
const double w = 2*pi*3e-5*3275;
const Complex<double> I(0.0,1.0);

#endif
```


A.3 Main

main.cc

```
#include "Header.h"
using namespace std;

int main()
{
    int calc=7;
    //calc=1 for PS
    //calc=2 for 2D
    //calc=3 for 2D envelope
    //calc=4 for dispersed PP in frequency
    //calc=5 for time decay of dispersed PP
    //calc=6 for absorbance lineshape
    //calc=7 for PS fitting

    int i,j,k,l,tsize;

    //set up time vector
    tsize=8192;//8192 for corrm number 1 to do the FFT
    Vector<double> t(tsize), corr(tsize), lsf(tsize);
    for(i=0;i<tsize;i++)
        t[i]=i;

    int dt=10;

    //define up R1 (-k1+k2+k3) for t1=(0,520), t2=(0,2400), t3=(0,700)
    int i1=52,j1=240,k1=70;
    //int i1=32,j1=540,k1=70; //for long pump-probe scans
    Vector<double> t11(i1), t12(j1), t13(k1);
    for(i=0;i<i1;i++) {t11[i]=t[dt*i];}
    for(j=0;j<j1;j++) {t12[j]=t[dt*j];}
    for(k=0;k<k1;k++) {t13[k]=t[dt*k];}

    //define up R2 (+k1-k2+k3) for t1=(0,520), t2=(0,2400), t3=(0,700)
    int i2=52,j2=240,k2=70;
    //int i2=32,j2=540,k2=70; //for long pump-probe scans
    Vector<double> t21(i2), t22(j2), t23(k2);
    for(i=0;i<i2;i++) {t21[i]=t[dt*i];}
    for(j=0;j<j2;j++) {t22[j]=t[dt*j];}
    for(k=0;k<k2;k++) {t23[k]=t[dt*k];}
```

```

//define up R3 (+k1+k2-k3) for t1=(0,520), t2=(0,500), t3=(0,700)
int i3=52,j3=50,k3=70;//1/18/04 changed j3 from 240 to 50
Vector<double> t31(i3), t32(j3), t33(k3);
for(i=0;i<i3;i++) {t31[i]=t[dt*i];}
for(j=0;j<j3;j++) {t32[j]=t[dt*j];}
for(k=0;k<k3;k++) {t33[k]=t[dt*k];}

double ***R1r;
R1r = new double **[i1];
R1r[0] = new double *[i1*j1];
R1r[0][0] = new double [i1*j1*k1];
double ***R1i;
R1i = new double **[i1];
R1i[0] = new double *[i1*j1];
R1i[0][0] = new double [i1*j1*k1];
double ***R2r;
R2r = new double **[i2];
R2r[0] = new double *[i2*j2];
R2r[0][0] = new double [i2*j2*k2];
double ***R2i;
R2i = new double **[i2];
R2i[0] = new double *[i2*j2];
R2i[0][0] = new double [i2*j2*k2];
double ***R3i;
R3i = new double **[i3];
R3i[0] = new double *[i3*j3];
R3i[0][0] = new double [i3*j3*k3];
double ***R3r;
R3r = new double **[i3];
R3r[0] = new double *[i3*j3];
R3r[0][0] = new double [i3*j3*k3];

```

```

//assign pointer matrices for all response functions
make3D(R1r,i1,j1,k1);
make3D(R1i,i1,j1,k1);
make3D(R2r,i2,j2,k2);
make3D(R2i,i2,j2,k2);
make3D(R3r,i3,j3,k3);
make3D(R3i,i3,j3,k3);

```

```

//construct the signal matrix of dimensions x,y,z
//tau1 delays are given by x*dx in the range -100 to 150 fs
//tau2 delays are given by experimental values for T

```

//tau3 delays are given by $z \cdot dz$ in the range $-2 \cdot pd$ (since signal can not be radiated before the start of the third pulse) to 450 (so that we can scan the LO out to ~ 300) (note: we can go to ~ 550 since the RFs are out to 700)

//note that Jonas defines $t=0$ as the center of the third pulse, while Jaeyoung defines $t=0$ as the center of the first pulse; to be more clear, I will use tau3 as the time from the center of the third pulse to the detection time, and follow Jaeyoung for t

```
double PD=70.0; //also need to change PD in envelope
//set 2*PD as a multiple of dzi for fft to work properly in heterodyne
//set all pulse timings to have a point at time 0 (especially tau1 and lo for transform)
```

```
Vec_DP m(8);
```

```
//classical, no rot, no pop, no HGS
```

```
//0219-1 pulses
```

```
//8.7 -- needs to be fit further -- reduce lib!
```

```
//m[0]=0.0027, m[1]=110.0, m[2]=0.0013, m[3]=1287.0, m[4]=0.0000018, m[5]=0.018,
m[6]=0.035,m[7]=0.0000009;
```

```
m[0]=0.0027, m[1]=110.0, m[2]=0.0017, m[3]=1400.0, m[4]=0.0000022, m[5]=0.018,
m[6]=0.035,m[7]=0.0000009;
```

```
if(calc==1)//PS
```

```
{
  int x=41,xi=161,y=27,z=41,zi=161;
  Vec_DP tau1(x),tau1i(xi), tau2(y), tau3(z), tau3i(zi);
  for(j=0;j<19;j++) {tau2[j]=10.0*j;}
```

```
tau2[19]=200.0,tau2[20]=240.0,tau2[21]=375.0,tau2[22]=500.0,tau2[23]=750.0,tau2[24]=1000.0,tau2[25]=1500.0,tau2[26]=2000.0;
```

```
double dx=10.0,dxi=dx*(x-1)/(xi-1),dz=10.0,dzi=dz*(z-1)/(zi-1);
for(i=0;i<x;i++) {tau1[i]=dx*i-200.0;}
for(i=0;i<xi;i++) {tau1i[i]=dxi*i-200.0;}
for(k=0;k<z;k++) {tau3[k]=dz*k-2.0*PD;}
for(k=0;k<zi;k++) {tau3i[k]=dzi*k-2.0*PD;}

```

```
double ***S;
S = new double **[xi];
S[0] = new double *[xi*y];
S[0][0] = new double [xi*y*zi];
```

```

make3D(S,xi,y,zi);

//for calculations of the peak shift
Vector<double> peakshift(y);
double difference;

//calcPS(m,t,S,R1r,R1i,R2r,R2i,R3r,R3i,i1,j1,k1,i2,j2,k2,i3,j3,k3,dt,tau1,tau1i,tau2,tau3,tau3i
,PD,peakshift);
//difference only valid with all 27 tau2 points

difference=fitPS(m,t,S,R1r,R1i,R2r,R2i,R3r,R3i,i1,j1,k1,i2,j2,k2,i3,j3,k3,dt,tau1,tau1i,tau2,t
au3,tau3i,PD,peakshift);
cout<<"difference"<<difference<<endl;
//save the peak shift values
ofstream fout1("ps.dat");
for(j=0;j<y;j++)
    fout1<<tau2[j]<<'\t'<<peakshift[j]<<endl;
fout1.close();

/*
//save the total polarization matrix by stacking in three dimensions
ofstream fout2("pol.dat");
for(i=0;i<xi;i++)
    {
        for(j=0;j<y;j++)
            {
                for(k=0;k<zi;k++)
                    {
                        fout2<<tau1i[i]<<'\t'<<tau2[j]<<'\t'<<tau3i[k]<<'\t'<<S[i][j][k]<<endl;
                    }
            }
    }
fout2.close();
*/

if(S!=0) del3D(S);
}

if(calc==2)//2D heterodyne matrix
{
int x=41,xi=161,y=6,z=56,zi=221;
Vec_DP tau1(x),tau1i(xi), tau2(y), tau3(z), tau3i(zi);

```

```

double dx=10.0,dxi=dx*(x-1)/(xi-1),dz=10.0,dzi=dz*(z-1)/(zi-1);
for(i=0;i<x;i++) {tau1[i]=dx*i-200.0;}
for(i=0;i<xi;i++) {tau1i[i]=dxi*i-200.0;}
for(k=0;k<z;k++) {tau3[k]=dz*k-2.0*PD;}
for(k=0;k<zi;k++) {tau3i[k]=dzi*k-2.0*PD;}
tau2[0]=0.0,tau2[1]=80.0,tau2[2]=160.0,tau2[3]=240.0,tau2[4]=500.0,tau2[5]=1000.0;

```

//tau3 was used for t, so the center position of the local oscillator will be denoted by LO, and the heterodyne signal will be denoted HET

```

int w=201;
double dw=2.5;
Vec_DP LO(w);
for(l=0;l<w;l++){LO[l]=dw*l-150;}

```

```

double ***S;
S = new double **[xi];
S[0] = new double *[xi*y];
S[0][0] = new double [xi*y*zi];
make3D(S,xi,y,zi);

```

```

double ***HET;
HET = new double **[xi];
HET[0] = new double *[xi*y];
HET[0][0] = new double [xi*y*w];
make3D(HET,xi,y,w);

```

heterodyne(m,t,HET,S,R1r,R1i,R2r,R2i,R3r,R3i,i1,j1,k1,i2,j2,k2,i3,j3,k3,dt,tau1,tau1i,tau2,tau3,tau3i,LO,PD);

```

//save the heterodyne signal matrix by stacking in three dimensions
ofstream fout3("het.dat");
for(i=0;i<xi;i++)
{
    for(j=0;j<y;j++)
    {
        for(l=0;l<w;l++)
        {
            fout3<<tau1i[i]<<'\t'<<tau2[j]<<'\t'<<LO[l]<<'\t'<<HET[i][j][l]<<endl;
        }
    }
}
fout3.close();

if(S!=0) del3D(S);
if(HET!=0) del3D(HET);

```

```

}

if(calc==3)//2D heterodyne envelope
{
  int x=41,xi=161,y=6,z=56,zi=221;
  Vec_DP tau1(x),tau1i(xi), tau2(y), tau3(z), tau3i(zi);

  double dx=10.0,dxi=dx*(x-1)/(xi-1),dz=10.0,dzi=dz*(z-1)/(zi-1);
  for(i=0;i<x;i++) {tau1[i]=dx*i-200.0;}
  for(i=0;i<xi;i++) {tau1i[i]=dxi*i-200.0;}
  for(k=0;k<z;k++) {tau3[k]=dz*k-2.0*PD;}
  for(k=0;k<zi;k++) {tau3i[k]=dzi*k-2.0*PD;}
  tau2[0]=0.0,tau2[1]=80.0,tau2[2]=160.0,tau2[3]=240.0,tau2[4]=500.0,tau2[5]=1000.0;

  //tau3 was used for t, so the center position of the local oscillator will be denoted by LO,
  and the heterodyned signal will be denoted HET
  int w=201;
  double dw=2.5;
  Vec_DP LO(w);
  for(l=0;l<w;l++){LO[l]=dw*l-150;}

  double ***S;
  S = new double **[xi];
  S[0] = new double *[xi*y];
  S[0][0] = new double [xi*y*zi];
  make3D(S,xi,y,zi);

  double ***HET;
  HET = new double **[xi];
  HET[0] = new double *[xi*y];
  HET[0][0] = new double [xi*y*w];
  make3D(HET,xi,y,w);

  //use same time axes for envelope for ease of wrap around
  double ***ENV;
  ENV = new double **[xi];
  ENV[0] = new double *[xi*y];
  ENV[0][0] = new double [xi*y*w];
  make3D(ENV,xi,y,w);

  extractenv(m,t,ENV,HET,S,R1r,R1i,R2r,R2i,R3r,R3i,i1,j1,k1,i2,j2,k2,i3,j3,k3,dt,tau1,tau1i,t
  au2,tau3,tau3i,LO,PD);

```



```

double dfreq=1/(dw*len*0.00003);
Vector<double> freq(len/2);
for(l=0;l<len/2;l++){freq[l]=l*dfreq;}

```

```

//2D matrix for dispersed pump probe
double **PP;
PP = new double *[y];
PP[0] = new double [y*len/2];
for(j=1;j<y;j++)
    PP[j]=PP[j-1]+len/2;

```

```

dispPP(m,t,PP,R1r,R1i,R2r,R2i,R3r,R3i,i1,j1,k1,i2,j2,k2,i3,j3,k3,dt,tau2,tau3,tau3i,LO,PD);

```

```

//save the frequency dispersed pump probe by stacing in two dimensions

```

```

ofstream fout5("dpp.dat");
for(j=0;j<y;j++)
    {
        for(l=0;l<len/2;l++)
            {
                fout5<<tau2[j]<<'\t'<<freq[l]<<'\t'<<PP[j][l]<<endl;
            }
    }
fout5.close();

if(PP!=0)
    {
        delete [] (PP[0]);
        delete [] (PP);
    }
}

```

```

if(calc==5)//time decay of dispersed PP

```

```

{
    int x=41,xi=161,y=201,z=56,zi=221;
    Vec_DP tau1(x),tau1i(xi), tau2(y), tau3(z), tau3i(zi);

    double dx=10.0,dxi=dx*(x-1)/(xi-1),dz=10.0,dzi=dz*(z-1)/(zi-1);
    for(i=0;i<x;i++) {tau1[i]=dx*i-200.0;}
    for(i=0;i<xi;i++) {tau1i[i]=dxi*i-200.0;}
    for(k=0;k<z;k++) {tau3[k]=dz*k-2.0*PD;}
    for(k=0;k<zi;k++) {tau3i[k]=dzi*k-2.0*PD;}
    for(j=0;j<y;j++) {tau2[j]=10*j;}
}

```



```
//for(j=0;j<y;j++) {tau2[j]=25*j;}//for long pump-probe scans (also changecommented
lines in size of R1 and R2)
```

```
//tau3 was used for t, so the center position of the local oscillator will be denoted by LO,
and the heterodyned signal will be denoted HET
```

```
int w=201;
double dw=2.5;
Vec_DP LO(w);
for(l=0;l<w;l++){LO[l]=dw*l-150;}
```

```
//for the decay of the dispersed PP at a given frequency, just set up a vector of size tau2
Vector<double> PPdecay(tau2.size());
//returns dispersed pump probe at frequency value of index + frequency value of
(index+1) -- since filter width is ~50 cm-1
int index=130;//gives PP values at ~3385 cm-1
```

```
dPPtime(m,t,PPdecay,index,R1r,R1i,R2r,R2i,R3r,R3i,i1,j1,k1,i2,j2,k2,i3,j3,k3,dt,tau2,tau3,ta
u3i,LO,PD);
```

```
//save the dispersed pump probe decay values
ofstream fout6("tdpp.dat");
for(j=0;j<y;j++)
    fout6<<tau2[j]<<'t'<<PPdecay[j]<<endl;
fout6.close();
}
```

```
if(calc==6)//absorbance lineshape
```

```
{
//absorbance lineshape assumes transform length of 512 and spacing of 2.5 fs -- input
vector abs(len/2) which is the real part of the absorbance for positive frequencies and a
double width that is ~FWHM of the absorption line
```

```
int i,len=2048;
double dw=2.5, dfreq=1/(dw*len*0.00003),width;
Vector<double> tt(len/2);
Vec_DP freq(len/2), abs(len/2);
for(i=0;i<len/2;i++){freq[i]=i*dfreq;}
```

```
abslshp(m,abs,width);
```

```
cout<<"absorption linewidth ~ "<<width<<endl;
```

```

//save the absorption spectrum
ofstream fout7("abs.dat");
for(i=0;i<len/2;i++)
    fout7<<freq[i]<<'\t'<<abs[i]<<endl;
fout7.close();

}

if(calc==7)//PS fitting
{
    int x=41,xi=161,y=27,z=41,zi=161;
    Vec_DP tau1(x),tau1i(xi), tau2(y), tau3(z), tau3i(zi);
    for(j=0;j<19;j++) {tau2[j]=10.0*j;}

tau2[19]=200.0,tau2[20]=240.0,tau2[21]=375.0,tau2[22]=500.0,tau2[23]=750.0,tau2[24]=10
00.0,tau2[25]=1500.0,tau2[26]=2000.0;

    double dx=10.0,dxi=dx*(x-1)/(xi-1),dz=10.0,dzi=dz*(z-1)/(zi-1);
    for(i=0;i<x;i++) {tau1[i]=dx*i-200.0;}
    for(i=0;i<xi;i++) {tau1i[i]=dxi*i-200.0;}
    for(k=0;k<z;k++) {tau3[k]=dz*k-2.0*PD;}
    for(k=0;k<zi;k++) {tau3i[k]=dzi*k-2.0*PD;}

    double ***S;
    S = new double **[xi];
    S[0] = new double *[xi*y];
    S[0][0] = new double [xi*y*zi];
    make3D(S,xi,y,zi);

    Vector<double> peakshift(y);
    double difference;

    Vec_DP m0=m,m1=m,m2=m,m3=m,m4=m,m5=m,m6=m,m7=m;
    double pct=0.9;
    m0[0]=m[0]*pct;
    m1[1]=m[1]*pct;
    m2[2]=m[2]*pct;
    m3[3]=m[3]*pct;
    m4[4]=m[4]*pct;
    m5[5]=m[5]*pct;
    m6[6]=m[6]*pct;
    m7[7]=m[7]*pct;

```

```
//m8[8]=m[8]*pct;
//m9[9]=m[9]*pct;
//m10[10]=m[10]*pct;
//m11[11]=m[11]*pct;
```

```
Mat_DP p(9,8);
for(i=0;i<8;i++)
{
    p[0][i]=m[i];
    p[1][i]=m0[i];
    p[2][i]=m1[i];
    p[3][i]=m2[i];
    p[4][i]=m3[i];
    p[5][i]=m4[i];
    p[6][i]=m5[i];
    p[7][i]=m6[i];
    p[8][i]=m7[i];
    //p[9][i]=m8[i];
    //p[10][i]=m9[i];
    //p[11][i]=m10[i];
    //p[12][i]=m11[i];
}
```

```
Vec_DP evals(9);
```

```
evals[0]=fitPS(m,t,S,R1r,R1i,R2r,R2i,R3r,R3i,i1,j1,k1,i2,j2,k2,i3,j3,k3,dt,tau1,tau1i,tau2,tau3,tau3i,PD,peakshift);
```

```
cout<<"initial guess "<<evals[0]<<endl;
```

```
evals[1]=fitPS(m0,t,S,R1r,R1i,R2r,R2i,R3r,R3i,i1,j1,k1,i2,j2,k2,i3,j3,k3,dt,tau1,tau1i,tau2,tau3,tau3i,PD,peakshift);
```

```
cout<<"variation 1: "<<evals[1]<<endl;
```

```
evals[2]=fitPS(m1,t,S,R1r,R1i,R2r,R2i,R3r,R3i,i1,j1,k1,i2,j2,k2,i3,j3,k3,dt,tau1,tau1i,tau2,tau3,tau3i,PD,peakshift);
```

```
cout<<"variation 2: "<<evals[2]<<endl;
```

```
evals[3]=fitPS(m2,t,S,R1r,R1i,R2r,R2i,R3r,R3i,i1,j1,k1,i2,j2,k2,i3,j3,k3,dt,tau1,tau1i,tau2,tau3,tau3i,PD,peakshift);
```

```
cout<<"variation 3: "<<evals[3]<<endl;
```

```
evals[4]=fitPS(m3,t,S,R1r,R1i,R2r,R2i,R3r,R3i,i1,j1,k1,i2,j2,k2,i3,j3,k3,dt,tau1,tau1i,tau2,tau3,tau3i,PD,peakshift);
```

```
cout<<"variation 4: "<<evals[4]<<endl;
```

```

evals[5]=fitPS(m4,t,S,R1r,R1i,R2r,R2i,R3r,R3i,i1,j1,k1,i2,j2,k2,i3,j3,k3,dt,tau1,tau1i,tau2,ta
u3,tau3i,PD,peakshift);
    cout<<"variation 5: "<<evals[5]<<endl;

evals[6]=fitPS(m5,t,S,R1r,R1i,R2r,R2i,R3r,R3i,i1,j1,k1,i2,j2,k2,i3,j3,k3,dt,tau1,tau1i,tau2,ta
u3,tau3i,PD,peakshift);
    cout<<"variation 6: "<<evals[6]<<endl;

evals[7]=fitPS(m6,t,S,R1r,R1i,R2r,R2i,R3r,R3i,i1,j1,k1,i2,j2,k2,i3,j3,k3,dt,tau1,tau1i,tau2,ta
u3,tau3i,PD,peakshift);
    cout<<"variation 7: "<<evals[7]<<endl;

evals[8]=fitPS(m7,t,S,R1r,R1i,R2r,R2i,R3r,R3i,i1,j1,k1,i2,j2,k2,i3,j3,k3,dt,tau1,tau1i,tau2,ta
u3,tau3i,PD,peakshift);
    cout<<"variation 8: "<<evals[8]<<endl;

//evals[9]=fitPS(m8,t,S,R1r,R1i,R2r,R2i,R3r,R3i,i1,j1,k1,i2,j2,k2,i3,j3,k3,dt,tau1,tau1i,tau2,t
au3,tau3i,PD,peakshift);
    //cout<<"variation 9: "<<evals[9]<<endl;

//evals[10]=fitPS(m9,t,S,R1r,R1i,R2r,R2i,R3r,R3i,i1,j1,k1,i2,j2,k2,i3,j3,k3,dt,tau1,tau1i,tau2
,tau3,tau3i,PD,peakshift);
    //cout<<"variation 10: "<<evals[10]<<endl;

//evals[11]=fitPS(m10,t,S,R1r,R1i,R2r,R2i,R3r,R3i,i1,j1,k1,i2,j2,k2,i3,j3,k3,dt,tau1,tau1i,tau
2,tau3,tau3i,PD,peakshift);
    //cout<<"variation 11: "<<evals[11]<<endl;

//evals[12]=fitPS(m11,t,S,R1r,R1i,R2r,R2i,R3r,R3i,i1,j1,k1,i2,j2,k2,i3,j3,k3,dt,tau1,tau1i,tau
2,tau3,tau3i,PD,peakshift);
    //cout<<"variation 12: "<<evals[12]<<endl;

    double ftol=0.001;//final 0.005
    int nfunk;

amoeba(p,evals,ftol,nfunk,t,S,R1r,R1i,R2r,R2i,R3r,R3i,i1,j1,k1,i2,j2,k2,i3,j3,k3,dt,tau1,tau1i
,tau2,tau3,tau3i,PD,peakshift);

    //replace m with one of the valid fit values and write it to a file
    ofstream fout8("psfitvals.dat");
    for(i=0;i<8;i++)
    {
        m[i]=p[0][i];
        fout8<<m[i]<<endl;
    }

```

```

fout8.close();

//difference only valid with all 27 tau2 points

difference=fitPS(m,t,S,R1r,R1i,R2r,R2i,R3r,R3i,i1,j1,k1,i2,j2,k2,i3,j3,k3,dt,tau1,tau1i,tau2,tau3,tau3i,PD,peakshift);
cout<<"difference"<<difference<<endl;

//save the peak shift values
ofstream fout9("ps.dat");
for(j=0;j<y;j++)
    fout9<<tau2[j]<<"\t"<<peakshift[j]<<endl;
fout9.close();

if(S!=0) del3D(S);
}

//delete Response function pointers
if(R1r!=0) del3D(R1r);
if(R1i!=0) del3D(R1i);
if(R2r!=0) del3D(R2r);
if(R2i!=0) del3D(R2i);
if(R3r!=0) del3D(R3r);
if(R3i!=0) del3D(R3i);

return 0;
}

```

A.4 Functions

Functions.h

```
#ifndef FUNCTIONS_H
#define FUNCTIONS_H
#include "Header.h"
using namespace std;

Vector<Complex<double>> corrm(const Vector<double> &t,const Vec_DP &m);
Vector<Complex<double>> LSF(const Vector<double> &t, const
Vector<Complex<double>> &c);
void make3D(double ***R, const int &si, const int &sj, const int &sk);
void del3D(double ***R);
double Rrot(const int &t1, const int &t2, const int &t3);
void RF1(const Vector<double> &t, const Vector<Complex<double>> &lsf, double
***R1r,double ***R1i, const int &i1, const int &j1, const int &k1, const int &dt);
void RF2(const Vector<double> &t, const Vector<Complex<double>> &lsf, double
***R2r,double ***R2i, const int &i2, const int &j2, const int &k2, const int &dt);
void RF3(const Vector<double> &t, const Vector<Complex<double>> &lsf, double
***R3r,double ***R3i, const int &i3, const int &j3, const int &k3, const int &dt);
double interpR(double ***R, const int &dt, const double &t1, const double &t2, const
double &t3);
double envelope(const double &t);
Complex<double> envelopec(const double &t);
Complex<double> P1abc(double ***R1r, double ***R1i, const int &dt, const double &t1,
const double &t2, const double &t3, const double &tau1, const double &tau2, const double
&tau3, const int &cond);
Complex<double> P1acb(double ***R1r, double ***R1i, const int &dt, const double &t1,
const double &t2, const double &t3, const double &tau1, const double &tau2, const double
&tau3, const int &cond);
Complex<double> P2bac(double ***R2r, double ***R2i, const int &dt, const double &t1,
const double &t2, const double &t3, const double &tau1, const double &tau2, const double
&tau3, const int &cond);
Complex<double> P2cab(double ***R2r, double ***R2i, const int &dt, const double &t1,
const double &t2, const double &t3, const double &tau1, const double &tau2, const double
&tau3, const int &cond);
Complex<double> P3bca(double ***R3r, double ***R3i, const int &dt, const double &t1,
const double &t2, const double &t3, const double &tau1, const double &tau2, const double
&tau3, const int &cond);
Complex<double> P3cba(double ***R3r, double ***R3i, const int &dt, const double &t1,
const double &t2, const double &t3, const double &tau1, const double &tau2, const double
&tau3, const int &cond);
void calcPri(double ***Sr, double ***Si, double ***R1r, double ***R1i, double ***R2r,
double ***R2i, double ***R3r, double ***R3i, const int &dt, const Vec_DP &tau1, const
```

```

Vec_DP &tau1i, const Vec_DP &tau2, const Vec_DP &tau3, const Vec_DP &tau3i, const
double &PD, const int &cond);
void calcP(double ***S, double ***R1r, double ***R1i, double ***R2r, double ***R2i,
double ***R3r, double ***R3i, const int &dt, const Vec_DP &tau1, const Vec_DP &tau1i,
const Vec_DP &tau2, const Vec_DP &tau3, const Vec_DP &tau3i, const double &PD, const
int &cond);
Vector<double> PS(double ***S, const Vec_DP &tau1, const Vec_DP &tau2, const
Vec_DP &tau3);
void gauss(const DP t, Vec_I_DP &a, DP &y, Vec_O_DP &dyda);
void calcPS(const Vec_DP &m, const Vector<double> &t, double ***S, double ***R1r,
double ***R1i, double ***R2r, double ***R2i, double ***R3r, double ***R3i, const int
&i1, const int &j1, const int &k1, const int &i2, const int &j2, const int &k2, const int &i3,
const int &j3, const int &k3, const int &dt, const Vec_DP &tau1, const Vec_DP &tau1i,
const Vec_DP &tau2, const Vec_DP &tau3, const Vec_DP &tau3i, const double &PD,
Vector<double> &peakshift);
double fitPS(const Vec_DP &m, const Vector<double> &t, double ***S, double ***R1r,
double ***R1i, double ***R2r, double ***R2i, double ***R3r, double ***R3i, const int
&i1, const int &j1, const int &k1, const int &i2, const int &j2, const int &k2, const int &i3,
const int &j3, const int &k3, const int &dt, const Vec_DP &tau1, const Vec_DP &tau1i,
const Vec_DP &tau2, const Vec_DP &tau3, const Vec_DP &tau3i, const double &PD,
Vector<double> &peakshift);
void heterodyne(const Vec_DP &m, const Vector<double> &t, double ***HET, double
***S, double ***R1r, double ***R1i, double ***R2r, double ***R2i, double ***R3r,
double ***R3i, const int &i1, const int &j1, const int &k1, const int &i2, const int &j2, const
int &k2, const int &i3, const int &j3, const int &k3, const int &dt, const Vec_DP &tau1,
const Vec_DP &tau1i, const Vec_DP &tau2, const Vec_DP &tau3, const Vec_DP &tau3i,
const Vec_DP &LO, const double &PD);
void extractenv(const Vec_DP &m, const Vector<double> &t, double ***ENV, double
***HET, double ***S, double ***R1r, double ***R1i, double ***R2r, double ***R2i,
double ***R3r, double ***R3i, const int &i1, const int &j1, const int &k1, const int &i2,
const int &j2, const int &k2, const int &i3, const int &j3, const int &k3, const int &dt, const
Vec_DP &tau1, const Vec_DP &tau1i, const Vec_DP &tau2, const Vec_DP &tau3, const
Vec_DP &tau3i, const Vec_DP &LO, const double &PD);
void dispPP(const Vec_DP &m, const Vector<double> &t, double **PP, double ***R1r,
double ***R1i, double ***R2r, double ***R2i, double ***R3r, double ***R3i, const int
&i1, const int &j1, const int &k1, const int &i2, const int &j2, const int &k2, const int &i3,
const int &j3, const int &k3, const int &dt, const Vec_DP &tau2, const Vec_DP &tau3, const
Vec_DP &tau3i, const Vec_DP &LO, const double &PD);
void dPPtime(const Vec_DP &m, const Vector<double> &t, Vector<double> &PPdecay,
const int index, double ***R1r, double ***R1i, double ***R2r, double ***R2i, double
***R3r, double ***R3i, const int &i1, const int &j1, const int &k1, const int &i2, const int
&j2, const int &k2, const int &i3, const int &j3, const int &k3, const int &dt, const Vec_DP
&tau2, const Vec_DP &tau3, const Vec_DP &tau3i, const Vec_DP &LO, const double
&PD);
void abs1shp(const Vec_DP &m, Vec_DP &abs, double &width);

```

```

Complex<double> P13ab_c(double ***R1r,double ***R1i,double ***R2r,double
***R2i,double ***R3r,double ***R3i,const double &eq_lower,const double
&eq_upper,const double &ind_lower,const double &ind_upper,const double &tau1,const
double &tau2,const double &tau3,const int &dt,const int &eq_steps,const int &ind_steps,
const int &cond);
Complex<double> P13bc_a(double ***R1r,double ***R1i,double ***R2r,double
***R2i,double ***R3r,double ***R3i,const double &eq_lower,const double
&eq_upper,const double &ind_lower,const double &ind_upper,const double &tau1,const
double &tau2,const double &tau3,const int &dt,const int &eq_steps,const int &ind_steps,
const int &cond);
Complex<double> P23ac_b(double ***R1r,double ***R1i,double ***R2r,double
***R2i,double ***R3r,double ***R3i,const double &eq_lower,const double
&eq_upper,const double &ind_lower,const double &ind_upper,const double &tau1,const
double &tau2,const double &tau3,const int &dt,const int &eq_steps,const int &ind_steps,
const int &cond);
Complex<double> Integrate(double ***R1r,double ***R1i,double ***R2r,double
***R2i,double ***R3r,double ***R3i,const double &tauamin,const double &tauamax,const
double &taubmin,const double &taubmax,const double &taucmin,const double
&taucmax,const double &tau1,const double &tau2, const double &tau3,const int &dt, const
int &a_steps, const int &b_steps, const int &c_steps, const int &cond);

#endif

```

Functions.cc

```

#include "Functions.h"

/*
Vector<Complex<double>> corrm(const Vector<double> &t,const Vec_DP &m)
//old correlation function – new form is the next funtion
//correlation function based on two overdamped oscillators (~200 and ~1000 fs)and two
underdamped oscillator (~200 fs and ~450 fs)
{
int i, s=t.size(),dex;
double dt=(t[1]-t[0]), dfreq=1/(dt*2*s*0.00003);
if(s!=8192){cout<<"check t size"<<endl;}
Vector<double> zr(s);
Vector<Complex<double>> zc(s);
Vec_DP ztr(0.0,4*s), freq(4*s);
//double scale=0.0012, a1=0.166, g1=0.245, w1=0.0896, a2=0.119, g2=0.0751, w2=
0.0216, a3=0.262, g3=0.0293, w3=0.0339;
double scale=0.0013, a1,g1,w1,a2,g2,w2,a3,g3,w3,a4,g4,w4;

```



```

a1=m[0],g1=m[1],w1=m[2],a2=m[3],g2=m[4],w2=m[5],a3=m[6],g3=m[7],w3=m[8],a4=m[9
],g4=0.05,w4=0.08;
double sp1 = 0.5*g1 * sqrt(0.25*g1*g1 + 0.25*w1*w1), sm1 = 0.5*g1 * sqrt(0.25*g1*g1 -
0.25*w1*w1);
double sp2 = 0.5*g2 * sqrt(0.25*g2*g2 + 0.25*w2*w2), sm2 = 0.5*g2 * sqrt(0.25*g2*g2 -
0.25*w2*w2);
double wr3 = sqrt(w3*w3 - 0.25*g3*g3);
double wr4 = sqrt(w4*w4 - 0.25*g4*g4);
for(i=0;i<s;i++)
{
    zr[i] = a1 * ((sp1/(sp1-sm1))*exp(-sm1*t[i]) - (sm1/(sp1-sm1))*exp(-sp1*t[i])) + a2 *
((sp2/(sp2-sm2))*exp(-sm2*t[i]) - (sm2/(sp2-sm2))*exp(-sp2*t[i])) + a3 * (exp(-g3*0.5*t[i])
* (cos(wr3*t[i]) + (g3/(2*wr3))*sin(wr3*t[i]))) + a4 * (exp(-g4*0.5*t[i]) * (cos(wr4*t[i]) +
(g4/(2*wr4))*sin(wr4*t[i])));

    dex=2*i;
    ztr[dex]=zr[i];//put cf into vector for transform
    freq[dex]=i*dfreq;
    freq[dex+1]=i*dfreq;
}

for(i=1;i<s;i++)
{
    dex=4*s-2*i;
    ztr[dex]=zr[i];//wrap around cf with time symmetry -- excluding t=0 point
    freq[dex]=-1*i*dfreq;
    freq[dex+1]=-1*i*dfreq;
}
ztr[2*s]=ztr[2*s-2];//just set extra poing (largest/smallest t) to neighboring point
freq[2*s]=-1*s*dfreq;
freq[2*s+1]=-1*s*dfreq;

//FT
NR::four1(ztr,1);

for(i=0;i<4*s;i++)
{
    /*"standard" quantum correction G_qm=G_cl*2/(1+exp(-beta*hbar*omega))
    /*"standard" qc does not affect the real part of the cf, just adds an imaginary part
    zr[i]=ztr[i]*2/(1+exp(-0.005*freq[i]));
}

//FT back
NR::four1(ztr,-1);

```

```

//write real and imaginary parts of the correlation function
for(i=0;i<s;i++)
{
//for a quantum corrected correlation function
zc[i]=ztr[2*i]/(2*s)+I*ztr[2*i+1]/(2*s);
//for a classical correlation function
//zc[i]=ztr[2*i]/(2*s);
}

ofstream fout1("cppcf.dat");
for(i=0;i<s;i++)
{
double saver=scale*zc[i].Real(),savei=scale*zc[i].Imag();
fout1<<t[i]<<'t'<<saver<<'t'<<savei<<endl;
}
fout1.close();

return scale*zc;
}
*/

Vector<Complex<double>> corrm(const Vector<double> &t,const Vec_DP &m)
//new correlation function -- 2/1/04
//correlation function based on two overdamped oscillators (~200 and ~1000 fs)and two
underdamped oscillator (~200 fs and ~450 fs)
{
int i, s=t.size();
Vector<Complex<double>> zr(s), zi(s), zc(s);
double scale=1.0, a1,g1,a2,g2,a3,g3,w3,a4,g4,w4;

a1=m[0],g1=m[1],a2=m[2],g2=m[3],a3=m[4],g3=m[5],w3=m[6],a4=m[7],g4=0.05,w4=0.08;

if(w3<g3||w4<g4){cout<<"problem with frequency & damping constants"<<endl;}
double beta=1/(293.0*0.695), hbar=5300;
double L1=1.0/g1, L2=1.0/g2, cot1=cos(beta*hbar*L1/2.0)/sin(beta*hbar*L1/2.0),
cot2=cos(beta*hbar*L2/2.0)/sin(beta*hbar*L2/2.0);
double s3=sqrt(w3*w3-0.25*g3*g3), s4=sqrt(w4*w4-0.25*g4*g4);
Complex<double> p3=g3/2.0+I*s3, p4=g4/2.0+I*s4, hbip3=beta*hbar*(I*p3)/2.0,
hbip4=beta*hbar*(I*p4)/2.0, coth3=(Exp(hbip3)+Exp(-hbip3))/(Exp(hbip3)-Exp(-hbip3)),
coth4=(Exp(hbip4)+Exp(-hbip4))/(Exp(hbip4)-Exp(-hbip4));

for(i=0;i<s;i++)
{

```

```

    zr[i] = a1*(L1*cot1*exp(-L1*t[i])) + a2*(L2*cot2*exp(-L2*t[i])) + -2*a3*(coth3*Exp(-
p3*t[i])).Real()/s3 + -2*a4*(coth4*Exp(-p4*t[i])).Real()/s4;
    zi[i] = a1*(L1*exp(-L1*t[i])) + a2*(L2*exp(-L2*t[i])) + 2*a3*(exp(-
0.5*g3*t[i])*sin(s3*t[i]))/s3 + 2*a4*(exp(-0.5*g4*t[i])*sin(s4*t[i]))/s4;

```

```

    //complex
    //zc[i] = zr[i]-I*zi[i];
    //real
    zc[i] = zr[i];
}

```

```

ofstream fout1("cppcf.dat");
for(i=0;i<s;i++)
{
    double saver=scale*zc[i].Real(),savei=scale*zc[i].Imag();
    fout1<<t[i]<<'\t'<<saver<<'\t'<<savei<<endl;
}
fout1.close();

```

```

return scale*zc;
}

```

```

Vector<Complex<double>> LSF(const Vector<double> &t, const
Vector<Complex<double>> &c)
//performs double (trapezoidal) integration to construct lineshape function
{
    int i, s=t.size();
    double dt=(t[1]-t[0]);
    Vector<Complex<double>> in(0.0,s), z(0.0,s);
    for(i=1;i<s;i++)
        in[i]=0.5*dt*(c[i]+c[i-1])+in[i-1];
    for(i=1;i<s;i++)
        z[i]=0.5*dt*(in[i]+in[i-1])+z[i-1];
    return z;
}

```

```

void make3D(double ***R, const int &si, const int &sj, const int &sk)
//sets up pointers for a 3D matrix
{
    int i,j,k;
    for(j=1;j<sj;j++)

```

```

    R[0][j] = R[0][j-1] + sk;
for(i=1;i<si;i++)
{
    R[i] = R[i-1] + sj;
    R[i][0] = R[i-1][0] + sj*sk;
    for(j=1;j<sj;j++)
        R[i][j] = R[i][j-1] + sk;
}
}

```

```

void del3D(double ***R)
//deletes pointers for a 3D matrix
{
    delete [] (R[0][0]);
    delete [] (R[0]);
    delete [] (R);
}

```

```

double Rrot(const int &t1, const int &t2, const int &t3)
//rotational part of the correlation function
//NOTE: the rotational response function still needs to be modified to account for proper
time orderings
{
    double x1=t1,x2=t2,x3=t3,c1t1,c2t2,c1t3,Dor1=1.0/18000.0,Dor2=1.0/360.0;
    /*
    //c1,c2,c3 taken from fits to Legendre polynomials from Joel's simulation -- note check
normalization before using
    c1t1=0.0347*exp(-x1/27.2)*cos(x1/15.5)+0.0462*exp(-x1/238.0)+0.576*exp(-x1/4100.0);
    c2t2=0.0508*exp(-x2/30.3)*cos(x2/14.1)+0.0606*exp(-x2/141.0)+0.280*exp(-x2/1810.0);
    c1t3=0.0347*exp(-x3/27.2)*cos(x3/15.5)+0.0462*exp(-x3/238.0)+0.576*exp(-x3/4100.0);
    return c1t1*(1.0+0.8*c2t2)*c1t3*0.1111;
    */

    //Dor taken from anisotropy measurement on 4/11/03 -- normalization 5/9
    //return exp(-2.0*Dor1*x1)*(1.0+0.8*exp(-6.0*Dor1*x2))*exp(-2.0*Dor1*x3)*0.5555;
    //add a fast time component into the results from the anisotropy measurement from 4/11/03
    //zzzz
    //return (0.8*exp(-2.0*Dor1*x1)+0.2*exp(-2.0*Dor2*x1))*(1.0+0.8*(0.8*exp(-
6.0*Dor1*x2)+0.2*exp(-6.0*Dor2*x2)))*(0.8*exp(-2.0*Dor1*x3)+0.2*exp(-
2.0*Dor2*x3))*0.5555;
    //zzyy

```

```
//return (0.8*exp(-2.0*Dor1*x1)+0.2*exp(-2.0*Dor2*x1))*(1.0-0.4*(0.8*exp(-
6.0*Dor1*x2)+0.2*exp(-6.0*Dor2*x2)))*(0.8*exp(-2.0*Dor1*x3)+0.2*exp(-
2.0*Dor2*x3))*0.5555;
```

```
//no rotations
return 1.0;
}
```

```
void RF1(const Vector<double> &t, const Vector<Complex<double> > &lsf, double
***R1r,double ***R1i, const int &i1, const int &j1, const int &k1, const int &dt)
//fills response function for R1, with carrier frequency factored for t1&3
{
int i,j,k;
double z11=1.0, z12=2.0, z21=2.0, z22=4.0, T1=700.0;
double m10=1.0, m21=sqrt(2.0)*m10;
//assume harmonic scaling, so h22=2*h12=2*h21=4*h11
Complex<double> F3_0101, F4_0101, F2_0121;
Complex<double> R;
for(i=0;i<i1;i++)
{
Complex<double> h11t11=z11*lsf[dt*i];
for(j=0;j<j1;j++)
{
Complex<double> h11t12=z11*lsf[dt*j], h11t11t12=z11*lsf[dt*i+dt*j],
h12t12=z12*(lsf[dt*j]), h21t11t12=z21*lsf[dt*i+dt*j];
for(k=0;k<k1;k++)
{
Complex<double> h11t13=z11*lsf[dt*k], h11t12t13=z11*lsf[dt*j+dt*k],
h11t11t12t13=z11*lsf[dt*i+dt*j+dt*k], h12t13=z12*(lsf[dt*k]), h21t13=z21*lsf[dt*k],
h22t13=z22*lsf[dt*k], h12t12t13=z12*(lsf[dt*j+dt*k]),
h21t11t12t13=z21*lsf[dt*i+dt*j+dt*k];

F3_0101 = Exp(-Conj(h11t11-h11t12+Conj(h11t13))+h11t11t12+h11t12t13-
h11t11t12t13));
F4_0101 = Exp(-Conj(h11t11-Conj(h11t12)+h11t13+h11t11t12+Conj(h11t12t13)-
h11t11t12t13));
F2_0121 = Exp(-(h11t11+Conj(h11t12)-Conj(h12t12)+Conj(h11t13)-Conj(h12t13)-
Conj(h21t13)+Conj(h22t13)-h11t11t12+h21t11t12-
Conj(h11t12t13)+Conj(h12t12t13)+h11t11t12t13-h21t11t12t13));

//no population relaxation
R = ((F3_0101+F4_0101)-2.0*Exp(-I*(w21-
w10)*k*dt))*Conj(F2_0121))*Rrot(dt*i,dt*j,dt*k);
```

//add in population relaxation, $1/(2*T1)$ for 1st and 3rd time period and $1/T1$ for the second -- not exactly sure how to scale for $v=1/v=2$ coherence during 3rd period but I'm using the average $v=1/v=2$ rate

```
//R = ((F3_0101+F4_0101)*exp(-(dt*i)/(2.0*T1)-(dt*j)/T1-(dt*k)/(2.0*T1))-
2.0*Exp(-I*(w21-w10)*k*dt)*Conj(F2_0121)*exp(-(dt*i)/(2.0*T1)-(dt*j)/T1-
(dt*k)/(4.0/3.0*T1)))*Rrot(dt*i,dt*j,dt*k);
```

/"correlated hot ground state" -- same as above, with Jaeyoung's theory, rotations and phenomenological population relaxation during t1 and t3 plus the HGS of Stenger, et. al.(modified with change in transition dipole) during tau2

```
double dw = 2*pi*3e-5*12, dm = 0.91;
//R = ((F3_0101+F4_0101*exp(-(dt*j)/T1)-dm*Exp(-I*dw*k*dt)*(F3_0101*(1.0-
exp(-(dt*j)/T1))))*exp(-(dt*i)/(2.0*T1)-(dt*k)/(2.0*T1))-2.0*Exp(-I*(w21-
w10)*k*dt)*Conj(F2_0121)*exp(-(dt*i)/(2.0*T1)-(dt*j)/T1-
(dt*k)/(4.0/3.0*T1)))*Rrot(dt*i,dt*j,dt*k);
```

```
    R1r[i][j][k] = R.Real();
    R1i[i][j][k] = R.Imag();
}
}
}
return;
}
```

```
void RF2(const Vector<double> &t, const Vector<Complex<double>> &lsf, double
***R2r,double ***R2i, const int &i2, const int &j2, const int &k2, const int &dt)
```

//fills response function for R2, with carrier frequency factored for t1&3

```
{
int i,j,k;
double m10=1.0, m21=sqrt(2.0)*m10;
//assume harmonic scaling, so h22=2*h12=2*h21=4*h11
double z11=1.0, z12=2.0, z21=2.0, z22=4.0, T1=700.0;
Complex<double> F1_0101, F2_0101, F4_0121;
Complex<double> R;

for(i=0;i<i2;i++)
{
Complex<double> h11t21=z11*lsf[dt*i];
for(j=0;j<j2;j++)
{
Complex<double> h11t22=z11*lsf[dt*j], h11t21t22=z11*lsf[dt*i+dt*j],
h12t22=z12*(lsf[dt*j]), h21t21t22=z21*lsf[dt*i+dt*j];
for(k=0;k<k2;k++)
```

```

    {
        Complex<double> h11t23=z11*lsf[dt*k], h11t22t23=z11*lsf[dt*j+dt*k],
        h11t21t22t23=z11*lsf[dt*i+dt*j+dt*k], h12t23=z12*(lsf[dt*k]), h21t23=z21*lsf[dt*k],
        h22t23=z22*lsf[dt*k], h12t22t23=z12*(lsf[dt*j+dt*k]),
        h21t21t22t23=z21*lsf[dt*i+dt*j+dt*k];

        F1_0101 = Exp(-(h11t21+h11t22+h11t23-h11t21t22-h11t22t23+h11t21t22t23));
        F2_0101 = Exp(-(h11t21+Conj(h11t22)+Conj(h11t23)-h11t21t22-
        Conj(h11t22t23)+h11t21t22t23));
        F4_0121 = Exp(-Conj(h11t21-Conj(h11t22)+Conj(h12t22)+h11t23-h12t23-
        h21t23+h22t23+h11t21t22-h21t21t22+Conj(h11t22t23)-Conj(h12t22t23)-
        h11t21t22t23+h21t21t22t23));

        //no population relaxation
        R = ((F1_0101+F2_0101)-2.0*Exp(-I*(w21-
        w10)*k*dt)*Conj(F4_0121))*Rrot(dt*i,dt*j,dt*k);

        //add in population relaxation, 1/(2*T1) for 1st and 3rd time period and 1/T1 for the
        second -- not exactly sure how to scale for v=1/v=2 coherence during 3rd period but I'm
        using the average v=1/v=2 rate
        //R = ((F1_0101+F2_0101)*exp(-(dt*i)/(2.0*T1)-(dt*j)/T1-(dt*k)/(2.0*T1))-
        2.0*Exp(-I*(w21-w10)*k*dt)*Conj(F4_0121)*exp(-(dt*i)/(2.0*T1)-(dt*j)/T1-
        (dt*k)/(4.0/3.0*T1)))*Rrot(dt*i,dt*j,dt*k);

        // "correlated hot ground state" -- same as above, with Jaeyoung's theory, rotations
        and phenomenological population relaxation during t1 and t3 plus the HGS of Stenger, et. al.
        (modified with change in transition dipole) during tau2
        double dw = 2*pi*3e-5*12, dm = 0.91;
        //R = ((F1_0101+F2_0101*exp(-(dt*j)/T1)-dm*Exp(-I*dw*k*dt)*(F1_0101*(1.0-
        exp(-(dt*j)/T1))))*exp(-(dt*i)/(2.0*T1)-(dt*k)/(2.0*T1))-2.0*Exp(-I*(w21-
        w10)*k*dt)*Conj(F4_0121)*exp(-(dt*i)/(2.0*T1)-(dt*j)/T1-
        (dt*k)/(4.0/3.0*T1)))*Rrot(dt*i,dt*j,dt*k);

        R2r[i][j][k] = R.Real();
        R2i[i][j][k] = R.Imag();
    }
}
return;
}

```

```

void RF3(const Vector<double> &t, const Vector<Complex<double> > &lsf, double
***R3r,double ***R3i, const int &i3, const int &j3, const int &k3, const int &dt)
//fills response function for R3, with carrier frequency factored for t1,2&3

```

```

{
  int i,j,k;
  double m10=1.0, m21=sqrt(2.0)*m10;
  //assume harmonic scaling, so h22=2*h12=2*h21=4*h11
  double z11=1.0, z12=2.0, z21=2.0, z22=4.0, T1=700.0;
  Complex<double> F1_0121, F3_0121;
  Complex<double> R;

  for(i=0;i<i3;i++)
  {
    Complex<double> h11t31=z11*lsf[dt*i], h21t31=z21*lsf[dt*i];
    for(j=0;j<j3;j++)
    {
      Complex<double> h11t32=z11*lsf[dt*j], h11t31t32=z11*lsf[dt*i+dt*j],
      h12t32=z12*(lsf[dt*j]), h21t32=z21*lsf[dt*j], h21t31t32=z21*lsf[dt*i+dt*j],
      h22t32=z22*lsf[dt*j];
      for(k=0;k<k3;k++)
      {
        Complex<double> h11t33=z11*lsf[dt*k], h11t32t33=z11*lsf[dt*j+dt*k],
        h11t31t32t33=z11*lsf[dt*i+dt*j+dt*k], h12t33=z12*Conj(lsf[dt*k]),
        h12t32t33=z12*Conj(lsf[dt*j+dt*k]), h21t32t33=z21*lsf[dt*j+dt*k],
        h21t31t32t33=z21*lsf[dt*i+dt*j+dt*k], h22t32t33=z22*lsf[dt*j+dt*k];

        F1_0121 = Exp(-(h11t31-h21t31+h11t32-h12t32-h21t32+h22t32+h11t33-h12t33-
        h11t31t32+h21t31t32-h11t32t33+h12t32t33+h11t31t32t33));
        F3_0121 = Exp(-Conj(h11t31-h21t31-h11t32+h12t32+Conj(h11t33)-
        Conj(h12t33)+h11t31t32+h11t32t33-h12t32t33-h21t32t33+h22t32t33-
        h11t31t32t33+h21t31t32t33));

        //no population relaxation
        R = 2.0*((F1_0121)-Exp(-I*(w21-
        w10)*k*dt)*Conj(F3_0121))*Rrot(dt*i,dt*j,dt*k);

        //add in population relaxation, 1/(2*T1) for 1st and 3rd time period and 1/T1 for the
        second -- not exactly sure how to scale for v=1/v=2 coherence during 3rd period but I'm
        using the average v=1/v=2 rate -- for v=0/v=2 coherence, I use T1=T1(v=1)/2
        //R = 2.0*((F1_0121)*exp(-(dt*i)/(2.0*T1)-(dt*j)/(0.5*T1)-(dt*k)/(2.0*T1))-Exp(-
        I*(w21-w10)*k*dt)*Conj(F3_0121)*exp(-(dt*i)/(2.0*T1)-(dt*j)/(0.5*T1)-
        (dt*k)/(4.0/3.0*T1)))*Rrot(dt*i,dt*j,dt*k);

        // "correlated hot ground state" -- same as above, with Jaeyoung's theory, rotations
        and phenomenological population relaxation during t1 and t3 plus the HGS of Stenger, et. al.
        (modified with change in transition dipole) during tau2 -- note that nothing was done to S3,
        both because of the absence of population during t2 and because it only exists when pulses
        are overlapped

```



```

//R = 2.0*((F1_0121)*exp(-(dt*i)/(2.0*T1)-(dt*j)/(0.5*T1)-(dt*k)/(2.0*T1))-Exp(-
I*(w21-w10)*k*dt)*Conj(F3_0121)*exp(-(dt*i)/(2.0*T1)-(dt*j)/(0.5*T1)-
(dt*k)/(4.0/3.0*T1)))*Rrot(dt*i,dt*j,dt*k);

```

```

    R3r[i][j][k] = R.Real();
    R3i[i][j][k] = R.Imag();
}
}
}
return;
}

```

```

double interpR(double ***R, const int &dt, const double &t1, const double &t2, const
double &t3)

```

```

//interpolates response functions
{
    double idt=1/double(dt);
    int i=(idt*t1), j=(idt*t2), k=(idt*t3);
    double a=(t1*idt-i), b=(t2*idt-j), c=(t3*idt-k);
    double y = (1-a)*((1-b)*((1-c)*R[i][j][k]+c*R[i][j][k+1])+b*((1-
c)*R[i][j+1][k]+c*R[i][j+1][k+1]))+a*((1-b)*((1-c)*R[i+1][j][k]+c*R[i+1][j][k+1])+b*((1-
c)*R[i+1][j+1][k]+c*R[i+1][j+1][k+1]));
    //cout<<i<<'\t'<<j<<'\t'<<k<<'\t'<<R[i][j][k]<<'\t'<<y<<'\t'<<R[i][j][k+1]<<endl;
    return y;
}

```

```

double envelope(const double &t)

```

```

//defines envelope amplitude for a (transform limited) normalized gaussian pulse centered at
t=0

```

```

//use is determined by cond in calcP
{
    double PD=50.0; //remember to change PD in main.cc
    double invdel=1/PD;

    //sqrt(4*ln(2)/pi)/(1.414*PD)*exp(-4*ln(2)*t^2/(1.414*PD)^2);
    return 0.6644*invdel*exp(-1.387*invdel*invdel*t*t);
    //return exp(-1.387*invdel*invdel*t*t);
}

```

```

Complex<double> envelopec(const double &t)
//defines envelope amplitude for a chirped, normalized pulse centered at t=0
//use is determined by cond in calcP
{
/*
double PD=50.0; //remember to change PD in main.cc
double invdel=1/PD;
double B=-1.0;
//sqrt(4*ln(2)/pi)/(1.414*PD)*Exp(-4*ln(2)*t^2/(1.414*PD)^2*(1-B*I));
return 0.6644*invdel*Exp(-1.387*invdel*invdel*t*t*(1-B*I));
*/

Vector<double> re(31),im(31);

/*
//0930 data; normalization is 1/89.9
re[0]=0.001, re[1]=0.005, re[2]= 0.018, re[3]=0.033, re[4]=0.038, re[5]=0.025, re[6]=-
0.003, re[7]=-0.027, re[8]=-0.015, re[9]=0.062, re[10]=0.218, re[11]=0.435, re[12]=0.663,
re[13]=0.851, re[14]=0.966, re[15]=0.998, re[16]=0.959, re[17]=0.858, re[18]=0.707,
re[19]=0.52, re[20]=0.329, re[21]=0.167, re[22]=0.062, re[23]=0.016, re[24]=0.01,
re[25]=0.017, re[26]=0.02, re[27]=0.016, re[28]=0.01, re[29]=0.005, re[30]=0.003;
im[0]=-0.004, im[1]=-0.002, im[2]=-0.005, im[3]=-0.018, im[4]=-0.038, im[5]=-0.052,
im[6]=-0.041, im[7]=0.007, im[8]=0.094, im[9]=0.202, im[10]=0.294, im[11]=0.326,
im[12]=0.278, im[13]=0.165, im[14]=0.036, im[15]=-0.057, im[16]=-0.081, im[17]=-0.034,
im[18]=0.054, im[19]=0.139, im[20]=0.182, im[21]=0.168, im[22]=0.115, im[23]=0.056,
im[24]=0.017, im[25]=0.005, im[26]=0.007, im[27]=0.011, im[28]=0.010, im[29]=0.005,
im[30]=0.0;
double norm = 1/89.9;
*/
/*
//0930 data refit; normalization is 1/90.2
re[0]=0.01, re[1]=0.01, re[2]=0.012, re[3]=0.021, re[4]=0.041, re[5]=0.058, re[6]=0.044,
re[7]=-0.02, re[8]=-0.115, re[9]=-0.177, re[10]=-0.133, re[11]=0.051, re[12]=0.33,
re[13]=0.608, re[14]=0.803, re[15]=0.882, re[16]=0.844, re[17]=0.705, re[18]=0.492,
re[19]=0.254, re[20]=0.05, re[21]=-0.075, re[22]=-0.109, re[23]=-0.08, re[24]=-0.035,
re[25]=-0.004, re[26]=0.008, re[27]=0.007, re[28]=0.004, re[29]=0.003, re[30]=0.005;
im[0]=-0.003, im[1]=-0.001, im[2]=0.007, im[3]=0.017, im[4]=0.017, im[5]=-0.008,
im[6]=-0.049, im[7]=-0.073, im[8]=-0.03, im[9]=0.11, im[10]=0.321, im[11]=0.526,
im[12]=0.638, im[13]=0.632, im[14]=0.552, im[15]=0.469, im[16]=0.43, im[17]=0.442,
im[18]=0.469, im[19]=0.459, im[20]=0.378, im[21]=0.242, im[22]=0.107, im[23]=0.02,
im[24]=-0.011, im[25]=-0.008, im[26]=0.003, im[27]=0.007, im[28]=0.007, im[29]=0.006,
im[30]=0.004;
double norm = 1/90.2;
*/

//0219 data; normalization is 1/83.0

```

```

re[0]=0.0, re[1]=0.001, re[2]=0.002, re[3]=0.006, re[4]=0.012, re[5]=0.021, re[6]=0.032,
re[7]=0.038, re[8]=0.035, re[9]=0.016, re[10]=-0.02, re[11]=-0.067, re[12]=-0.115, re[13]=-
0.15, re[14]=-0.16, re[15]=-0.143, re[16]=-0.105, re[17]=-0.06, re[18]=-0.023, re[19]=-
0.006, re[20]=-0.012, re[21]=-0.034, re[22]=-0.06, re[23]=-0.08, re[24]=-0.086, re[25]=-
0.078, re[26]=-0.06, re[27]=-0.039, re[28]=-0.022, re[29]=-0.01, re[30]=-0.004;
im[0]=-0.003, im[1]=0.004, im[2]=0.005, im[3]=-0.002, im[4]=-0.016, im[5]=-0.027,
im[6]=-0.024, im[7]=0.001, im[8]=0.058, im[9]=0.15, im[10]=0.276, im[11]=0.432,
im[12]=0.605, im[13]=0.774, im[14]=0.911, im[15]=0.985, im[16]=0.973, im[17]=0.868,
im[18]=0.683, im[19]=0.454, im[20]=0.225, im[21]=0.04, im[22]=-0.075, im[23]=-0.117,
im[24]=-0.102, im[25]=-0.06, im[26]=-0.018, im[27]=0.006, im[28]=0.01, im[29]=0.002,
im[30]=-0.007;
double norm = 1/83.0;

/*
//0219 data refit; normalization is 94.3
re[0]=0.023, re[1]=0.046, re[2]=0.051, re[3]=0.026, re[4]=-0.031, re[5]=-0.109, re[6]=-
0.18, re[7]=-0.209, re[8]=-0.161, re[9]=-0.022, re[10]=0.195, re[11]=0.454, re[12]=0.7,
re[13]=0.887, re[14]=0.986, re[15]=0.992, re[16]=0.913, re[17]=0.775, re[18]=0.61,
re[19]=0.449, re[20]=0.309, re[21]=0.198, re[22]=0.111, re[23]=0.042, re[24]=-0.009,
re[25]=-0.04, re[26]=-0.049, re[27]=-0.046, re[28]=-0.039, re[29]=-0.031, re[30]=-0.02;
im[0]=-0.024, im[1]=-0.019, im[2]=0.003, im[3]=0.027, im[4]=0.031, im[5]=0.0, im[6]=-
0.065, im[7]=-0.138, im[8]=-0.186, im[9]=-0.187, im[10]=-0.143, im[11]=-0.077, im[12]=-
0.018, im[13]=0.011, im[14]=0.0, im[15]=-0.041, im[16]=-0.092, im[17]=-0.137, im[18]=-
0.167, im[19]=-0.181, im[20]=-0.177, im[21]=-0.156, im[22]=-0.119, im[23]=-0.076,
im[24]=-0.039, im[25]=-0.015, im[26]=-0.002, im[27]=0.0, im[28]=0.011, im[29]=0.012,
im[30]=0.008;
double norm = 1/94.3;
*/

//interpolation of real pulses
if(t>-150 && t<150)
{
double B=-1.0;
int i = (t+150.0)*0.1;//assume 10 fs steps
double a = (t-i*10.0+150.0)*0.1;
return ((1-a)*(re[i]-B*I*im[i])+a*(re[i+1]-B*I*im[i+1]))*norm;
}
else
return 0;
}

```

```

Complex<double> P1abc(double ***R1r, double ***R1i, const int &dt, const double &t1,
const double &t2, const double &t3, const double &tau1, const double &tau2, const double
&tau3, const int &cond)
//calculate the polarization for S1 diagrams with interaction order abc given,
t1,t2,t3,tau1,tau2,tau3(t)
{
Complex<double> P1;
//double w1 = 2*pi*3e-5*3275, w2=w1, w3=w1; //remember to change w in totalP
//double w = 2*pi*3e-5*3276;
double idt=1/double(dt);
int i=(idt*t1), j=(idt*t2), k=(idt*t3);
double a=(t1*idt-i), b=(t2*idt-j), c=(t3*idt-k);
double r1r = (1-a)*((1-b)*((1-c)*R1r[i][j][k]+c*R1r[i][j][k+1]))+b*((1-
c)*R1r[i][j+1][k]+c*R1r[i][j+1][k+1]))+a*((1-b)*((1-
c)*R1r[i+1][j][k]+c*R1r[i+1][j][k+1]))+b*((1-c)*R1r[i+1][j+1][k]+c*R1r[i+1][j+1][k+1]));
double r1i = (1-a)*((1-b)*((1-c)*R1i[i][j][k]+c*R1i[i][j][k+1]))+b*((1-
c)*R1i[i][j+1][k]+c*R1i[i][j+1][k+1]))+a*((1-b)*((1-
c)*R1i[i+1][j][k]+c*R1i[i+1][j][k+1]))+b*((1-c)*R1i[i+1][j+1][k]+c*R1i[i+1][j+1][k+1]));

if(tau1>=0)
{
//assume all light fields have the same carrier frequency, w=w1=w2=w3, and factor out
exp(-i*w*tau3+i*w*tau1)
if(cond==0)
P1 = (r1r+I*r1i)*Exp(I*(-w10+w)*t3+I*(w10-w)*t1)*envelope(tau1+tau2+tau3-t3-
t2-t1)*envelope(tau2+tau3-t3-t2)*envelope(tau3-t3);
else
P1 = (r1r+I*r1i)*Exp(I*(-w10+w)*t3+I*(w10-
w)*t1)*Conj(envelopec(tau1+tau2+tau3-t3-t2-t1))*envelopec(tau2+tau3-t3-
t2)*envelopec(tau3-t3);
}
else
{
if(cond==0)
P1 = (r1r+I*r1i)*Exp(I*(-w10+w)*t3+I*(w10-w)*t1)*envelope(tau2+tau3-t3-t2-
t1)*envelope(-tau1+tau2+tau3-t3-t2)*envelope(tau3-t3);
else
P1 = (r1r+I*r1i)*Exp(I*(-w10+w)*t3+I*(w10-w)*t1)*Conj(envelopec(tau2+tau3-t3-
t2-t1))*envelopec(-tau1+tau2+tau3-t3-t2)*envelopec(tau3-t3);
}

return P1;
}

```

```

Complex<double> P1acb(double ***R1r, double ***R1i, const int &dt, const double &t1,
const double &t2, const double &t3, const double &tau1, const double &tau2, const double
&tau3, const int &cond)
//calculate the polarization for S1 diagrams with interaction order acb given,
t1,t2,t3,tau1,tau2,tau3(t)
{
Complex<double> P1;
//double w1 = 2*pi*3e-5*3275, w2=w1, w3=w1; //remember to change w in totalP
//double w = 2*pi*3e-5*3275;
double idt=1/double(dt);
int i=(idt*t1), j=(idt*t2), k=(idt*t3);
double a=(t1*idt-i), b=(t2*idt-j), c=(t3*idt-k);
double r1r = (1-a)*((1-b)*((1-c)*R1r[i][j][k]+c*R1r[i][j][k+1])+b*((1-
c)*R1r[i][j+1][k]+c*R1r[i][j+1][k+1]))+a*((1-b)*((1-
c)*R1r[i+1][j][k]+c*R1r[i+1][j][k+1])+b*((1-c)*R1r[i+1][j+1][k]+c*R1r[i+1][j+1][k+1]));
double r1i = (1-a)*((1-b)*((1-c)*R1i[i][j][k]+c*R1i[i][j][k+1])+b*((1-
c)*R1i[i][j+1][k]+c*R1i[i][j+1][k+1]))+a*((1-b)*((1-
c)*R1i[i+1][j][k]+c*R1i[i+1][j][k+1])+b*((1-c)*R1i[i+1][j+1][k]+c*R1i[i+1][j+1][k+1]));

if(tau1>=0)
{
//assume all light fields have the same carrier frequency, w=w1=w2=w3, and factor out
exp(-i*w*tau3+i*w*tau1)
if(cond==0)
P1 = (r1r+I*r1i)*Exp(I*(-w10+w)*t3+I*(w10-w)*t1)*envelope(tau1+tau2+tau3-t3-
t2-t1)*envelope(tau2+tau3-t3)*envelope(tau3-t3-t2);
else
P1 = (r1r+I*r1i)*Exp(I*(-w10+w)*t3+I*(w10-
w)*t1)*Conj(envelopec(tau1+tau2+tau3-t3-t2-t1))*envelopec(tau2+tau3-t3)*envelopec(tau3-
t3-t2);
}
else
{
if(cond==0)
P1 = (r1r+I*r1i)*Exp(I*(-w10+w)*t3+I*(w10-w)*t1)*envelope(tau2+tau3-t3-t2-
t1)*envelope(-tau1+tau2+tau3-t3)*envelope(tau3-t3-t2);
else
P1 = (r1r+I*r1i)*Exp(I*(-w10+w)*t3+I*(w10-w)*t1)*Conj(envelopec(tau2+tau3-t3-
t2-t1))*envelopec(-tau1+tau2+tau3-t3)*envelopec(tau3-t3-t2);
}

return P1;
}

```

```

Complex<double> P2bac(double ***R2r, double ***R2i, const int &dt, const double &t1,
const double &t2, const double &t3, const double &tau1, const double &tau2, const double
&tau3, const int &cond)
//calculate the polarization for S2 diagrams with interaction order bac given,
t1,t2,t3,tau1,tau2,tau3(t)
{
Complex<double> P2;
//double w1 = 2*pi*3e-5*3275, w2=w1, w3=w1; //remember to change w in totalP
//double w = 2*pi*3e-5*3275;
double idt=1/double(dt);
int i=(idt*t1), j=(idt*t2), k=(idt*t3);
double a=(t1*idt-i), b=(t2*idt-j), c=(t3*idt-k);
double r2r = (1-a)*((1-b)*((1-c)*R2r[i][j][k]+c*R2r[i][j][k+1]))+b*((1-
c)*R2r[i][j+1][k]+c*R2r[i][j+1][k+1]))+a*((1-b)*((1-
c)*R2r[i+1][j][k]+c*R2r[i+1][j][k+1]))+b*((1-c)*R2r[i+1][j+1][k]+c*R2r[i+1][j+1][k+1]));
double r2i = (1-a)*((1-b)*((1-c)*R2i[i][j][k]+c*R2i[i][j][k+1]))+b*((1-
c)*R2i[i][j+1][k]+c*R2i[i][j+1][k+1]))+a*((1-b)*((1-
c)*R2i[i+1][j][k]+c*R2i[i+1][j][k+1]))+b*((1-c)*R2i[i+1][j+1][k]+c*R2i[i+1][j+1][k+1]));

if(tau1<0)
{
//assume all light fields have the same carrier frequency, w=w1=w2=w3, and factor out
exp(-i*w*tau3+i*w*tau1)
if(cond==0)
P2 = (r2r+I*r2i)*Exp(I*(-w10+w)*t3+I*(-w10+w)*t1)*envelope(tau2+tau3-t3-
t2)*envelope(-tau1+tau2+tau3-t3-t2-t1)*envelope(tau3-t3);
else
P2 = (r2r+I*r2i)*Exp(I*(-w10+w)*t3+I*(-w10+w)*t1)*Conj(envelopec(tau2+tau3-
t3-t2))*envelopec(-tau1+tau2+tau3-t3-t2-t1)*envelopec(tau3-t3);
}
else
{
if(cond==0)
P2 = (r2r+I*r2i)*Exp(I*(-w10+w)*t3+I*(-w10+w)*t1)*envelope(tau1+tau2+tau3-t3-
t2)*envelope(tau2+tau3-t3-t2-t1)*envelope(tau3-t3);
else
P2 = (r2r+I*r2i)*Exp(I*(-w10+w)*t3+I*(-
w10+w)*t1)*Conj(envelopec(tau1+tau2+tau3-t3-t2))*envelopec(tau2+tau3-t3-t2-
t1)*envelopec(tau3-t3);
}

return P2;
}

```

```

Complex<double> P2cab(double ***R2r, double ***R2i, const int &dt, const double &t1,
const double &t2, const double &t3, const double &tau1, const double &tau2, const double
&tau3, const int &cond)
//calculate the polarization for S2 diagrams with interaction order cab given,
t1,t2,t3,tau1,tau2,tau3(t)
{
Complex<double> P2;
//double w1 = 2*pi*3e-5*3275, w2=w1, w3=w1; //remember to change w in totalP
//double w = 2*pi*3e-5*3275;
double idt=1/double(dt);
int i=(idt*t1), j=(idt*t2), k=(idt*t3);
double a=(t1*idt-i), b=(t2*idt-j), c=(t3*idt-k);
double r2r = (1-a)*((1-b)*((1-c)*R2r[i][j][k]+c*R2r[i][j][k+1])+b*((1-
c)*R2r[i][j+1][k]+c*R2r[i][j+1][k+1]))+a*((1-b)*((1-
c)*R2r[i+1][j][k]+c*R2r[i+1][j][k+1])+b*((1-c)*R2r[i+1][j+1][k]+c*R2r[i+1][j+1][k+1]));
double r2i = (1-a)*((1-b)*((1-c)*R2i[i][j][k]+c*R2i[i][j][k+1])+b*((1-
c)*R2i[i][j+1][k]+c*R2i[i][j+1][k+1]))+a*((1-b)*((1-
c)*R2i[i+1][j][k]+c*R2i[i+1][j][k+1])+b*((1-c)*R2i[i+1][j+1][k]+c*R2i[i+1][j+1][k+1]));

if(tau1<0)
{
//assume all light fields have the same carrier frequency, w=w1=w2=w3, and factor out
exp(-i*w*tau3+i*w*tau1)
if(cond==0)
P2 = (r2r+I*r2i)*Exp(I*(-w10+w)*t3+I*(-w10+w)*t1)*envelope(tau2+tau3-t3-
t2)*envelope(-tau1+tau2+tau3-t3)*envelope(tau3-t3-t2-t1);
else
P2 = (r2r+I*r2i)*Exp(I*(-w10+w)*t3+I*(-w10+w)*t1)*Conj(envelopec(tau2+tau3-
t3-t2))*envelopec(-tau1+tau2+tau3-t3)*envelopec(tau3-t3-t2-t1);
}
else
{
if(cond==0)
P2 = (r2r+I*r2i)*Exp(I*(-w10+w)*t3+I*(-w10+w)*t1)*envelope(tau1+tau2+tau3-t3-
t2)*envelope(tau2+tau3-t3)*envelope(tau3-t3-t2-t1);
else
P2 = (r2r+I*r2i)*Exp(I*(-w10+w)*t3+I*(-
w10+w)*t1)*Conj(envelopec(tau1+tau2+tau3-t3-t2))*envelopec(tau2+tau3-
t3)*envelopec(tau3-t3-t2-t1);
}
}

return P2;
}

```

```

Complex<double> P3bca(double ***R3r, double ***R3i, const int &dt, const double &t1,
const double &t2, const double &t3, const double &tau1, const double &tau2, const double
&tau3, const int &cond)
//calculate the polarization for S3 diagrams with interaction order bca given,
t1,t2,t3,tau1,tau2,tau3(t)
{
Complex<double> P3;
//double w1 = 2*pi*3e-5*3275, w2=w1, w3=w1; //remember to change w in totalP
//double w = 2*pi*3e-5*3275;
double idt=1/double(dt);
int i=(idt*t1), j=(idt*t2), k=(idt*t3);
double a=(t1*idt-i), b=(t2*idt-j), c=(t3*idt-k);
double r3r = (1-a)*((1-b)*((1-c)*R3r[i][j][k]+c*R3r[i][j][k+1]))+b*((1-
c)*R3r[i][j+1][k]+c*R3r[i][j+1][k+1]))+a*((1-b)*((1-
c)*R3r[i+1][j][k]+c*R3r[i+1][j][k+1]))+b*((1-c)*R3r[i+1][j+1][k]+c*R3r[i+1][j+1][k+1]));
double r3i = (1-a)*((1-b)*((1-c)*R3i[i][j][k]+c*R3i[i][j][k+1]))+b*((1-
c)*R3i[i][j+1][k]+c*R3i[i][j+1][k+1]))+a*((1-b)*((1-
c)*R3i[i+1][j][k]+c*R3i[i+1][j][k+1]))+b*((1-c)*R3i[i+1][j+1][k]+c*R3i[i+1][j+1][k+1]));

if(tau1<0)
{
//assume all light fields have the same carrier frequency, w=w1=w2=w3, and factor out
exp(-i*w*tau3+i*w*tau1)
if(cond==0)
P3 = (r3r+I*r3i)*Exp(-I*2*w*tau2+I*(-w10+w)*t3+I*(-w20+2*w)*t2+I*(-
w10+w)*t1)*envelope(tau2+tau3-t3)*envelope(-tau1+tau2+tau3-t3-t2-t1)*envelope(tau3-t3-
t2);
else
P3 = (r3r+I*r3i)*Exp(-I*2*w*tau2+I*(-w10+w)*t3+I*(-w20+2*w)*t2+I*(-
w10+w)*t1)*Conj(envelopec(tau2+tau3-t3))*envelope(-tau1+tau2+tau3-t3-t2-
t1)*envelopec(tau3-t3-t2);
}
else
{
if(cond==0)
P3 = (r3r+I*r3i)*Exp(-I*2*w*tau2+I*(-w10+w)*t3+I*(-w20+2*w)*t2+I*(-
w10+w)*t1)*envelope(tau1+tau2+tau3-t3)*envelope(tau2+tau3-t3-t2-t1)*envelope(tau3-t3-
t2);
else
P3 = (r3r+I*r3i)*Exp(-I*2*w*tau2+I*(-w10+w)*t3+I*(-w20+2*w)*t2+I*(-
w10+w)*t1)*Conj(envelopec(tau1+tau2+tau3-t3))*envelopec(tau2+tau3-t3-t2-
t1)*envelopec(tau3-t3-t2);
}
}

return P3;
}

```



```

Complex<double> P3cba(double ***R3r, double ***R3i, const int &dt, const double &t1,
const double &t2, const double &t3, const double &tau1, const double &tau2, const double
&tau3, const int &cond)
//calculate the polarization for S3 diagrams with interaction order cba given,
t1,t2,t3,tau1,tau2,tau3(t)
{
Complex<double> P3;
//double w1 = 2*pi*3e-5*3275, w2=w1, w3=w1; //remember to change w in totalP
//double w = 2*pi*3e-5*3275;
double idt=1/double(dt);
int i=(idt*t1), j=(idt*t2), k=(idt*t3);
double a=(t1*idt-i), b=(t2*idt-j), c=(t3*idt-k);
double r3r = (1-a)*((1-b)*((1-c)*R3r[i][j][k]+c*R3r[i][j][k+1])+b*((1-
c)*R3r[i][j+1][k]+c*R3r[i][j+1][k+1]))+a*((1-b)*((1-
c)*R3r[i+1][j][k]+c*R3r[i+1][j][k+1])+b*((1-c)*R3r[i+1][j+1][k]+c*R3r[i+1][j+1][k+1]));
double r3i = (1-a)*((1-b)*((1-c)*R3i[i][j][k]+c*R3i[i][j][k+1])+b*((1-
c)*R3i[i][j+1][k]+c*R3i[i][j+1][k+1]))+a*((1-b)*((1-
c)*R3i[i+1][j][k]+c*R3i[i+1][j][k+1])+b*((1-c)*R3i[i+1][j+1][k]+c*R3i[i+1][j+1][k+1]));

if(tau1<0)
{
//assume all light fields have the same carrier frequency, w=w1=w2=w3, and factor out
exp(-i*w*tau3+i*w*tau1)
if(cond==0)
P3 = (r3r+I*r3i)*Exp(-I*2*w*tau2+I*(-w10+w)*t3+I*(-w20+2*w)*t2+I*(-
w10+w)*t1)*envelope(tau2+tau3-t3)*envelope(-tau1+tau2+tau3-t3-t2)*envelope(tau3-t3-t2-
t1);
else
P3 = (r3r+I*r3i)*Exp(-I*2*w*tau2+I*(-w10+w)*t3+I*(-w20+2*w)*t2+I*(-
w10+w)*t1)*Conj(envelopec(tau2+tau3-t3))*envelopec(-tau1+tau2+tau3-t3-
t2)*envelopec(tau3-t3-t2-t1);
}
else
{
if(cond==0)
P3 = (r3r+I*r3i)*Exp(-I*2*w*tau2+I*(-w10+w)*t3+I*(-w20+2*w)*t2+I*(-
w10+w)*t1)*envelope(tau1+tau2+tau3-t3)*envelope(tau2+tau3-t3-t2)*envelope(tau3-t3-t2-
t1);
else
P3 = (r3r+I*r3i)*Exp(-I*2*w*tau2+I*(-w10+w)*t3+I*(-w20+2*w)*t2+I*(-
w10+w)*t1)*Conj(envelopec(tau1+tau2+tau3-t3))*envelopec(tau2+tau3-t3-
t2)*envelopec(tau3-t3-t2-t1);
}
}
}

```

```

return P3;
}

```

```

void calcPri(double ***Sr, double ***Si, double ***R1r, double ***R1i, double ***R2r,
double ***R2i, double ***R3r, double ***R3i, const int &dt, const Vec_DP &tau1, const
Vec_DP &tau1i, const Vec_DP &tau2, const Vec_DP &tau3, const Vec_DP &tau3i, const
double &PD, const int &cond)

```

```

//Calculates the real and imaginary parts of the envelope function without oscillations in
tau1 and tau3 -- to be added with interpolation in calcP

```

```

{

int cont=1;
//the value of cont determines which integrals contribute to the polarization-- >=0 includes
normal contributions, while <=0 includes double counted contributions

int i,j,k;
double ta1,ta2,ta3,t;
//double w=2*pi*3e-5*3275;
double
tauamin,tauamax,taubmin,taubmax,taucmin,taucmax,eq_lower,eq_upper,ind_lower,ind_upper;
Complex<double> integral,temp_integral1=0,temp_integral2=0;
int eq_steps,ind_steps,a_steps,b_steps,c_steps;
int width=20, msteps=6;
//width sets the integration width, with a minum of msteps divisions
Vec_DP limits(6);

for(j=0;j<tau2.size();j++)
{
ta2=tau2[j];
//cout<<"j "<<j<<endl;
for(i=0;i<tau1.size();i++)
{
ta1=tau1[i];
for(k=0;k<tau3.size();k++)
{
ta3=tau3[k];

if(ta1>=0)
{

```

```

    limits[0]=ta3+ta2+ta1+2.0*PD; //tauamin
    limits[3]=ta3+ta2+ta1-2.0*PD; //tauamax
    limits[1]=ta3+ta2+2.0*PD; //taubmin
    limits[4]=ta3+ta2-2.0*PD; //taubmax
    limits[2]=ta3+2.0*PD; //taucmin
    limits[5]=ta3-2.0*PD; //taucmax
  }
else
  {
    limits[0]=ta3+ta2+2.0*PD; //tauamin
    limits[3]=ta3+ta2-2.0*PD; //tauamax
    limits[1]=ta3+ta2-ta1+2.0*PD; //taubmin
    limits[4]=ta3+ta2-ta1-2.0*PD; //taubmax
    limits[2]=ta3+2.0*PD; //taucmin
    limits[5]=ta3-2.0*PD; //taucmax
  }

if(limits[3]<=0.0) {limits[3]=0.0; if(limits[0]==0.0) limits[0]=0.01;}
if(limits[4]<=0.0) {limits[4]=0.0; if(limits[1]==0.0) limits[1]=0.01;}
if(limits[5]<=0.0) {limits[5]=0.0; if(limits[2]==0.0) limits[2]=0.01;}

tauamin=limits[0]; tauamax=limits[3]; taubmin=limits[1]; taubmax=limits[4];
taucmin=limits[2]; taucmax=limits[5];

//try direct integration using gauleg
if(int((tauamin-tauamax)/width<=msteps)) a_steps=msteps;
else a_steps=int((tauamin-tauamax)/width);
if(int((taubmin-taubmax)/width<=msteps)) b_steps=msteps;
else b_steps=int((taubmin-taubmax)/width);
if(int((taucmin-taucmax)/width<=msteps)) c_steps=msteps;
else c_steps=int((taucmin-taucmax)/width);

//to include single counted contributions, set cont >=0
if(cont>=0)

temp_integral1=Integrate(R1r,R1i,R2r,R2i,R3r,R3i,tauamin,tauamax,taubmin,taubmax,tauc
min,taucmax,ta1,ta2,ta3,dt,a_steps,b_steps,c_steps,cond);

//to include double-counted interactions, set cont <=0
if(cont<=0)
{

```

```

if(ta1>=0)
{
    if(taubmax<taucmin)//b&c overlap
    {
        if(tauamax<taubmin)//a&b overlap
        {
            if(tauamax<taucmin)//a,b&c overlap
            {

                //b&c overlapped in region taucmin to taubmax
                //taub=tauc, scan taua
                eq_lower=taucmin; eq_upper=taubmax;
                ind_lower=tauamin; ind_upper=tauamax;
                if(int((eq_lower-eq_upper)/width<=msteps)) eq_steps=msteps;
                else eq_steps=int((eq_lower-eq_upper)/width);
                if(int((ind_lower-ind_upper)/width<=msteps)) ind_steps=msteps;
                else ind_steps=int((ind_lower-ind_upper)/width);

temp_integral2=P13bc_a(R1r,R1i,R2r,R2i,R3r,R3i,eq_lower,eq_upper,ind_lower,ind_upper,
ta1,ta2,ta3,dt,eq_steps,ind_steps,cond);
                //cout<<"abc+ bc
"<<eq_lower<<"\t"<<eq_upper<<"\t"<<ind_lower<<"\t"<<ind_upper<<"\t"<<eq_steps<<"\t"<<in
d_steps<<endl;

                //a&b overlapped in region taubmin to tauamax
                //taua=taub, scan tauc
                eq_lower=taubmin; eq_upper=tauamax;
                ind_lower=taucmin; ind_upper=taucmax;
                if(int((eq_lower-eq_upper)/width<=msteps)) eq_steps=msteps;
                else eq_steps=int((eq_lower-eq_upper)/width);
                if(int((ind_lower-ind_upper)/width<=msteps)) ind_steps=msteps;
                else ind_steps=int((ind_lower-ind_upper)/width);

temp_integral2=temp_integral2+P13ab_c(R1r,R1i,R2r,R2i,R3r,R3i,eq_lower,eq_upper,ind_l
ower,ind_upper,ta1,ta2,ta3,dt,eq_steps,ind_steps,cond);
                //cout<<"abc+ ab
"<<eq_lower<<"\t"<<eq_upper<<"\t"<<ind_lower<<"\t"<<ind_upper<<"\t"<<eq_steps<<"\t"<<in
d_steps<<endl;

                //a&c overlapped in region taucmin to tauamax
                //taua=tauc,scan taub
                eq_lower=taucmin; eq_upper=tauamax;
                ind_lower=taubmin; ind_upper=taubmax;
                if(int((eq_lower-eq_upper)/width<=msteps)) eq_steps=msteps;
                else eq_steps=int((eq_lower-eq_upper)/width);
                if(int((ind_lower-ind_upper)/width<=msteps)) ind_steps=msteps;

```

```

else ind_steps=int((ind_lower-ind_upper)/width);

temp_integral2=temp_integral2+P23ac_b(R1r,R1i,R2r,R2i,R3r,R3i,eq_lower,eq_upper,ind_l
ower,ind_upper,ta1,ta2,ta3,dt,eq_steps,ind_steps,cond);
//cout<<"abc+ ac
"<<eq_lower<<"\t"<<eq_upper<<"\t"<<ind_lower<<"\t"<<ind_upper<<"\t"<<eq_steps<<"\t"<<in
d_steps<<endl;

}
else//b&c overlapped, a&b overlapped, a&c not overlapped
{

//b&c overlapped in region tauamin to taubmax
//taua>taub=tauc
eq_lower=taucmin; eq_upper=taubmax;
ind_lower=tauamin; ind_upper=tauamax;
if(int((eq_lower-eq_upper)/width<=msteps)) eq_steps=msteps;
else eq_steps=int((eq_lower-eq_upper)/width);
if(int((ind_lower-ind_upper)/width<=msteps)) ind_steps=msteps;
else ind_steps=int((ind_lower-ind_upper)/width);

temp_integral2=P13bc_a(R1r,R1i,R2r,R2i,R3r,R3i,eq_lower,eq_upper,ind_lower,ind_upper,
ta1,ta2,ta3,dt,eq_steps,ind_steps,cond);
//cout<<"abc+ bc
"<<eq_lower<<"\t"<<eq_upper<<"\t"<<ind_lower<<"\t"<<ind_upper<<"\t"<<eq_steps<<"\t"<<in
d_steps<<endl;

//a&b overlapped in region taubmin to tauamax
//taua=taub>tauc
eq_lower=taubmin; eq_upper=tauamax;
ind_lower=taucmin; ind_upper=taucmax;
if(int((eq_lower-eq_upper)/width<=msteps)) eq_steps=msteps;
else eq_steps=int((eq_lower-eq_upper)/width);
if(int((ind_lower-ind_upper)/width<=msteps)) ind_steps=msteps;
else ind_steps=int((ind_lower-ind_upper)/width);

temp_integral2=temp_integral2+P13ab_c(R1r,R1i,R2r,R2i,R3r,R3i,eq_lower,eq_upper,ind_l
ower,ind_upper,ta1,ta2,ta3,dt,eq_steps,ind_steps,cond);
//cout<<"abc+ ac
"<<eq_lower<<"\t"<<eq_upper<<"\t"<<ind_lower<<"\t"<<ind_upper<<"\t"<<eq_steps<<"\t"<<in
d_steps<<endl;

}
}
else//b&c overlapped, a&b not overlapped

```

```

    {
        //b&c overlapped in region taucmin to taubmax
        //taua>taub=tauc
        eq_lower=taucmin; eq_upper=taubmax;
        ind_lower=tauamin; ind_upper=tauamax;
        if(int((eq_lower-eq_upper)/width<=msteps)) eq_steps=msteps;
        else eq_steps=int((eq_lower-eq_upper)/width);
        if(int((ind_lower-ind_upper)/width<=msteps)) ind_steps=msteps;
        else ind_steps=int((ind_lower-ind_upper)/width);

        temp_integral2=P13bc_a(R1r,R1i,R2r,R2i,R3r,R3i,eq_lower,eq_upper,ind_lower,ind
_upper,ta1,ta2,ta3,dt,eq_steps,ind_steps,cond);
        //cout<<"bc+
"<<eq_lower<<"\t"<<eq_upper<<"\t"<<ind_lower<<"\t"<<ind_upper<<"\t"<<eq_steps<<"\t"<<in
d_steps<<endl;

    }
}
else if(tauamax<taubmin)//a&b overlapped, b&c not overlapped
{

    //a&b overlapped in region taubmin to tauamax
    //taua=taub>tauc
    eq_lower=taubmin; eq_upper=tauamax;
    ind_lower=taucmin; ind_upper=taucmax;
    if(int((eq_lower-eq_upper)/width<=msteps)) eq_steps=msteps;
    else eq_steps=int((eq_lower-eq_upper)/width);
    if(int((ind_lower-ind_upper)/width<=msteps)) ind_steps=msteps;
    else ind_steps=int((ind_lower-ind_upper)/width);

    temp_integral2=P13ab_c(R1r,R1i,R2r,R2i,R3r,R3i,eq_lower,eq_upper,ind_lower,ind_upper,
    ta1,ta2,ta3,dt,eq_steps,ind_steps,cond);
    //cout<<"ab+
"<<eq_lower<<"\t"<<eq_upper<<"\t"<<ind_lower<<"\t"<<ind_upper<<"\t"<<eq_steps<<"\t"<<in
d_steps<<endl;

}
else//none overlapped
{
    temp_integral2=0+0*I;
    //cout<<"none+"<<endl;
}
}

else//(ta1<0)
{

```

```

if(tauamax<taucmin)//a&c overlap
{
  if(taubmax<tauamin)//a&b overlap
  {
    if(taubmax<taucmin)//a,b&c overlap
    {

      //a&c overlapped in region taucmin to tauamax
      //taua=tauc, scan taub
      eq_lower=taucmin; eq_upper=tauamax;
      ind_lower=taubmin; ind_upper=taubmax;
      if(int((eq_lower-eq_upper)/width<=msteps)) eq_steps=msteps;
      else eq_steps=int((eq_lower-eq_upper)/width);
      if(int((ind_lower-ind_upper)/width<=msteps)) ind_steps=msteps;
      else ind_steps=int((ind_lower-ind_upper)/width);

temp_integral2=P23ac_b(R1r,R1i,R2r,R2i,R3r,R3i,eq_lower,eq_upper,ind_lower,ind_upper,
ta1,ta2,ta3,dt,eq_steps,ind_steps,cond);
      //cout<<"abc- ac
"<<<eq_lower<<"\t"<<eq_upper<<"\t"<<ind_lower<<"\t"<<ind_upper<<"\t"<<eq_steps<<"\t"<<in
d_steps<<endl;

      //a&b overlapped in region tauamin to taubmax
      //taua=taub, scan tauc
      eq_lower=tauamin; eq_upper=taubmax;
      ind_lower=taucmin; ind_upper=taucmax;
      if(int((eq_lower-eq_upper)/width<=msteps)) eq_steps=msteps;
      else eq_steps=int((eq_lower-eq_upper)/width);
      if(int((ind_lower-ind_upper)/width<=msteps)) ind_steps=msteps;
      else ind_steps=int((ind_lower-ind_upper)/width);

temp_integral2=temp_integral2+P13ab_c(R1r,R1i,R2r,R2i,R3r,R3i,eq_lower,eq_upper,ind_l
ower,ind_upper,ta1,ta2,ta3,dt,eq_steps,ind_steps,cond);
      //cout<<"abc- ab
"<<<eq_lower<<"\t"<<eq_upper<<"\t"<<ind_lower<<"\t"<<ind_upper<<"\t"<<eq_steps<<"\t"<<in
d_steps<<endl;

      //b&c overlapped in region taucmin to taubmax
      //taub=tauc, scan taua
      eq_lower=taucmin; eq_upper=taubmax;
      ind_lower=tauamin; ind_upper=tauamax;
      if(int((eq_lower-eq_upper)/width<=msteps)) eq_steps=msteps;
      else eq_steps=int((eq_lower-eq_upper)/width);
      if(int((ind_lower-ind_upper)/width<=msteps)) ind_steps=msteps;
      else ind_steps=int((ind_lower-ind_upper)/width);

```

```

temp_integral2=temp_integral2+P13bc_a(R1r,R1i,R2r,R2i,R3r,R3i,eq_lower,eq_upper,ind_l
ower,ind_upper,ta1,ta2,ta3,dt,eq_steps,ind_steps,cond);
    //cout<<"abc- bc
"<<eq_lower<<"\t"<<eq_upper<<"\t"<<ind_lower<<"\t"<<ind_upper<<"\t"<<eq_steps<<"\t"<<in
d_steps<<endl;

    }
else//a&c overlapped, a&b overlapped, b&c not overlapped
{

    //a&c overlapped in region tauamin to tauamax
    //taub>taua=tauc
    eq_lower=taucmin; eq_upper=tauamax;
    ind_lower=taubmin; ind_upper=taubmax;
    if(int((eq_lower-eq_upper)/width<=msteps)) eq_steps=msteps;
    else eq_steps=int((eq_lower-eq_upper)/width);
    if(int((ind_lower-ind_upper)/width<=msteps)) ind_steps=msteps;
    else ind_steps=int((ind_lower-ind_upper)/width);

temp_integral2=P23ac_b(R1r,R1i,R2r,R2i,R3r,R3i,eq_lower,eq_upper,ind_lower,ind_upper,
ta1,ta2,ta3,dt,eq_steps,ind_steps,cond);
    //cout<<"acab- ac
"<<eq_lower<<"\t"<<eq_upper<<"\t"<<ind_lower<<"\t"<<ind_upper<<"\t"<<eq_steps<<"\t"<<in
d_steps<<endl;

    //a&b overlapped in region tauamin to taubmax
    //taua=taub>tauc
    eq_lower=tauamin; eq_upper=taubmax;
    ind_lower=taucmin; ind_upper=taucmax;
    if(int((eq_lower-eq_upper)/width<=msteps)) eq_steps=msteps;
    else eq_steps=int((eq_lower-eq_upper)/width);
    if(int((ind_lower-ind_upper)/width<=msteps)) ind_steps=msteps;
    else ind_steps=int((ind_lower-ind_upper)/width);

temp_integral2=temp_integral2+P13ab_c(R1r,R1i,R2r,R2i,R3r,R3i,eq_lower,eq_upper,ind_l
ower,ind_upper,ta1,ta2,ta3,dt,eq_steps,ind_steps,cond);
    //cout<<"acab- ab
"<<eq_lower<<"\t"<<eq_upper<<"\t"<<ind_lower<<"\t"<<ind_upper<<"\t"<<eq_steps<<"\t"<<in
d_steps<<endl;

    }
}
else//a&c overlapped, a&b not overlapped
{
    //a&c overlapped in region tauamin to tauamax

```



```

        //taub>taua=tauc
        eq_lower=taucmin; eq_upper=tauamax;
        ind_lower=taubmin; ind_upper=taubmax;
        if(int((eq_lower-eq_upper)/width<=msteps)) eq_steps=msteps;
        else eq_steps=int((eq_lower-eq_upper)/width);
        if(int((ind_lower-ind_upper)/width<=msteps)) ind_steps=msteps;
        else ind_steps=int((ind_lower-ind_upper)/width);

        temp_integral2=P23ac_b(R1r,R1i,R2r,R2i,R3r,R3i,eq_lower,eq_upper,ind_lower,ind
_upper,ta1,ta2,ta3,dt,eq_steps,ind_steps,cond);
        //cout<<"ac-
"<<eq_lower<<"\t"<<eq_upper<<"\t"<<ind_lower<<"\t"<<ind_upper<<"\t"<<eq_steps<<"\t"<<in
d_steps<<endl;

    }
}
else if(taubmax<tauamin)//a&b overlapped, a&c not overlapped
{
    //a&b overlapped in region tauamin to taubmax
    //taua=taub>tauc
    eq_lower=tauamin; eq_upper=taubmax;
    ind_lower=taucmin; ind_upper=taucmax;
    if(int((eq_lower-eq_upper)/width<=msteps)) eq_steps=msteps;
    else eq_steps=int((eq_lower-eq_upper)/width);
    if(int((ind_lower-ind_upper)/width<=msteps)) ind_steps=msteps;
    else ind_steps=int((ind_lower-ind_upper)/width);

temp_integral2=P13ab_c(R1r,R1i,R2r,R2i,R3r,R3i,eq_lower,eq_upper,ind_lower,ind_upper,
ta1,ta2,ta3,dt,eq_steps,ind_steps,cond);
    //cout<<"ab-
"<<eq_lower<<"\t"<<eq_upper<<"\t"<<ind_lower<<"\t"<<ind_upper<<"\t"<<eq_steps<<"\t"<<in
d_steps<<endl;

}
else//none overlapped
{
    temp_integral2=0+0*I;
    //cout<<"none-"<<endl;
}
}
}

//cout<<"original integral "<<temp_integral1<<endl;
//cout<<"double counting contribution "<<temp_integral2<<endl;

integral=-temp_integral1-temp_integral2;

```

```

        Sr[i][j][k]=integral.Real();
        Si[i][j][k]=integral.Imag();

        }//ends loop over k, tau3
    }//ends loop over i, tau1
} //ends loop over j, tau2

return;
}

void calcP(double ***S, double ***R1r, double ***R1i, double ***R2r, double ***R2i,
double ***R3r, double ***R3i, const int &dt, const Vec_DP &tau1, const Vec_DP &tau1i,
const Vec_DP &tau2, const Vec_DP &tau3, const Vec_DP &tau3i, const double &PD, const
int &cond)

    //Interpolates the real and imaginary part of the envelope functions in tau1 and tau3 to
    calculate the total polarizaiton, Eq. 56
    {

        int x=tau1.size(), xi=tau1i.size(), y=tau2.size(), z=tau3.size(), zi=tau3i.size();

        double ***Sr;
        Sr = new double **[x];
        Sr[0] = new double *[x*y];
        Sr[0][0] = new double [x*y*z];
        make3D(Sr,x,y,z);

        double ***Si;
        Si = new double **[x];
        Si[0] = new double *[x*y];
        Si[0][0] = new double [x*y*z];
        make3D(Si,x,y,z);

        calcPri(Sr,Si,R1r,R1i,R2r,R2i,R3r,R3i,dt,tau1,tau1i,tau2,tau3,tau3i,PD,cond);

        int i,j,k;
        double ta1,ta2,ta3,t,tdr,tdi;
        //double w=2*pi*3e-5*3275;
        Complex<double> tc;
        Vec_DP tvr3(tau3.size()), tvi3(tau3.size()), dtvr3(tau3.size()), dtvi3(tau3.size()),
tvr1(tau1.size()), tvi1(tau1.size()), dtvr1(tau1.size()), dtvi1(tau1.size());

        double **tmr;

```

```

tmr = new double *[tau1.size()];
tmr[0] = new double [tau1.size()*tau3.size()];
for(i=1;i<tau1.size();i++)
    tmr[i]=tmr[i-1]+tau3.size();
double **tmi;
tmi = new double *[tau1.size()];
tmi[0] = new double [tau1.size()*tau3.size()];
for(i=1;i<tau1.size();i++)
    tmi[i]=tmi[i-1]+tau3.size();

for(j=0;j<y;j++)
{

    for(k=0;k<z;k++)
    {

        for(i=0;i<x;i++)
        {
            tvr1[i]=Sr[i][j][k];
            tvi1[i]=Si[i][j][k];
        }//ends loop over i, tau1

        //interpolate in tau1
        NR::spline(tau1,tvr1,1.0e30,1.0e30,dtvr1);
        NR::spline(tau1,tvi1,1.0e30,1.0e30,dtvi1);

        for(i=0;i<xi;i++)
        {
            NR::splint(tau1,tvr1,dtvr1,tau1i[i],tdr);
            NR::splint(tau1,tvi1,dtvi1,tau1i[i],tdi);
            tc=(tdr+I*tdi)*Exp(I*w*tau1i[i]);
            tmr[i][k]=tc.Real();
            tmi[i][k]=tc.Imag();
        }
    }//ends loop over k, tau3

    for(i=0;i<xi;i++)
    {

        for(k=0;k<z;k++)
        {
            tvr3[k]=tmr[i][k];
            tvi3[k]=tmi[i][k];
        }

        //interpolate in tau3

```

```

NR::spline(tau3,tvr3,1.0e30,1.0e30,dtvr3);
NR::spline(tau3,tvi3,1.0e30,1.0e30,dtvi3);

for(k=0;k<zi;k++)
{
NR::splint(tau3,tvr3,dtvr3,tau3i[k],tdr);
NR::splint(tau3,tvi3,dtvi3,tau3i[k],tdi);
tc=(tdr+I*tdi)*Exp(-I*w*tau3i[k]);
S[i][j][k]=tc.Real();
}
}
} //ends loop over j, tau2

if(tmr!=0)
{
delete [] (tmr[0]);
delete [] (tmr);
}
if(tmi!=0)
{
delete [] (tmi[0]);
delete [] (tmi);
}

/*
//save the real and imaginary parts of the polarization envelope by stacking in three
dimensions
ofstream fout10("ri.dat")
for(i=0;i<x;i++)
{
for(j=0;j<y;j++)
{
for(k=0;k<z;k++)
{

fout10<<tau1[i]<<"\t"<<tau2[j]<<"\t"<<tau3[k]<<"\t"<<Sr[i][j][k]<<"\t"<<Si[i][j][k]<<e
ndl;
}
}
}
}
fout10.close();
*/

if(Sr!=0) del3D(Sr);
if(Si!=0) del3D(Si);

```

```

return;
}

```

```

Vector<double> PS(double ***S, const Vec_DP &tau1, const Vec_DP &tau2, const
Vec_DP &tau3)
//finds the peak shift from a 3D polarization matrix (trapezoidal integration over tau3, then
fits the echo to a gaussian to obtain tau1*)
//input the S (polarization) matrix and take the mod squared below
{
//sigsub determines the number of points around the maximum used to fit the echo (was 17
for Science paper)
int i, j, k, x=tau1.size(), y=tau2.size(), z=tau3.size(), maxindex,sub=41;
Vector<double> shift(0.0,y);
Vec_DP data(x),datasub(sub),sig(0.1,x),sigsub(0.1,sub),tau1sub(sub),a(3),b(3);
Vec_BOOL ia(1,3);
Mat_DP covar(3,3),alpha(3,3);
DP max,chisq,lastchisq,alamda,out;
//b and out used as a dummy vars to alpha to output the echo for plotting

```

```

if((tau1[1]-tau1[0])!=2.5) cout<<"tau1 steps not equal to 2.5 fs, so change fit range in the
PS"<<endl;

```

```

double **IS;
IS = new double *[x];
IS[0] = new double [x*y];
for(i=1;i<x;i++)
    IS[i]=IS[i-1]+y;

```

```

double dt=(tau3[1]-tau3[0]);
for(i=0;i<x;i++)
{
    for(j=0;j<y;j++)
    {
        IS[i][j]=0.0;
        for(k=0;k<z;k++)
        {
            //take the mod squared for homodyne signal
            IS[i][j] += 0.5*(S[i][j][k]*S[i][j][k]+S[i][j][k-1]*S[i][j][k-1])*dt;
        }
    }
}

```

```

for(j=0;j<y;j++)

```

```

{
  for(i=0;i<x;i++)
    data[i]=IS[i][j];

  max=IS[0][j];
  maxindex=0;
  for(i=0;i<x;i++)
    if(IS[i][j]>max)
      {
        max=IS[i][j];
        maxindex=i;
      }
  for(i=0;i<sub;i++)
    //just take the sub (was 17) points around the maximum (+/- 2.5*(sub-1)/2 was(20 fs))
    {
      datasub[i]=IS[i+maxindex-(sub-1)/2][j];
      tau1sub[i]=tau1[i+maxindex-(sub-1)/2];
    }

  a[0]=max,a[1]=tau1[maxindex],a[2]=50.0;
  chisq=0,lastchisq=1,alamda=-1;
  while(lastchisq-chisq>(lastchisq/1000)||lastchisq<chisq)
    {
      lastchisq=chisq;
      NR::mrqmin(tau1sub,datasub,sigsub,a,ia,covar,alpha,chisq,gauss,alamda);
    }

  shift[j]=a[1];

  /*
  //save the echo and fit for a particular value of tau2
  //if(j==0)
  {
    //ofstream fout1("echo.dat");
    //ofstream fout2("fit.dat");
    for(i=0;i<x;i++)
      {
        gauss(tau1[i],a,out,b);
        fout1<<tau1[i]<<'t'<<data[i]<<endl;
        fout2<<tau1[i]<<'t'<<out<<endl;
      }
    //fout1.close();
    //fout2.close();
  }
  */

```

```

    }

    if(IS!=0)
    {
        delete [] (IS[0]);
        delete [] (IS);
    }
    return shift;
}

```

```

void gauss(const DP t, Vec_I_DP &a, DP &y, Vec_O_DP &dyda)
//gaussian to fit echo based on NR fgauss
{
    double arg,ex,fac;
    arg=(t-a[1])/a[2];
    ex=exp(-arg*arg);
    fac=a[0]*ex*2*arg;
    y=a[0]*ex;
    dyda[0]=ex;
    dyda[1]=fac/a[2];
    dyda[2]=fac*arg/a[2];
}

```

```

void calcPS(const Vec_DP &m, const Vector<double> &t, double ***S, double ***R1r,
double ***R1i, double ***R2r, double ***R2i, double ***R3r, double ***R3i, const int
&i1, const int &j1, const int &k1, const int &i2, const int &j2, const int &k2, const int &i3,
const int &j3, const int &k3, const int &dt, const Vec_DP &tau1, const Vec_DP &tau1i,
const Vec_DP &tau2, const Vec_DP &tau3, const Vec_DP &tau3i, const double &PD,
Vector<double> &peakshift)
{
    //calculate the polarization, then use it to find the PS

    int cond=1;
    //cond determines if the envelope is the transform limited pulse (cond=0) or if the chirped
    pulse envelopes (envelopec for cond=1) are used in the calculations

    //define correlation function and lineshape function
    int tsize=t.size();
    Vector<Complex<double> > corr(tsize), lsf(tsize);
    corr = corrm(t,m);
    lsf = LSF(t, corr);
}

```

```

//fill Response function matrices
RF1(t,lsf,R1r,R1i,i1,j1,k1,dt);
RF2(t,lsf,R2r,R2i,i2,j2,k2,dt);
RF3(t,lsf,R3r,R3i,i3,j3,k3,dt);

calcP(S,R1r,R1i,R2r,R2i,R3r,R3i,dt,tau1,tau1i,tau2,tau3,tau3i,PD,cond);

//calculate the peak shift from the total signal matrix
peakshift = PS(S,tau1i,tau2,tau3i);
}

double fitPS(const Vec_DP &m, const Vector<double> &t, double ***S, double ***R1r,
double ***R1i, double ***R2r, double ***R2i, double ***R3r, double ***R3i, const int
&i1, const int &j1, const int &k1, const int &i2, const int &j2, const int &k2, const int &i3,
const int &j3, const int &k3, const int &dt, const Vec_DP &tau1, const Vec_DP &tau1i,
const Vec_DP &tau2, const Vec_DP &tau3, const Vec_DP &tau3i, const double &PD,
Vector<double> &peakshift)
{
//calculate the polarization, use it to find the PS, then compare to the experimental values to
return a difference

calcPS(m,t,S,R1r,R1i,R2r,R2i,R3r,R3i,i1,j1,k1,i2,j2,k2,i3,j3,k3,dt,tau1,tau1i,tau2,tau3,tau3i,
PD,peakshift);

int j, y=tau2.size();
double difference=0;

Vector<double> expPS(27);
//expPS[0]=19, expPS[1]=17.625, expPS[2]=16, expPS[3]=15.125, expPS[4]=14.125,
expPS[5]=13.125, expPS[6]=12.375, expPS[7]=12.125, expPS[8]=12.375, expPS[9]=12.5,
expPS[10]=13, expPS[11]=13.75, expPS[12]=13.75, expPS[13]=13.875, expPS[14]=13.875,
expPS[15]=13.625, expPS[16]=13.625, expPS[17]=13, expPS[18]=12.625, expPS[19]=11.5,
expPS[20]=10.375, expPS[21]=8.875, expPS[22]=8.25, expPS[23]=6.625, expPS[24]=5.125,
expPS[25]=3.5, expPS[26]=1.625;
expPS[0]=27.7, expPS[1]=23.8, expPS[2]=20.9, expPS[3]=18.0, expPS[4]=16.0,
expPS[5]=14.5, expPS[6]=12.9, expPS[7]=12.5, expPS[8]=12.4, expPS[9]=12.0,
expPS[10]=12.6, expPS[11]=12.3, expPS[12]=12.5, expPS[13]=12.8, expPS[14]=12.9,
expPS[15]=12.9, expPS[16]=12.7, expPS[17]=12.2, expPS[18]=12.1, expPS[19]=10.8,
expPS[20]=9.0, expPS[21]=7.2, expPS[22]=6.5, expPS[23]=5.5, expPS[24]=4.9,
expPS[25]=3.5, expPS[26]=2.0;

for(j=0;j<y;j++)

```



```

    {
        //difference += abs(peakshift[j]-expPS[j])/abs(expPS[j]);
        difference += abs(peakshift[j]-expPS[j]);
    }

return difference;
}

void heterodyne(const Vec_DP &m, const Vector<double> &t, double ***HET, double
***S, double ***R1r, double ***R1i, double ***R2r, double ***R2i, double ***R3r,
double ***R3i, const int &i1, const int &j1, const int &k1, const int &i2, const int &j2, const
int &k2, const int &i3, const int &j3, const int &k3, const int &dt, const Vec_DP &tau1,
const Vec_DP &tau1i, const Vec_DP &tau2, const Vec_DP &tau3, const Vec_DP &tau3i,
const Vec_DP &LO, const double &PD)
{

    int cond=0;
    //cond determines if the envelope is the transform limited pulse (cond=0) or if the chirped
    pulse envelopes (envelopec for cond=1) are used in the calculations

    /*
    //tabulate the Szvitzky-Golay coefficients for the calculation of numerical derivatives --
    remember that the vector sgcoeff is in wrap-around order ((c(0) c(1) c(2) c(-2) c(-1)) and so
    on)
    Vec_DP sgcoeff(5);
    int np=5, nl=2, nr=2, ld=1, mm=4;
    NR::savgol(sgcoeff,np,nl,nr,ld,mm);
    */

    //define correlation function and lineshape function
    int tsize=t.size();
    Vector<Complex<double> > corr(tsize), lsf(tsize);
    corr = corrm(t,m);
    lsf = LSF(t, corr);

    //fill Response function matrices
    RF1(t,lsf,R1r,R1i,i1,j1,k1,dt);
    RF2(t,lsf,R2r,R2i,i2,j2,k2,dt);
    RF3(t,lsf,R3r,R3i,i3,j3,k3,dt);

    calcP(S,R1r,R1i,R2r,R2i,R3r,R3i,dt,tau1,tau1i,tau2,tau3,tau3i,PD,cond);
}

```

```

int i,j,k,l,len=512,zzero=-tau3i[0]/(tau3i[1]-tau3i[0]),dex;
double ta3,lo,tgral,dzi=(tau3i[1]-tau3i[0]),dfreq=1/(dzi*len*0.00003),freq;
//double w=2*pi*3e-5*3275;
Vec_DP tv(tau3i.size());
Complex<double> ef;

for(j=0;j<tau2.size();j++)
{
  for(i=0;i<tau1i.size();i++)
  {

    //take the derivative of the polarization:
    Vec_DP pollong1(0.0,2*len), pollong2(0.0,2*len);
    for(k=zzero;k<tau3i.size();k++)
    {
      dex=2*(k-zzero);
      pollong1[dex]=S[i][j][k];
    }
    for(k=0;k<zzero;k++)
    {
      dex=2*len-2*(zzero-k);
      pollong1[dex]=S[i][j][k];
    }
    NR::four1(pollong1,1);
    for(k=0;k<len/2;k++)
    {
      freq=dfreq*k;
      pollong2[2*k+1]=pollong1[2*k]*freq;
      pollong2[2*k]=-pollong1[2*k+1]*freq;
    }
    for(k=len/2;k<len;k++)
    {
      freq=dfreq*(k-len);
      pollong2[2*k+1]=pollong1[2*k]*freq;
      pollong2[2*k]=-pollong1[2*k+1]*freq;
    }
    NR::four1(pollong2,-1);
    for(k=zzero;k<tau3i.size();k++)
    {
      dex=2*(k-zzero);
      tv[k]=pollong2[dex];
    }
  }
}

```

```

    dex=2*len-2*(zizero-k);
    tv[k]=pollong2[dex];
}

//now step the lo and calculate the convolution
for(l=0;l<LO.size();l++)
{
    lo=LO[l];
    tgral=0.0;

    for(k=0;k<tau3i.size();k++)
    {
        ta3=tau3i[k];
        if(cond==0)
            tgral += envelope(ta3-lo)*cos(w*(ta3-lo))*tv[k];
        else
        {
            ef = envelopec(ta3-lo)*Exp(-I*w*(ta3-lo));
            tgral += ef.Real()*tv[k];
        }
    }
    HET[i][j][l]=tgral;
}
}
}

return;
}

void extractenv(const Vec_DP &m, const Vector<double> &t, double ***ENV, double
***HET, double ***S, double ***R1r, double ***R1i, double ***R2r, double ***R2i,
double ***R3r, double ***R3i, const int &i1, const int &j1, const int &k1, const int &i2,
const int &j2, const int &k2, const int &i3, const int &j3, const int &k3, const int &dt, const
Vec_DP &tau1, const Vec_DP &tau1i, const Vec_DP &tau2, const Vec_DP &tau3, const
Vec_DP &tau3i, const Vec_DP &LO, const double &PD)
{
    //return a pointer to a 3D array containing 2D extracted envelopes for each value of tau2

heterodyne(m,t,HET,S,R1r,R1i,R2r,R2i,R3r,R3i,i1,j1,k1,i2,j2,k2,i3,j3,k3,dt,tau1,tau1i,tau2,tau3,tau3i,LO,PD);

```

```

int i,j,k,l,len=512,winlen=157,xizero=-tau1i[0]/(tau1i[1]-tau1i[0]),LOzero=-LO[0]/(LO[1]-LO[0]),dex;
double dxi=(tau1i[1]-tau1i[0]),dLO=(LO[1]-LO[0]),dfreq=1/(dxi*len*0.00003),freq;
if(dxi!=dLO){cout<<"time steps not equal in envelope extraction"<<endl;}
Vec_DP data(0.0,2*len*len), filter(winlen) ,filter1(0.0,2*len*len), filter2(0.0,2*len*len);
NRVec<int> nn(len,2);

```

```

//define filters -- allow width to change but center around 3307 cm-1 (and 0 cm-1)
assuming 2.5 fs steps and 512 transforms -- i.e. around points 127 and 385 (and 0)

```

```

for(i=0;i<winlen;i++)
{
    filter[i]=0.5*(1-cos(2.0*pi*i/(winlen-1)));
}

```

```

int f1a=127-(winlen-1)/2, f1b=127+(winlen-1)/2, f2a=385-(winlen-1)/2, f2b=385+(winlen-1)/2, f0a=len-(winlen-1)/2, f0b=0+(winlen-1)/2;

```

```

for(i=f1a;i<(f1b+1);i++)
{
    for(k=f2a;k<(f2b+1);k++)
    {
        dex=2*(i+k*len);
        filter1[dex]=filter[i-f1a]*filter[k-f2a];
        filter1[dex+1]=filter[i-f1a]*filter[k-f2a];
    }
}

```

```

for(i=f2a;i<(f2b+1);i++)
{
    for(k=f1a;k<(f1b+1);k++)
    {
        dex=2*(i+k*len);
        filter1[dex]=filter[i-f2a]*filter[k-f1a];
        filter1[dex+1]=filter[i-f2a]*filter[k-f1a];
    }
}

```

```

for(i=f0a;i<len;i++)
{
    for(k=f0a;k<len;k++)
    {
        dex=2*(i+k*len);
        filter2[dex]=filter[i-f0a]*filter[k-f0a];
        filter2[dex+1]=filter[i-f0a]*filter[k-f0a];
    }
}

```

```

    }
    for(k=0;k<(f0b+1);k++)
    {
        dex=2*(i+k*len);
        filter2[dex]=filter[i-f0a]*filter[k+(winlen-1)/2];
        filter2[dex+1]=filter[i-f0a]*filter[k+(winlen-1)/2];
    }
}
for(i=0;i<(f0b+1);i++)
{
    for(k=f0a;k<len;k++)
    {
        dex=2*(i+k*len);
        filter2[dex]=filter[i+(winlen-1)/2]*filter[k-f0a];
        filter2[dex+1]=filter[i+(winlen-1)/2]*filter[k-f0a];
    }
    for(k=0;k<(f0b+1);k++)
    {
        dex=2*(i+k*len);
        filter2[dex]=filter[i+(winlen-1)/2]*filter[k+(winlen-1)/2];
        filter2[dex+1]=filter[i+(winlen-1)/2]*filter[k+(winlen-1)/2];
    }
}
}

```

```

for(j=0;j<tau2.size();j++)
{
    //fill the data matrix in the correct wrap around order
    for(l=LOzero;l<LO.size();l++)
    {
        for(i=xizero;i<tau li.size();i++)
        {
            dex=2*((i-xizero)+(l-LOzero)*len);
            data[dex]=HET[i][j][l];
        }
        for(i=0;i<xizero;i++)
        {
            dex=2*((len-(xizero-i)+(l-LOzero)*len);
            data[dex]=HET[i][j][l];
        }
    }
}
for(l=0;l<LOzero;l++)
{
    for(i=xizero;i<tau li.size();i++)

```

```

        {
            dex=2*((i-xizero)+(len-(LOzero-1))*len);
            data[dex]=HET[i][j][1];
        }
    for(i=0;i<xizero;i++)
        {
            dex=2*((len-(xizero-i)+(len-(LOzero-1))*len);
            data[dex]=HET[i][j][1];
        }
    }

//FT to frequency
NR::fourn(data,nn,1);

//multiply by first filter
for(k=0;k<2*len*len;k++)
    {
        data[k]=data[k]*filter1[k]/(filter1[k]+0.0001);
    }

//IFT to time
NR::fourn(data,nn,-1);

//rectify
for(k=0;k<2*len*len;k++)
    {
        if(data[k]<0.0)
            {
                data[k]=0.0;
            }
    }

//FT to frequency
NR::fourn(data,nn,1);

//multiply by second filter
for(k=0;k<2*len*len;k++)
    {
        data[k]=data[k]*filter2[k]/(filter2[k]+0.0001);
    }

//IFT to time
NR::fourn(data,nn,-1);

//put the envelope back into the correct time order

```

```

for(l=LOzero;l<LO.size();l++)
{
    for(i=xizero;i<tau li.size();i++)
    {
        dex=2*((i-xizero)+(l-LOzero)*len);
        ENV[i][j][l]=data[dex];
    }
    for(i=0;i<xizero;i++)
    {
        dex=2*((len-(xizero-i)+(l-LOzero)*len);
        ENV[i][j][l]=data[dex];
    }
}
for(l=0;l<LOzero;l++)
{
    for(i=xizero;i<tau li.size();i++)
    {
        dex=2*((i-xizero)+(len-(LOzero-l))*len);
        ENV[i][j][l]=data[dex];
    }
    for(i=0;i<xizero;i++)
    {
        dex=2*((len-(xizero-i)+(len-(LOzero-l))*len);
        ENV[i][j][l]=data[dex];
    }
}
}

return;
}

```

```

void dispPP(const Vec_DP &m, const Vector<double> &t, double **PP, double ***R1r,
double ***R1i, double ***R2r, double ***R2i, double ***R3r, double ***R3i, const int
&i1, const int &j1, const int &k1, const int &i2, const int &j2, const int &k2, const int &i3,
const int &j3, const int &k3, const int &dt, const Vec_DP &tau2, const Vec_DP &tau3, const
Vec_DP &tau3i, const Vec_DP &LO, const double &PD)

```

```

//Calculates the frequency dispersed pump probe
//Sets up 2D time domain matrices for calculaion of the polarization in tau2 and tau3 for
tau1=0, then calls calcPri, and interpolates in tau3 to get the total polarization. For each tau2,

```

the radiated field is calculated and convolved with the LO, then Fourier transformed to get the dispersed PP.

//Note that this could all be done by calling heterodyne and simply transforming in tau3, but to conserve space for applications where we want to calculate a large number of tau2 points, we don't need a full set of tau1 delays, just tau1=0.

```
{  
  
    int cond=0;  
    //cond determines if the envelope is the transform limited pulse (cond=0) or if the chirped  
    pulse envelopes (envelopec for cond=1) are used in the calculations  
  
    //set up temporary Sr, Si, S and HET matrices  
  
    int x=1, y=tau2.size(), z=tau3.size(), zi=tau3i.size(), ww=LO.size();  
    Vec_DP tau1(x), tau1i(x);  
    tau1[0]=0.0;  
    tau1i[0]=0.0;  
  
    double ***Sr;  
    Sr = new double **[x];  
    Sr[0] = new double *[x*y];  
    Sr[0][0] = new double [x*y*z];  
    make3D(Sr,x,y,z);  
  
    double ***Si;  
    Si = new double **[x];  
    Si[0] = new double *[x*y];  
    Si[0][0] = new double [x*y*z];  
    make3D(Si,x,y,z);  
  
    double ***S;  
    S = new double **[x];  
    S[0] = new double *[x*y];  
    S[0][0] = new double [x*y*zi];  
    make3D(S,x,y,zi);  
  
    double ***HET;  
    HET = new double **[x];  
    HET[0] = new double *[x*y];  
    HET[0][0] = new double [x*y*ww];  
    make3D(HET,x,y,ww);  
}
```



```

//define correlation function and lineshape function
int tsize=t.size();
Vector<Complex<double> > corr(tsize), lsf(tsize);
corr = corrm(t,m);
lsf = LSF(t, corr);

//fill Response function matrices
RF1(t,lsf,R1r,R1i,i1,j1,k1,dt);
RF2(t,lsf,R2r,R2i,i2,j2,k2,dt);
RF3(t,lsf,R3r,R3i,i3,j3,k3,dt);

calcPri(Sr,Si,R1r,R1i,R2r,R2i,R3r,R3i,dt,tau1,tau1i,tau2,tau3,tau3i,PD,cond);

int i,j,k,l,len=512,zzero=-tau3i[0]/(tau3i[1]-tau3i[0]),LOzero=-LO[0]/(LO[1]-LO[0]),dex;
double ta3,lo,tdr,tdi,tgral,dzi=(tau3i[1]-tau3i[0]),dfreq=1/(dzi*len*0.00003),freq;
//double w=2*pi*3e-5*3275;
Complex<double> tc,ef;
Vec_DP tvr(tau3.size()), tvi(tau3.size()), dtvr(tau3.size()), dtvi(tau3.size()),tv(tau3i.size());

i=0;
{

for(j=0;j<y;j++)
{

//interpolate in tau3
for(k=0;k<z;k++)
{
tvk[k]=Sr[i][j][k];
tvi[k]=Si[i][j][k];
} //ends loop over k, tau3

//interpolate in tau3
NR::spline(tau3,tvr,1.0e30,1.0e30,dtvr);
NR::spline(tau3,tvi,1.0e30,1.0e30,dtvi);

for(k=0;k<zi;k++)
{
NR::splint(tau3,tvr,dtvr,tau3i[k],tdr);
NR::splint(tau3,tvi,dtvi,tau3i[k],tdi);
tc=(tdr+I*tdi)*Exp(-I*w*tau3i[k]);
S[i][j][k]=tc.Real();
}
}
}

```

```

//take the derivative of the polarization:
Vec_DP pollong1(0.0,2*len), pollong2(0.0,2*len);
for(k=zizero;k<tau3i.size();k++)
{
    dex=2*(k-zizero);
    pollong1[dex]=S[i][j][k];
}
for(k=0;k<zizero;k++)
{
    dex=2*len-2*(zizero-k);
    pollong1[dex]=S[i][j][k];
}
NR::four1(pollong1,1);
for(k=0;k<len/2;k++)
{
    freq=dfreq*k;
    pollong2[2*k+1]=pollong1[2*k]*freq;
    pollong2[2*k]=-pollong1[2*k+1]*freq;
}
for(k=len/2;k<len;k++)
{
    freq=dfreq*(k-len);
    pollong2[2*k+1]=pollong1[2*k]*freq;
    pollong2[2*k]=-pollong1[2*k+1]*freq;
}
NR::four1(pollong2,-1);
for(k=zizero;k<tau3i.size();k++)
{
    dex=2*(k-zizero);
    tv[k]=pollong2[dex];
}
for(k=0;k<zizero;k++)
{
    dex=2*len-2*(zizero-k);
    tv[k]=pollong2[dex];
}

//now step the lo and calculate the convolution
for(l=0;l<LO.size();l++)
{
    lo=LO[l];
    tgral=0.0;

    for(k=0;k<tau3i.size();k++)

```

```

    {
        ta3=tau3i[k];
        if(cond==0)
            tgral += envelope(ta3-lo)*cos(w*(ta3-lo))*tv[k];
        else
            {
                ef = envelopepec(ta3-lo)*Exp(-I*w*(ta3-lo));
                tgral += ef.Real()*tv[k];
            }
    }
    HET[i][j][l]=tgral;
}

//take the Fourier transform of the slice in the LO dimension
Vec_DP het(0.0,2*len);
for(l=LOzero;l<LO.size();l++)
{
    dex=2*(l-LOzero);
    het[dex]=HET[i][j][l];
}
for(l=0;l<LOzero;l++)
{
    dex=2*len-2*(LOzero-l);
    het[dex]=HET[i][j][l];
}
NR::four1(het,1);

//dispersed PP is the real part of the transform
for(l=0;l<len/2;l++)
{
    dex=2*l+1;
    PP[j][l]=het[dex];
}

} //ends loop over j, tau2
} //ends i=0, tau1=0

if(Sr!=0) del3D(Sr);
if(Si!=0) del3D(Si);
if(S!=0) del3D(S);
if(HET!=0) del3D(HET);

```

```

return;
}

```

```

void dPPtime(const Vec_DP &m, const Vector<double> &t, Vector<double> &PPdecay,
const int index, double ***R1r, double ***R1i, double ***R2r, double ***R2i, double
***R3r, double ***R3i, const int &i1, const int &j1, const int &k1, const int &i2, const int
&j2, const int &k2, const int &i3, const int &j3, const int &k3, const int &dt, const Vec_DP
&tau2, const Vec_DP &tau3, const Vec_DP &tau3i, const Vec_DP &LO, const double
&PD)

```

```

//set up a PP matrix, run the dispPP and extract a vector of amplitudes
{
int j,len=512;

double **PP;
PP = new double *[tau2.size()];
PP[0] = new double [tau2.size()*len/2];
for(j=1;j<tau2.size();j++)
    PP[j]=PP[j-1]+len/2;

dispPP(m,t,PP,R1r,R1i,R2r,R2i,R3r,R3i,i1,j1,k1,i2,j2,k2,i3,j3,k3,dt,tau2,tau3,tau3i,LO,PD);

for(j=0;j<tau2.size();j++)
{
    PPdecay[j]=(PP[j][index]+PP[j][index+1])*0.5;
}

return;
}

```

```

void abslshp(const Vec_DP &m, Vec_DP &abs, double &width)
//calculate the absorption lineshape and width
{
int i,len=2048,dex;
double dw=2.5, dfreq=1/(dw*len*0.00003), Dor1=1.0/18000.0, Dor2=1.0/360.0, T1=700.0;
Vector<double> tt(len/2);
Vector<Complex<double>> corr(len/2),lsf(len/2);
for(i=0;i<len/2;i++){tt[i]=i*dw;}
corr = corrm(tt,m);
lsf = LSF(tt, corr);

Vec_DP freq(len/2), absft(0.0,2*len);

```

```

double abstr;
Complex<double> abstc;
for(i=0;i<len/2;i++){freq[i]=i*dfreq;}
for(i=0;i<len/2;i++)
{
    //abst=real(exp(-i*w10*t-h11(t)))=cos(w10*t)*exp(-h11(t));
    abstc=Exp(I*w10*tt[i]-lsf[i])*(0.8*exp(-2.0*Dor1*tt[i])+0.2*exp(-
2.0*Dor2*tt[i]))*exp(-tt[i]/(2.0*T1));

    /*
    //lineshape for "hot ground state"
    double dw = 2*pi*3e-5*12, dm = 0.91;
    abstc=dm*Exp(I*dw*tt[i])*Exp(I*w10*tt[i]-lsf[i])*(0.8*exp(-2.0*Dor1*tt[i])+0.2*exp(-
2.0*Dor2*tt[i]))*exp(-tt[i]/(2.0*T1));
    */

    abstr=abstc.Real();

    dex=2*i;
    absft[dex]=abstr;
}

//FT
NR::four1(absft,1);

//write real part of the transform for positive frequencies, subtracting off the zero frequency
offset
for(i=0;i<len/2;i++)
{
    dex=2*i;
    abs[i]=absft[dex]-absft[0];
}

//fit the absorption line with a Gaussian -- not the best functional form, but a Lorentzian
doesn't work either, and it's easy since I already have a function for fitting Gaussians
Vec_DP sig(0.1,len/2),a(3),b(3);
Vec_BOOL ia(1,3);
Mat_DP covar(3,3),alpha(3,3);
DP chisq,lastchisq,alamda,out;
//b and out used as a dummy vars to alpha to output for plotting
a[0]=10.0,a[1]=3400.0,a[2]=200.0;
chisq=0,lastchisq=1,alamda=-1;
while(lastchisq-chisq>(lastchisq/1000)||lastchisq<chisq)
{
    lastchisq=chisq;

```

```

    NR::mrqmin(freq,abs,sig,a,ia,covar,alpha,chisq,gauss,alamda);
}

//a[2] is delta effective
//for a gaussian lineshape, a[2] = delta/sqrt(4ln2) = delta/1.67
//lineshape is actually between gaussian and lorentzian, so I find a fudge factor of ~1.55
works well

width=a[2]*1.55;

/*
//save the fit
ofstream fout11("absfit.dat");
for(i=0;i<len/2;i++)
{
    gauss(freq[i],a,out,b);
    fout11<<freq[i]<<'\t'<<out<<endl;
}
fout11.close();
*/
}

```

```

Complex<double> P13ab_c(double ***R1r,double ***R1i,double ***R2r,double
***R2i,double ***R3r,double ***R3i,const double &eq_lower,const double
&eq_upper,const double &ind_lower,const double &ind_upper,const double &tau1,const
double &tau2,const double &tau3,const int &dt,const int &eq_steps,const int
&ind_steps,const int &cond)

```

```

//integral for tau_a=tau_b, scanning tau_c

{
    int i,j;
    double tauab,tauc,t1,t2,t3;
    double re=0.0,im=0.0;
    Complex<double> tgral=0;
    Vec_DP eq(eq_steps),eq_w(eq_steps),ind(ind_steps),ind_w(ind_steps);
    NR::gauleg(eq_lower,eq_upper,eq,eq_w);
    NR::gauleg(ind_lower,ind_upper,ind,ind_w);

    for(i=0;i<eq_steps;i++)
    {
        tauab=eq[i];
        for(j=0;j<ind_steps;j++)

```

```

    {
        tauc=ind[j];

        if(tauc>tauab)
        {
            t1=tauc-tauab,t2=0.0,t3=tauab;
            tgral=tgral+eq_w[i]*ind_w[j]*P3cba(R3r,R3i,dt,t1,t2,t3,tau1,tau2,tau3,cond);
        }

        else//tauc<=tauab
        {
            t1=0.0,t2=tauab-tauc,t3=tauc;
            tgral=tgral+eq_w[i]*ind_w[j]*P1abc(R1r,R1i,dt,t1,t2,t3,tau1,tau2,tau3,cond);
        }
    }
}

return tgral;
}

```

```

Complex<double> P13bc_a(double ***R1r,double ***R1i,double ***R2r,double
***R2i,double ***R3r,double ***R3i,const double &eq_lower,const double
&eq_upper,const double &ind_lower,const double &ind_upper,const double &tau1,const
double &tau2,const double &tau3,const int &dt,const int &eq_steps,const int
&ind_steps,const int &cond)
//integral for tau_b=tau_c, scanning tau_a
{
    int i,j;
    double taubc,taua,t1,t2,t3;
    double re=0.0,im=0.0;
    Complex<double> tgral=0;
    Vec_DP eq(eq_steps),eq_w(eq_steps),ind(ind_steps),ind_w(ind_steps);
    NR::gauleg(eq_lower,eq_upper,eq,eq_w);
    NR::gauleg(ind_lower,ind_upper,ind,ind_w);

    for(i=0;i<eq_steps;i++)
    {
        taubc=eq[i];
        for(j=0;j<ind_steps;j++)
        {
            taua=ind[j];

            if(taua>taubc)

```

```

    {
        t1=taua-tauc,t2=0.0,t3=tauc;
        tgral=tgral+eq_w[i]*ind_w[j]*P1abc(R1r,R1i,dt,t1,t2,t3,tau1,tau2,tau3,cond);
    }

else if(taua<tauc)
    {
        t1=0.0,t2=tauc-taua,t3=taua;
        tgral=tgral+eq_w[i]*ind_w[j]*P3bca(R3r,R3i,dt,t1,t2,t3,tau1,tau2,tau3,cond);
    }

else//taua=tauc
    {
        tgral=tgral;
    }
}
}

return tgral;
}

```

Complex<double> P23ac_b(double ***R1r,double ***R1i,double ***R2r,double ***R2i,double ***R3r,double ***R3i,const double &eq_lower,const double &eq_upper,const double &ind_lower,const double &ind_upper,const double &tau1,const double &tau2,const double &tau3,const int &dt,const int &eq_steps,const int &ind_steps,const int &cond)
//integral for tau_a=tau_c, scanning taub

```

{
    int i,j;
    double tauac,taub,t1,t2,t3;
    double re=0.0,im=0.0;
    Complex<double> tgral=0;
    Vec_DP eq(eq_steps),eq_w(eq_steps),ind(ind_steps),ind_w(ind_steps);
    NR::gauleg(eq_lower,eq_upper,eq,eq_w);
    NR::gauleg(ind_lower,ind_upper,ind,ind_w);

    for(i=0;i<eq_steps;i++)
    {
        tauac=eq[i];
        for(j=0;j<ind_steps;j++)
        {
            taub=ind[j];

```



```

    if(taub>=tauac)
    {
        t1=taub-tauac,t2=0.0,t3=tauac;
        tgral=tgral+eq_w[i]*ind_w[j]*P3bca(R3r,R3i,dt,t1,t2,t3,tau1,tau2,tau3,cond);
    }

    else//tauac>taub
    {
        t1=0.0,t2=tauac-taub,t3=taub;
        tgral=tgral+eq_w[i]*ind_w[j]*P2cab(R2r,R2i,dt,t1,t2,t3,tau1,tau2,tau3,cond);
    }

}
}

return tgral;
}

```

```

Complex<double> Integrate(double ***R1r,double ***R1i,double ***R2r,double
***R2i,double ***R3r,double ***R3i,const double &tauamin,const double &tauamax,const
double &taubmin,const double &taubmax,const double &taucmin,const double
&taucmax,const double &tau1,const double &tau2, const double &tau3,const int &dt, const
int &a_steps, const int &b_steps, const int &c_steps, const int &cond)
//try integrating in three dimensions with the gauleg routine
{
    int i,j,k;
    Vector<double> x(3);
    double t1,t2,t3;
    //double re=0.0,im=0.0;
    Complex<double> tgral=0;
    Vec_DP
    taua(a_steps),taua_w(a_steps),taub(b_steps),taub_w(b_steps),tauc(c_steps),tauc_w(c_steps);

    NR::gauleg(tauamin,tauamax,taua,taua_w);
    NR::gauleg(taubmin,taubmax,taub,taub_w);
    NR::gauleg(taucmin,taucmax,tauc,tauc_w);
    //gauleg sets eveluation points taua, taub, and tauc and corresponding weights taua_w,
    taub_w and tauc_w

    for(i=0;i<a_steps;i++)
    {
        x[0]=taua[i];
        for(j=0;j<b_steps;j++)

```

```

{
  x[1]=taub[j];
  for(k=0;k<c_steps;k++)
  {
    x[2]=tauc[k];

    if(x[1]>=x[2])
    {
      if(x[0]>x[1])// tau_a > tau_b >= tau_c
      {
        t1=x[0]-x[1],t2=x[1]-x[2],t3=x[2];

        //if(t1>500||t1<=-1||t2>2400||t2<=-1||t3>700||t3<=-1) cout<<"P1r-1 t:
"<<t1<<" "<<t2<<" "<<t3<<" tau: "<<x[0]<<" "<<x[1]<<" "<<x[2]<<endl;

//re+=taua_w[i]*taub_w[j]*tauc_w[k]*P1rabc(R1r,R1i,dt,t1,t2,t3,tau1,tau2,tau3,cond);

//im+=taua_w[i]*taub_w[j]*tauc_w[k]*P1iabc(R1r,R1i,dt,t1,t2,t3,tau1,tau2,tau3,cond);

tgral=tgral+taua_w[i]*taub_w[j]*tauc_w[k]*P1abc(R1r,R1i,dt,t1,t2,t3,tau1,tau2,tau3,cond);

        //cout<<"iteration
"<<i<<"\t"<<j<<"\t"<<k<<"\t"<<x[0]<<"\t"<<x[1]<<"\t"<<x[2]<<"\t"<<"P1-1:
"<<P1abc(R1r,R1i,dt,t1,t2,t3,tau1,tau2,tau3,cond)<<endl;
      }
      else if(x[0]>=x[2])// tau_b >= tau_a >= tau_c
      {
        t1=x[1]-x[0],t2=x[0]-x[2],t3=x[2];

        //if(t1>500||t1<=-1||t2>2400||t2<=-1||t3>700||t3<=-1) cout<<"P2r-2 t:
"<<t1<<" "<<t2<<" "<<t3<<" tau: "<<x[0]<<" "<<x[1]<<" "<<x[2]<<endl;

//re+=taua_w[i]*taub_w[j]*tauc_w[k]*P2rbac(R2r,R2i,dt,t1,t2,t3,tau1,tau2,tau3,cond);

//im+=taua_w[i]*taub_w[j]*tauc_w[k]*P2ibac(R2r,R2i,dt,t1,t2,t3,tau1,tau2,tau3,cond);

tgral=tgral+taua_w[i]*taub_w[j]*tauc_w[k]*P2bac(R2r,R2i,dt,t1,t2,t3,tau1,tau2,tau3,cond);

        //cout<<"iteration
"<<i<<"\t"<<j<<"\t"<<k<<"\t"<<x[0]<<"\t"<<x[1]<<"\t"<<x[2]<<"\t"<<"P2-2:
"<<P2bac(R2r,R2i,dt,t1,t2,t3,tau1,tau2,tau3,cond)<<endl;

```

```

    }
    else if(x[1]!=x[2])// tau_b > tau_c > tau_a
    {
        t1=x[1]-x[2],t2=x[2]-x[0],t3=x[0];

        //if(t1>500||t1<=-1||t2>500||t2<=-1||t3>700||t3<=-1) cout<<"P3r-3 t:
        "<<t1<<" "<<t2<<" "<<t3<<" tau: "<<x[0]<<" "<<x[1]<<" "<<x[2]<<endl;

//re+=taua_w[i]*taub_w[j]*tauc_w[k]*P3rbca(R3r,R3i,dt,t1,t2,t3,tau1,tau2,tau3,cond);

//im+=taua_w[i]*taub_w[j]*tauc_w[k]*P3ibca(R3r,R3i,dt,t1,t2,t3,tau1,tau2,tau3,cond);

tgral=tgral+taua_w[i]*taub_w[j]*tauc_w[k]*P3bca(R3r,R3i,dt,t1,t2,t3,tau1,tau2,tau3,cond);

        //cout<<"iteration
        "<<i<<"\t"<<j<<"\t"<<k<<"\t"<<x[0]<<"\t"<<x[1]<<"\t"<<x[2]<<"\t"<<"P3-3:
        "<<P3bca(R3r,R3i,dt,t1,t2,t3,tau1,tau2,tau3,cond)<<endl;
    }
    else// tau_c = tau_b > tau_a
    {
        t1=x[2]-x[1],t2=x[1]-x[0],t3=x[0];

        //if(t1>500||t1<=-1||t2>500||t2<=-1||t3>700||t3<=-1) cout<<"P3r-4 t:
        "<<t1<<" "<<t2<<" "<<t3<<" tau: "<<x[0]<<" "<<x[1]<<" "<<x[2]<<endl;

//re+=taua_w[i]*taub_w[j]*tauc_w[k]*P3rcba(R3r,R3i,dt,t1,t2,t3,tau1,tau2,tau3,cond);

//im+=taua_w[i]*taub_w[j]*tauc_w[k]*P3icba(R3r,R3i,dt,t1,t2,t3,tau1,tau2,tau3,cond);

tgral=tgral+taua_w[i]*taub_w[j]*tauc_w[k]*P3cba(R3r,R3i,dt,t1,t2,t3,tau1,tau2,tau3,cond);

        //cout<<"iteration
        "<<i<<"\t"<<j<<"\t"<<k<<"\t"<<x[0]<<"\t"<<x[1]<<"\t"<<x[2]<<"\t"<<"P3-4:
        "<<P3cba(R3r,R3i,dt,t1,t2,t3,tau1,tau2,tau3,cond)<<endl;
    }
}
else //(x[2]>x[1])
{
    if(x[0]>=x[2])// tau_a >= tau_c > tau_b
    {
        t1=x[0]-x[2],t2=x[2]-x[1],t3=x[1];

```

```

//if(t1>500||t1<=-1||t2>2400||t2<=-1||t3>700||t3<=-1) cout<<"P1r-5 t:
"<<t1<<" "<<t2<<" "<<t3<<" tau: "<<x[0]<<" "<<x[1]<<" "<<x[2]<<endl;

//re+=taua_w[i]*taub_w[j]*tauc_w[k]*P1racb(R1r,R1i,dt,t1,t2,t3,tau1,tau2,tau3,cond);

//im+=taua_w[i]*taub_w[j]*tauc_w[k]*P1iacb(R1r,R1i,dt,t1,t2,t3,tau1,tau2,tau3,cond);

tgral=tgral+taua_w[i]*taub_w[j]*tauc_w[k]*P1acb(R1r,R1i,dt,t1,t2,t3,tau1,tau2,tau3,cond);

//cout<<"iteration
"<<i<<"\t"<<j<<"\t"<<k<<"\t"<<x[0]<<"\t"<<x[1]<<"\t"<<x[2]<<"\t"<<"P1-5:
"<<P1acb(R1r,R1i,dt,t1,t2,t3,tau1,tau2,tau3,cond)<<endl;
}
else if(x[0]>=x[1])// tau_c > tau_a >= tau_b
{
t1=x[2]-x[0],t2=x[0]-x[1],t3=x[1];

//if(t1>500||t1<=-1||t2>2400||t2<=-1||t3>700||t3<=-1) cout<<"P2r-6 t:
"<<t1<<" "<<t2<<" "<<t3<<" tau: "<<x[0]<<" "<<x[1]<<" "<<x[2]<<endl;

//re+=taua_w[i]*taub_w[j]*tauc_w[k]*P2rcab(R2r,R2i,dt,t1,t2,t3,tau1,tau2,tau3,cond);

//im+=taua_w[i]*taub_w[j]*tauc_w[k]*P2icab(R2r,R2i,dt,t1,t2,t3,tau1,tau2,tau3,cond);

tgral=tgral+taua_w[i]*taub_w[j]*tauc_w[k]*P2cab(R2r,R2i,dt,t1,t2,t3,tau1,tau2,tau3,cond);

//cout<<"iteration
"<<i<<"\t"<<j<<"\t"<<k<<"\t"<<x[0]<<"\t"<<x[1]<<"\t"<<x[2]<<"\t"<<"P2-6:
"<<P2cab(R2r,R2i,dt,t1,t2,t3,tau1,tau2,tau3,cond)<<endl;
}
else// tau_c > tau_b > tau_a
{
t1=x[2]-x[1],t2=x[1]-x[0],t3=x[0];

//if(t1>500||t1<=-1||t2>500||t2<=-1||t3>700||t3<=-1) cout<<"P3r-4 t:
"<<t1<<" "<<t2<<" "<<t3<<" tau: "<<x[0]<<" "<<x[1]<<" "<<x[2]<<endl;

//re+=taua_w[i]*taub_w[j]*tauc_w[k]*P3rcba(R3r,R3i,dt,t1,t2,t3,tau1,tau2,tau3,cond);

//im+=taua_w[i]*taub_w[j]*tauc_w[k]*P3icba(R3r,R3i,dt,t1,t2,t3,tau1,tau2,tau3,cond);

```

```

tgral=tgral+taua_w[i]*taub_w[j]*tauc_w[k]*P3cba(R3r,R3i,dt,t1,t2,t3,tau1,tau2,tau3,cond);

        //cout<<"iteration
" << i << "\t" << j << "\t" << k << "\t" << x[0] << "\t" << x[1] << "\t" << x[2] << "\t" << "P3-7:
" << P3cba(R3r,R3i,dt,t1,t2,t3,tau1,tau2,tau3,cond) << endl;
    }
}
}
}

//tgral=re+I*im;

return tgral;
}

```

A.5 Amoeba and Amotry

Amoeba.h

```
#ifndef _AMOEBEA
#define _AMOEBEA
#include "Header.h"
```

```
void amoeba(Mat_IO_DP &p, Vec_IO_DP &y, const DP ftol, int &nfunk, const
Vector<double> &t, double ***S, double ***R1r, double ***R1i, double ***R2r, double
***R2i, double ***R3r, double ***R3i, const int &i1, const int &j1, const int &k1, const int
&i2, const int &j2, const int &k2, const int &i3, const int &j3, const int &k3, const int &dt,
const Vec_DP &tau1, const Vec_DP &tau1i, const Vec_DP &tau2, const Vec_DP &tau3,
const Vec_DP &tau3i, const double &PD, Vector<double> &peakshift);
```

```
#endif
```

Amoeba.cc

//based on code from W.H. Press, S.A. Teukolsky, W.T. Vetterling and B.P. Flannery,
Numerical Recipes in C++ (Cambridge University Press, Cambridge, 2002).

```
#include "Header.h"
```

```
using namespace std;
```

```
namespace {
    inline void get_psum(Mat_I_DP &p, Vec_O_DP &psum)
    {
        int i,j;
        DP sum;

        int mpts=p.nrows();
        int ndim=p.ncols();
        for (j=0;j<ndim;j++) {
            for (sum=0.0,i=0;i<mpts;i++)
                sum += p[i][j];
            psum[j]=sum;
        }
    }
}
```

```

    }
}

```

```

void amoeba(Mat_IO_DP &p, Vec_IO_DP &y, const DP ftol, int &nfunk, const
Vector<double> &t, double ***S, double ***R1r, double ***R1i, double ***R2r, double
***R2i, double ***R3r, double ***R3i, const int &i1, const int &j1, const int &k1, const int
&i2, const int &j2, const int &k2, const int &i3, const int &j3, const int &k3, const int &dt,
const Vec_DP &tau1, const Vec_DP &tau1i, const Vec_DP &tau2, const Vec_DP &tau3,
const Vec_DP &tau3i, const double &PD, Vector<double> &peakshift)

```

```

{
    const int NMAX=5000;
    const DP TINY=1.0e-10;
    int i,ih,i,ilo,inhi,j,k;
    DP rtol,ysave,ytry;

    int mpts=p.nrows();
    int ndim=p.ncols();
    Vec_DP psum(ndim);
    nfunk=0;
    get_psum(p,psum);
    for (;) {

        ilo=0;
        ih = y[0]>y[1] ? (inhi=1,0) : (inhi=0,1);
        for (i=0;i<mpts;i++) {
            if (y[i] <= y[ilo]) ilo=i;
            if (y[i] > y[ihi]) {
                inhi=ihi;
                ih=i;
            } else if (y[i] > y[inhi] && i != ih) inhi=i;
        }
        rtol=2.0*fabs(y[ihi]-y[ilo])/(fabs(y[ihi])+fabs(y[ilo])+TINY);
        if (rtol < ftol) {
            SWAP(y[0],y[ilo]);
            for (i=0;i<ndim;i++) SWAP(p[0][i],p[ilo][i]);
            break;
        }
        if (nfunk >= NMAX) NR::nrerror("NMAX exceeded");
        nfunk += 2;
        ytry=amotry(p,y,psum,ih,-
1.0,t,S,R1r,R1i,R2r,R2i,R3r,R3i,i1,j1,k1,i2,j2,k2,i3,j3,k3,dt,tau1,tau1i,tau2,tau3,tau3i,PD,pea
kshift);

        if (ytry <= y[ilo])

```

```

ytry=amotry(p,y,psum,ihl,2.0,t,S,R1r,R1i,R2r,R2i,R3r,R3i,i1,j1,k1,i2,j2,k2,i3,j3,k3,dt
,tau1,tau1i,tau2,tau3,tau3i,PD,peakshift);

```

```

    else if (ytry >= y[ihl]) {
        ysave=y[ihl];

```

```

ytry=amotry(p,y,psum,ihl,0.5,t,S,R1r,R1i,R2r,R2i,R3r,R3i,i1,j1,k1,i2,j2,k2,i3,j3,k3,dt
,tau1,tau1i,tau2,tau3,tau3i,PD,peakshift);

```

```

        if (ytry >= ysave) {
            for (i=0;i<mpts;i++) {
                if (i != ilo) {
                    for (j=0;j<ndim;j++){
                        p[i][j]=psum[j]=0.5*(p[i][j]+p[ilo][j]);
                    }
                }
                //y[i]=funkt(psum);

```

```

y[i]=fitPS(psum,t,S,R1r,R1i,R2r,R2i,R3r,R3i,i1,j1,k1,i2,j2,k2,i3,j3,k3,dt,tau1,tau1i,tau2,tau3
,tau3i,PD,peakshift);

```

```

        }
    }
    nfunk += ndim;
    get_psum(p,psum);
}
} else --nfunk;

```

```

cout<<"iteration: "<<nfunk<<" value: "<<ytry<<endl;

```

```

//save the current fit values
ofstream fout("currentfit.dat");
fout<<"iteration: "<<nfunk<<" value: "<<ytry<<endl;
for(k=0;k<8;k++)
{
    fout<<psum[k]/9<<endl;
}
fout.close();

```

```

}
}

```


Amotry.h

```
#ifndef _AMOTRY
#define _AMOTRY
#include "Header.h"
```

```
DP amotry(Mat_IO_DP &p, Vec_O_DP &y, Vec_IO_DP &psum, const int ihi, const DP
fac, const Vector<double> &t, double ***S, double ***R1r, double ***R1i, double ***R2r,
double ***R2i, double ***R3r, double ***R3i, const int &i1, const int &j1, const int &k1,
const int &i2, const int &j2, const int &k2, const int &i3, const int &j3, const int &k3, const
int &dt, const Vec_DP &tau1, const Vec_DP &tau1i, const Vec_DP &tau2, const Vec_DP
&tau3, const Vec_DP &tau3i, const double &PD, Vector<double> &peakshift);
```

```
#endif
```

Amotry.cc

```
//based on code from W.H. Press, S.A. Teukolsky, W.T. Vetterling and B.P. Flannery,
Numerical Recipes in C++ (Cambridge University Press, Cambridge, 2002).
```

```
#include "Header.h"
```

```
DP amotry(Mat_IO_DP &p, Vec_O_DP &y, Vec_IO_DP &psum, const int ihi, const DP
fac, const Vector<double> &t, double ***S, double ***R1r, double ***R1i, double ***R2r,
double ***R2i, double ***R3r, double ***R3i, const int &i1, const int &j1, const int &k1,
const int &i2, const int &j2, const int &k2, const int &i3, const int &j3, const int &k3, const
int &dt, const Vec_DP &tau1, const Vec_DP &tau1i, const Vec_DP &tau2, const Vec_DP
&tau3, const Vec_DP &tau3i, const double &PD, Vector<double> &peakshift)
```

```
{
    int j;
    DP fac1,fac2,ytry;

    int ndim=p.ncols();
    Vec_DP ptry(ndim);
    fac1=(1.0-fac)/ndim;
    fac2=fac1-fac;
    for (j=0;j<ndim;j++)
        ptry[j]=psum[j]*fac1-p[ihi][j]*fac2;
```

```
ytry=fitPS(ptry,t,S,R1r,R1i,R2r,R2i,R3r,R3i,i1,j1,k1,i2,j2,k2,i3,j3,k3,dt,tau1,tau1i,tau2,tau3,tau3i,PD,peakshift);
```

```
//ytry=funk(ptry);  
if (ytry < y[ihi]) {  
    y[ihi]=ytry;  
    for (j=0;j<ndim;j++) {  
        psum[j] += ptry[j]-p[ihi][j];  
        p[ihi][j]=ptry[j];  
    }  
}  
return ytry;  
}
```

A.6 Complex class

Complex.h

```
// a template complex class
#ifndef COMPLEX_H_
#define COMPLEX_H_

#include <iostream>
#include <cmath>

using namespace std;

// template prototypes
template <typename T> T Abs(T x); //operator+(T x);

// template Complex
template <class T = float>
class Complex
{
private:
    T real;
    T imag;
public:
    Complex(T re, T im=0) :real(re) ,imag(im) {} // constructor
    Complex() :real(0), imag(0) {} // default constructor
    ~Complex() {} // destructor
    Complex<T> (const Complex<T> & c); // copy constructor
    Complex<T> & operator= (const Complex<T> & c); //assignment operator
    T Real() const {return real;}
    T Imag() const {return imag;}
    friend ostream & operator<< <T>(ostream & os, const Complex<T> & c);
    // mathematical operators
    friend T Abs <>(const Complex<T> & c);
    friend Complex<T> Conj <>(const Complex<T> & c);
    friend Complex<T> operator- <>(const Complex<T> & c);
    friend Complex<T> Exp <>(const Complex<T> & c);
    friend Complex<T> operator+ <>(const Complex<T> & c1, const Complex<T> & c2);
    friend Complex<T> operator- <>(const Complex<T> & c1, const Complex<T> & c2);
    friend Complex<T> operator* <>(const Complex<T> & c1, const Complex<T> & c2);
    friend Complex<T> operator/ <>(const Complex<T> & c1, const Complex<T> & c2);
};

//copy constructor
```

```

template<typename T>
Complex<T>::Complex<T>(const Complex<T> & c)
{
    real = c.real;
    imag = c.imag;
}

//assignment operator
template<typename T>
Complex<T> & Complex<T>::operator= (const Complex<T> & c)
{
    if (this == &c)
        return *this;
    real = c.real;
    imag = c.imag;
    return *this;
}

// output operator
template<typename T>
ostream & operator<< (ostream & os, const Complex<T> & c)
{
    os << c.real << " + " << c.imag << "i";
    return os;
}

// mathematical operators

template<typename T>
T Abs (const Complex<T> & c)
{
    return sqrt(1.0*c.real*c.real + 1.0*c.imag*c.imag); //multiply by 1.0 for ints
}

template<typename T>
Complex<T> Conj(const Complex<T> & c)
{
    return Complex<T>(c.real, -c.imag);
}

template<typename T>
Complex<T> operator- (const Complex<T> & c)
{
    return Complex<T>(-c.real, -c.imag);
}

```

```

template<typename T>
Complex<T> Exp (const Complex<T> & c)
{
    return Complex<T>(exp(1.0*c.real)*cos(1.0*c.imag), exp(1.0*c.real)*sin(1.0*c.imag));
//multiply by 1.0 for ints
}

template<typename T>
Complex<T> operator+ (const Complex<T> & c1, const Complex<T> & c2)
{
    return Complex<T>(c1.real + c2.real, c1.imag + c2.imag);
}

template<typename T>
Complex<T> operator- (const Complex<T> & c1, const Complex<T> & c2)
{
    return Complex<T>(c1.real - c2.real, c1.imag - c2.imag);
}

template<typename T>
Complex<T> operator* (const Complex<T> & c1, const Complex<T> & c2)
{
    return Complex<T>(c1.real*c2.real - c1.imag*c2.imag, c1.real*c2.imag + c1.imag*c2.real);
}

template<typename T>
Complex<T> operator/ (const Complex<T> & c1, const Complex<T> & c2)
{
    return Complex<T>((c1.real*c2.real + c1.imag*c2.imag)/(c2.real*c2.real +
c2.imag*c2.imag),(c1.real*(-c2.imag) + c1.imag*c2.real)/(c2.real*c2.real +
c2.imag*c2.imag));
}

#endif

```

Christopher J. Fecko

cfecko@mit.edu

1122 Evergreen Drive
Wilmington, MA 01887

Work: 617-253-7372
Home: 978-988-3621

Education

Massachusetts Institute of Technology

Cambridge, MA

Doctor of Philosophy in Chemistry, June 2004

Advisor: Andrei Tokmakoff, Ph.D.

Dissertation: Spectroscopic investigations of hydrogen bonding in liquid water

Swarthmore College

Swarthmore, PA

Bachelor of Arts in Chemistry, High Honors, May 1998

Bachelor of Arts in Physics, May 1998

Advisor: Thomas A. Stephenson, Ph.D.

Thesis: Collision induced electronic transitions from the $E(0_g^+)$ ($v=0$) state of iodine

Research Expertise

- IR, Raman and optical spectroscopy
- Time-resolved nonlinear spectroscopy
- Laser induced fluorescence
- Lasers, nonlinear optics and optical devices
- Chemical reaction dynamics
- Computer assisted data modeling

Research Experience

Doctoral Research (1998 – present)

MIT Department of Chemistry

- Performed time-resolved infrared spectroscopy on water to elucidate transient structural information and dynamics associated with hydrogen bonding in liquid water
- Developed experimental technique for a novel Raman spectroscopic measurement of molecular motions in liquids, leading to observation of a new intermolecular vibrational band in water
- Built a cavity-dumped Ti:sapphire laser for the production of 15 fs, 25 nJ near-infrared pulses
- Designed and fabricated a novel BBO/KNbO₃ optical parametric amplifier, which produces the shortest duration mid-infrared pulses (42 fs) reported to date
- Responsible for selecting, purchasing and interfacing all equipment required to build a fully functional \$500,000 time-resolved infrared laser laboratory from the ground up
- Wrote extensive C++ code to model experimental data

Industrial Research (Summer Intern 1998)

The Liposome Company, Princeton, NJ

Supervisor: Walter R. Perkins, Ph.D.

- Determined drug mobility within liposome by measuring fluorescence anisotropy and electron spin resonance (ESR) order parameters
- Assisted in synthetic modification of existing drugs to increase molecular hydrophobicity

Undergraduate Honors Research (1996 – 1998)

Swarthmore College Department of Chemistry

- Performed laser induced fluorescence studies to investigate gas phase energy transfer during collisions between electronically excited I₂ molecules and inert collision partners
- Maintained Quantel and Laser Photonics Nd:YAG, Nitrogen and dye lasers
- Developed a capillary electrophoresis based technique for measuring the dissociation constants of various charged molecules and chiral, uncharged alpha-cyclodextrin
- Gained additional research experience performing one and two dimensional NMR, gas chromatography, HPLC, and mass spectroscopy

Teaching Experience

Teaching Assistant (1998 – 2002)

MIT Department of Chemistry

- Recitation instructor in undergraduate “Thermodynamics and Kinetics” class
- Laboratory instructor in the spectroscopy section of an advanced undergraduate laboratory class
- Substitute lecturer in graduate quantum mechanics class on several occasions

Teaching Assistant (1996 – 1998)

Swarthmore College Department of Chemistry

- Assisted in teaching general, organic, analytical and inorganic chemistry laboratory classes

Publications

1. Fecko, C.J., Eaves, J.D., Loparo, J.J., Tokmakoff, A., Geissler, P.L., Ultrafast hydrogen bond dynamics in the infrared spectroscopy of water. *Science*. **301**, 1698 (2003).
2. Eaves, J.D., Fecko, C.J., Stevens, A.L., Peng, P., Tokmakoff, A., Polarization-selective femtosecond Raman spectroscopy of low-frequency motions in hydrated protein films. *Chem. Phys. Lett.* **376**, 20 (2003).
3. Fecko, C.J., Eaves, J.D., Tokmakoff, A., Isotropic and anisotropic Raman scattering from molecular liquids measured by spatially masked optical Kerr effect spectroscopy. *J. Chem. Phys.* **117**, 1139-1154 (2002).
4. Fecko, C.J., Freedman, M.A., Stephenson, T.A., Collision-induced electronic energy transfer from $v = 0$ of the E(0g⁺) ion-pair state in I₂: Collisions with He and Ar. *J. Chem. Phys.* **116**, 1361-1369 (2002).
5. Fecko, C.J., Freedman, M.A., Stephenson, T.A., Collision-induced electronic energy transfer from $v = 0$ of the E(0g⁺) ion-pair state in I₂: Collisions with I₂(X). *J. Chem. Phys.* **115**, 4132-4138 (2001).
6. Perkins, W.R., Ahmad, I., Li, X., Hirsh, D.J., Masters G.R., Fecko, C.J., Lee, J., Ali, S., Nguyen, J., Schupsky, J., Herbert, C., Janoff, A.S., Mayhew, E., Novel therapeutic nanoparticles (lipocores): Trapping poorly water soluble compounds. *Int. J. Pharm.* **200**, 27-39 (2000).
7. Khalil, M., Demirdoven, N., Golonzka, O., Fecko, C.J., Tokmakoff, A., A phase-sensitive detection method using diffractive optics for polarization-selective femtosecond Raman spectroscopy. *J. Phys. Chem. A* **104**, 5711-5715 (2000).
8. Khalil, M., Golonzka, O., Demirdoven, N., Fecko, C.J., Tokmakoff, A., Polarization-selective femtosecond Raman spectroscopy of isotropic and anisotropic vibrational dynamics in liquids. *Chem. Phys. Lett.* **321**, 231-237 (2000).

Selected Presentations

1. Fecko, C.J., Loparo, J.J., Eaves, J.D., Geissler, P.L., Tokmakoff, A., “Hydrogen Bond Dynamics In the Ultrafast Infrared Spectroscopy of Water” Oral presentation as part of the Modern Optics and Spectroscopy Seminary Series at MIT. October 2003.
2. Fecko, C.J., Eaves, J.D., Loparo, J.J., Geissler, P.L., Tokmakoff, A., “Vibrational dynamics of liquid water observed by vibrational echo peak shift spectroscopy” Oral presentation at the 225th Meeting of the American Chemical Society, New Orleans, LA. March 2003.
3. Fecko, C.J., Eaves, J.D., Tokmakoff, A., “Polarization selective Raman spectroscopy of liquids” Invited oral presentation at the American Chemical Society New England Regional Meeting, Durham, NH. June 2001.

Professional Memberships:

Phi Beta Kappa
Sigma Xi Scientific Research Society
American Chemical Society